FUNDAMENTAL STUDIES OF THE INTERACTION BETWEEN FEMTOSECOND LASER AND PATTERNED MONOLAYER PLASMONIC NANOSTRUCTURES

A Dissertation
Presented to
The Academic Faculty

by

Wenyu Huang

In Partial Fulfillment
of the Requirements for the Degree
Doctor of Philosophy in the
School of Chemistry and Biochemistry

Georgia Institute of Technology
August 2007

FUNDAMENTAL STUDIES OF THE INTERACTION BETWEEN FEMTOSECOND LASER AND PATTERNED MONOLAYER PLASMONIC NANOSTRUCTURES

Approved by:

Dr. Mostafa A. El-Sayed, Advisor
School of Chemistry and Biochemistry
Georgia Institute of Technology

Dr. Robert L. Whetten
School of Chemistry and Biochemistry
Georgia Institute of Technology

Dr. Joseph W. Perry
School of Chemistry and Biochemistry
Georgia Institute of Technology

Dr. Z. John Zhang
School of Chemistry and Biochemistry
Georgia Institute of Technology

Dr. Mohan Srinivasarao
School of Polymer, Textile and Fiber Engineering
Georgia Institute of Technology

Date Approved: June 26, 2007

Dedicated To My Family

ACKNOWLEDGEMENTS

I would like to give my dearest thanks and deepest respect to my supervisor *Professor Mostafa A. El-Sayed* for giving me the great opportunity to do my PhD studies at the Laser Dynamics Laboratory, School of Chemistry and Biochemistry, Georgia Institute of Technology. He is an incredible person with outstanding motivation abilities and profound knowledge. His guidance and inspiration helped me to grow as a better scientist and stronger person.

I also would like to express my appreciation and thanks to the members of my committee who have provided me knowledge, insight, and experience helping throughout my work.

Many thanks go to both past and present group members of the Laser Dynamics Laboratory for their help, support, friendship, and for the many interesting and useful discussions. Especially I would like to thank *Dr. Wei Qian* for the femtosecond experiment and valuable discussions on my research. I would like to thank *Mr. Tabor Christopher*, who gave me great help with my English writing. I wish them all the best in their research and career. I would also like to thank all of my friends in Georgia Institute of Technology who made my life greatly enjoyable.

Finally, I would like to extend a special thank you to my wife, my parents, my brother and sister. I could not have accomplished all that I have in my life without their love and support. I cannot express the depth of my appreciation for their love, understanding, and support for me as I pursued my degree.

TABLE OF CONTENTS

Page

ACKNOWLEDGEMENTS iv

LIST OF TABLES ix

LIST OF FIGURES x

SUMMARY xxiii

CHAPTER

1 INTRODUCTION 1

1.1 Optical Properties of Plasmonic Nanoparticles 4

1.2 Nanosphere Lithography in Making Nanoparticles 11

1.3 Electron-Phonon Relaxation in Plasmonic Nanoparticles 22

1.4 Coherent Lattice (Phonon) Oscillation in Plasmonic Nanoparticles 27

1.5 Optical Modulation 37

1.6 Pulsed Laser Photothermal Annealing of Plasmonic Nanoparticles 42

1.7 Thesis Focus and Organization 48

1.8 References 52

2 FABRICATION AND CHARACTERIZATION OF METALLIC NANOPARTICLE ARRAYS 64

2.1 Nanosphere Lithography 64

2.2 Angle-Resolved Nanosphere Lithography 71

2.3 Electron Beam Lithography 73

2.4 Scanning Electron Microscopy and Transmission Electron Microscopy 74

2.5 Absorption Spectroscopy 75

2.6 Femtosecond Pump-Probe Transient Transmission Spectroscopy · · · · · 76

2.7 Femtosecond Photothermal Annealing and Ablation · · · · · · · · · · · · · · · · 77

2.8 References · 79

3 THE EFFECT OF LATTICE CRYSTALLINITY ON ELECTRON-PHONON RELAXATION RATES IN GOLD NANOPARTICLES · · · · · · · · · 80

3.1 Introduction · 81

3.2 Experimental Section · 84

3.3 Results and Discussion · 85

3.4 Conclusion · 98

3.5 References · 100

4 COHERENT PHONON OSCILLATIONS IN GOLD PRISMATIC MONOLAYER PERIODIC NANOPARTICLE ARRAYS · · · · · · · · · · · · · · · 103

4.1 Introduction · 104

4.2 Experimental Section · 105

4.3 Results and Discussion · 107

4.4 Conclusion · 128

4.5 References · 129

5 COHERENT PHONON OSCILLATIONS IN SILVER AND GOLD MONOLAYER PERIODIC NANOPRISM ARRAYS: THE EFFECT OF INTERPARTICLE INTERACTION · · · · · · · · · · · · · · · · · · ·

6 THE DISTANCE DEPENDENCE OF THE EFFECT OF SURFACE PLASMON FIELD ON THE COHERENT LATTICE PHONON OSCILLATION IN ELECTRON BEAM NANOFABRICATED GOLD PARTICLE PAIRS 159

6.1 Introduction 160

6.2 Experimental Section 162

6.3 Results and Discussion 164

6.4 Conclusion 176

6.5 References 177

7 GIGAHERTZ OPTICAL MODULATION RESULTING FROM COHERENT LATTICE OSCILLATIONS INDUCED BY FEMTOSECOND LASER PUMPING OF 2D PHOTONIC CRYSTALS OF GOLD CAPPED POLYSTYRENE MICRO-SPHERES 180

7.1 Introduction 181

7.2 Experimental Section 183

7.3 Results and Discussion 185

7.4 Conclusion 197

7.5 References 199

8 PHOTOTHERMAL RESHAPING OF PRISMATIC GOLD NANOPARTICLES IN PERIODIC MONOLAYER ARRAYS BY FEMTOSECOND LASER PULSES 202

8.1 Introduction 203

8.2 Experimental Section 204

8.3 Results and Discussion 207

8.4 Conclusion 221

8.5 References 223

9 GOLD NANOPARTICLE PROPULSION FUELED BY ABSORPTION OF FEMTOSECOND LASER PULSE AT THEIR SURFACE PLASMON RESONANCE 227

9.1 Introduction 228
9.2 Experimental Section 229
9.3 Results and Discussion 230
9.4 Conclusion 243
9.5 References 244
APPENDIX: LIST OF PUBLICATIONS 245

LIST OF TABLES

Page

Table 1-1: The structural parameters of nanoparticles that show the extinction spectra in Figure 1-7 18

Table 4-1: Comparison of the observed and calculated oscillation amplitude for the 104 and 166 nm array particles at different probe wavelengths 127

LIST OF FIGURES

Page

Figure 1-1: The excitation of a dipolar localized surface plasmon polariton by the electric field of an incident light wave of frequency $v = v_{sp} = 1/T$ · · · · · · · 5

Figure 1-2: Images of the Lycurgus Cup that was made by Roman around the fourth century AD. When illuminate from the outside, it shows green (a). When illuminate from the inside, it glows red (b). The cup was made of glass but contains about 40 parts per million of gold and about 300 parts per million of silver. It was later discovered that the cup contains gold and silver nanoparticles of ~ 70 nm · · · · · · · · · · · · · · · · · 5

Figure 1-3: (a) Size dependent LSPR absorption of spherical gold nanoparticles. (b) Size dependent plasmon bandwidth. (c) Size dependent molar absorption coefficient, which shows a linear dependence on double logarithmic scales · · · · · · · · · · · · · · · · ·

Figure 1-8: (a) The LSPR band of a single Ag nanoparticle in various media (left to right): nitrogen, methanol, 1-propanol, chloroform, and benzene. (b) The linear dependence of the LSPR extinction maximum on the refractive index of the medium · · ·

Figure 1-14: (a) A schematic diagram of the breathing mode of the coherent lattice (phonon) oscillation of a spherical plasmonic nanoparticle. The lattice oscillation changes the size of the nanoparticle and the free electron density in the nanoparticle. The LSPR band oscillates with the change of the free electron density in the nanoparticle. (b) If the LSPR band oscillation is monitored at a fixed wavelength (green line in (a)), the intensity of the transmission light will be modulated at the same frequency as the coherent lattice oscillation · · · · · · · · · · · · · · · · · · · 32

Figure 1-15: The extensional mode and the breathing mode of a vibrating cylinder (larger aspect ratio). The breathing mode is characterized by a pure expansion and contraction along the transversal (radial) direction of the rod, while the extensional mode involved dimension changes in both transversal and longitudinal directions · 35

Figure 1-16: The effective absorption coefficient spectra of a germanium quantum-well structure on silicon, which shows a strong quantum confined stark effect with the applied electric field from zero to 4 volts · · · · · · · · · · · · · · · · · · ·

Figure 2-2: An optical microscope image of a 70×53 μm nanosphere mask formed via natural self-assembly · · · · · 67

Figure 2-3: A SEM image of the monolayer of PS spheres made with air-water interface self-assembly. (a) and (b) are low and high magnification images of the closely packed PS sphere monolayer, respectively. (c) is an optical image of the PS sphere monolayer. The greenish color is due to the diffraction of the visible light by the PS sphere crystal, which shows the PS sphere monolayer can cover the substrate in square centimeter scale · · · · · 70

Figure 2-4: Scheme of the apparatus used for AR-NSL. The angle between the atomic beam propagation and the substrate surface normal is represented by θ · · · · · 72

Figure 2-5: SEM image of monolayer periodic gold nanoparticle arrays fabricated with the atomic beam of the gold deposition (a) being perpendicular to the PS sphere monolayer or (b) having 30 degree to the surface normal of the PS sphere monolayer. Two steps of 30 nm gold deposition each at $\theta = 0^o$ and $\theta = 30^o$ is performed to form the nanostructure shown in (c) · · · · · 72

Figure 2-6: Scheme of electron beam lithography. If the substrate is insulator, a thin layer of gold (~ 10 nm) is deposited before electron beam writing to dissipate excess electrons from the substrate · · · · · 74

Figure 2-7: The schematic diagram of the pump-probe transient transmission spectroscopy. The time delay between the pump and probe pulses is tuned by a computer controlled optical delay line with a spatial resolution of 3 μm (temporal resolution of 20 fs) · · · · · 77

Figure 2-8: The schematic diagram of the apparatus for femtosecond photothermal annealing and ablation experiments · · · · · 78

Figure 3-1: (a) and (b) are SEM images of the gold nanoprism and nanosphere arrays, respectively. The periodic arrays of spherical gold nanoparticles are formed by thermal annealing the original prismatic gold nanoparticle arrays sample in an oven at 1000 ^{o}C for 90 seconds · · 86

Figure 3-2: (a) is a TEM image of the gold nanoprism array. After *in situ* heading the sample to 771 ^{o}C in the TEM chamber, the morphology of gold particles is more like spherical array, which is displayed in (b). The different grain size of gold particles in nanoprism and nanosphere arrays can be identified in their dark-field TEM images, which are displayed in (c) and (d), respectively · · · · · 87

Figure 3-3: (a) and (b) are dark-field TEM images of a gold nanoprism and a nanosphere respectively. The different contrast in the dark-field image (a) indicates that the as-deposited gold nanoparticle is polycrystalline. The well-observed thickness fringes in the dark-field image of the nanosphere indicate that the thermal annealed particle is a single grain. The polycrystalline and single crystalline structures of nanoprism and nanosphere can be further confirmed by their selected-area electron diffraction patterns, which are displayed in (c) and (d), respectively · · ·

Figure 4-3: The dependence of the wavelength maxima (λ_{max}) of the surface plasmon absorption spectra on the size of gold spherical nanoparticles [1,27] (●) and prismatic array nanoparticles (▲). This illustrates the much more pronounced sensitivity of λ_{max} on the size of prismatic nanoparticles compared to spherical nanoparticles. For gold spherical nanoparticles, the plasmon absorption maximum increases by 0.64 nm for every 1 nm increase in the diameter of nanospheres. For gold prismatic array nanoparticles, the plasmon absorption maximum increases by 4.4 nm for every 1 nm increase in the bisector, *a*, of the nanoprism · · ·

Figure 4-8: The wavelength dependence of the amplitude (the % transmission change of the monitoring light as a result of laser pump) and phase (the sign of the change) resulting from the coherent lattice phonon oscillation in a = 104 nm (a) and a = 166 nm (b) gold particle arrays. The observed oscillation is fitted to a damped cosine function (dash line). It is interesting to observe that as we decrease the monitoring wavelength of the bleach created by the 400 nm pump laser, the amplitude decreases, reaches zero value (i.e. the oscillation disappears), and then reappears with opposite sign (phase). From the wavelength at which the oscillation disappears, the absorption maximum, and its dependence on size, the change in the nanoparticle size during the oscillation is estimated · 123

Figure 4-9: Estimation of the size change during lattice symmetric vibration. The black spectrum is the Lorentzian fit of the experimental absorption spectrum of the gold array sample of nanoparticle of size a = 104 (a) and 166 nm (b). The blue and the red spectra correspond to the assumed absorption spectra of the vibrating nanoparticle at its extreme contracting (blue) and its extreme expanding configuration (red), respectively (see text). Each of the colored spectra are drawn with the same band width but at half the integrated intensity of that of the observed non-vibrating nanoparticles (black spectrum). The energies of the maxima of the colored spectra are adjusted so that the difference between the sum of their intensity and that of the black spectra disappear at the observed wavelength (indicated by the dashed vertical lines) where the oscillation amplitude disappears · · · · · 126

Figure 5-1: SEM images of the prismatic silver (a-c) and gold (d-f) nanoparticles monolayer arrays (in white color) made with nanosphere lithograph technique. The black spheres represent the positions of the PS spheres mask that is used during the Au deposition. The diameters of the PS spheres are 0.26 (a, d), 0.36 (b, e) and 0.45 μm (c, f), respectively. The deposition thickness is 30 nm. (g) Low magnification SEM image of a silver nanoparticles monolayer arrays made with 0.26 μm PS spheres mask. The scale bars in (a-f) represent 250 nm · · · · · · · · · · · · · · · · · · ·

Figure 5-3: The dependence of the melting temperature on the radius of spherical gold and silver nanoparticles. The calculation is based on the solid-liquid interfacial tension γ_{sl} = 2 N m^{-1} and the melting layer thickness $\delta = 0.25r$ · · ·

Figure 5-7: (a) The unit cell (in solid line) of the monolayer periodic nanoparticle arrays, which have two particles per unit cell. (b) The proposed coupling model for the nanoparticles of the array samples. The energy of the system will decrease first by D due to the interaction between an excited particle with its unexcited partner and split by $2I$ due to energy exchange term according to the exciton dipolar coupling model. This model is found to explain the deviation of the experimental lattice vibration period from theoretical calculation based on single particle · · ·

Figure 7-1: (a) SEM image of a 50 nm gold capped PS sphere on quartz substrate. The PS spheres form a close-packed triangular monolayer lattice. (b) The 60^{o} view of the gold capped PS sphere monolayer array from a cleavage site. (c) The 90^{o} view (side view) of the gold capped PS sphere monolayer array from a cleavage site · 186

Figure 7-2: (a) The black spectrum is recorded on a close packed 740 nm PS sphere monolayer. After deposition of 50 nm Gold, the spectrum is shown by the red line. After lift-off of the PS sphere, the formed gold prismatic nanoparticle array shows a spectrum as the green line. The surface plasmon resonance band of the gold nanoparticle array is located at 997 nm. (b) The black spectrum is recorded on a close packed 600 nm PS sphere monolayer. After deposition of 50 nm Gold, the spectrum is shown by the red line · 188

Figure 7-3: The scaled (λ/D, D is the diameter of the PS sphere) transmission spectra of the PS sphere monolayer and the 50 nm gold capped PS monolayer. The spectra from the PS sphere monolayer of two different sizes are overlap with each other, which means the bands are come from the size dependent scattering. After gold coating, the dips of the transmission spectra of the two different sized PS sphere monolayer do not overlap with each other (slight shift), which could be due to the gold induced refractive index change and the surface plasmon absorption of gold (highly dependent on the dimension of the gold) · · · · · · · · · · · · · · · · · · ·

Figure 8-1: Micro-absorption spectra of a periodic monolayer array of prismatic gold nanoparticles after irradiation with 400 nm femtosecond laser pulses at different intensities. The numbers in the plot correspond to different power densities (W/cm^2) of the examined region on the substrate within the laser profile calculated by assuming the energy in the laser pulse has a Gaussian distribution. The arrow shows the energy density goes from low to high as one moves from the edge to the center of the laser irradiation profile on the array. The diameter of the laser spot on the array was 250 μm 208

Figure 8-2: The SEM images of periodic monolayer prismatic gold nanoparticle arrays at exposed regions within the laser pulse profile (i.e. at different laser power densities) (a) before and (b-e) after irradiation with 400 nm femtosecond laser. From the Gaussian laser energy distribution profile, the calculated laser energy densities are: (b) 3.1 (c) 3.5, (d) 3.9, and (e) 5.1 W/cm^2 210

Figure 8-3: A proposed energy potential curve of nanoparticle arrays of different shapes. The surface potential decreases as the original prismatic nanoparticle changes to a tripodal shape and finally to a spherical shape as the laser energy input increases. The tripodal shape is believed to be a metastable configuration during the transformation (the gold tripod nanoparticles have also been synthesized in solution) 212

Figure 8-4: Micro-absorption spectra of a periodic monolayer array of prismatic gold nanoparticles after 800 nm femtosecond laser irradiation at various intensities. The numbers in the plot correspond to different power densities (W/cm^2) of the examined region on the substrate within the laser profile, calculated by assuming the energy in the laser pulse has a Gaussian distribution. The arrow indicates that the energy density moves from low to high as the selected area shifts from the edge to the center of the laser irradiation profile on the array. The diameter of the laser spot on the array is 250 μm 215

Figure 8-5: SEM images of the periodic monolayer prismatic gold nanoparticle array at various exposed regions within the laser pulse profile (i.e. at different laser power densities) after irradiation with 800 nm femtosecond laser. From the Gaussian laser energy distribution profile, the calculated laser energy densities are (a) 2.1, (b) 3.0, (c) 4.5, (d) 5.0, (e) 5.6, and (f) 5.9 W/cm^2 216

Figure 8-6: Micro-absorption spectra of a periodic monolayer array of prismatic gold nanoparticles after irradiation with 700 nm femtosecond laser pulses at different intensities. The numbers in the plot correspond to various power densities (W/cm^2) of the examined region on the substrate within the laser profile calculated by assuming the energy in the laser pulse has a Gaussian distribution. The arrow shows the energy density increasing from low to high as the selected area moves from the edge to the center of the laser irradiation profile on the array. The diameter of the laser spot on the array is 250 μm 219

Figure 8-7: SEM images of the periodic monolayer prismatic gold nanoparticle arrays at exposed regions within the laser pulse profile (i.e. at different laser power densities) after irradiation with 700 nm femtosecond laser pulses. From the Gaussian laser energy distribution profile, the calculated laser densities are (a) 1.8, (b) 2.8, (c) 3.1, (d) 4.5, (e) 5.6, and (f) 6.0 W/cm^2 220

Figure 9-1: (a) An SEM image taken at the femtosecond laser irradiation area with a laser pulse energy density of 4.1 mJ/cm^2. It is clear that particles 1 and 2 stand up vertically, while particle 3 stands at a tilt. (b) Flying prismatic gold nanoprisms: The SEM image of assembled gold nanoprisms in a monolayer array after exposure to femtosecond laser pulses with an energy density of 5.1 mJ/cm^2. It is clear that particle 1 jumped from its original position, flew away, and then landed on top of another particle (green arrow). While maintaining its prismatic shape, it is reduced in size due to atomic ablation. Particles 2 and 3, which absorbed less energy, seem to be "stuck" at one corner but flipped over. The difference in the behavior depends on the intensity of the laser at each prism, the absorption profile of the individual nanoprism, and the anisotropy of the interaction at the substrate-nanoparticle interfaces 231

Figure 9-2: (a) An AFM image of a standing nanoparticle. The height of the standing particle is found to be very near the value of its bisector. This observation indicates that the particle is standing on its base. (b) The displaced prisms are thinner: An AFM image of a displaced nanoparticle. Its thickness (indicated by the red cursor) is thinner than the undisplaced one (indicated by the green cursor) 233

Figure 9-3: SEM images of Au array nanoparticles on the surface of a quartz substrate irradiated near the jumping threshold. From (a) to (c), the irradiation power increases 240

Figure 9-4: SEM images of Au nanoparticles in an array on the surface of a SiO_2 single crystal irradiated near the jumping threshold. From (a) to (c), the irradiation power increases 241

Figure 9-5: The horizontal displacement of jumping nanoparticles on rough quartz and smooth SiO_2 substrate 242

SUMMARY

This dissertation is focused on the interaction between femtosecond laser and patterned two-dimensional gold nanostructures. The sample was prepared by two different techniques, the nanosphere lithography and the electron beam lithography. Characterization was carried out with Scanning Electron Microscopy, Transmission Electron Microscopy, Atomic Force Microscopy, and UV-vis absorption spectroscopy. Femtosecond transient absorption spectroscopy was used to answer a number of fundamental questions regarding the interaction between femtosecond laser pulses and plasmonic nanoparticles.

Under a low density irradiation of a femtosecond laser, we examined the effect of the lattice crystallinity on the electron-phonon relaxation rates in monolayer periodic array nanoparticles prepared with nanosphere lithography. We found that the electron-phonon relaxation rate was faster in polycrystalline nanoparticles and decreases greatly when polycrystalline prismatic gold nanoparticles are annealed and transformed into single crystalline nanospheres. The fast electron-phonon relaxation in polycrystalline prismatic gold nanoparticles is explained by the presence of high density grain boundaries.

The ultrafast laser-induced coherent phonon oscillations in patterned gold nanoparticles are also fully characterized with the femtosecond transient transmission technique. We studied the effect of size, shape, thickness, monitoring wavelength, and materials of the prismatic array nanoparticles on the period of their coherent phonon oscillations.

In a gold nanodisk pair system made with electron beam lithography, we measured the coherent phonon vibration frequency in the presence of plasmonic field as a function of the interparticle separation. We found that the fractional change in the vibration frequency increases exponentially with decreasing the ratio of the interparticle separation to the particle diameter. The increase in the vibration period of coherent phonons when two nanodisks are closely placed to one another in the presence of plasmonic field is due to the coupling of the induced electric field in one nanodisk by the strong surface plasmon field of its pair partner. This was concluded from the fact that for the same set of nanoparticle pairs, the observed scaling exponential law governing the coherent phonon vibration frequency with distance is the same as that observed for the change in the surface plasmon electronic resonance frequency with distance. They both have an exponential behavior with the same decay constant, which suggest the same dipole-dipole interaction nature of the coupled coherent electron and lattice oscillation in the close-placed pair nanodisks.

Based on the coherent phonon oscillation of gold caps on a polystyrene sphere monolayer array, a new all-optical modulation technique is developed. Most of the previously reported high frequency modulation of light is induced by electrical, acoustic, or optical gate signals that are modulated at the same frequency. In many cases, the generation of a high frequency gate signal is difficult. In our experiment, the tunable gigahertz optical modulation is “generated” by a low repetition rate femtosecond laser.

Under a high density irradiation of a femtosecond laser, the melting and ablation processes can be induced in gold nanoparticles. We studied femtosecond laser induced shape and localized surface plasmon resonance band changes of the monolayer periodic

gold prismatic array nanoparticles. We also observed that the femtosecond laser irradiation of the nanoprisms at the surface plasmon resonance absorption maximum can cause a nanoparticle to detach from the substrate and "fly away" at an average threshold energy of 740 fJ/particle. Atomic force microscopy measurements revealed that the displaced nanoparticles are thinner and smaller than the undisplaced ones, which supports an atomic ablation mechanism. At threshold or higher laser power fluence, atomic ablation rapidly builds up pressure underneath the nanoparticle. Approximate calculation shows that the pressure under the particle creates an impulse that propels the nanoparticle away from the substrate within time of 40 ps. From the kinetic energy associated with the flying nanoparticle, an initial velocity of 164 m/s (367 miles/hour) is calculated. These mechanical properties are much more powerful than those recently determined in a Science paper for the same types of nanoparticles when nanosecond laser pulses are used (Habenicht, A. et al., *Science* **2005,** 309(5743), 2043-2045). In that report, a change in surface energy and in the particle's center of mass is proposed to be the mechanism by which propels the nanoparticle away from the substrate with a velocity of 20 m/s.

CHAPTER 1

INTRODUCTION

Of the many useful and interesting nanoparticles now available, by far the most important plasmonic nanoparticles are made of gold. Gold, which originally was discovered as shinny rocks in creeks by ancient man, became the most precious material in the history of human civilization because of its brilliant color, great malleability and permanence. The geological extraction of gold began early, around the 5th millennium B.C., in Bulgaria [1]. The marvelous gold mask of king Tutankhamun, made around 1300 B.C., is still shinning in the Egyptian museum. During that period, the yield of gold had already reached 10 tons per year in Egypt. Due to the broad geographical distribution of gold though, it became the unit of value in nearly every country around the world, which allowed trade between various countries to be very convenient in ancient time. Even today, gold remains one of the most important parameters that reflects the economic status of a country.

Due to the precious value of gold, many activities of mankind have been centered on gold, which brought about many gold related themes in the history of civilization. One of them is the discovery and application of "soluble" gold (gold colloidal solution) which appeared around the 5th century B.C. in Egypt and China, making it the most ancient of plasmonic nanoparticles [1]. From that time on, gold colloids were used in making fabulous glassware, such as the Lycurgus Cup (4th century AD) and ruby glass (17th century AD), due to their beautiful pinkish color. In 1857, Faraday described his systematic study of the preparation of gold colloids and the observation of their ruby

color in various conditions [2]. The color is caused by the absorption and scattering of white light by the small gold nanoparticles, which Mie first explained theoretically in 1908 by solving Maxwell's equation [3]. Gold colloids were also well known for their medicinal power to cure many diseases, such as dysentery, epilepsy, and tumors, which were first detailed by Francisci Antonii in 1618 [4]. The curative power of gold colloids, termed "drinkable gold", was illustrated in another book by Johann Kunckels in 1676 [5]. In the book, he described that "gold must be present in such a degree of communition that it is not visible to the human eye", which today is represented in the length scale in nanoscience and nanotechnology.

With the emergence and development of nanoscience and nanotechnology in the later half of the 20th century, gold plasmonic nanoparticles have received exponentially increased attention due to their novel properties of wavelength tunable light absorption and scattering, enhanced surface electromagnetic field, and strong photothermal effect. These specific and distinct properties will make gold plasmonic nanoparticle as one of the most important nanomaterials in the 21st century.

It is well known that the localized surface plasmon resonance (LSPR) band of plasmonic nanoparticles is highly sensitive to the particle's size [6], shape [7], local environment [8], and coupling between nearby nanoparticles [9-12]. These superior properties promote many applications of plasmonic nanoparticles in subwavelength optical energy transfer waveguides [13-15], biosensors [16-22], imaging [23], and cancer diagnostics and therapy [23-25]. For all of these applications of plasmonic nanoparticles, it is extremely important to understand these properties, such as the laser induced shape

transformation [26], the thermal stability [27], and electron [28] and phonon [29,30] dynamics.

Extensive studies have been performed on nanoparticles randomly distributed in solutions. However, to produce new functional materials and advanced devices, a well-defined system of assembled nanoparticles is highly desired. This well-defined system is also superior for studying the fundamental physical and chemical properties of the particles. Optical lithographic methods have been commercially used in making two-dimensional micro-structures on substrates in the semiconductor industry. In nanoscience and nanotechnology, two dimensional nanoparticle arrays can be prepared with well defined sizes, shapes and interparticle separations by nanosphere lithography (NSL) and electron beam lithography (EBL) [31]. Two dimensional periodic nanostructures fabricated by these two nano-lithographic techniques have been used for fundamental research [9-11,32-35] on the coupling between nanoparticles aligned in an array structure and for designed applications [19,21,22,36] in biological sensing systems. Compared to nanoparticles prepared in solution, nanoparticles fabricated with lithographic methods have no organic passivating surface. On the clean surface of these nanoparticles, biological functional groups can be easily attached, which greatly simplifies the biological sensing applications of these nanoparticles. Non-spherical nanoparticles can also be easily fabricated with lithographic techniques. The extraordinary electro-magnetic field confined at the sharp tips of non-spherical nanoparticles can be used to study particle-particle interactions [37] and in applications to surface enhanced spectroscopies [38] and subwavelength optical waveguides [15,39].

1.1 Optical Properties of Plasmonic Nanoparticles

Upon electromagnetic wave excitation, the conductive electrons of a small metal particle will oscillate collectively (**Figure 1-1**) if the frequency of the electromagnetic wave is in resonance with the electron oscillation frequency. This collective oscillation of electrons is called the localized surface plasmon resonance (LSPR). The term "surface" of the LSPR needs further clarification. It is present because the surface polarization is the major effect generating the restoring force (**Figure 1-1**), although all of the electrons are oscillating relative to the positive ion lattice background [40]. The strong absorption and scattering of light by the LSPR have been used since ancient times. **Figure 1-2** is an image of the Lycurgus Cup, which was made by the Romans around the fourth century AD [41]. When illuminated from the outside, the cup appears green (**Figure 1-2a**). When illuminated from the inside, it glows red (**Figure 1-2b**). The cup is made of glass but contains about 40 parts per million of gold and about 300 parts per million of silver. It was later discovered that the gold and silver form nanoparticles of ~ 70 nm, composed of 30 % gold and 70 % silver [42]. The red color comes from the absorption of small gold and silver nanoparticles centered around 500 nm.

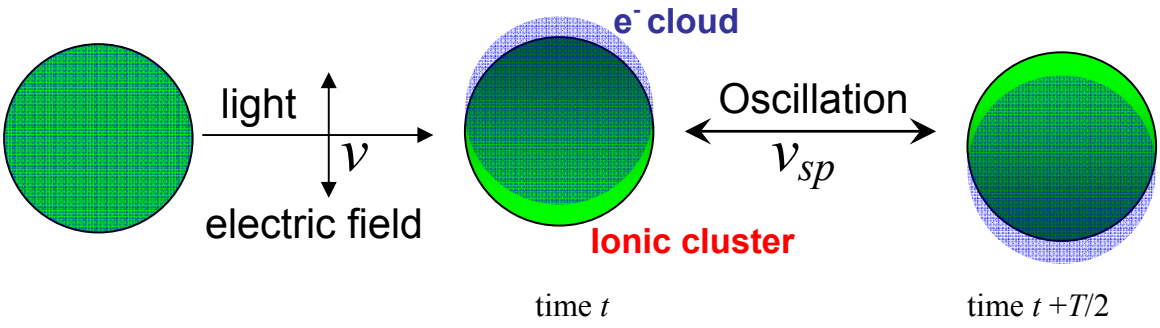

Figure 1-1: The excitation of a dipolar localized surface plasmon polariton by the electric field of an incident light wave of frequency $\nu = \nu_{sp} = 1/T$ [40].

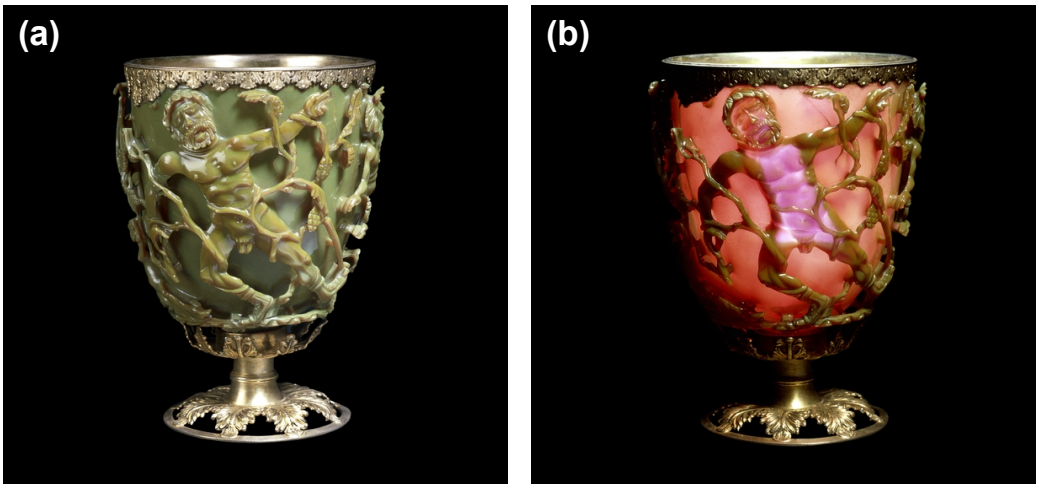

Figure 1-2: Images of the Lycurgus Cup that was made by Roman around the fourth century AD [41]. When illuminate from the outside, it shows green (a). When illuminate from the inside, it glows red (b). The cup was made of glass but contains about 40 parts per million of gold and about 300 parts per million of silver. It was later discovered that the cup contains gold and silver nanoparticles of ~ 70 nm [42].

Faraday was the first to systematically study gold colloidal solutions. In his Bakerian lecture [2], he described his method in making gold nanoparticles and the observation of the ruby color of the colloidal solution in different conditions. The color

came from the absorption and scattering of white light by the small gold nanoparticles, which was first explained theoretically by Mie in 1908 by solving Maxwell's equation for spherical nanoparticles [3].

For a free electron metal nanoparticle of a small size (much smaller than the wavelength of incident light), the quasistatic response of the nanoparticle to an electric field gives a LSPR frequency ($\nu_{sp}^{\max}$) of

$$\nu_{sp}^{\max} = \sqrt{\frac{ne^2}{\varepsilon_0 m_e (1+2\varepsilon_m)}}, \tag{1-1}$$

where n is the free electron density, ε_0 is the vacuum permittivity, and ε_m is the medium dielectric constant [40]. Equation (1-1) shows that the frequency of the LSPR is sensitive to the free electron density in the nanoparticle.

Using Mie theory, one can perform the exact electrodynamic calculation for spherical metal clusters. When the size of the spherical nanoparticle is much smaller than the wavelength of incident light, the extinction of the nanoparticle, $\sigma_{ext}(\omega)$, is given by [3]

$$\sigma_{ext}(\omega) = 9\frac{\omega}{c}\varepsilon_m^{3/2} V_0 \frac{\varepsilon_2(\omega)}{[\varepsilon_1(\omega)+2\varepsilon_m]^2 + \varepsilon_2(\omega)^2}, \tag{1-2}$$

where ω is the frequency of light, c is the speed of light, V_0 is the volume of the spherical nanoparticle, ε_m is the dielectric constant of the surrounding medium (assumed to be a positive, frequency-independent, real number) and $\varepsilon(\omega) = \varepsilon_1(\omega) + i\varepsilon_2(\omega)$ is the dielectric function of the particle material ($\varepsilon_1(\omega)$ is the

real portion and $\varepsilon_2(\omega)$ is the imaginary portion of the frequency dependent dielectric function of the metallic nanosphere). The extinction maximum of the nanosphere's LSPR of the nanosphere occurs when

$$\varepsilon_1(\omega) + 2\varepsilon_m = 0\,, \tag{1-3}$$

that's when $\varepsilon_1(\omega) = -2\varepsilon_m$. This equation neglects the phase retardation and effects of higher multipoles, so it only holds for sufficiently small particles. Equation (1-2) shows that the intensity of the localized surface plasmon extinction peak are affected by the size of the metal nanoparticles, the dielectric constant of the metal, and the dielectric constant of the particle's surrounding medium.

Experimentally, Link and El-Sayed [43] have observed a red shift of the localized surface plasmon band with an increase in the size of gold nanoparticles. They also found the bandwidth of the localized surface plasmon band decreases with an increase in the size of nanoparticles when the diameter of nanoparticles is less than ~10 nm (intrinsic size region). If the diameter of the nanoparticles is larger than ~10 nm (extrinsic size region), the localized surface plasmon band broadens with the increase in particle size. They also found the molar extinction coefficients of the localized surface plasmon band of gold nanoparticles are linearly dependent on the volume of nanoparticles on a double logarithmic scale. All of the above experimental observations are in agreement with Mie theory [3].

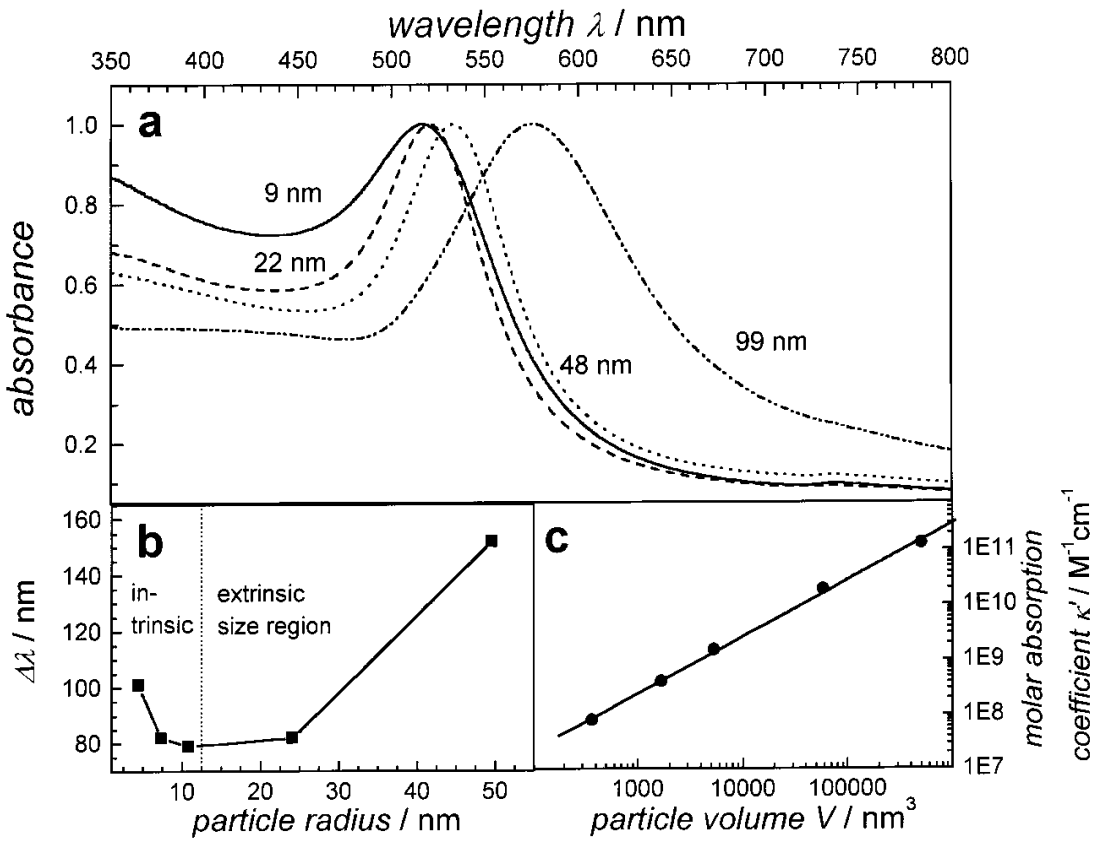

Figure 1-3: (a) Size dependent LSPR absorption of spherical gold nanoparticles. (b) Size dependent plasmon bandwidth. (c) Size dependent molar absorption coefficient, which shows a linear dependence on double logarithmic scales [43]. Reprinted with permission from *J. Phys. Chem. B* **1999,** 103, (40), 8410-8426. Copyright 1999 American Chemical Society.

For particles of nonspherical shapes, Maxwell's equation becomes difficult to solve analytically. For cylindrical or oblate nanoparticles, their LSPR spectrum can be simulated with an extension of Mie's theory, Gan's treatment [44], with dipole approximation. To model the LSPR spectrum of more complicated shapes, alternative numerical methods have been developed, such as the discrete dipole approximation (DDA) method [45-48], the multiple multipole method [49], and the finite difference time domain method [50-52]. The DDA method is proven to be a suitable method for

calculating isolated nanoparticles of arbitrary shape and imbedded in a complex surrounding medium [53]. It is also able to calculate the plasmon resonance spectrum of interacting nanoparticle systems [54]. The details of the DDA method are described in reference [48]. Briefly, the object is represented by *N* polarizable cubes. Each cube can be considered as a virtual point dipole upon exposure to an electric field. The local electric field of each dipole is determined by the sum of the applied electric field and the electric field generated by all of the point dipoles. This treatment simplifies the solution of Maxwell's equations to an algebraic problem of coupled dipoles, which can be solved numerically by using fast Fourier transform and complex-conjugate gradient methods developed by Draine and co-workers [46,47,55]. **Figure 1-4a** shows the extinction efficiency of nanoprisms calculated by the DDA method upon different electric field polarizations along the three major symmetry axes. The edge length, thickness, and snip of the nanoprism are 100, 16, and 10 nm, respectively. **Figure 1-4b** shows the perfect match between the measured (solid line) and calculated (dash line) UV-vis spectra of trigonal Ag prisms with the same dimensions. The measured spectrum is broader than the calculated spectrum, which could be due to the broad size distribution of the nanoprism sample. The calculated spectrum is orientation-averaged to represent the fact that nanoparticles are randomly distributed in the solution [53].

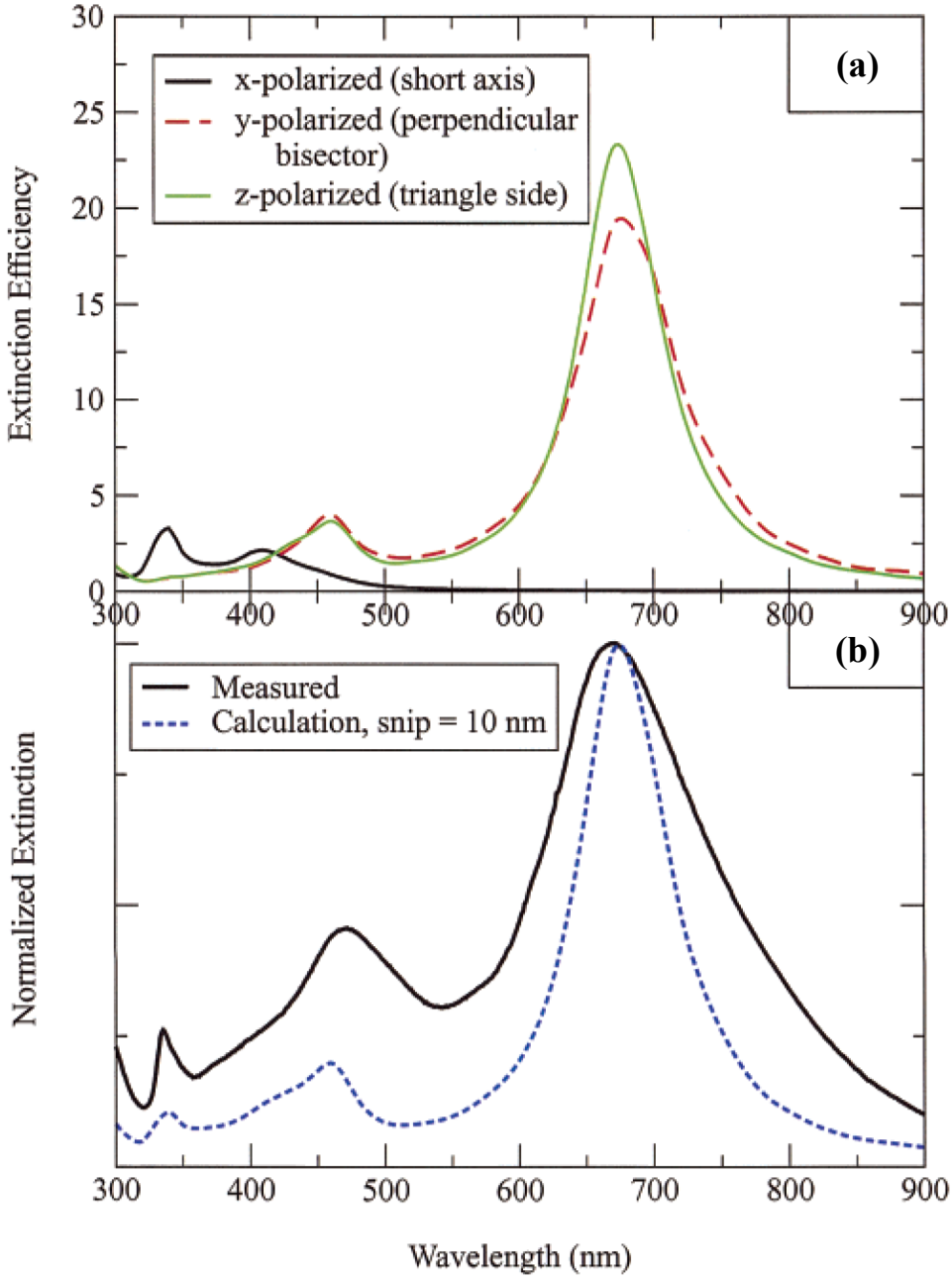

Figure 1-4: (a) The extinction efficiency of nanoprisms calculated by the DDA method upon different electric fields of polarization along the three major symmetry axes. The edge length, thickness, and snip of the nanoprism are 100, 16, and 10 nm, respectively. (b)Measured (solid line) and calculated (dash line) UV-vis spectra of trigonal Ag prisms with the same dimension as in (a). The calculated spectrum is orientation-averaged to represent the fact that nanoparticles are randomly distributed in the solution [53]. Reprinted with permission from *J. Phys. Chem. B* **2003,** 107, (3), 668-677. Copyright 2003 American Chemical Society.

In summary, the LSPR band of plasmonic nanoparticles is highly sensitive to the particle's size, shape, local environment, and the coupling between neighboring nanoparticles. For spherical nanoparticles, the extinction spectrum can be well characterized by solving Maxwell's equation. The experiments performed on spherical nanoparticles are in agreement with Mie's prediction. For nanoparticles of arbitrary geometry, the DDA method has proven to be a powerful method to simulate the extinction spectrum of nanoparticles.

1.2 Nanosphere Lithography in Making Nanoparticles

Since the properties of nanoparticles are highly dependent on their size, a narrow particle size distribution is always preferred to study their fundamental physical and chemical properties [9-11,32-35] and to produce new functional materials and advanced devices [19,21,22,36]. A monodisperse nanoparticle system can be achieved with special techniques such as radiation chemistry [56,57], tensile deformation [58], and improved wet chemistry methods [59]. Another popular way to make nanoparticles of a narrow size and shape distribution is by using lithographic techniques [31]. With the NSL technique [31], two dimensional nanoparticle arrays can be prepared possessing a well defined size, shape and interparticle separation. The absence of the organic passivating surface and the easily achieved non-spherical shapes make these lithographically made nanostructures attractive for studying particle-particle interactions and applying them in surface enhanced spectroscopy and catalysis [60]. The easily achieved non-spherical shape leads to a high electron density confined in the sharp apexes, which induces a high E-field enhancement under an incident electromagnetic field and significant dipole moments

within the array structures [37,53,61,62].Unlike serial lithographic techniques (such as electron beam lithography), NSL is a parallel technique that is inherently inexpensive, high-throughput, and material and substrate general [31]. It is an ideal technique to be used for studying size-dependent properties of nanoparticles.

The concept of nanosphere lithography was introduced by Fischer and Zingsheim in 1981 [63], where they use a small drop of 10 % PS latex spheres (weight percentage) suspension on glass substrate. After spreading and drying, patches of closely packed PS monolayer are formed with diameters up to $10\,\mu m$. The formed PS monolayer is used as a mask for contact imaging with visible light. The feature resolution achieved with 400 nm blue light was ~ 100 nm, which was only achievable by x-ray and e-beam lithography at that time. Deckman et al. [64] used the same PS sphere monolayer as a mask for material deposition and etching and termed this technique "natural lithography" because of the natural assembly of the nanospheres into closely packed arrays.

The nanosphere lithographic technique is used extensively before its self-assembly mechanism was fully understood. Denkov et al. studied the self-assembly process by taking pictures of the assembly process of a $1.7\,\mu m$ diameter particles suspension [65]. The camera that they used was able to record the track of a fast moving particle. As shown in **Figure 1-5a**, they imaged the tracks of fast moving particles towards the edge of the close packed crystal where they were trapped when they reached the boundary of the closely packed monolayer. This process could be slowed down by adding 0.2 wt% glucose to the suspension as shown in **Figure 1-5b**. The self-assembly mechanism was revealed by the fact that in all experiments the initial assembly always started after the thickness of the solvent decreased to the diameter of the particle. When

the solvent evaporated further, particles partially protruded from the solvent thin layer. The capillary attraction force generated between particles brought them together to form a closely packed crystal as shown in **Figure 1-5c**. Between closely packed hydrophilic spheres, the solvent formed menisci, which prevented the further decrease of the solvent thin layer due to the surface tension. As the water evaporated from the top of the closely packed spheres, the solvent flowed from the thick part of the solvent toward the sphere lattice, which brought in free spheres to join the crystal. This convective transfer mechanism can also explain the ring-shaped stain formed when a drop of coffee drying on a solid surface [66]. Based on the same mechanism, Dimitrov et al. developed a method to assemble microspheres on a vertically oriented substrate that was slowly pulled out from a microsphere suspension [67]. The optimized pulling speed for the substrate to form a microsphere crystal of k layers is given by

$$v_w = \frac{\beta l}{0.605} \frac{j_e \varphi}{kd(1-\varphi)}, \tag{1-4}$$

where β is the coefficient of proportionality that depends on the strength of particle-particle and particle-substrate interactions, l is the evaporation length, j_e is the water evaporation rate, φ is the particle volume fraction, and d is the diameter of particles. Gu et al. studied the effect of wettability of the substrate on the self-assembly process of microspheres [68]. They found that different shapes of microsphere crystals can be formed by varying the concentration of the microsphere suspension on hydrophilic and hydrophobic substrates.

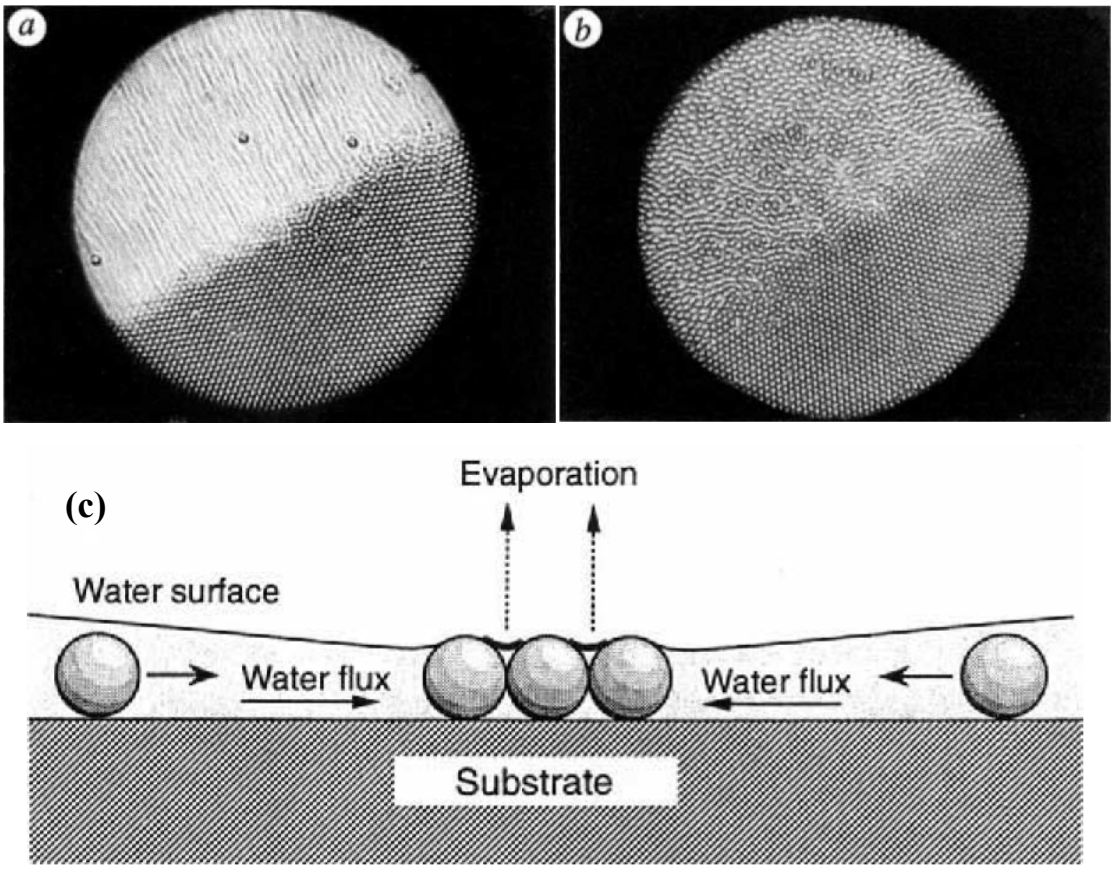

Figure 1-5: Photographs of the self-assembly process of a 1.7 μm diameter particle suspension. The lines in (a) are the tracks of fast moving particles that move towards the ordered zone. Particles are trapped when they reach the boundary of the closely packed monolayer. In (b), the movement of particles is slowed down by adding a 0.2 wt% glucose solution to the suspension [65]. Reprinted by permission from Macmillan Publishers Ltd: Nature, copyright (1993).

This technique was renamed nanosphere lithography by Van Duyne's group [6,31,69,70], who made many great contributions. They used the atomic force microscopy (AFM) to study these structures [69]. They extended the original monolayer NSL technique to double layer NSL [69]. The schematic illustrations and the resulting nanostructure patterns of monolayer and double layer NSL are shown in **Figure 1-6**.

Compared to the metallic particle pattern formed by monolayer NSL, double layer NSL produces a pattern with a half particle density since every other three-fold hole is blocked by the PS sphere in the top layer. The size of the nanoparticle is controlled by the diameter of the PS sphere (D) by geometric relations. For the pattern created with a monolayer PS sphere mask, the bisector of the particle (a_{ml}) is given by

$$a_{ml} = \frac{3}{2}\left(\sqrt{3} - 1 - \frac{1}{\sqrt{3}}\right)D . \tag{1-5}$$

For the pattern created with a double layer PS sphere mask, the diameter of the formed nanoparticle (a_{dl}) is given by

$$a_{dl} = \left(\sqrt{3} - 1 - \frac{1}{\sqrt{3}}\right)D . \tag{1-6}$$

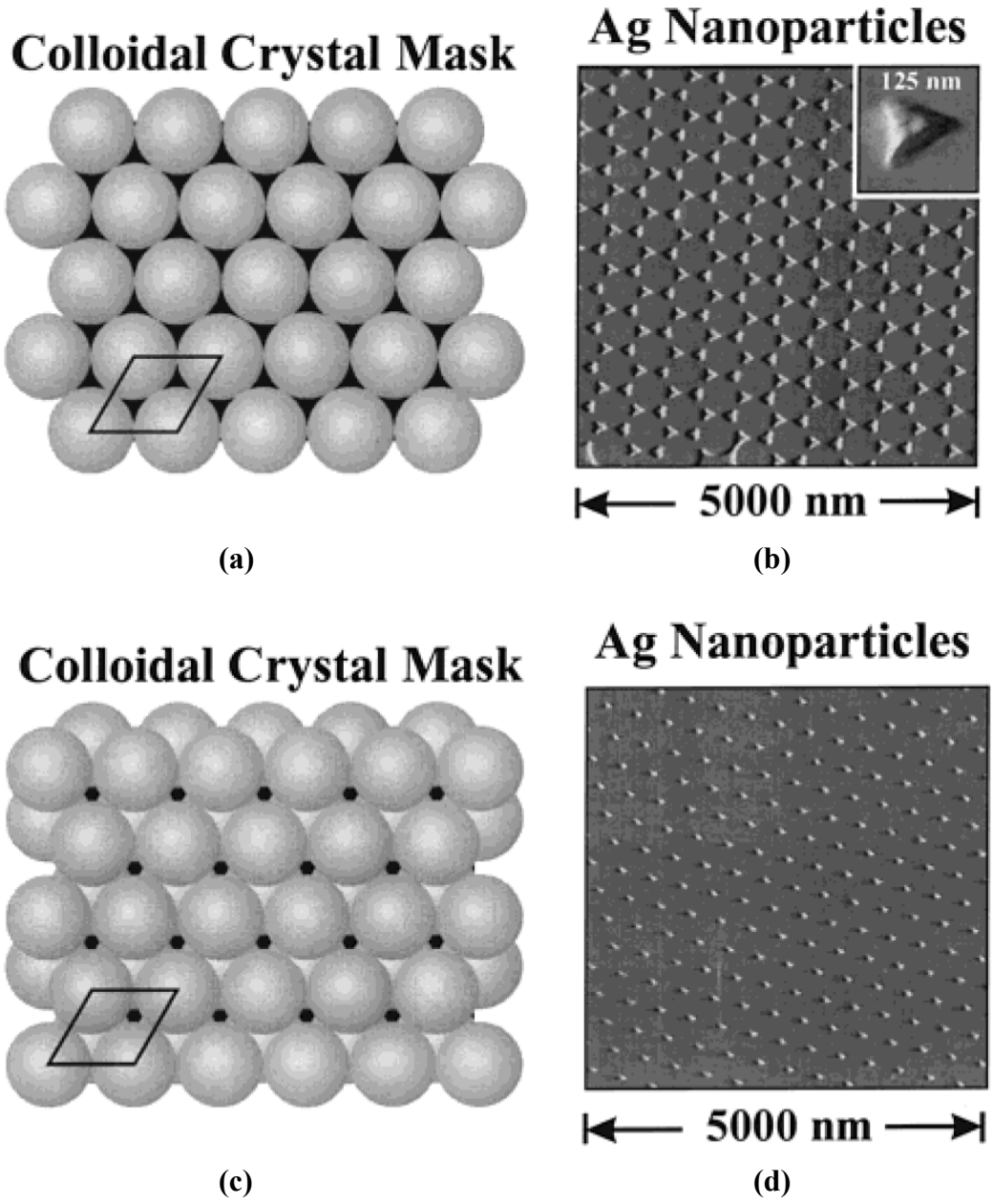

Figure 1-6: (a) Schematic diagram of monolayer NSL. (b) AFM image of the nanostructure pattern created with single layer NSL. (c) Schematic diagram of double layer NSL. (d) AFM image of the nanostructure pattern created with double layer NSL [31]. Reprinted with permission from *J. Phys. Chem. B* **2001**, 105, (24), 5599-5611. Copyright 2001 American Chemical Society.

NSL is a great technique to create patterned nanoparticles of different sizes. Van Duyne and his co-workers made silver nanoparticles that have LSPR bands centered at different wavelengths ranging from the visible to the infrared region as shown in **Figure 1-7** [6]. Since the LSPR band is very sensitive to the size and shape of the nanoparticle, tuning of the LSPR band is accomplished by changing the size of the PS spheres and annealing the as-deposited triangle shaped nanoparticle to an ellipsoidal shape, which is the thermal dynamically more stable shape.

.

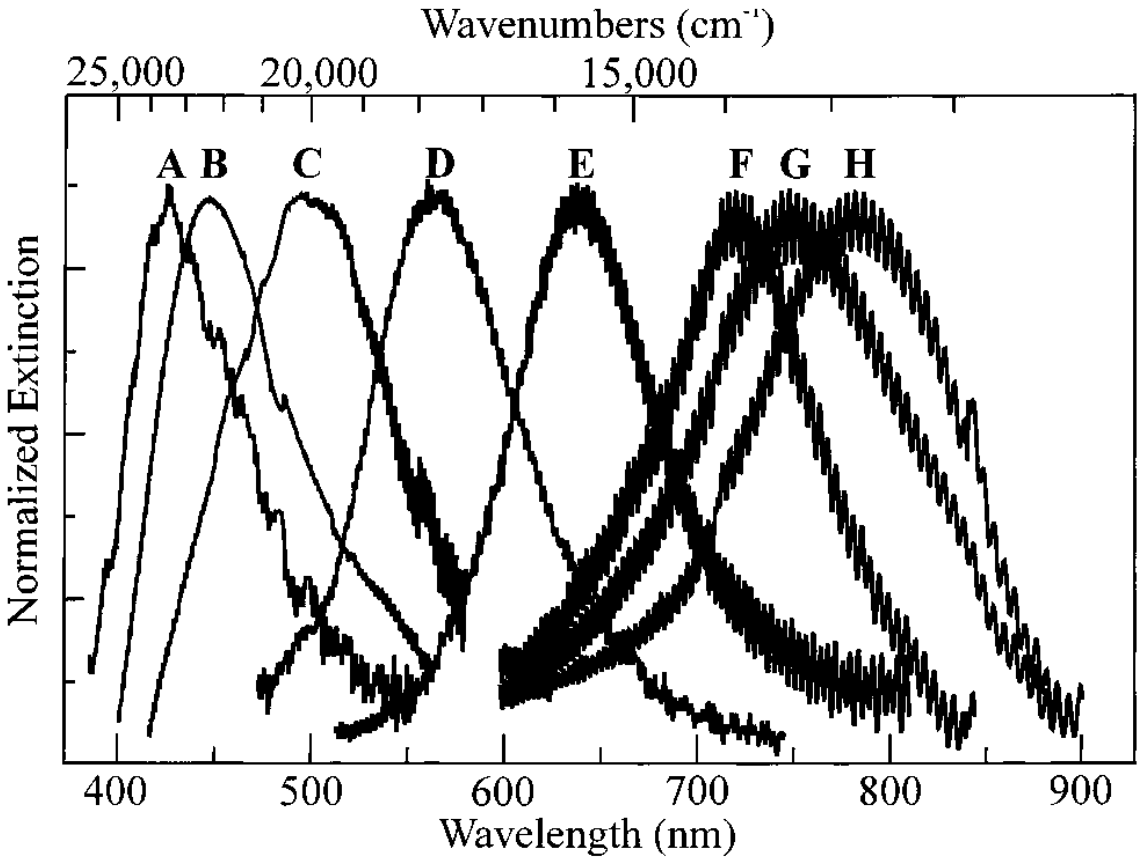

Figure 1-7: UV-vis extinction spectra of arrays of silver nanoparticles fabricated with NSL on mica substrates. The structural parameters of nanoparticles are shown in **Table 1-1** [6]. Reprinted with permission from *J. Phys. Chem. B* **2000**, 104, (45), 10549-10556. Copyright 2000 American Chemical Society.

Table 1-1: The structural parameters of nanoparticles that show the extinction spectra in Figure 1-7 [6]. Reprinted with permission from *J. Phys. Chem. B* **2000**, 104, (45), 10549-10556. Copyright 2000 American Chemical Society.

	A[a]	B[a]	C[a]	D	E	F	G	H
a[b](nm)	120 ± 12	150 ± 15	150 ± 15	90 ± 6	120 ± 6	145 ± 6	145 ± 6	145 ± 6
b (nm)	42 ± 5	70 ± 8	62 ± 8	46 ± 3	46 ± 3	59 ± 4	55 ± 4	50 ± 4
D (nm)	401 ± 7	542 ± 7	542 ± 7	310 ± 9	401 ± 7	542 ± 7	542 ± 7	542 ± 7
d_m (nm)	48	70	62	46	48	60	55	50
substrate	mica	mica	mica	mica	mica	mica	mica	mica
in-plane shape[c]	E	E	E	T	T	T	T	T
λ_{max} (nm)	426	446	497	565	638	720	747	782
λ_{max} (cm^{-1})	23,474	22,422	20,121	17,699	15,674	13,889	13,387	12,788
Γ (cm^{-1})	3460	3883	3940	2788	2180	1826	2483	2063
Q	6.78	5.77	5.11	6.35	7.19	7.61	5.39	6.20
extinction scaling factor	3.7	2.5	2.7	1.6	1.0	1.9	1.3	0.7

[a] Annealed at 300 °C for 1 h. [b] Not corrected for AFM tip convolution. [c] E = elliptical, T = triangular.

NSL prepared substrate bound nanoparticles can be directly used as a biosensor, based on the sensitivity of the nanoparticle's LSPR band to the dielectric constant of the surrounding environment, as shown by Equation (1-1) and (1-2). A model demonstration by Malinsky et al. [71] showed a linear dependence of the LSPR band maximum on the alkane chain length of adsorbed alkanethiols. The LSPR band shift was attributed to the dielectric constant change of the surrounding medium induced by the thickness change of the alkanethiol layer. McFarland et al. [17] measured the LSPR band shift of a single silver nanoparticle upon changing of the medium dielectric constant as shown by **Figure 1-8**. The nanoparticle was placed in nitrogen, methanol, 1-propanol, chloroform, and benzene. The LSPR band of the single Ag nanoparticle linearly shifted to longer wavelength with the increase of the refractive index of the media. Based on this dependence of the LSPR band shift on the medium dielectric constant, Van Duyne and co-workers [19,20] demonstrated the diagnosis of Alzheimer's disease.

The non-spherical shape of nanoparticles synthesized with NSL also induces higher electromagnetic fields around the sharp apexes of particles, which leads to other interesting applications, such as surface enhanced Raman spectroscopy [38,72] and second harmonic excitation spectroscopy [73].

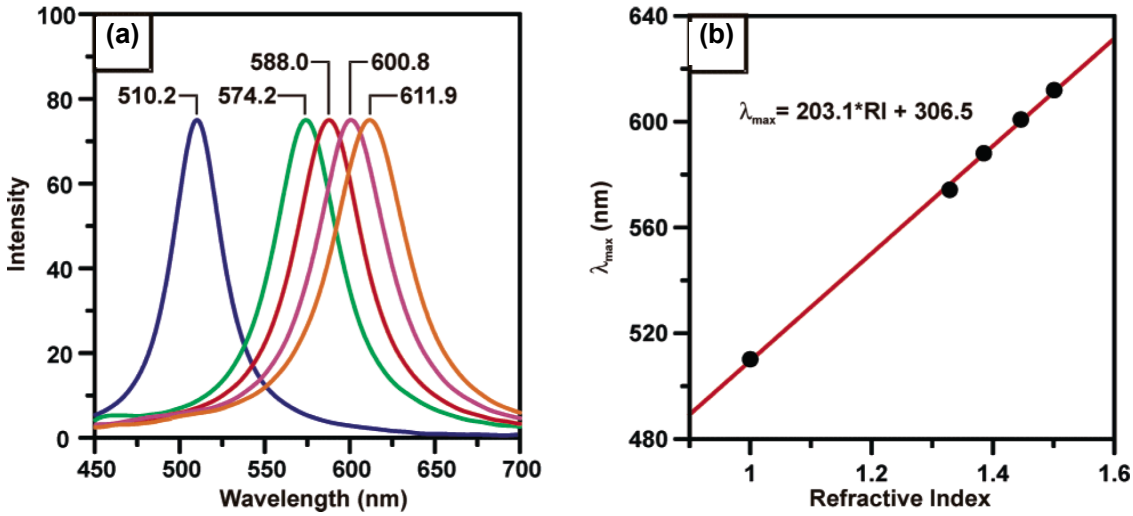

Figure 1-8: (a) The LSPR band of a single Ag nanoparticle in various media (left to right): nitrogen, methanol, 1-propanol, chloroform, and benzene. (b) The linear dependence of the LSPR extinction maximum on the refractive index of the medium [17]. Reprinted with permission from *Nano Lett.* **2003,** 3, (8), 1057-1062. Copyright 2003 American Chemical Society.

Recently, the ability of NSL has been greatly extended to produce different nanostructures. Van Duyne et al. [70] introduced the angle-resolved nanosphere lithography (AR NSL) technique, where the substrate is tilted at certain angle(s) during the metal deposition. Tilting the microsphere monolayer mask reduces the size of the

triangular nanoparticles, changes the shape of the nanoparticles from that of an equilateral triangle, and shifts the position of the nanoparticle from the center position of the interstitial void between the microspheres. The AR NSL was used to produce nanostructures (shown in **Figure 1-9**) that showed dichroic optical properties [74]. Kosiorek et al. [75] further extended the AR NSL to shadow NSL, where the substrate is tilted and rotated during the metal deposition as shown in the schematic of **Figure 1-10a**. **Figure 1-10b** is a structure fabricated using the shadow NSL. A nanostructure fabricated first with a Cr deposition while rotating the substrate at a tilting angle of $\theta = 25^{o}$ followed by a second deposition of Ni at $\theta = 0^{o}$ without rotation. The resulting nanostructures were Ni dots sitting in a Cr cups. The pattern created with NSL can also be used as the template to create other structures such as 2D periodic carbon nanotubes [76,77], aligned ZnO nanorods [78], ordered nanobowl arrays [79], liftable inverted-nanobowl sheets [80], triangular nanopores [81], and aligned nanopillars [82].

NSL is the most important sample preparation technique used in this thesis work. We renovated the powerful NSL technique to create prismatic nanoparticle patterns on a centimeter scale. The as-deposited prismatic nanoparticle can be easily transferred to spherical morphologies by thermal annealing. These high quality patterns facilitated our studies about the electron and lattice dynamics, the coupling, and the ultrafast laser induced photothermal properties of plasmonic nanoparticles.

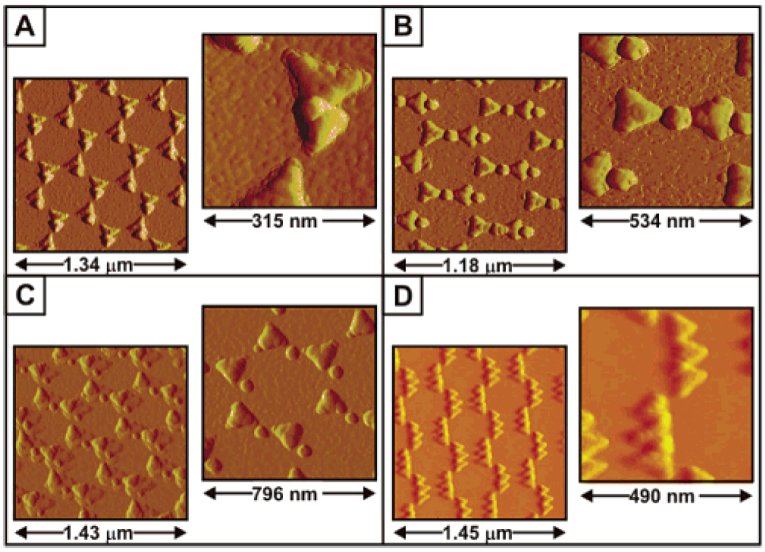

Figure 1-9: Atomic force microscopy images of structures made with angle-resolved nanosphere lithography. After deposition at 0^{o} the second deposition is performed at (A) 17.5^{o}, (B) 23.5^{o}, (C) 30^{o}, and (D) 15^{o} and -15^{o} [74]. Reprinted with permission from *Nano Lett.* **2003,** 3, (7), 939-943. Copyright 2003 American Chemical Society.

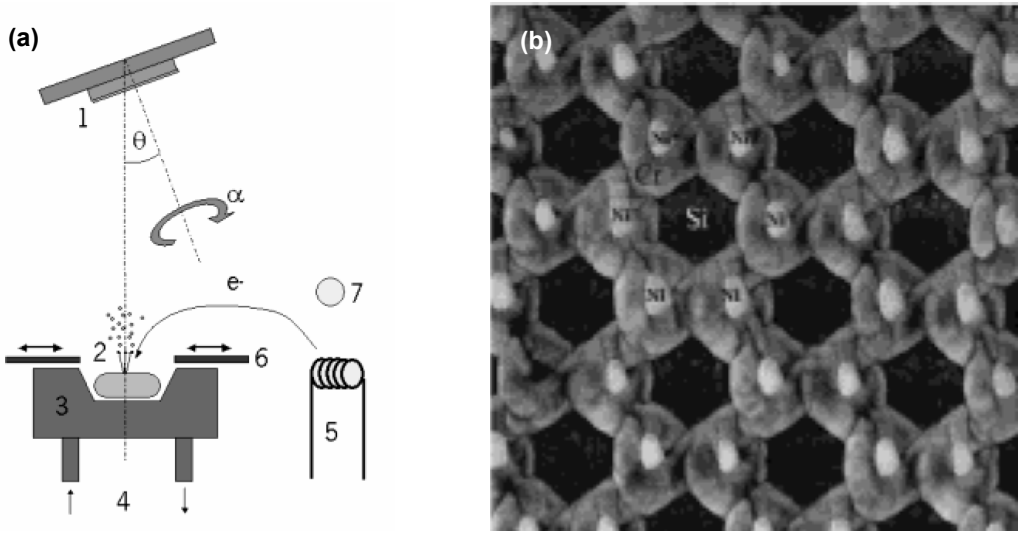

Figure 1-10: (a) Schematic diagram of the apparatus used for shadow nanosphere lithography. During deposition, the substrate was tilted at an angle θ and rotated. (b) A nanostructure fabricated first by a Cr deposition with the substrate rotating at a tilted angle of $\theta = 25^{o}$ and a subsequent deposition of Ni at $\theta = 0^{o}$ without rotation [75]. Reprinted with permission from *Nano Lett.* **2004**, 4, (7), 1359-1363. Copyright 2004 American Chemical Society.

1.3 Electron-Phonon Relaxation in Plasmonic Nanoparticles

Great interest has been directed lately to the interaction between noble metal nanoparticles and lasers [30,43,83-94]. One of the most active research fields is the study on electronic energy relaxation processes of laser excited plasmonic nanoparticles [7,43,95-97]. This is because the electron phonon interaction is the most important energy relaxation process in materials and determines many important properties, such as the thermal conductivity, the electrical conductivity, and the nature of superconductivity [98]. With the advancement of laser technology, ultrafast pulsed laser based time-resolved transient absorption/transmission and reflectivity spectroscopies provide a powerful tool to measure the electron-phonon and phonon-phonon relaxation dynamics in thin metal films [83,99-101] and small metal particles [30,43,84-94].

The relaxation processes of ultrafast laser excited coherent electrons start with the rapid loss of their phases via electron-electron interaction. Due to the high electron density in metals, the electron-electron interaction is very strong, which leads to a very fast electron thermalization time on a scale of tens of femtoseconds [102]. As described by the two-temperature model (TTM) [103,104], we can treat the electron gas and the lattice as two interacting systems due to the substantial difference in their heat capacities (the electron gas has a much smaller heat capacity than the lattice). Laser energy is directly absorbed by the electrons during laser excitation, which leads to a nascent ultrahigh temperature of the electron gas after the electron thermalization. Thus, a non-equilibrium temperature difference is established between the electron gas and the lattice. The electron lattice thermal equilibrium state is reached on a sub-picosecond to several picosecond time scale by transferring electronic energy to the lattice through electron-

phonon interactions. The time required to reach the electron lattice thermal equilibrium is given by the TTM [104]:

$$C_e(T_e)\frac{\partial T_e}{\partial t} = -g(T_e - T_1) + \nabla \cdot (\kappa' \nabla T_e) + \mathrm{LP}(z,t), \tag{1-7}$$

$$C_l \frac{\partial T_l}{\partial t} = g(T_e - T_1), \tag{1-8}$$

where C_e and C_l are the heat capacity of the electron gas and the lattice, respectively, g is the electron-phonon coupling constant, κ' is the electronic thermal conductivity that describe the rate of heat transporting out of the laser excitation spot, and $\mathrm{LP}(z,t)$ is the spatial and temporal evolution of the excitation laser pulse. C_e is usually assumed to be a linear function of the electron temperature T_e. For nanoparticles, κ' can be neglected since their dimensions are much smaller than the diameter of the laser excitation spot. Laser deposited energy is finally transferred to the environment by phonon-phonon interactions, which are dependent on the thermal conductivity and the heat capacity of the medium and the coupling between nanoparticles and their surrounding medium.

The effect of the size and shape of plasmonic nanoparticles on their electron-phonon relaxation dynamics has been studied extensively with the advancement of ultrafast laser spectroscopic techniques [99,105-112]. Quantum-kinetic calculations predict that the electron-phonon relaxation rate increases if the size of the nanoparticle is decreased below the mean free path of conductive electrons (40-50 nm in gold) as a result of the interaction between electrons and surface phonons. However, experiments by our group and Hartland's group didn't find such a trend. For gold nanoparticles of sub 10 nm and 30 nm diameters, Ahmadi et al. [106,107] in our group found there is no difference in

their electron-phonon relaxation dynamics. Link et al. [113] found that the electron-phonon relaxation times for gold nanoparticles of 9 and 48 nm are very close to each other. The shape dependent electronic energy relaxation has also been studied in our group by Link et al. [108], where they found the electron-phonon relaxation times for gold nanorods (aspect ratio of 3.8) probed at both their longitudinal (700 nm) and transverse (520 nm) plasmon band are around 3 ps as shown in **Figure 1-11**. The same value was also observed in gold nanospheres of 15 and 48 nm [43,108]. These observations indicate that the changes in the gold nanoparticle shape, size, and the mode of LSPR do not affect their electronic energy relaxation dynamics. These observations also exclude the electron-surface phonon interaction as the major electronic energy relaxation channel.

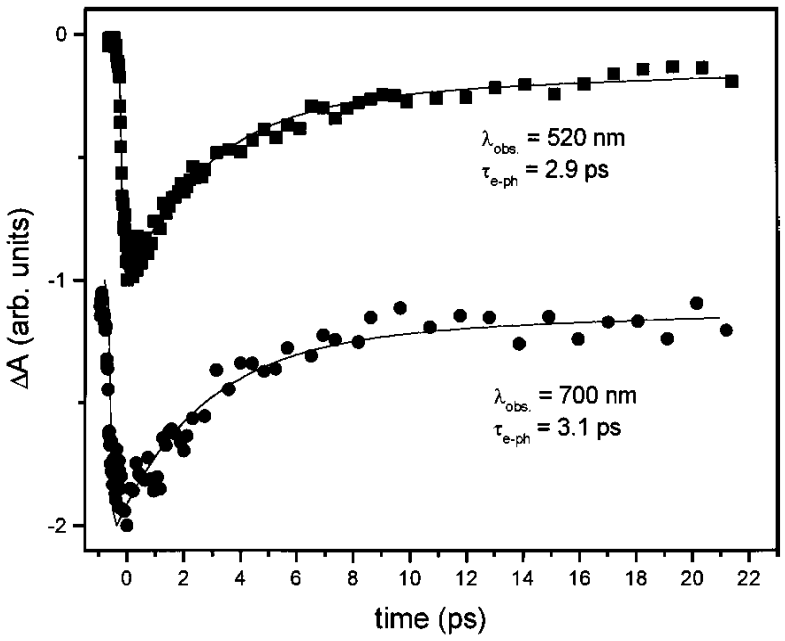

Figure 1-11: The effect of shape on the electron-phonon relaxation time. From top to bottom: the LSPR bleach recovery of nanorods monitored at their transverse (520 nm) and longitudinal (700 nm) LSPR band. The aspect ratio is 3.8. The energy deposition to the sample is adjusted to the same level by changing the laser intensity and the absorption of the sample. It is clear that the electron-phonon relaxation time is independent of the shape of nanoparticles [108]. Reproduced with permission from *Phys. Rev. B* 2000, 61, (9), 6086-6090. Copyright 2000 APS (http://prola.aps.org/abstract/PRB/v61/i9/p6086_1).

Hartland's group [105,109,114] studied silver nanoparticles of 10 to 50 nm and gold nanoparticles of 4.6 to 120 nm in aqueous solutions. They found that the electron-phonon coupling constants are very close to each other for the nanoparticles of different sizes. They also found the coupling constants of gold and silver nanoparticles to be similar to corresponding bulk values [109,115]. The observed size independence of the electron-phonon relaxation of gold and silver plasmonic nanoparticles was attributed to the relative small contributions of surface phonon modes due to their weak electron-

phonon coupling. The coupling constant is known to be proportional to the ratio of the metal atomic valence to its atomic mass (n/m) [115,116].

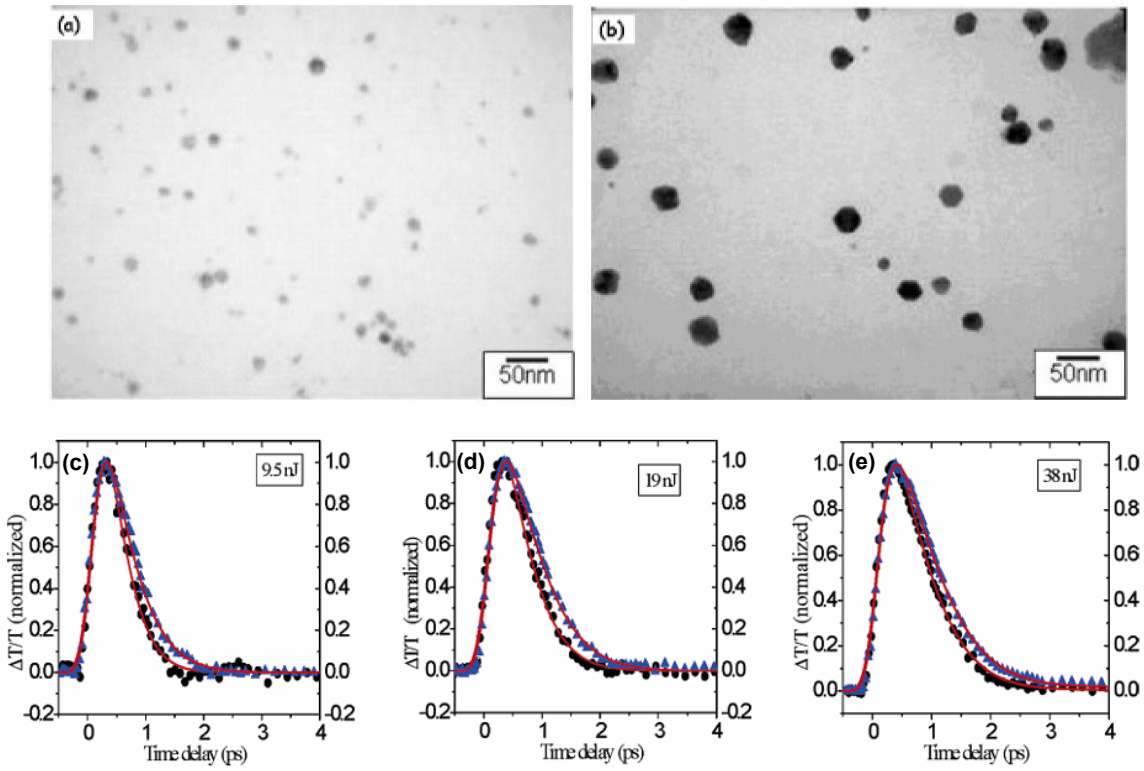

Figure 1-12: (a, b) TEM images of copper nanoparticles of 12 and 30 nm in diameter, respectively. (c-e) The electron-phonon relaxation dynamics recorded for these two copper samples. The pump powers were (c) 9.5 nJ, (d) 19 nJ, and (e) 38 nJ [117]. Reprinted with permission from *J. Phys. Chem. B* **2006,** 110, (1), 143-149. Copyright 2006 American Chemical Society.

For sub-10 nm silver nanoparticles imbedded in a glass matrix, Del Fatti et al. [110] and Halte et al. [118] found the electron-phonon relaxation rate increases with a decrease in the diameter of nanoparticles. These results were explained by the enhanced interaction between electrons and surface phonons, while the effect of heat transfer to the matrix environment could also play a large role, especially for small nanoparticles that

had high surface to volume ratios [118]. Darugar et al. [117] in our group found the size-dependent electronic energy relaxation in spherical copper nanoparticles of 12 and 30 nm as shown in **Figure 1-12**. The contribution of surface phonon modes to the total e-ph coupling is given by the ratio of the valence of the metal to its atomic mass (n/m) [115,116]. The ratio for copper is twice as large as that for silver and three times as large as that for gold. Therefore, the size dependent electron-phonon relaxation dynamics resulting from the influence of surface phonons in copper nanoparticles was detected more readily. This can explain why we observe the size dependent electron-phonon relaxation dynamics in copper nanoparticles (larger than 10 nm) but not in gold or silver nanoparticles of the same size regime.

The size and shape of gold and silver nanoparticles have no effect on their electron-phonon relaxation dynamics. We are interested in the effect of lattice crystallinity on the electron phonon relaxation dynamics of plasmonic nanoparticles. A simple thermal annealing is used to transform as-deposited polycrystalline prismatic nanoparticles prepared with NSL into nearly single crystalline spherical nanoparticles.

1.4 Coherent Lattice (Phonon) Oscillation in Plasmonic Nanoparticles

With the advancement of ultrafast laser technology, pulsed laser based time-resolved transient absorption spectroscopy provides a powerful tool to measure the electron-phonon and phonon-phonon relaxation dynamics in thin metal films [83,99] and small metal particles [30,43,84-94]. Combined with ultrafast X-ray [119,120] and electron [121-123] diffraction experimental techniques, the ultrafast laser pulse induced coherent lattice motion of nanostructures has been directly observed. Besides X-ray and

electron diffraction techniques that can directly observe the lattice oscillation by monitoring changes in the diffraction pattern, another broadly used indirect technique to observe the coherent lattice oscillation is by monitoring the optical signal of the system (i.e. transmission, reflection, absorption, and scattering), which is modulated by the coherent lattice oscillation. The detection of the coherent lattice oscillation of metallic nanoparticles provides a powerful tool to characterize the mechanical and structural properties of nanostructures.

1.4.1 Optical Detection of Coherent Phonon Oscillation

Figure 1-13a is a time-resolved transient reflectivity experiment on femtosecond laser pulse excited coherent phonon oscillations at the surface of (100)-oriented bulk GaAs [124]. The excitation density is 10^{18} cm^{-3} for the orthogonal polarized pump and probe beams. The angle θ represents the angle between the polarization of the probe beam and the **[010]** crystal axis. This experiment was the first observation of coherent phonon oscillation at the surface of bulk GaAs by the transient pump-probe reflectivity technique. The author observed that the reflectivity modulation is dependent on the polarization of the probe laser beam. At $\theta = 90^{o}$, the reflectivity shows no modulation. At $\theta = 45^{o}$, the reflectivity signal shifts to a higher level and a modulation with a frequency of ~ 8.8 THz is observed. At $\theta = 135^{o}$, the reflectivity signal shifts to a lower level and a modulation with the same frequency but a phase shift of π is observed. This dependence of reflectivity modulation on the polarization of the probe beam suggests an electro-optic origin of the coherent phonon oscillation in the GaAs system [124].

Machol et al. [125] reported their observation on the absorption modulation in PbS quantum dots by using the time-resolved ultrafast pump-probe technique (shown in **Figure 1-13b**). The PbS quantum dots were synthesized in solution and dispersed on a thin film. The frequency of the absorption modulation (2.6 THz) matches the frequency of the transverse-optical phonon mode measured by far-infrared spectroscopy (90 cm^{-1}), which indicates that the observed absorption modulation represents the coherently oscillated transverse-optical phonons [125].

Vallee and co-workers [83] measured the time-resolved transient transmission of a 23 nm thick silver film probed at 435 nm as shown in **Figure 1-13c**. The measured modulation is induced by femtosecond laser pulse heating and has a period of 12.3 ps. This number agrees with the period of expansion and contraction mode of a film of 23 nm thickness [126].

Hartland and co-workers [109] measured the time-resolved transient absorption spectra of gold nanoparticles with diameters between 8 and 120 nm. **Figure 1-13d** is the measured coherent phonon oscillation for a 60 nm gold nanosphere sample, which has an oscillation period of ~ 15 ps. The frequencies of the coherent phonon oscillations are inversely proportional to the diameter of the nanoparticle.

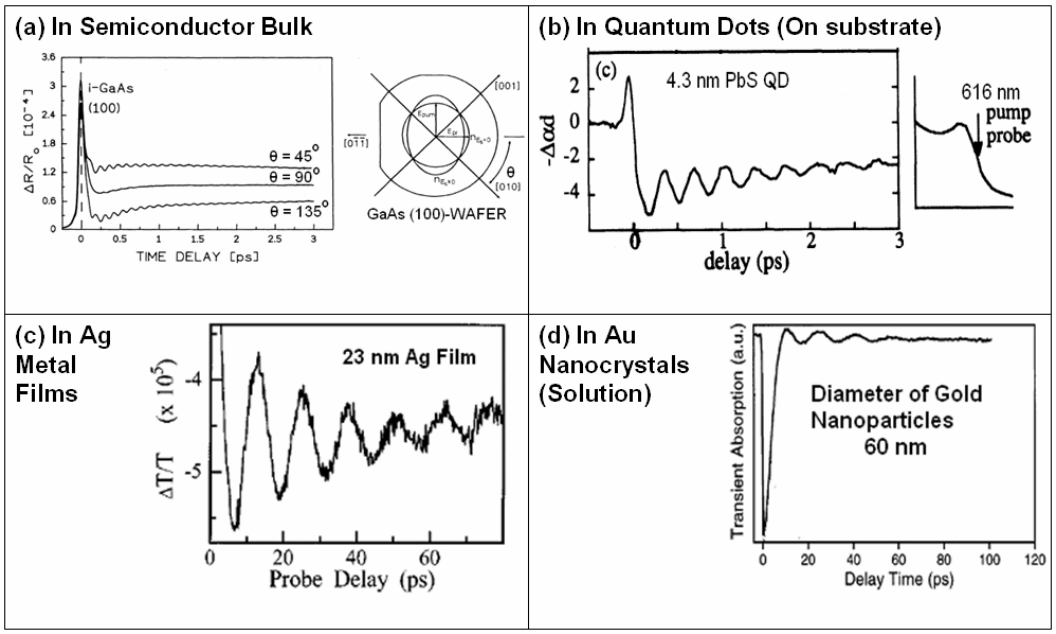

Figure 1-13: Previous studies on optically detected coherent phonon oscillations in many different systems. (a) Femtosecond laser pulse excited coherent phonon oscillations at the surface of (100)-oriented bulk GaAs monitored by time-resolved transient reflectivity. The excitation density was 10^{18} cm^{-3} for the orthogonal polarized pump and probe beams. The angle θ represents the angle between the polarization of the probe beam and the **[010]** crystal axis [124]. Reproduced with permission from *Phys. Rev. Lett.* 1990, 65, (6), 764-766. Copyright 2006 APS (http://prola.aps.org/abstract/PRL/v65/i6/p764_1). (b) Femtosecond laser induced absorption modulation in PbS quantum dots. The absorption modulation is induced by the coherently oscillating transverse-optical phonons [125]. Reproduced with permission from *Phys. Rev. B* 1993, 48, (4), 2819-2822 Copyright 2006 APS (http://prola.aps.org/abstract/PRB/v48/i4/p2819_1). (c) The time-resolved transient transmission of a 23 nm silver film probed at 435 nm. The measured modulation is induced by femtosecond laser pulses and has a period of 12.3 ps [83]. Reprinted with permission from *J. Phys. Chem. A* **2000,** 104, (18), 4321-4326. Copyright 2000 American Chemical Society. (d) The time-resolved transient absorption measurement of gold nanoparticles of 60 nm in diameter [109]. The period of the oscillation is ~ 15 ps. Reused with permission from Jose H. Hodak, Arnim Henglein, and Gregory V. Hartland, *Journal of Chemical Physics*, 111, 8613 (1999). Copyright 1999, American Institute of Physics.

1.4.2 Photothermal Excitation and Optical Detection Mechanism of Coherent Phonon Oscillation:

The excitation mechanism of phonon oscillations in metal nanoparticle is an impulsive heating by ultrafast laser pulses. During the electron-phonon relaxation (~ 1 ps)

[43,108,113], the lattice of the nanoparticle is heated up instantly. The lattice heating is much faster than the lattice movement (the period breathing mode vibration). Therefore, the size of the nanoparticle remains unchanged during the heating of the nanoparticle. The higher lattice temperature requires the nanoparticle to expand to a new equilibrium size. Thus, all of lattice atoms move to a new equilibrium position simultaneously and oscillate around the new equilibrium position due to their inertia. As shown by equation (1-1), in plasmonic nanoparticles the LSPR band is proportional to the square root of the free electron density in the particle. Therefore, the oscillation of the lattice changes the free electron density of the nanoparticle and the LSPR band oscillates correspondingly, as shown by **Figure 1-14a**. If the LSPR band oscillation is monitored at a fixed wavelength (green line in **Figure 1-14a**), the intensity of the transmission light will be modulated at the same frequency as the coherent lattice oscillation (**Figure 1-14b)**. Experiments using frequency-domain spectroscopies to study these low frequency coherent phonon oscillations are very difficult because of the strong Rayleigh scattering background.

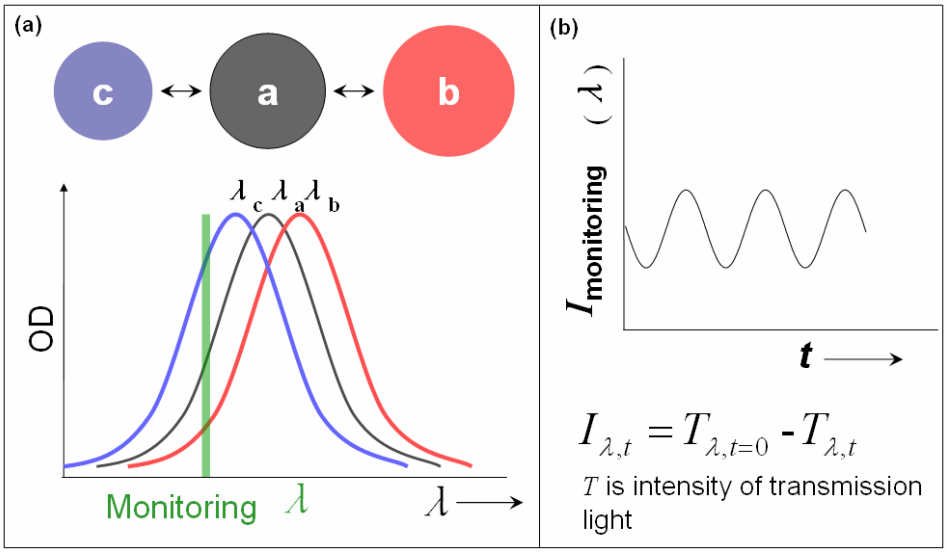

Figure 1-14: (a) A schematic diagram of the breathing mode of the coherent lattice (phonon) oscillation of a spherical plasmonic nanoparticle. The lattice oscillation changes the size of the nanoparticle and the free electron density in the nanoparticle. The LSPR band oscillates with the change of the free electron density in the nanoparticle. (b) If the LSPR band oscillation is monitored at a fixed wavelength (green line in (a)), the intensity of the transmission light will be modulated at the same frequency as the coherent lattice oscillation [127]. Reproduced with permission from "Optically Detected Coherent Picosecond Lattice Oscillations in Two Dimensional Arrays of Gold Nanocrystals of Different Sizes and Shapes Induced by Femtosecond Laser Pulses" in Plasmonics: Metallic Nanostructures and Their Optical Properties III, Proc. of SPIE, Vol. 5927, 592701 (2005).

1.4.3 Shape Dependence of Coherent Phonon Oscillations:

Ultrafast laser-induced phonon oscillations have been observed for spherical, ellipsoidal, cylindrical, cubic, prismatic, and core-shell noble metal nanoparticles. The period of these oscillations is found to be proportional to the dimension of the nanoparticle as predicted by classical mechanics calculations [86,88,128,129]. These coherent phonon oscillations have been observed in silver nanoparticles imbedded in a glass matrix of spherical [84] and ellipsoidal [88] shapes. They have also been observed in gold nanoparticles dispersed in colloidal solution of spherical [109,130,131] and

cylindrical shapes [59,132] as well as from aggregated gold particles in solution [133]. For prismatic shapes, coherent phonon oscillations have been observed in nanoparticles both distributed in colloidal solution [134,135] and arranged periodically on a glass substrate [30,136]. For spherical nanoparticles, the coherent oscillations have been attributed to the acoustic lattice vibration (periodic size change) of the metal nanoparticles caused by ultrafast laser-induced heating of the lattice [131]. For gold nanorods, the dominant coherent lattice vibration is found to be the extension mode [59]. In all of these nanoparticles mentioned we believe that it is the totally symmetric breathing modes that induce the largest change in the free electron density in the nanoparticles during their oscillation. As a result, they are the most effective modes in changing the wavelength maximum of the localized surface plasmon absorption and thus can be clearly detected by optical methods.

The vibration of spherical nanoparticles can be treated as an elastic sphere and its vibration mode is well understood by the classical mechanics model [128,137]. In this model, there are two different kinds of vibrations: torsional modes and spheroidal modes. Torsional modes do not have a lattice displacement along the radial direction of the sphere, while spheroidal modes have a lattice displacement both along and perpendicular to the radial direction of the sphere. The electron density of the particle does not change in torsional modes, so torsional modes can not be detected by the optical method, which is based on the shift of the LSPR band. Spheroidal vibration modes are discriminated by a solution number n and an angular momentum number l (both are integers). For the most easily detected breathing mode, l is equal to zero and the period of these modes (τ_{sphere}) is given by

$$\tau_{sphere} = \frac{2\pi R}{\eta c_l}, \tag{1-9}$$

where R is the radius of the nanoparticle, c_l is the longitudinal speed of sound in the material, and η is an eigenvalue that depends on the transversal and longitudinal speeds of sound [128], which is given by

$$\eta \cot \eta = 1 - \left(\frac{\eta c_l}{2 c_t} \right)^2, \tag{1-10}$$

where c_t is the transversal speed of sound in the material. For the breathing mode, η is calculated to be 2.93 for gold [109].

For rod-shaped gold nanoparticles of large aspect ratios, Hu et al. [59] performed theoretical and experimental studies on their coherent phonon oscillation modes. They found that two types of modes can be excited by the femtosecond laser impulse heating, the extensional mode and the breathing mode, as shown by **Figure 1-15**. The breathing mode is characterized by a pure expansion and contraction along the transverse (radial) direction of the rod, while the extensional mode involves dimension changes in both transverse and longitudinal directions [59]. The vibration period of the extensional mode is calculated by the equation [59,138]

$$\tau_{rod}^{ext(n)} = \frac{2L}{(2n+1)\sqrt{E/\rho}}, \tag{1-11}$$

where L is the length of the rod, E and ρ are Young's modulus and the density of the material, respectively. The vibration period of the breathing mode is calculated by the equation

$$\tau_{rod}^{br(n)} = \frac{2\pi R}{\varphi_n c_l}, \tag{1-12}$$

where R is the radius of the cylinder and φ_n is an eigenvalue given by

$$\varphi_n J_0(\varphi_n) = \frac{(1-2\nu)J_1(\varphi_n)}{(1-\nu)}, \tag{1-13}$$

where ν is Poisson's ratio. The value for φ_0 is calculated to be 2.28 for the fundamental breathing mode by using Poisson's ratio for bulk gold [139]. The measured coherent phonon oscillation period from experiments confirmed the vibration mode in the cylinder was the extensional mode.

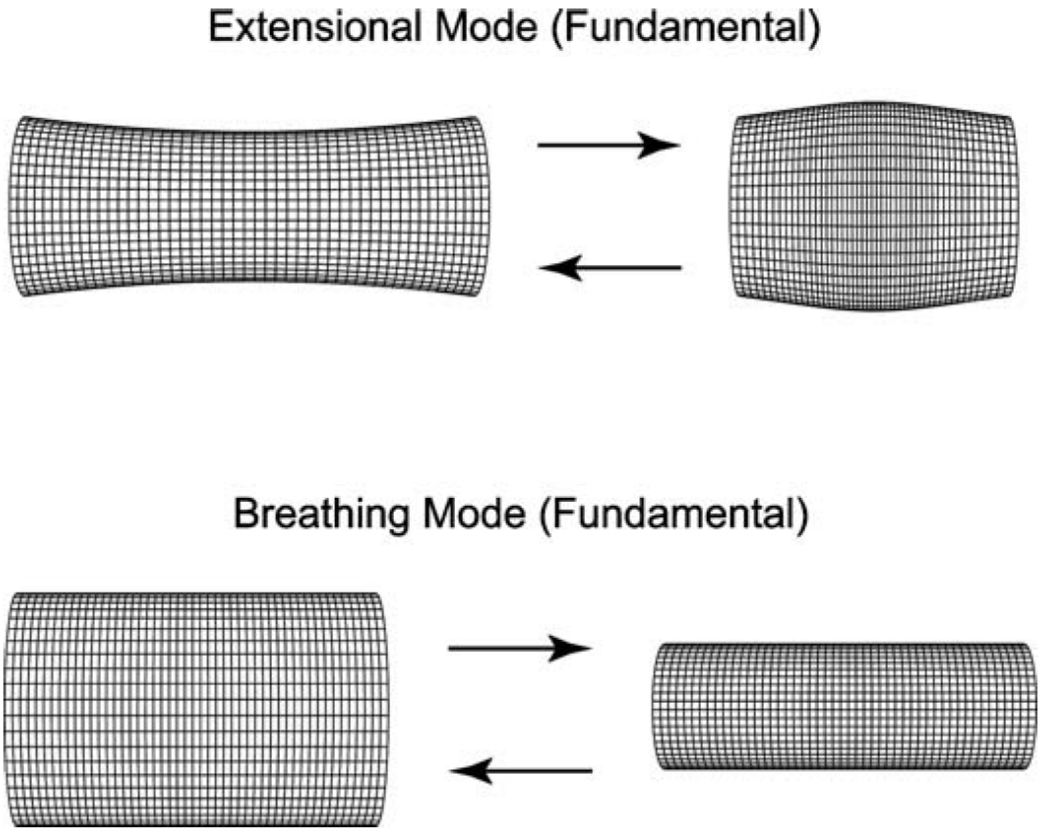

Figure 1-15: The extensional mode and the breathing mode of a vibrating cylinder (larger aspect ratio). The breathing mode is characterized by a pure expansion and contraction along the transversal (radial) direction of the rod, while the extensional mode involved dimension changes in both transversal and longitudinal directions [59]. Reprinted with permission from *J. Am. Chem. Soc.* **2003,** 125, (48), 14925-14933. Copyright 2003 American Chemical Society.

The vibration modes of cubic shaped nanoparticles were recently studied by Petrova et al. [140]. Two modulation periods from two vibrational modes were observed. The two periods were assigned to a breathing mode and a non-symmetric mode by finite element analysis. The generation of the breathing mode was attributed to homogeneous heating of the cubic nanoparticle while the generation of the non-symmetric mode was attributed to non-uniform energy absorption of the pump laser. The non-symmetric mode was only observable for large particles where the dimensions of particles were larger than the skin depth of the pump laser [140].

The vibrational modes of two kinds of core-shell nanoparticles were also studied. Hodak et al. [85] performed the experiment on the coherent excitation of vibration modes in bimetallic Au-Pb core-shell nanoparticles. A theoretical model which explains the observed vibrational periods was developed later based on classical continuum mechanics [141]. Guillon et al. [142] performed both experimental and theoretical studies on the coherent acoustic vibration of a dielectric-metallic core-shell nanoparticle (Au_2S/Au). From their theoretical calculation, the vibrational mode of the dielectric-metal core-shell system was found to be a fundamental breathing mode [142]. Several parameters affect the calculation of the coherent phonon oscillation period, such as the relative thickness of the shell to the over-all size, the density of the shell, and the sound velocity in the shell material. For a thin heavy shell, where the ratio of core radius to overall radius is close to one and the density of the shell is much higher than that of the surrounding medium, the coherent phonon oscillation period is given by [142]

$$T \approx \frac{R_2}{2c_l^s \beta_s (3-4\beta_s^2)^{1/2}}, \tag{1-14}$$

where R_2 is the overall radius of the core-shell particle, $\beta_s = c_t^s / c_l^s$, c_t^s and c_l^s are the respective transverse and longitudinal velocity of sound in the shell (for gold, c_t^s and c_l^s are 1200 and 3240 m/s, respectively).

We are interested in the coherent lattice oscillation of the prismatic plasmonic nanoparticle prepared with NSL. Due to the strong absorption of the dipolar LSPR oscillation and the sensitivity of the oscillation frequency to the size of prismatic nanoparticles with sharp tips, it is possible to obtain excellent oscillation amplitudes from a monolayer array of these nanoparticles with a good signal to noise ratio. The well defined two-dimensional array also allows us to find the effect of interparticle coupling on the coherent phonon oscillation of prismatic nanoparticles. The coupling effect is studied in detail with sets of nanodisk pairs fabricated by electron beam lithography and vary the separation between particles within the dimer pair.

1.5 Optical Modulation

Ultrafast modulation of light in a compact system is an important study area in many research fields, such as optical communications, inter-electronic chip optical connections, and photonic circuits [143-145]. The importance of the modulation of light has driven extensive efforts in the discovery of new techniques and the optimization of existing light modulation techniques [146-157].

Several techniques have been used to modulate light in optical modulators. One of them is the quantum-confined stark effect [146,147], which is induced by applying electric fields perpendicular to quantum well layers. The applied electric field pulls electrons and holes within quantum well layers towards opposite directions. The

separation of electrons and holes reduces the excitation energy of electron-hole pairs, thus the absorption spectra shift to lower wavelength (red shift) as shown by **Figure 1-16**. By applying a periodic electric field, the light passing through the quantum well layers is modulated accordingly. Due to the ultrafast response time (sub-picosecond), it is expected that the quantum wells can modulate light at a terahertz bandwidth [148,149]. Experimentally, Lewen et al. [150] fabricated a device that can modulate light at a frequency greater than 50 GHz. However, the quantum wells with strong quantum-confined stark effects were usually made from III-V semiconductors such as InP, GaAs, and their alloys, which were hard to be integrated with current silicon devices. Recently, a breakthrough was demonstrated in a silicon-based germanium quantum-well structure, which had a strong quantum-confined stark effect comparable to the III-V semiconductor structures [147].

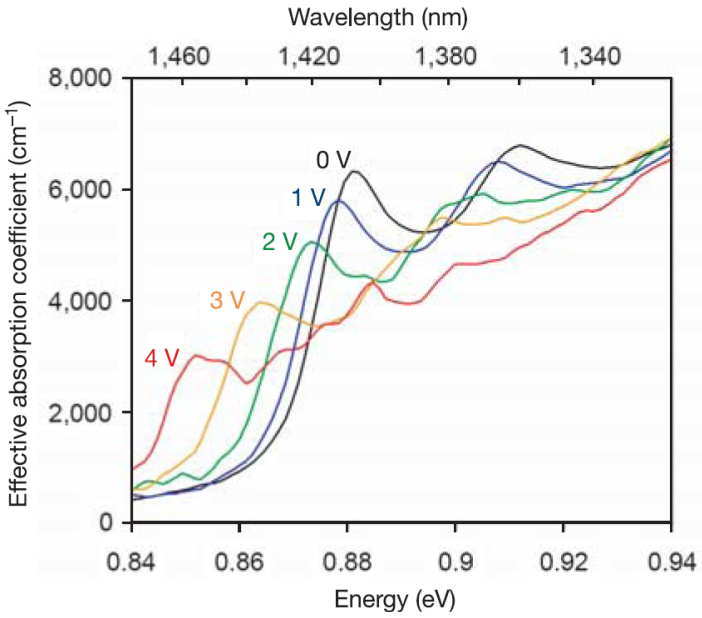

Figure 1-16: The effective absorption coefficient spectra of a germanium quantum-well structure on silicon, which shows a strong quantum confined stark effect with the applied electric field from zero to 4 volts [147]. Reprinted by permission from Macmillan Publishers Ltd: Nature, copyright (2005).

Another widely used technique to modulate light is based on the Mach-Zehnder interferometer [151-154], where the source waveguide is split into two arms, the gate arm and the reference arm. The optical source signal in the gate arm is phase shifted by an electrically produced critical carrier concentration perturbation. The optical source signal in the reference arm is left unaltered. When the gate arm and the reference arms are recombined, the phase shifted optical signal in the gate arm interferes with the original optical signal in the reference arm. An intensity modulation of the optical source signal is then generated as shown in **Figure 1-17**. Based on the Mach-Zehnder geometry, Lee and co-workers [152] fabricated a polymeric electro-optical modulator that modulated light at 200 GHz. Shi et al. [151] demonstrated that by using a certain chromophore, a polymeric

electro-optic modulator could operate at a voltage as low as 0.8 V. Compared to the typical operating voltage of polymeric and lithium niobate modulators (~ 5 V), the tremendous decrease in the attenuation voltage was attributed to strong electrostatic interactions between molecules [151].

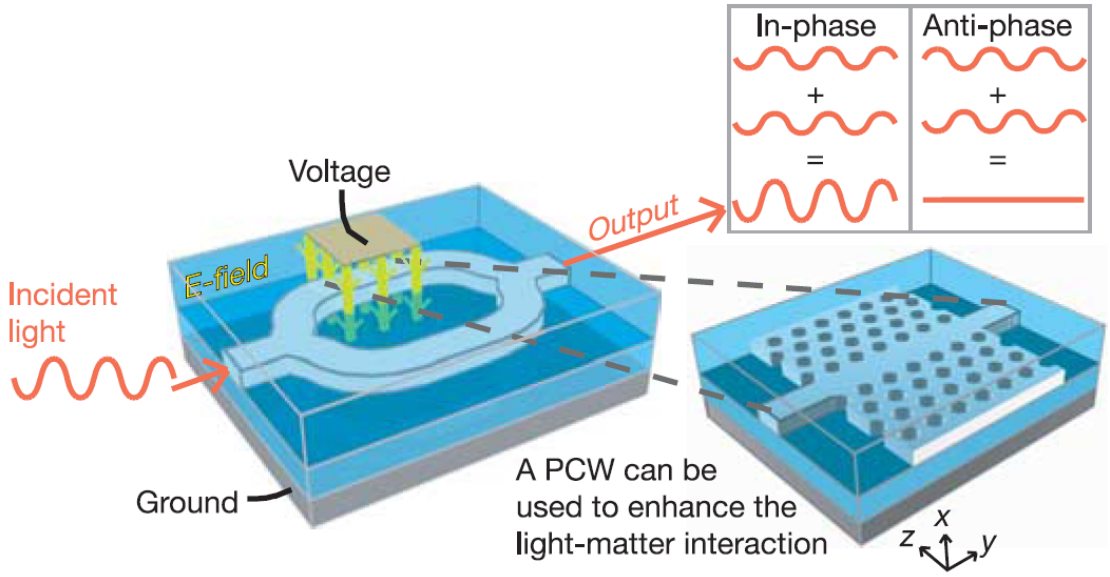

Figure 1-17: A schematic diagram of the Mach-Zehnder interferometer [154]. The source waveguide is split into two arms, the gate arm and the reference arm. The optical source signal in the gate arm is phase shifted by an electrically produced critical carrier concentration perturbation. When the optical signals in the gate and the reference arms are recombined, the phase shifted optical signal in the gate arm interferes with the original optical signal in the reference arm. An intensity modulation of the optical source signal is then generated. Reprinted by permission from Macmillan Publishers Ltd: Nature, copyright (2006).

Other techniques to modulate light have also been reported. Solgaard et al. [155] fabricated an attenuated total internal reflection modulator driven by photon-LSPR coupling. Jones et al. [156] reported an optical modulation in a silicon waveguide based on stimulated Raman scattering with a bandwidth of 80 MHz. de Lima et al. [157]

demonstrated a compact optical waveguide modulator driven by surface acoustic waves, which induced changes in the refractive index based on an elasto-optical effect.

Recently, all-optical modulation has received substantial attention due to its potential to realize terahertz optical modulations, optical system miniaturizations, and all-optical computation [158-161]. Almeida et al. [158] fabricated a silicon planar ring resonator that was functioned as an all-optical gate with a picosecond laser excitation. The enhanced transmission response from a small refractive index variation in silicon was based on a highly confined resonant structure. Marki et al. [160] used a planar photonic crystal silicon waveguide to modulate the in-plane transmission by an optical pump induced microcavity change. Hochberg and Baehr-Jones et al. [161] fabricated an optically controlled modulator in a silicon-polymer hybrid system based on the Mach-Zehnder interferometer. The phase shift of the optical source signal in the gate arm of the interferometer was optically induced by the nonlinear Kerr effect. Ebbesen et al. [162] used the LSPR related transmission change from a subwavelength hole array to modulate light. The transmission change is induced by the refractive index change that came from the excitation of chromophore molecules.

In the above mentioned modulation techniques, the mechanisms of the modulation of light in high frequencies are all involve electrical, acoustic, or optical gate signals modulated at the same frequency. More research efforts are necessary to discover new mechanisms and to optimize existing mechanisms to modulate light. This is important to realize the application of optical modulation in many research fields.

1.6 Pulsed Laser Photothermal Annealing of Plasmonic Nanoparticles

The interaction between noble metal nanoparticles and pulsed lasers [30,43,83-94,163-181] has received great research efforts. A distinct merit of pulsed lasers is their extremely high intensities at substantially reduced laser energies, which makes the interaction of materials with pulsed lasers inherently different from traditional thermal processing techniques. The irradiation of metallic nanoparticles with a laser pulse results in ultrafast temperature rises of the nanoparticle lattice (within a few picoseconds when using femtosecond laser pulses) [43,108,113], while the temperature of the environment initially remains constant. Since the phonon-phonon relaxation time is usually on the order of hundreds of picoseconds [43,87], femtosecond pulsed laser irradiation can lead to size and shape changes of the nanoparticles before the deposited laser energy is given to the surrounding medium. These distinct photothermal properties of ultrafast lasers lead to many important chemical and physical applications in the preparation and modification of nanoparticles.

1.6.1 Pulsed Laser Ablation in Nanoparticle Synthesis:

Metallic nanoparticles have been synthesized with pulsed laser ablation of metallic bulk materials in solution [163-171]. **Figure 1-18a** is a schematic diagram of the laser irradiation apparatus used by Mafune et al. in making metallic nanoparticles [164]. **Figure 1-18b** is a TEM image of gold nanoparticles produced by 1064 nm nanosecond laser irradiation in a 10^{-4} M sodium dodecyl sulfate (SDS) aqueous solution. The laser pulse energy was 80 mJ. The nanoparticles were formed rapidly from laser ablation of the bulk material and the growth was slowed down and terminated by the surfactant coating.

Therefore, the nanoparticles formed in a solution of high surfactant concentration were smaller than those formed in a solution of low surfactant concentration. The same method can also be used to make silver [163], platinum [182], titanium, and silicon [171] nanoparticles. Tsuji et al. [167]studied the effect of laser wavelength on the size of silver nanoparticles prepared with the irradiation of a nanosecond laser. They found the size of formed nanoparticles decreased from 29 to 12 nm with the decrease in the laser wavelength. Chen et al. [170] studied the effect of different surfactants on the size of the silver nanoparticles produced by laser ablation. They found that nanoparticles formed in the anionic SDS had a diameter of 4.2 nm and those formed in the cationic cetyltrimethylammonium bromide (CTAB) had a diameter of 7.8 nm. They also found that a lesser laser intensity produces larger nanoparticles.

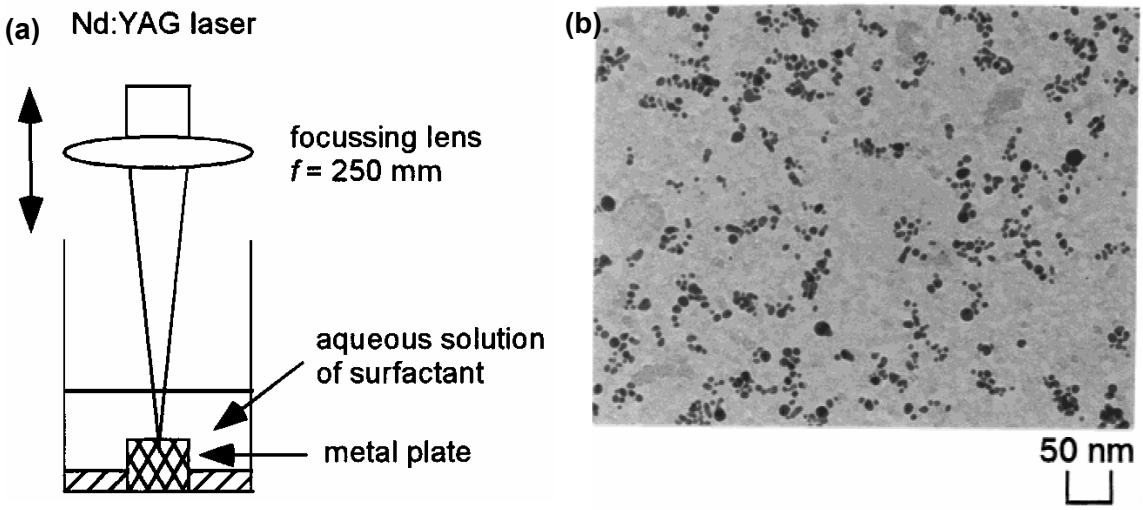

Figure 1-18: (a) A schematic diagram of the laser irradiation apparatus in making metal nanoparticles. (b) TEM image of gold nanoparticles produced by 1064 nm laser irradiation in a 10^{-4} M sodium dodecyl sulfate aqueous solution. The laser pulse energy was 80 mJ [164]. Reprinted with permission from *J. Phys. Chem. B* **2001,** 105, (22), 5114-5120. Copyright 2001 American Chemical Society.

Kabashin et al. [165,183] used femtosecond laser ablation of a gold plate in a cyclodextrin aqueous solution to create highly monodisperse gold nanoparticle samples that are extremely stable. Cyclodextrin consists of glucopyranose units and has a conical torus-like structure. The interior cavity of cyclodextrin is hydrophobic and its exterior is hydrophilic. By increasing the pH of the cyclodextrin solution from 3 to 9, the size of the gold nanoparticles can be tuned from 16 to 2 nm [166]. Kabashin et al. [165] also reported two different material ablation mechanisms in making gold nanoparticle. At low laser fluence (< 400 J/cm^2), monodisperse gold nanoparticles of a small diameter (3 – 10 nm) were produced by a thermal-free femtosecond ablation. At high laser fluence, larger nanoparticles of a broader size distribution were formed by a plasma-induced heating and ablation. Tsuji et al. [169] compared the difference between femtosecond and nanosecond laser in making silver nanoparticles. They found that nanosecond laser pulses are more efficient in making nanoparticles than femtosecond laser pulses, while nanoparticles prepared by the femtosecond laser irradiation had a smaller size distribution than those prepared by nanosecond laser pulses.

Metallic nanoparticles have also been synthesized by pulsed laser deposition (PLD) techniques on substrates [172-175]. Ausanio et al. [172] fabricated films of nickel nanoparticles by femtosecond PLD in a vacuum chamber. These nanoparticle films had unique magnetic properties due to their peculiar shape and orientation anisotropy of nanoparticles formed by the femtosecond laser deposition. Gonzalo et al. [173] made Ag-Cu nanocrystals in an amorphous Al_2O_3 matrix by alternating ablation of the pure metals. By controlling the relative content of the silver and copper, they selectively tuned the LSPR band of the nanoparticles from 424 to 572 nm. They proposed that Ag-Cu

nanoparticles were produced from a metastable solid solution of the silver and copper. Pham et al. [174] fabricated a $PbZr_{0.53}Ti_{0.47}O_3$ (PZT) thin film with a high dielectric constant that contained Pt nanoparticles of 3 – 10 nm in diameter. Chen et al. [175] prepared silicon nanocrystal films on quartz substrates with a nanosecond KrF excimer laser. Pereira et al. [181] found that aggregated iron oxide nanoparticles could be directly formed on a bulk steel surface with a pulsed laser irradiation.

1.6.2 Pulsed Laser Annealing in Nanoparticle Modification

It is also found that the pulsed laser is a convenient tool to control the size and shape distribution of inhomogeneous nanoparticle samples in colloidal solutions [176-178,184], in a glass matrix [93,94], and on a substrate [179,180]. Link et al. [176,184] used femtosecond and nanosecond lasers to transform rod-shaped gold nanoparticles into spherical particles. The wavelength of femtosecond and nanosecond lasers was tuned to the longitudinal LSPR band of gold nanorods at 800 nm. At moderate irradiation energy, the femtosecond laser pulse melted the nanorods to near spherical nanoparticles of comparable volumes, while nanosecond laser pulses made the nanoparticles dissociate to smaller nanospheres. At high energy, the femtosecond laser also fragmented rod shaped nanoparticles into smaller spheres. The difference is explained by the more efficient heating of nanoparticles by a nanosecond laser than that by a femtosecond laser because photons of a nanosecond pulse irradiated the nanoparticles continuously on a nanosecond time scale, while nanoparticles were cooled down after the irradiation of a femtosecond

laser pulse by releasing the energy to the environment through phonon-phonon relaxation [176,184].

Another strategy used by Stietz and co-workers [179,180] to control the size of nanoparticles formed on the surface of the substrate was using pulsed lasers of different wavelengths as irradiation sources. Since the LSPR absorption maximum of nanoparticles varies with the particle's size and shape, overlapping the laser wavelength with the LSPR band of unwanted nanoparticle components is an effective way to control the particle's dimensions. Thus, the size distribution of the nanoparticles can be substantially narrowed by eliminating smaller nanoparticles through laser ablation and reducing the size of larger nanoparticles through particle annealing. This method can be used with all nanoparticles that have size and shape dependent LSPR bands, including Au, Ag, Cu, Al, Ta, and alkali metal clusters [179].

Laser pulses of nanosecond and femtosecond durations at certain energy not only reduce the size and change the shape of nanoparticles, but also lead to other interesting phenomena. Habenicht et al. [185] showed that the melting of nanoprisms on a graphite substrate could lead to lifting of melted spheres from the substrate with a velocity of 20 m/s, as shown in **Figure 1-19**. In this experiment, fast heating of an initially flat nanostructure was achieved by irradiation with an intense nanosecond laser pulse that produced a liquid nanostrurture that was far from the most stable spherical shape. Due to the dewetting process of the liquid gold on the glass or graphite surface, the flat liquid nanostructure contracted to a spherical shape in a few nanoseconds. This contraction caused the mass center of the nanostructure to transfer away from the substrate surface, producing a moment shift that lifted the particle off of the substrate. By changing the

prismatic shape to the spherical shape, it was calculated that 20 % of the released surface energy was converted to kinetic energy. The study about this jumping process is important for a wide variety applications of coating and deposition, such as inkjet printing [186] and herbicide or pesticide spraying [187].

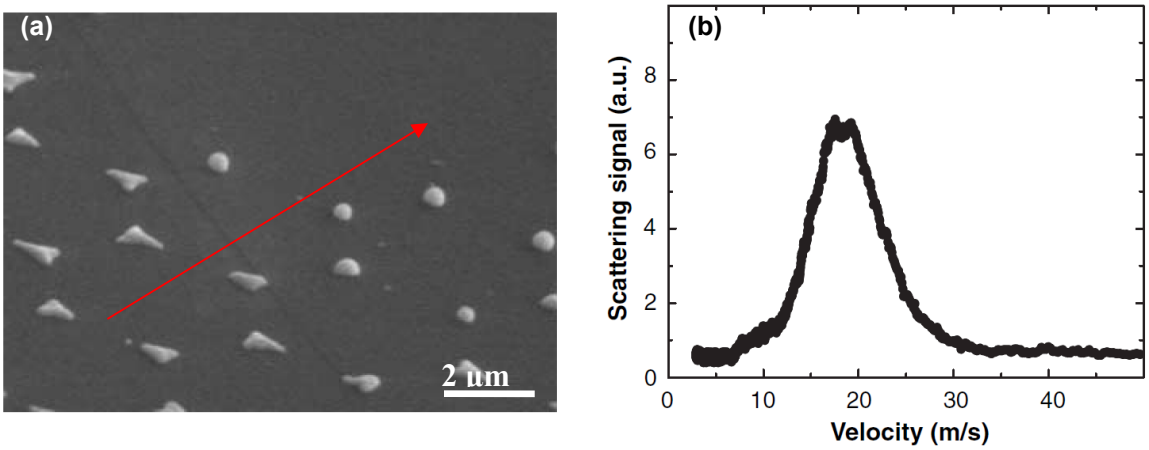

Figure 1-19: (a) A gold prism array irradiated by a nanosecond laser pulse. Due to the Gaussian distribution of the laser pulse profile, laser energy was increased from the down left to the top right as shown by the red arrow. Those particles originally sat on the empty space jumped off the substrate due to the nanosecond laser irradiation. (b) The jumping speed of nanoparticles measured by a light scattering method [185].

Most of pulsed laser photothermal studies have been focused on the laser irradiation of nanoparticles randomly distributed in a solution, on a substrate, or in a glass matrix. Due to the Gaussian distribution of laser pulse energy, the laser focus point on the sample has the highest power density in the center of the focus point and the lowest power on its edge. Most of the studies used total laser pulse energy as the control parameter and measured the TEM images of final irradiated products, which only gave an average result of the effect of pulsed laser irradiations, especially for solution samples.

More detailed study is needed to build the relationship between the nanoparticle shape and the "true" irradiation power density that induces those changes.

1.7 Thesis Focus and Organization

The rest of the thesis is structured as follows. In Chapter 2, the detailed sample preparation and characterization methods are described. The sample preparation methods include nanosphere lithography and electron beam lithography. The samples were characterized with Scanning Electron Microscopy, Transmission Electron Microscopy, Atomic Force Microscopy, UV-vis absorption spectroscopy, and femtosecond transient transmission spectroscopy. Based on the above characterization techniques, several studies on the interaction between femtosecond laser pulses and plasmonic nanoparticles are performed.

In Chapter 3, we examined the effect of the lattice crystallinity on the electron-phonon relaxation rates in monolayer periodic array nanoparticles prepared with NSL. In order to study the importance of surface phonons on the electron-phonon relaxation in plasmonic nanoparticles, the effect of size, shape and material have been studied. Gold and silver nanoparticle showed no dependence on size and shape but copper nanoparticles showed some size dependence. This suggests that the bulk phonons, which are sensitive to the bulk phase structure, are solely responsible for the relaxation of the hot electrons in gold and silver plasmonic nanoparticles. By the designed experiment, we found that the electron-phonon relaxation rate decreases greatly when polycrystalline prismatic gold nanoparticles are annealed and transformed into nearly single crystalline nanospheres.

The fast electron-phonon relaxation in polycrystalline prismatic gold nanoparticles is explained by the presence of high density grain boundaries.

In Chapter 4, we studied the ultrafast laser-induced coherent phonon oscillation in prismatic gold nanoparticles assembled in monolayer periodic arrays. We studied the effect of size, shape, and thickness of the prismatic array nanoparticles on the period of their coherent phonon oscillations. The amplitude and phase of the oscillation was also studied as we decreased the monitoring wavelength. From the wavelength at which the oscillation is not detected, the dependence of the absorption maxima on the size of the nanoparticles, the changes in the nanoparticle size are estimated during its oscillation.

In Chapter 5, we studied the optically detected laser-induced coherent phonon oscillations of monolayers periodic arrays of prismatic shaped silver and gold nanoparticles assembled by using the technique of nanosphere lithography. For both gold and silver nanoparticles, the coherent lattice oscillation periods were found to linearly depend on the size of nanoparticles. However, while the observed dependence for silver nanoparticle was found to follow the calculated dependence of single particle on size (based on a one-dimensional standing wave model), gold nanoparticle deviated and the deviation was found to increase with the size of nanoparticles. This deviation was explained by a simple interparticle lattice oscillating dipolar coupling mode. The absence of this deviation in the silver nanoparticle arrays was blamed on the weak interparticle coupling due to their rounded tips and the possibility of the oxidation of their surfaces.

In Chapter 6, we fabricated arrays of gold nanodisk pairs and used femtosecond transient transmission spectroscopy to optically determine the coherent phonon vibration frequency as a function of the interparticle separation. It is found that the fractional

change in the vibration frequency increases exponentially with decreasing the ratio of the interparticle separation to the particle diameter. The increase in the vibration period of the coherent phonon when two nanodisks are closely placed is due to the coupling of lattice oscillation dipoles. For the same set of nanoparticle pairs, we found that the observed scaling exponential law governing the coherent phonon vibration frequency with distance is the same as that observed for the change in the surface plasmon electronic resonance frequency with distance. They both have an exponential behavior with the same decay constant, which suggest the same dipole-dipole interaction nature of the coupled coherent electron and lattice oscillation in the close-placed pair nanodisks.

In Chapter 7, we describe a new all-optical modulation mechanism induced by an opto-mechanical Nano-system (OMNS), where the transmitted light is modulated by the coherent oscillation of the phonon modes of gold capped periodic polystyrene (PS) monolayer arrays. The modulation is caused by the phonon oscillations of gold caps on PS spheres in this two dimensional photonic crystal system. Most of the previously reported modulation of light in high frequency is induced by electrical, acoustic, or optical gate signals that are modulated at the same frequency. In many cases, the generation of a high frequency gate signal is difficult. In our experiment, the gigahertz optical modulation is “generated” by a low repetition rate femtosecond laser. We also demonstrated that the phonon oscillation of the OMNS modulates the transmitted light in gigahertz bandwidth, which is tunable by changing the diameter of the PS spheres.

In Chapter 8, we studied femtosecond laser induced shape and LSPR band changes of the monolayer periodic gold prismatic array nanoparticles. Since the laser pulse has a Gaussian distribution, using a solution sample can only determine the

relationship between the shape change of the nanoparticle and the averaged laser power density. In contrast, using a two-dimensional array sample allows us to accurately determine the shape and optical property changes of the nanoparticle under the "true" local laser density.

In Chapter 9, we observed that the femtosecond laser irradiation of the nanoprisms at the surface plasmon resonance absorption maximum can cause a nanoparticle to detach from the substrate and "fly away" at an average threshold energy of 740 fJ/particle. We believe that the forces involved in the motion of the nanoprisms are different from those proposed in the nanosecond laser pulse irradiation experiment, in which melting of the nanoparticle necessarily occurs prior to nanoparticle ejection. AFM measurements revealed that the displaced nanoparticles are thinner and smaller than the undisplaced ones, which supports an atomic ablation mechanism. A mechanical mechanism is proposed, in which at threshold or higher fluence rapid atomic ablation builds up pressure underneath the nanoparticle, which transfers a strong impulse to the nanoparticle. Depending on the laser fluence, this impulse can flip the nanoparticle over or, at higher fluences, can cause the nanoparticle to fly away.

1.8 References

[1] Daniel, M. C.; Astruc, D., *Chem. Rev.* **2004,** 104, (1), 293-346.

[2] Faraday, M., *Philos. Trans. R. Soc. London, A* **1857,** 147, 145-181.

[3] Mie, G., *Annalen Der Physik* **1908,** 25, (3), 377-445.

[4] Antonii, F., *Panacea Aurea-Auro Potabile*. Bibliopolio Frobeniano: Hamburg, **1618**.

[5] Kunckels, J., *Nuetliche Observationes oder Anmerkungen von Auro und Argento Potabili*. Schutzens: Hamburg, **1676**.

[6] Jensen, T. R.; Malinsky, M. D.; Haynes, C. L.; Van Duyne, R. P., *J. Phys. Chem. B* **2000,** 104, (45), 10549-10556.

[7] Link, S.; El-Sayed, M. A., *Int. Rev. Phys. Chem.* **2000,** 19, (3), 409-453.

[8] Haes, A. J.; Van Duyne, R. P., *J. Am. Chem. Soc.* **2002,** 124, (35), 10596-10604.

[9] Haynes, C. L.; McFarland, A. D.; Zhao, L. L.; Van Duyne, R. P.; Schatz, G. C.; Gunnarsson, L.; Prikulis, J.; Kasemo, B.; Kall, M., *J. Phys. Chem. B* **2003,** 107, (30), 7337-7342.

[10] Krenn, J. R.; Dereux, A.; Weeber, J. C.; Bourillot, E.; Lacroute, Y.; Goudonnet, J. P.; Schider, G.; Gotschy, W.; Leitner, A.; Aussenegg, F. R.; Girard, C., *Phys. Rev. Lett.* **1999,** 82, (12), 2590-2593.

[11] Rechberger, W.; Hohenau, A.; Leitner, A.; Krenn, J. R.; Lamprecht, B.; Aussenegg, F. R., *Opt. Commun.* **2003,** 220, (1-3), 137-141.

[12] Zhao, L. L.; Kelly, K. L.; Schatz, G. C., *J. Phys. Chem. B* **2003,** 107, (30), 7343-7350.

[13] Quinten, M.; Leitner, A.; Krenn, J. R.; Aussenegg, F. R., *Opt. Lett.* **1998,** 23, (17), 1331-1333.

[14] Schuck, P. J.; Fromm, D. P.; Sundaramurthy, A.; Kino, G. S.; Moerner, W. E., *Phys. Rev. Lett.* **2005,** 94, (1), 017402.

[15] Maier, S. A.; Kik, P. G.; Atwater, H. A.; Meltzer, S.; Harel, E.; Koel, B. E.; Requicha, A. A. G., *Nat. Mater.* **2003**, 229-232.

[16] Elghanian, R.; Storhoff, J. J.; Mucic, R. C.; Letsinger, R. L.; Mirkin, C. A., *Science* **1997,** 277, (5329), 1078-1081.

[17] McFarland, A. D.; Van Duyne, R. P., *Nano Lett.* **2003,** 3, (8), 1057-1062.

[18] Yonzon, C. R.; Haynes, C. L.; Zhang, X.; Walsh, J. T., Jr.; Van Duyne, R. P., *Anal. Chem.* **2004,** 76, (1), 78-85.

[19] Haes, A. J.; Hall, W. P.; Chang, L.; Klein, W. L.; Van Duyne, R. P., *Nano Lett.* **2004,** 4, (6), 1029-1034.

[20] Haes, A. J.; Chang, L.; Klein, W. L.; Van Duyne, R. P., *J. Am. Chem. Soc.* **2005,** 127, (7), 2264-2271.

[21] Riboh, J. C.; Haes, A. J.; McFarland, A. D.; Yonzon, C. R.; Van Duyne, R. P., *Journal of Physical Chemistry B* **2003,** 107, (8), 1772-1780.

[22] Haes, A. J.; Stuart, D. A.; Nie, S.; Van Duyne, R. P., *J. Fluoresc.* **2004,** 14, (4), 355-367.

[23] Loo, C.; Lowery, A.; Halas, N.; West, J.; Drezek, R., *Nano Lett.* **2005,** 5, (4), 709-711.

[24] El-Sayed, I. H.; Huang, X. H.; El-Sayed, M. A., *Nano Lett.* **2005,** 5, (5), 829-834.

[25] Huang, X. H.; El-Sayed, I. H.; Qian, W.; El-Sayed, M. A., *J. Am. Chem. Soc.* **2006,** 128, (6), 2115-2120.

[26] Huang, W. Y.; Qian, W.; El-Sayed, M. A., *J. Appl. Phys.* **2005,** 98, (11), 114301.

[27] Wang, Z. L.; Petroski, J. M.; Green, T. C.; El-Sayed, M. A., *J. Phys. Chem. B* **1998,** 102, (32), 6145-6151.

[28] El-Sayed, M. A., *Acc. Chem. Res.* **2001,** 34, (4), 257-264.

[29] Hartland, G. V., *Annu. Rev. Phys. Chem.* **2006,** 57, 403-430.

[30] Huang, W. Y.; Qian, W.; El-Sayed, M. A., *Nano Lett.* **2004,** 4, (9), 1741-1747.

[31] Haynes, C. L.; Van Duyne, R. P., *J. Phys. Chem. B* **2001,** 105, (24), 5599-5611.

[32] Heitmann, D.; Kotthaus, J. P., *Phys. Today* **1993,** 46, (6), 56-63.

[33] Marlo, M.; Harju, A.; Nieminen, R. M., *Phys. Rev. Lett.* **2003,** 91, (18), 187401.

[34] Zou, S.; Janel, N.; Schatz, G. C., *J. Chem. Phys.* **2004,** 120, (23), 10871-10875.

[35] Zhao, L.; Kelly, K. L.; Schatz, G. C., *J. Phys. Chem. B* **2003,** 107, (30), 7343-7350.

[36] McKnight, T. E.; Melechko, A. V.; Hensley, D. K.; Mann, D. G. J.; Griffin, G. D.; Simpson, M. L., *Nano Lett.* **2004,** 4, (7), 1213-1219.

[37] Fromm, D. P.; Sundaramurthy, A.; Schuck, P. J.; Kino, G.; Moerner, W. E., *Nano Lett.* **2004,** 4, (5), 957-961.

[38] Haynes, C. L.; Van Duyne, R. P., *J. Phys. Chem. B* **2003,** 107, (30), 7426-7433.

[39] Krasavin, A. V.; Zheludev, N. I., *Appl. Phys. Lett.* **2004,** 84, (8), 1416-1418.

[40] Kreibig, U.; Vollmer, M., *Optical properties of metal clusters*. Berlin: New York, 1995.

[41] The British Museum, "The art of glass", www.thebritishmuseum.ac.uk/explore/online_tours/general/the_art_of_glass/the_lycurgus_cup.aspx

[42] Barber, D. J.; Freestone, I. C., *Archaeometry* **1990,** 32, (1), 33-45.

[43] Link, S.; El-Sayed, M. A., *J. Phys. Chem. B* **1999,** 103, (40), 8410-8426.

[44] Gans, R., *Annalen Der Physik* **1915,** 47, (10), 270-U14.

[45] Purcell, E. M.; Pennypac.Cr, *Astrophys. J.* **1973,** 186, (2), 705-714.

[46] Draine, B. T.; Goodman, J., *Astrophys. J.* **1993,** 405, (2), 685-697.

[47] Draine, B. T.; Flatau, P. J., *Journal of the Optical Society of America a-Optics Image Science and Vision* **1994,** 11, (4), 1491-1499.

[48] Yang, W. H.; Schatz, G. C.; Vanduyne, R. P., *J. Chem. Phys.* **1995,** 103, (3), 869-875.

[49] Moreno, E.; Erni, D.; Hafner, C.; Vahldieck, R., *Journal of the Optical Society of America a-Optics Image Science and Vision* **2002,** 19, (1), 101-111.

[50] Novotny, L.; Pohl, D. W.; Hecht, B., *Opt. Lett.* **1995,** 20, (9), 970-972.

[51] Bian, R. X.; Dunn, R. C.; Xie, X. S., *Phys. Rev. Lett.* **1995,** 75, (26), 4772-4775.

[52] Novotny, L.; Bian, R. X.; Xie, X. S., *Phys. Rev. Lett.* **1997,** 79, (4), 645-648.

[53] Kelly, K. L.; Coronado, E.; Zhao, L. L.; Schatz, G. C., *J. Phys. Chem. B* **2003,** 107, (3), 668-677.

[54] Gunnarsson, L.; Rindzevicius, T.; Prikulis, J.; Kasemo, B.; Kall, M.; Zou, S. L.; Schatz, G. C., *J. Phys. Chem. B* **2005,** 109, (3), 1079-1087.

[55] Draine, B. T.; Flatau, P. J. *Program DDSCAT*, Scripps Institute of Oceanography, University of California: San Diego, CA.

[56] Henglein, A.; Meisel, D., *Langmuir* **1998,** 14, (26), 7392-7396.

[57] Henglein, A., *Langmuir* **1999,** 15, (20), 6738-6744.

[58] Borek, R.; Berg, K. J.; Berg, G., *Glass Sci. Technol.* **1998,** 71, (12), 352-359.

[59] Hu, M.; Wang, X.; Hartland, G. V.; Mulvaney, P.; Juste, J. P.; Sader, J. E., *J. Am. Chem. Soc.* **2003,** 125, (48), 14925-14933.

[60] Fan, H. Y.; Yang, K.; Boye, D. M.; Sigmon, T.; Malloy, K. J.; Xu, H. F.; Lopez, G. P.; Brinker, C. J., *Science* **2004,** 304, (5670), 567-571.

[61] Hao, E.; Schatz, G. C.; Hupp, J. T., *J. Fluoresc.* **2004,** 14, (4), 331-341.

[62] Hao, E.; Bailey, R. C.; Schatz, G. C.; Hupp, J. T.; Li, S., *Nano Lett.* **2004,** 4, (2), 327-330.

[63] Fischer, U. C.; Zingsheim, H. P., *J. Vac. Sci. Technol.* **1981,** 19, (4), 881-885.

[64] Deckman, H. W.; Dunsmuir, J. H., *J. Vac. Sci. Technol. B* **1983,** 1, (4), 1109-1112.

[65] Denkov, N. D.; Velev, O. D.; Kralchevsky, P. A.; Ivanov, I. B.; Yoshimura, H.; Nagayama, K., *Nature* **1993,** 361, (6407), 26-26.

[66] Deegan, R. D.; Bakajin, O.; Dupont, T. F.; Huber, G.; Nagel, S. R.; Witten, T. A., *Nature* **1997,** 389, (6653), 827-829.

[67] Dimitrov, A. S.; Nagayama, K., *Langmuir* **1996,** 12, (5), 1303-1311.

[68] Gu, Z. Z.; Yu, Y. H.; Zhang, H.; Chen, H.; Lu, Z.; Fujishima, A.; Sato, O., *Appl. Phys. A: Mater. Sci. Process.* **2005,** 81, (1), 47-49.

[69] Hulteen, J. C.; Van Duyne, R. P., *J. Vac. Sci. Technol. A* **1995,** 13, (3, Pt. 2), 1553-8.

[70] Haynes, C. L.; McFarland, A. D.; Smith, M. T.; Hulteen, J. C.; Van Duyne, R. P., *J. Phys. Chem. B* **2002,** 106, (8), 1898-1902.

[71] Malinsky, M. D.; Kelly, K. L.; Schatz, G. C.; Van Duyne, R. P., *J. Am. Chem. Soc.* **2001,** 123, (7), 1471-1482.

[72] Sherry, L. J.; Jin, R. C.; Mirkin, C. A.; Schatz, G. C.; Van Duyne, R. P., *Nano Lett.* **2006,** 6, (9), 2060-2065.

[73] Moran, A. M.; Sung, J. H.; Hicks, E. M.; Van Duyne, R. P.; Spears, K. G., *J. Phys. Chem. B* **2005,** 109, (10), 4501-4506.

[74] Haynes, C. L.; Van Duyne, R. P., *Nano Lett.* **2003,** 3, (7), 939-943.

[75] Kosiorek, A.; Kandulski, W.; Chudzinski, P.; Kempa, K.; Giersig, M., *Nano Lett.* **2004,** 4, (7), 1359-1363.

[76] Huang, Z. P.; Carnahan, D. L.; Rybczynski, J.; Giersig, M.; Sennett, M.; Wang, D. Z.; Wen, J. G.; Kempa, K.; Ren, Z. F., *Appl. Phys. Lett.* **2003,** 82, (3), 460-462.

[77] Kempa, K.; Kimball, B.; Rybczynski, J.; Huang, Z. P.; Wu, P. F.; Steeves, D.; Sennett, M.; Giersig, M.; Rao, D.; Carnahan, D. L.; Wang, D. Z.; Lao, J. Y.; Li, W. Z.; Ren, Z. F., *Nano Lett.* **2003,** 3, (1), 13-18.

[78] Wang, X.; Summers, C. J.; Wang, Z. L., *Nano Letters* **2004,** 4, (3), 423-426.

[79] Wang, X. D.; Graugnard, E.; King, J. S.; Zhong, L. W.; Summers, C. J., *Nano Lett.* **2004,** 4, (11), 2223-2226.

[80] Wang, X. D.; Lao, C. S.; Graugnard, E.; Summers, C. J.; Wang, Z. L., *Nano Lett.* **2005,** 5, (9), 1784-1788.

[81] Whitney, A. V.; Myers, B. D.; Van Duyne, R. P., *Nano Lett.* **2004,** 4, (8), 1507-1511.

[82] Cheung, C. L.; Nikolic, R. J.; Reinhardt, C. E.; Wang, T. F., *Nanotechnology* **2006,** 17, (5), 1339-1343.

[83] Del Fatti, N.; Voisin, C.; Christofilos, D.; Vallee, F.; Flytzanis, C., *J. Phys. Chem. A* **2000,** 104, (18), 4321-4326.

[84] Del Fatti, N.; Voisin, C.; Chevy, F.; Vallee, F.; Flytzanis, C., *J. Chem. Phys.* **1999,** 110, (23), 11484-11487.

[85] Hodak, J. H.; Henglein, A.; Hartland, G. V., *J. Phys. Chem. B* **2000,** 104, (21), 5053-5055.

[86] Hodak, J. H.; Henglein, A.; Hartland, G. V., *J. Phys. Chem. B* **2000,** 104, (43), 9954-9965.

[87] Perner, M.; Bost, P.; Lemmer, U.; vonPlessen, G.; Feldmann, J.; Becker, U.; Mennig, M.; Schmitt, M.; Schmidt, H., *Phys. Rev. Lett.* **1997,** 78, (11), 2192-2195.

[88] Perner, M.; Gresillon, S.; Marz, J.; von Plessen, G.; Feldmann, J.; Porstendorfer, J.; Berg, K. J.; Berg, G., *Phys. Rev. Lett.* **2000,** 85, (4), 792-795.

[89] Mohamed, M. B.; Ahmadi, T. S.; Link, S.; Braun, M.; El-Sayed, M. A., *Chem. Phys. Lett.* **2001,** 343, (1-2), 55-63.

[90] Link, S.; Hathcock, D. J.; Nikoobakht, B.; El-Sayed, M. A., *Adv. Mater.* **2003,** 15, (5), 393-396.

[91] Link, S.; Furube, A.; Mohamed, M. B.; Asahi, T.; Masuhara, H.; El-Sayed, M. A., *J. Phys. Chem. B* **2002,** 106, (5), 945-955.

[92] Link, S.; El-Sayed, M. A., *J. Chem. Phys.* **2001,** 114, (5), 2362-2368.

[93] Stepanov, A. L.; Hole, D. E.; Bukharaev, A. A.; Townsend, P. D.; Nurgazizov, N. I., *Appl. Surf. Sci.* **1998,** 136, (4), 298-305.

[94] Kaempfe, M.; Rainer, T.; Berg, K. J.; Seifert, G.; Graener, H., *Appl. Phys. Lett.* **1999,** 74, (9), 1200-1202.

[95] Zhang, J. Z., *Acc. Chem. Res.* **1997,** 30, (10), 423-429.

[96] Voisin, C.; Del Fatti, N.; Christofilos, D.; Vallee, F., *J. Phys. Chem. B* **2001,** 105, (12), 2264-2280.

[97] Link, S.; Ei-Sayed, M. A., *Annu. Rev. Phys. Chem.* **2003,** 54, 331-366.

[98] Lee, P. A.; Ramakrishnan, T. V., *Rev. Mod. Phys.* **1985,** 57, (2), 287-337.

[99] Sun, C. K.; Vallee, F.; Acioli, L. H.; Ippen, E. P.; Fujimoto, J. G., *Phys. Rev. B* **1994,** 50, (20), 15337-15348.

[100] Elsayedali, H. E.; Juhasz, T.; Smith, G. O.; Bron, W. E., *Phys. Rev. B* **1991,** 43, (5), 4488-4491.

[101] Elsayedali, H. E.; Juhasz, T., *Phys. Rev. B* **1993,** 47, (20), 13599-13610.

[102] Groeneveld, R. H. M.; Sprik, R.; Lagendijk, A., *Phys. Rev. B* **1995,** 51, (17), 11433-11445.

[103] Kaganov, M. I.; Lifshitz, I. M.; Tanatarov, L. V., *Soviet Phys. JETP* **1957,** 4, 173.

[104] Anisimov, L.; Kapeliovich, B. L.; Perel'man, T. L., *Soviet Phys. JETP* **1975,** 39, 375.

[105] Hodak, J.; Martini, I.; Hartland, G. V., *Chem. Phys. Lett.* **1998,** 284, (1-2), 135-141.

[106] Ahmadi, T. S.; Logunov, S. L.; ElSayed, M. A., *J. Phys. Chem.* **1996,** 100, (20), 8053-8056.

[107] Logunov, S. L.; Ahmadi, T. S.; ElSayed, M. A.; Khoury, J. T.; Whetten, R. L., *J. Phys. Chem. B* **1997,** 101, (19), 3713-3719.

[108] Link, S.; Burda, C.; Mohamed, M. B.; Nikoobakht, B.; El-Sayed, M. A., *Phys. Rev. B* **2000,** 61, (9), 6086-6090.

[109] Hodak, J. H.; Henglein, A.; Hartland, G. V., *J. Chem. Phys.* **1999,** 111, (18), 8613-8621.

[110] Del Fatti, N.; Flytzanis, C.; Vallee, F., *Appl. Phys. B-Lasers Opt.* **1999,** 68, (3), 433-437.

[111] Arbouet, A.; Voisin, C.; Christofilos, D.; Langot, P.; Del Fatti, N.; Vallee, F.; Lerme, J.; Celep, G.; Cottancin, E.; Gaudry, M.; Pellarin, M.; Broyer, M.; Maillard, M.; Pileni, M. P.; Treguer, M., *Phys. Rev. Lett.* **2003,** 90, (17), 177401.

[112] Roberti, T. W.; Smith, B. A.; Zhang, J. Z., *J. Chem. Phys.* **1995,** 102, (9), 3860-3866.

[113] Link, S.; Burda, C.; Wang, Z. L.; El-Sayed, M. A., *J. Chem. Phys.* **1999,** 111, (3), 1255-1264.

[114] Hodak, J. H.; Martini, I.; Hartland, G. V., *J. Phys. Chem. B* **1998,** 102, (36), 6958-6967.

[115] Hodak, J. H.; Henglein, A.; Hartland, G. V., *J. Chem. Phys.* **2000,** 112, (13), 5942-5947.

[116] Nisoli, M.; Stagira, S.; DeSilvestri, S.; Stella, A.; Tognini, P.; Cheyssac, P.; Kofman, R., *Phys. Rev. Lett.* **1997,** 78, (18), 3575-3578.

[117] Darugar, Q.; Qian, W.; El-Sayed, M. A.; Pileni, M. P., *J. Phys. Chem. B* **2006,** 110, (1), 143-149.

[118] Halte, V.; Bigot, J. Y.; Palpant, B.; Broyer, M.; Prevel, B.; Perez, A., *Appl. Phys. Lett.* **1999,** 75, (24), 3799-3801.

[119] Bargheer, M.; Zhavoronkov, N.; Gritsai, Y.; Woo, J. C.; Kim, D. S.; Woerner, M.; Elsaesser, T., *Science* **2004,** 306, (5702), 1771-1773.

[120] Plech, A.; Kotaidis, V.; Gresillon, S.; Dahmen, C.; von Plessen, G., *Phys. Rev. B* **2004,** 70, (19), 195423.

[121] Park, H.; Wang, X.; Nie, S.; Clinite, R.; Cao, J., *Solid State Commun.* **2005,** 136, (9-10), 559-563.

[122] Park, H.; Wang, X.; Nie, S.; Clinite, R.; Cao, J., *Phys. Rev. B* **2005,** 72, (10).

[123] Cao, J.; Hao, Z.; Park, H.; Tao, C.; Kau, D.; Blaszczyk, L., *Appl. Phys. Lett.* **2003,** 83, (5), 1044-1046.

[124] Cho, G. C.; Kutt, W.; Kurz, H., *Phys. Rev. Lett.* **1990,** 65, (6), 764-766.

[125] Machol, J. L.; Wise, F. W.; Patel, R. C.; Tanner, D. B., *Phys. Rev. B* **1993,** 48, (4), 2819-2822.

[126] Eringen, A. C.; Suhubi, E. S., *Elastodynamics - Vol. II*. Academic Press: New York, **1975**.

[127] Huang, W.; Qian, W.; El-Sayed, M. A., *Proc. SPIE-Int. Soc. Opt. Eng.* **2005,** 5927, (Plasmonics: Metallic Nanostructures and Their Optical Properties III), 592701.

[128] Lamb, H., *Proc. London Math. Soc.* **1882,** 13, 189.

[129] Bullen, K. E.; Bolt, B. A., *An introduction to the theory of seismology*. Cambridge: New York, **1985**.

[130] Hodak, J. H.; Martini, I.; Hartland, G. V., *J. Chem. Phys.* **1998,** 108, (22), 9210-9213.

[131] Hartland, G. V., *J. Chem. Phys.* **2002,** 116, (18), 8048-8055.

[132] Hartland, G. V.; Hu, M.; Wilson, O.; Mulvaney, P.; Sader, J. E., *J. Phys. Chem. B* **2002,** 106, (4), 743-747.

[133] Grant, C. D.; Schwartzberg, A. M.; Norman, T. J.; Zhang, J. Z., *J. Am. Chem. Soc.* **2003,** 125, (2), 549-553.

[134] Hu, M.; Petrova, H.; Wang, X.; Hartland, G. V., *J. Phys. Chem. B* **2005,** 109, (30), 14426-14432.

[135] Bonacina, L.; Callegari, A.; Bonati, C.; van Mourik, F.; Chergui, M., *Nano Lett.* **2006,** 6, (1), 7-10.

[136] Huang, W. Y.; Qian, W.; El-Sayed, M. A., *J. Phys. Chem. B* **2005,** 109, (40), 18881-18888.

[137] Tamura, A.; Higeta, K.; Ichinokawa, T., *Journal of Physics C-Solid State Physics* **1982,** 15, (24), 4975-4991.

[138] Landau, L. D.; Lifshitz, E. M., *Theory of Elasticity*. 2nd ed.; Pergamon Press: Oxford, **1970**.

[139] Simmons, G.; Wang, H., *Single Crystal Elastic Constants and Calculated Aggregate Properties: A Handbook*. MIT Press: Cambridge, **1971**.

[140] Petrova, H.; Lin, C. H.; de Liejer, S.; Hu, M.; McLellan, J. M.; Siekkinen, A. R.; Wiley, B. J.; Marquez, M.; Xia, Y. N.; Sader, J. E.; Hartland, G. V., *J. Chem. Phys.* **2007,** 126, (9).

[141] Sader, J. E.; Hartland, G. V.; Mulvaney, P., *J. Phys. Chem. B* **2002,** 106, (6), 1399-1402.

[142] Guillon, C.; Langot, P.; DelFatti, N.; Vallee, F.; Kirakosyan, A. S.; Shahbazyan, T. V.; Cardinal, T.; Treguer, M., *Nano Lett.* **2007,** 7, (1), 138-142.

[143] Miller, D. A. B., *Proc. IEEE* **2000,** 88, (6), 728-749.

[144] Eldada, L., *Rev. Sci. Instrum.* **2004,** 75, (3), 575-593.

[145] Winzer, P. J.; Essiambre, R. J., *Proc. IEEE* **2006,** 94, (5), 952-985.

[146] Miller, D. A. B.; Chemla, D. S.; Damen, T. C.; Gossard, A. C.; Wiegmann, W.; Wood, T. H.; Burrus, C. A., *Phys. Rev. Lett.* **1984,** 53, (22), 2173-2176.

[147] Kuo, Y. H.; Lee, Y. K.; Ge, Y. S.; Ren, S.; Roth, J. E.; Kamins, T. I.; Miller, D. A. B.; Harris, J. S., *Nature* **2005,** 437, (7063), 1334-1336.

[148] Schmittrink, S.; Chemla, D. S.; Knox, W. H.; Miller, D. A. B., *Opt. Lett.* **1990,** 15, (1), 60-62.

[149] Maslov, A. V.; Citrin, D. S., *J. Appl. Phys.* **2003,** 93, (12), 10131-10133.

[150] Lewen, R.; Irmscher, S.; Westergren, U.; Thylen, L.; Eriksson, U., *J. Lightwave Technol.* **2004,** 22, (1), 172-179.

[151] Shi, Y. Q.; Zhang, C.; Zhang, H.; Bechtel, J. H.; Dalton, L. R.; Robinson, B. H.; Steier, W. H., *Science* **2000,** 288, (5463), 119-122.

[152] Lee, M.; Katz, H. E.; Erben, C.; Gill, D. M.; Gopalan, P.; Heber, J. D.; McGee, D. J., *Science* **2002,** 298, (5597), 1401-1403.

[153] Gu, L. L.; Jiang, W.; Chen, X. N.; Wang, L.; Chen, R. T., *Appl. Phys. Lett.* **2007,** 90, (7), 071105.

[154] Jacobsen, R. S.; Andersen, K. N.; Borel, P. I.; Fage-Pedersen, J.; Frandsen, L. H.; Hansen, O.; Kristensen, M.; Lavrinenko, A. V.; Moulin, G.; Ou, H.; Peucheret, C.; Zsigri, B.; Bjarklev, A., *Nature* **2006,** 441, (7090), 199-202.

[155] Solgaard, O.; Ho, F.; Thackara, J. I.; Bloom, D. M., *Appl. Phys. Lett.* **1992,** 61, (21), 2500-2502.

[156] Jones, R.; Liu, A. S.; Rong, H. S.; Paniccia, M.; Cohen, O.; Hak, D., *Optics Express* **2005,** 13, (5), 1716-1723.

[157] de Lima, M. M.; Beck, M.; Hey, R.; Santos, P. V., *Appl. Phys. Lett.* **2006,** 89, (12), 121104.

[158] Almeida, V. R.; Barrios, C. A.; Panepucci, R. R.; Lipson, M., *Nature* **2004,** 431, (7012), 1081-1084.

[159] Xu, Q. F.; Schmidt, B.; Pradhan, S.; Lipson, M., *Nature* **2005,** 435, (7040), 325-327.

[160] Marki, I.; Salt, M.; Herzig, H. P.; Stanley, R.; El Melhaoui, L.; Lyan, P.; Fedeli, J. M., *Opt. Lett.* **2006,** 31, (4), 513-515.

[161] Hochberg, M.; Baehr-Jones, T.; Wang, G. X.; Shearn, M.; Harvard, K.; Luo, J. D.; Chen, B. Q.; Shi, Z. W.; Lawson, R.; Sullivan, P.; Jen, A. K. Y.; Dalton, L.; Scherer, A., *Nat. Mater.* **2006,** 5, (9), 703-709.

[162] Dintinger, J.; Robel, I.; Kamat, P. V.; Genet, C.; Ebbesen, T. W., *Adv. Mater.* **2006,** 18, (13), 1645-1648.

[163] Mafune, F.; Kohno, J.; Takeda, Y.; Kondow, T.; Sawabe, H., *J. Phys. Chem. B* **2000,** 104, (39), 9111-9117.

[164] Mafune, F.; Kohno, J.; Takeda, Y.; Kondow, T.; Sawabe, H., *J. Phys. Chem. B* **2001,** 105, (22), 5114-5120.

[165] Kabashin, A. V.; Meunier, M., *J. Appl. Phys.* **2003,** 94, (12), 7941-7943.

[166] Sylvestre, J. P.; Kabashin, A. V.; Sacher, E.; Meunier, M.; Luong, J. H. T., *J. Am. Chem. Soc.* **2004,** 126, (23), 7176-7177.

[167] Tsuji, T.; Iryo, K.; Watanabe, N.; Tsuji, M., *Appl. Surf. Sci.* **2002,** 202, (1-2), 80-85.

[168] Compagnini, G.; Scalisi, A. A.; Puglisi, O., *J. Appl. Phys.* **2003,** 94, (12), 7874-7877.

[169] Tsuji, T.; Kakita, T.; Tsuji, M., *Appl. Surf. Sci.* **2003,** 206, (1-4), 314-320.

[170] Chen, Y. H.; Yeh, C. S., *Colloids Surf. A-Physicochem. Eng. Asp.* **2002,** 197, (1-3), 133-139.

[171] Dolgaev, S. I.; Simakin, A. V.; Voronov, V. V.; Shafeev, G. A.; Bozon-Verduraz, F., *Appl. Surf. Sci.* **2002,** 186, (1-4), 546-551.

[172] Ausanio, G.; Barone, A. C.; Iannotti, V.; Lanotte, L.; Amoruso, S.; Bruzzese, R.; Vitiello, M., *Appl. Phys. Lett.* **2004,** 85, (18), 4103-4105.

[173] Gonzalo, J.; Babonneau, D.; Afonso, C. N.; Barnes, J. P., *J. Appl. Phys.* **2004,** 96, (9), 5163-5168.

[174] Pham, M. T. N.; Boukamp, B. A.; Rijnders, G.; Bouwmeester, H. J. M.; Blank, D. H. A., *Appl. Phys. A: Mater. Sci. Process.* **2004,** 79, (4-6), 907-910.

[175] Chen, X. Y.; Lu, Y. F.; Wu, Y. H.; Cho, B. J.; Yang, B. J.; Liew, T. Y. F., *J. Vac. Sci. Technol. B* **2004,** 22, (4), 1731-1737.

[176] Link, S.; Burda, C.; Nikoobakht, B.; El-Sayed, M. A., *J. Phys. Chem. B* **2000,** 104, (26), 6152-6163.

[177] Mafune, F.; Kohno, J.; Takeda, Y.; Kondow, T., *J. Phys. Chem. B* **2003,** 107, (46), 12589-12596.

[178] Miranda, M. H. G.; Falcao, E. L.; Rodrigues, J. J.; de Araujo, C. B.; Acioli, L. H., *Phys. Rev. B* **2004,** 70, (16), 161401.

[179] Wenzel, T.; Bosbach, J.; Goldmann, A.; Stietz, F.; Trager, F., *Appl. Phys. B: Lasers Opt.* **1999,** 69, (5-6), 513-517.

[180] Bosbach, J.; Martin, D.; Stietz, F.; Wenzel, T.; Trager, F., *Appl. Phys. Lett.* **1999,** 74, (18), 2605-2607.

[181] Pereira, A.; Cros, A.; Delaporte, P.; Georgiou, S.; Manousaki, A.; Marine, W.; Sentis, M., *Appl. Phys. A: Mater. Sci. Process.* **2004,** 79, (4-6), 1433-1437.

[182] Mafune, F.; Kohno, J. Y.; Takeda, Y.; Kondow, T., *J. Phys. Chem. B* **2003,** 107, (18), 4218-4223.

[183] Kabashin, A. V.; Meunier, M.; Kingston, C.; Luong, J. H. T., *J. Phys. Chem. B* **2003,** 107, (19), 4527-4531.

[184] Link, S.; Burda, C.; Mohamed, M. B.; Nikoobakht, B.; El-Sayed, M. A., *J. Phys. Chem. A* **1999,** 103, (9), 1165-1170.

[185] Habenicht, A.; Olapinski, M.; Burmeister, F.; Leiderer, P.; Boneberg, J., *Science* **2005,** 309, (5743), 2043-2045.

[186] Sirringhaus, H.; Kawase, T.; Friend, R. H.; Shimoda, T.; Inbasekaran, M.; Wu, W.; Woo, E. P., *Science* **2000,** 290, (5499), 2123-2126.

[187] Vance, B.; Bonn, D.; Martin, J. Y.; Vovelle, L., *Nature* **2000,** 405, (6788), 772-775.

CHAPTER 2

FABRICATION AND CHARACTERIZATION OF METALLIC NANOPARTICLE ARRAYS

Abstract

The experimental detail is described in this chapter. The preparation and modification methods of two dimensional nanoparticle arrays include nanosphere lithography (NSL), electron beam lithography (EBL), and thermal annealing. The prepared nanoparticle arrays are imaged with scanning electron microscopy (SEM) and transmission electron microscopy (TEM). The static optical properties of nanoparticle arrays are recorded with macro- and micro- absorption spectrometers. The electron phonon relaxation and coherent phonon oscillation dynamic properties are characterized with femtosecond pump-probe transient transmission spectroscopy.

2.1 Nanosphere Lithography

Figure 2-1 demonstrates the method of nanosphere lithography [1] in making periodic nanoparticle array. First, a monolayer of closely packed PS spheres is assembled on a flat substrate of quartz, ITO coated quartz, or silicon. The monolayer can be fabricated on a sub-millimeter dimensional scale. With modified assembly techniques, the monolayer can cover several square millimeters up to square centimeters on the substrate. Secondly, a thin layer of gold is deposited on the substrate in a high vacuum thermal evaporator. The gold forms a hemispherical shell on each PS sphere and a

prismatic nanoparticle on the substrate within the void between three closely packed PS spheres. Finally, the PS sphere mask is dissolved in an organic solvent.

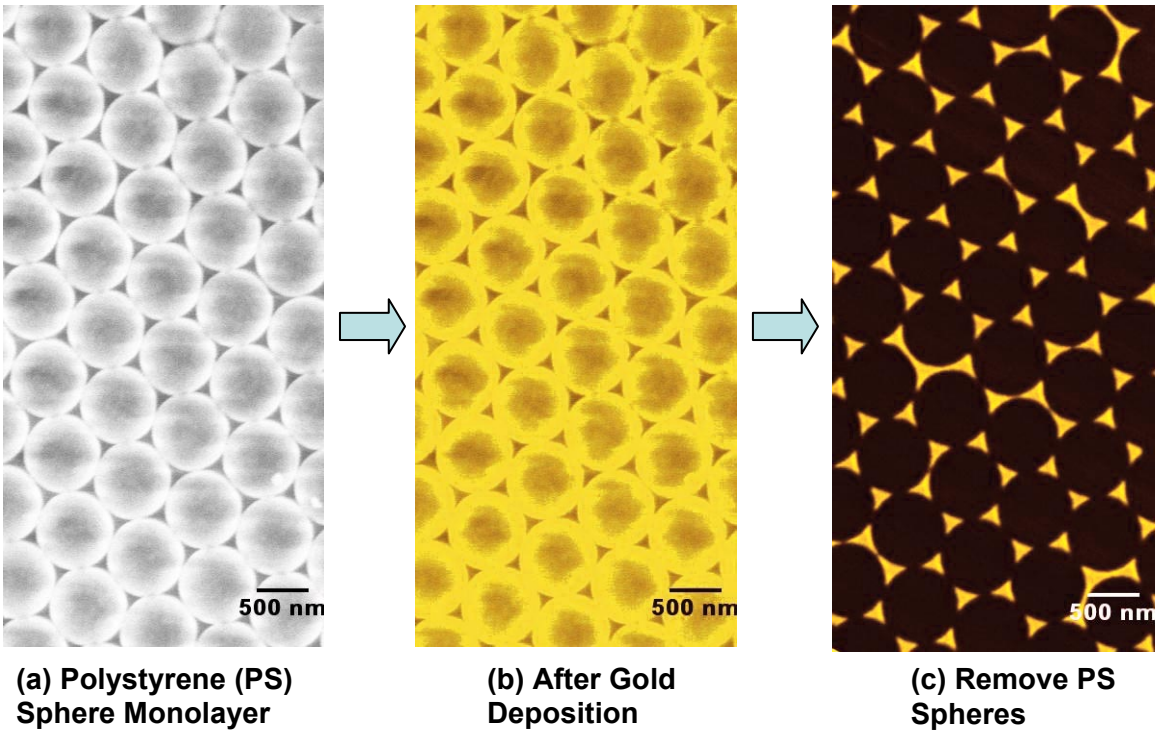

Figure 2-1: Representative images of the method of nanosphere lithography in making periodic nanoparticle array. (a) A self-assembled polystyrene sphere single layer; (b) Deposition of gold in a high vacuum thermal evaporator; (c) Removing PS spheres in ethanol, the gold periodic nanoparticle array formed in the void of the polystyrene spheres.

2.1.1 The First Version — Nature Self-assembly

Initially, we used the natural self-assembly process of polystyrene (PS) nanospheres to fabricate a two-dimensional array, which has been used extensively in Van Duyne's group [1]. We use a 2 % PS sphere suspension purchased from Polyscience,

Inc. The diameter of the spheres used in our experiments is 0.356 μm . Circular microscope cover glass (18CIR-2, Fisher Scientific) are used as the substrate and are cleaned in piranha solution (3:1 H_2SO_4:30% H_2O_2) at 80 ^oC for 1.5 h. The quartz slides are placed in a solution of 5:1:1 H_2O:NH_4OH:30%H_2O_2 and are sonicated for one hour. Five micro liters of the 2 % PS spheres suspension solution is deposited on the quartz slides, which is tilted to disperse the suspension solution evenly onto the substrate. After the evaporation of the water, the PS sphere monolayer forms in sub-millimeter dimension as shown in **Figure 2-2**. The mask is then mounted in a thermal evaporator (Denton DV-502A) to deposit 50 nm of gold (99.999%, Alfa Aesar) onto the mask in the voids between the spheres. The thickness of the deposited gold is monitored by a quartz crystal thickness monitor (Inficon). After deposition, the PS spheres are dissolved in a tetrahydrofuran (THF) solution.

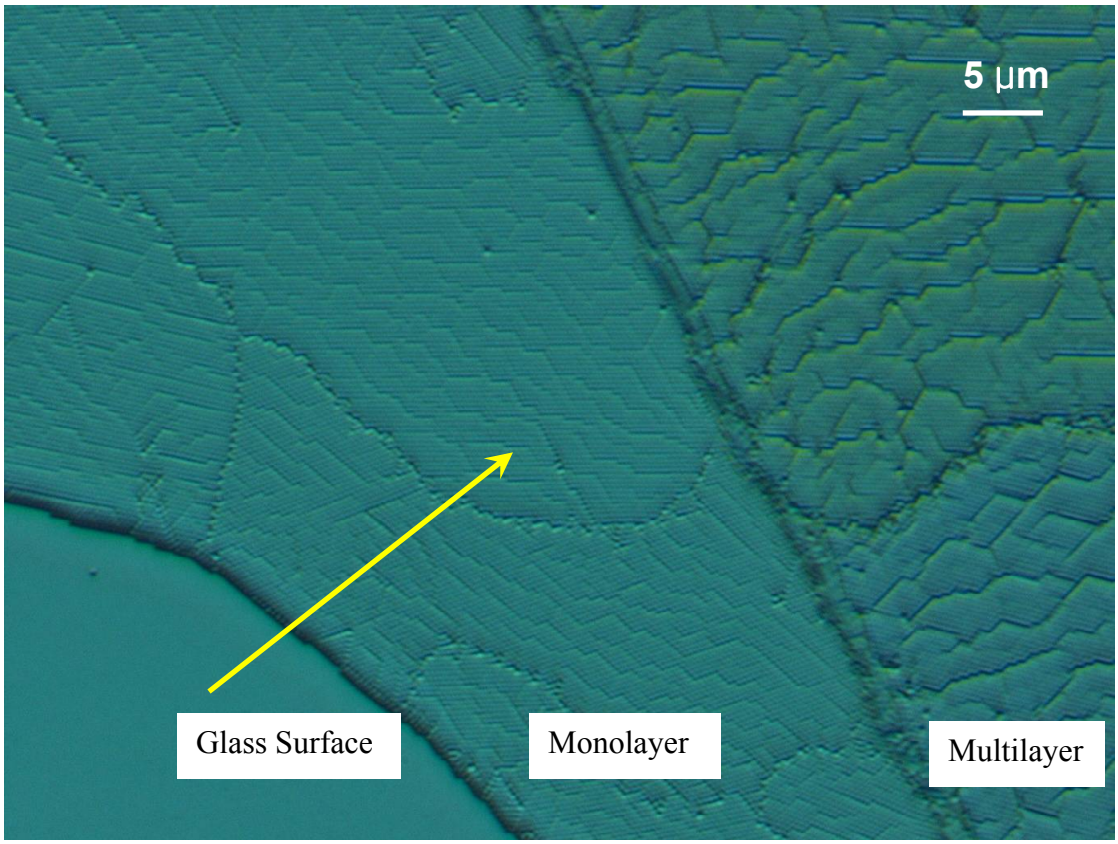

Figure 2-2: An optical microscope image of a 70×53 µm nanosphere mask formed via natural self-assembly.

The PS sphere concentration is the most important factor to form a closely packed monolayer mask. As shown in **Figure 2-2**, the dry front of the PS sphere suspension moves from down left to top right as shown by the yellow arrow. Initially, the concentration of PS sphere is too low to form a close packed monolayer, so a clean glass surface is left behind the dry front. As the water evaporates, the concentration of the PS sphere is in the correct range for forming a monolayer (the middle part in **Figure 2-2**). As the water evaporating further, the concentration of the PS becomes too high to form a monolayer mask, so a multilayer of PS sphere packing is left behind the dry front.

2.1.2 The Second Version — Concentration Optimized Self-assembly

Periodic arrays of gold nanoparticles are prepared using the method of NSL that was modified by Wang and coworkers [2]. The commercially available 10 % monodisperse polystyrene (PS) sphere suspensions were purchased from Duke Scientific Corp. and used as received. The diameters of the spheres used in our experiments are 0.45, 0.60 and 0.74 μm . Quartz slides (Technical Glass Products, Inc.) are used as the substrate and are processed with the same method as described in the first version assembly technique. Five micro liter of the 10 % PS sphere suspension solution is deposited on the quartz slides, which is tilted to disperse the suspension solution evenly on the substrate. Instead of letting it dry in air naturally, the substrate is slowly immersed in water. Excess PS spheres are dispersed in water. One drop of 2 % dodecylsodiumsulfate surfactant is then added to the water to separate the excess floating PS spheres from the substrate and the substrate is taken out from the clean area of the water in order to prevent additional deposition of the PS spheres. By this technique, the PS spheres left on the substrate have optimized concentration. After the evaporation of the water, the PS sphere monolayer forms and covers several square millimeters. The mask is then mounted in a thermal evaporator to deposit gold (99.999 %, Alfa Aesar). After deposition, the PS spheres are dissolved in tetrahydrofuran (THF) solution and the prismatic nanoparticle array is left on the substrate.

2.1.3 The Third Version — Air-Water Interface Self-assembly

The nanoparticles are synthesized on a quartz substrate using a modified nanosphere lithography (NSL) technique, air-water interface self-assembly. The commercially available monodisperse polystyrene (PS) sphere suspension is purchased from Duke Scientific Corp. and used as received. The diameter of the PS spheres used in our experiments is $0.45\,\mu m$. Quartz slides (Technical Glass Products, Inc.) are used as the substrate and are treated with the same methods as described in the first version. Circular microscope cover glass slides (18CIR-2, Fisher Scientific) are treated the same way as quartz slides and dried in ambient condition. Ten micro liters of a mixed solution of the PS spheres suspension and ethanol (1:1) are deposited on a piece of dried circular cover glass. Then, the cover glass is gently dropped on the surface of water. The polystyrene spheres are released from the cover glass and an uniform monolayer of close packed PS spheres are formed on the surface of the water. One drop of 2 % dodecylsodiumsulfate surfactant is then added to the water to tune its surface tension, which packs the polystyrene spheres tightly. A clean quartz slide is used to pick up the PS sphere monolayer. After the evaporation of the water, the PS sphere monolayer forms and covers a square centimeter on the substrate. The mask is then mounted in a thermal evaporator (PVD75 Filament Evaporator), where a layer of gold (99.99 %) is deposited in the void between the spheres. The thickness of the deposited gold is monitored by a quartz crystal thickness monitor. After deposition, the PS spheres are removed in ethanol solvent with sonication.

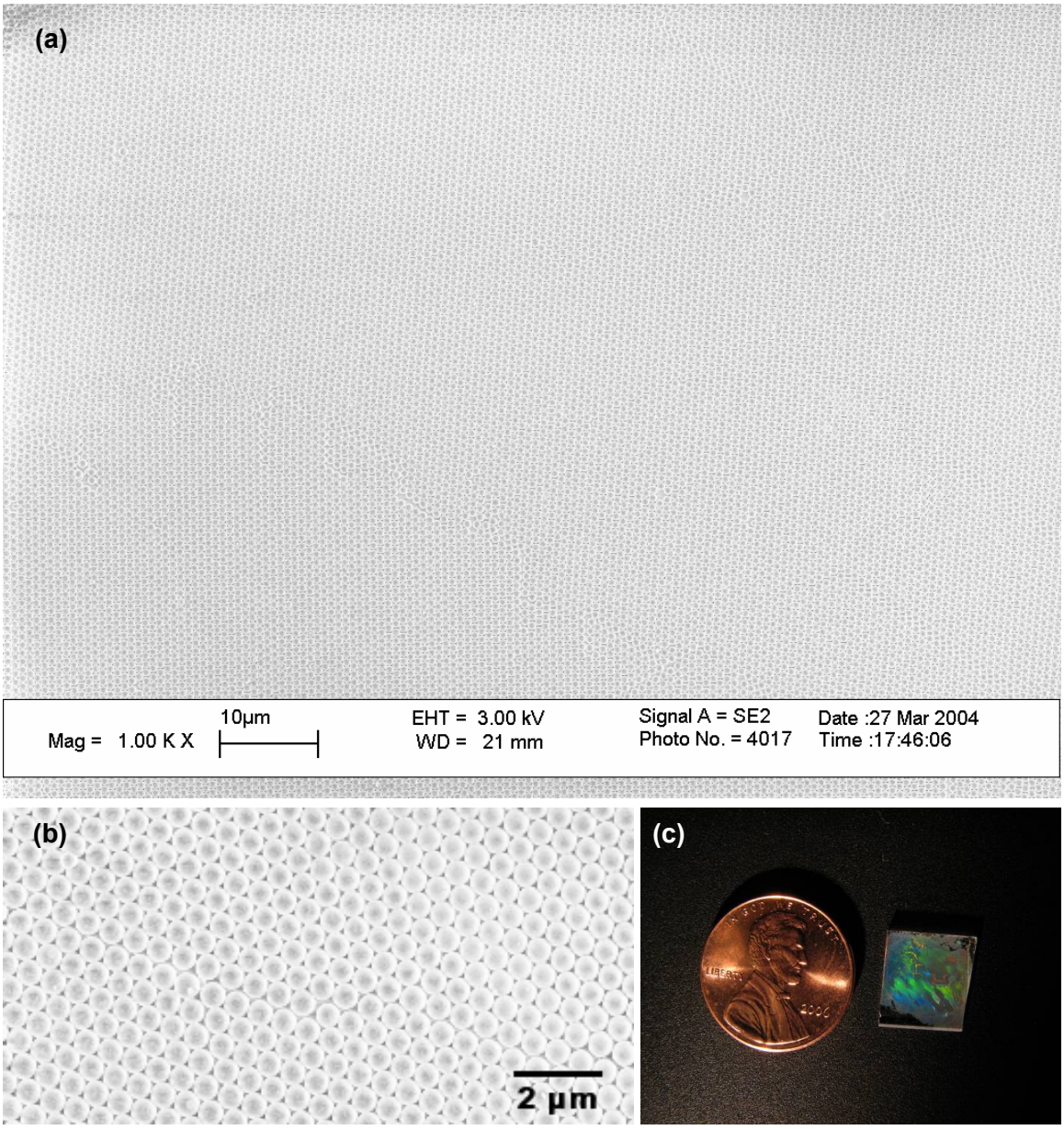

Figure 2-3: A SEM image of the monolayer of PS spheres made with air-water interface self-assembly. (a) and (b) are low and high magnification images of the closely packed PS sphere monolayer, respectively. (c) is an optical image of the PS sphere monolayer. The greenish color is due to the diffraction of the visible light by the PS sphere crystal, which shows the PS sphere monolayer can cover the substrate in square centimeter scale.

By modifying the surface tension, the PS sphere monolayer can be formed in a larger area. There is absolutely no double layer or multilayer formation as shown by **Figure 2-3a**. A closely packed PS sphere monolayer is shown clearer in **Figure 2-3b**. An optical image of the PS sphere monolayer coated quartz substrate is shown in **Figure 2-3c**. A closely packed PS sphere two dimensional crystal structure gives the beautiful greenish color due to the diffraction of visible light, which indicates the PS sphere monolayer can cover the substrate on the square centimeter scale.

2.2 Angle-Resolved Nanosphere Lithography

A more complicated nanostructure can be formed with the angle-resolved nanosphere lithography (AR-NSL) [3]. In this method, after an initial deposition with the atomic beam perpendicular to the nanosphere monolayer mask, a second deposition was performed with the atomic beam having an angle θ to the substrate surface as shown by **Figure 2-4**. **Figure 2-5a** is the nanoparticle array sample made with the atomic beam being perpendicular to the PS sphere monolayer. With 30 degree tilt of the PS sphere substrate ($\theta = 30^{o}$), the SEM image of the nanoparticle array is shown in **Figure 2-5b**. **Figure 2-5c** is a nanoparticle array made with two deposition steps, a normal deposition of 30 nm gold followed by another 30 nm of gold deposition at 30 degree tilt angle of the substrate surface normal to the atomic beam propagation. As shown by **Figure 2-5c**, the nanoparticles formed during the second deposition is smaller than those formed with one-step 30 degree gold deposition (**Figure 2-5c**). This is because the first deposition at normal atomic incidence angle coats the PS sphere and decreases the size of the pore between three connected PS spheres.

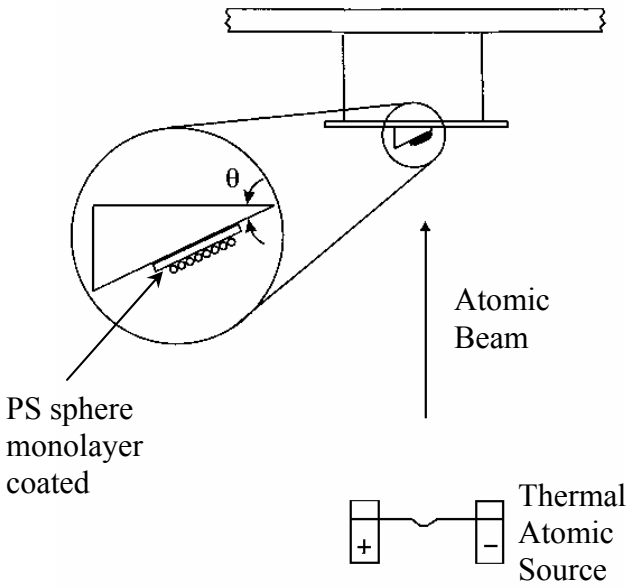

Figure 2-4: Scheme of the apparatus used for AR-NSL. The angle between the atomic beam propagation and the substrate surface normal is represented by θ.

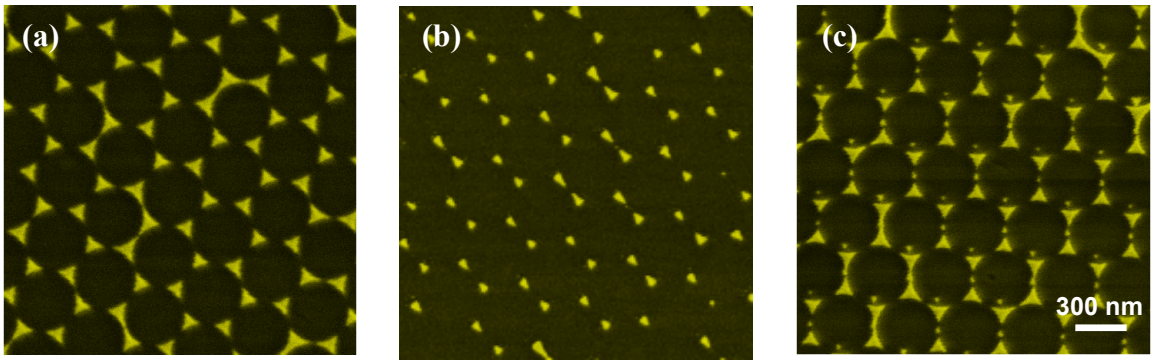

Figure 2-5: SEM image of monolayer periodic gold nanoparticle arrays fabricated with the atomic beam of the gold deposition (a) being perpendicular to the PS sphere monolayer or (b) having 30 degree to the surface normal of the PS sphere monolayer. Two steps of 30 nm gold deposition each at $\theta = 0^{o}$ and $\theta = 30^{o}$ is performed to form the nanostructure shown in (c).

2.3 Electron Beam Lithography

The gold nanoparticle pairs are prepared on quartz slides by electron-beam lithography (EBL) using a JEOL JBX-9300FS 100kV electron beam lithography system at the Microelectronics Research Center (MiRC) of Georgia Institute of Technology. A general scheme of the EBL process is shown in **Figure 2-6**. If the conductivity of the substrate is low, a thin layer of gold is deposited on top of the polymer layer. Quartz slides (Technical Glass Products, Inc.) are cleaned in piranha solution (3:1 H_2SO_4:30% H_2O_2) at 80 ^oC for 1.5 h and dried in air. The cleaned quartz slide is spin coated with 65 nm PMMA 950 k electron-sensitive resist and cured at 180 ^oC for 3 minutes. The slide is mounted in a thermal evaporator to coat a 10 nm thick gold layer, which makes the sample conductive. The JEOL JBX-9300FS EBL System is used to write the desired pattern on the substrate. The gold film is then etched in gold etchant GE-8148 (an aqueous solution of KI and I_2). The pattern is developed in 1:3 MIBK:IPA (Methyl Isobutyl Ketone : Isopropyl Alcohol) solvent for 180 s, followed by washing in IPA for 30 s and drying in pure N_2. The substrate was mounted in an electron beam evaporator to deposit a thin layer of Cr, roughly 0.4 nm in thickness, followed by 25 nm of Au at a deposition rate of 0.5 $\mathring{A}$/s . The Cr layer serves to increase the Au nanoparticle adhesion to the quartz substrate. We perform the lift-off step in hot acetone (~ 63 ^oC) to remove the resist and the metal film on top of it.

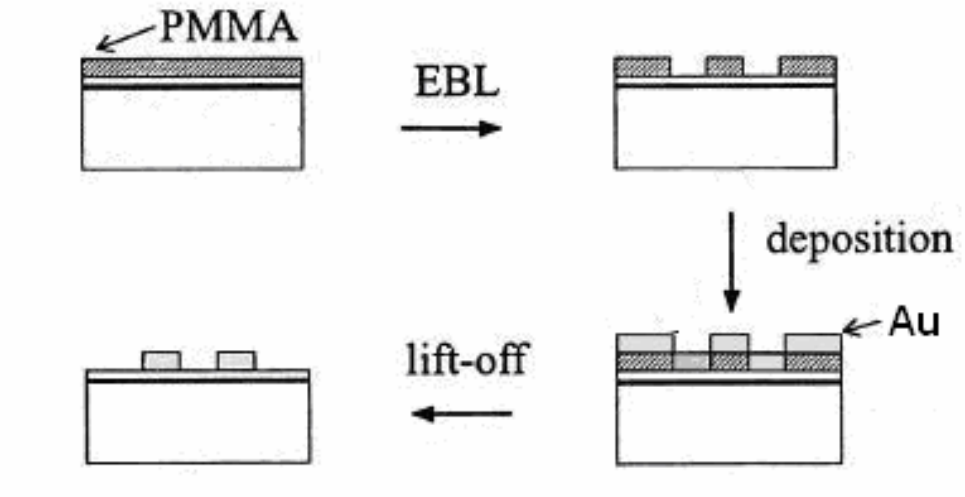

Figure 2-6: Scheme of electron beam lithography. If the substrate is insulator, a thin layer of gold (~ 10 nm) is deposited before electron beam writing to dissipate excess electrons from the substrate.

2.4 Scanning Electron Microscopy and Transmission Electron Microscopy

The formed monolayer gold nanoparticle arrays on quartz substrates are analyzed by scanning electron microscopy (LEO 1530 Thermally-Assisted Field Emission SEM, Zeiss/LEO). Because the substrate used in the experiment is an insulator, the accelerating voltage is kept below 5 kV to avoid charging effects. Two detectors are used to record images, an inlens and an SE2 detector.

The TEM images are recorded with a transmission electron microscope (JEOL 4000EX High Resolution TEM, JEOL Ltd.). For these images, a TEM grid is used to pick up the closely packed polystyrene sphere monolayer from the water surface. The gold deposition and PS sphere lift-off processes are kept the same as those performed on quartz substrate.

2.5 Absorption Spectroscopy

Two spectrophotometers are used to record the extinction spectra of the arrays prepared with NSL, a Shimadzu UV-3101-PC spectrophotometer and a Beckman DU-650 spectrophotometer. The incident light is perpendicular to the array substrate and the incident light bandwidth is 2.0 nm. The examined area of the nanoparticle array samples is several square millimeters, which allows us to check the absorbance of the nanoparticle arrays on a larger scale. The overall sample quality can be evaluated in this way because the intensity of the surface plasmon resonance absorption peak reflects the number of nanoparticles in the examined sample area of the array.

The micro-absorption spectrum is taken by an S.E.E. 1000 MSP visible-NIR micro-spectrometer in the transmission mode and the examined area is tunable by using objective lens of different magnification. The data is recorded with running the SEEScope version 4.0.0 software package (S.E.E. Inc, Middleboro, MA). The sampling areas are $3.75\times3.75\ \mu m^2$, $8\times8\ \mu m^2$, and $40\times40\ \mu m^2$ for the $50\times$, $20\times$, and $5\times$ objective lenses, respectively. The micro-spectrometer has a wavelength range of 400-1100 nm, thus the surface plasma absorption spectra of gold nanospheres and nanorods can be measured. With the micro-spectrometer, a well-ordered sample area can be viewed directly, which allows us to record the absorption of the array of nanoparticles and avoid most of the large defects.

All data taken is saved as .spc files and exported in ASCII format so that the data can be opened by Origin or Excel software. Since Sept 2005, the SEES Microscope software has been changed to CRAIC software because the SEE company shut down.

2.6 Femtosecond Pump-Probe Transient Transmission Spectroscopy

A femtosecond laser system [4] is used to perform the transient absorption experiment. A schematic diagram of the apparatus is shown in **Figure 2-7**. A frequency-doubled Nd:Vanadate laser (Coherent Verdi) is used as the pump for the Ti:Sapphire laser system (Clark MXR CPA 1000). This generates laser pulses of 100 fs duration (full width at half-maximum, fwhm) with energy of 1 mJ at 800 nm and a repetition rate of 1 kHz. A 400 nm pump pulse is generated by frequency doubling of the 800 nm fundamental in a 1 mm β-barium borate (BBO) crystal. The pump beam is mechanically chopped at 500 Hz by a synchronous light beam chopper (HMS 221), which is controlled by a master clock generator (Clark-MXR DT 505). A white-light continuum probe pulse is generated by focusing a small portion (~ 40 μJ) of the 800 nm fundamental beam of the Ti:Sapphire laser into a 1 mm sapphire plate. The wavelength range of the white-light femtosecond probe pulse is 400 to 1100 nm. The time delay between the pump and probe pulses is tuned by a computer controlled optical delay line with a spatial resolution of 3 μm (temporal resolution of 20 fs). The pump and probe laser pulses are focused and overlapped on the sample creating an overlap diameter of 250 μm . The laser pump pulse energy used in our experiment is reduced to the appropriate level with neutral density filters. The differential transmission signal $S(t)$ is recorded with a pair of silicon photodiodes (Thorlab) and a lock-in amplifier (Stanford Research Systems). The recorded signal $S(t)$ can be expressed as

$$S(\lambda,t)=\frac{\Delta T}{T}=\frac{I_{\lambda,t}-I_{\lambda,0}}{I_{\lambda,0}},$$

where $\Delta T/T$ is the % change in the transmission of the probe light; $I_{\lambda,t}$ is the intensity of the probe light at wavelength λ after a delay time t from the pump laser pulse, and $I_{\lambda,0}$ is the intensity of the probe light at λ without the pump. As a result, the recorded signal represent a transient bleach when $S(\lambda,t)$ is larger than zero.

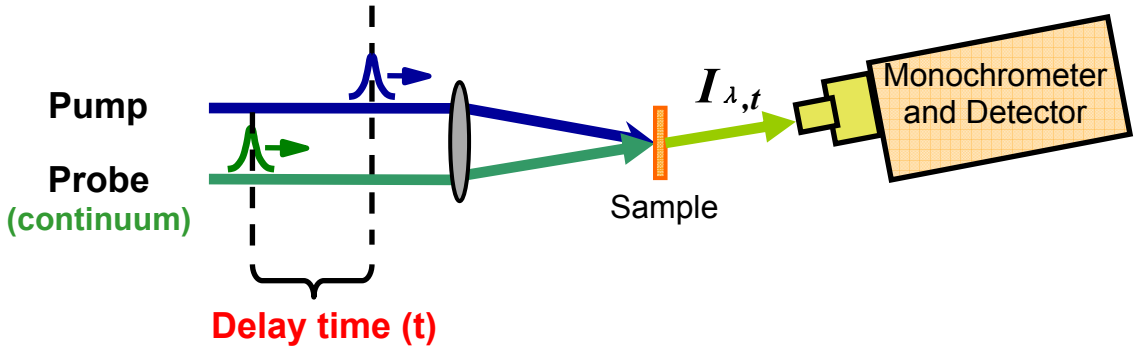

Figure 2-7: The schematic diagram of the pump-probe transient transmission spectroscopy. The time delay between the pump and probe pulses is tuned by a computer controlled optical delay line with a spatial resolution of 3 μm (temporal resolution of 20 fs).

2.7 Femtosecond Photothermal Annealing and Ablation

The same femtosecond laser system described in **Section 2.6** is used to perform the photothermal annealing and ablation experiment. The schematic diagram of the apparatus used in the experiment is described in **Figure 2-8**. The femtosecond laser is focused by a focal lens with a long focal length (30 cm). The horizontal laser beam is reflected to the sample by a reflection mirror. The sample is horizontally placed on a two dimensional transition stage, allowing us to select the sample area by positioning the substrate in the x-y direction. The laser intensity is controlled by a series of neutral

density filters. A minimum of 4 laser pulses of irradiation is realized by a mechanical chopper.

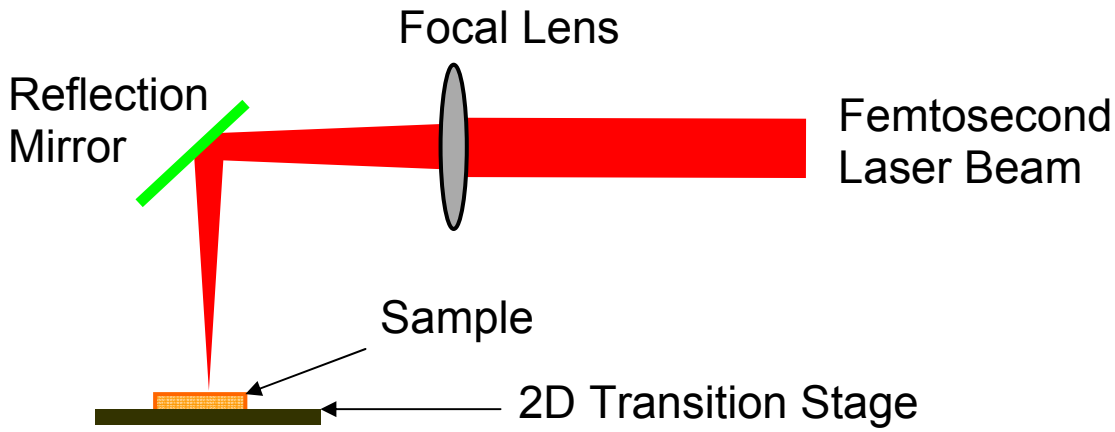

Figure 2-8: The schematic diagram of the apparatus for femtosecond photothermal annealing and ablation experiments.

2.8 References

[1] Hulteen, J. C.; Van Duyne, R. P., *J. Vac. Sci. Technol. A* **1995,** 13, (3, Pt. 2), 1553-8.

[2] Wang, X.; Summers, C. J.; Wang, Z. L., *Nano Letters* **2004,** 4, (3), 423-426.

[3] Haynes, C. L.; McFarland, A. D.; Smith, M. T.; Hulteen, J. C.; Van Duyne, R. P., *J. Phys. Chem. B* **2002,** 106, (8), 1898-1902.

[4] Logunov, S. L.; Volkov, V. V.; Braun, M.; El-Sayed, M. A., *Proc. Natl. Acad. Sci. U. S. A.* **2001,** 98, (15), 8475-8479.

CHAPTER 3

THE EFFECT OF LATTICE CRYSTALLINITY ON ELECTRON-PHONON RELAXATION RATES IN GOLD NANOPARTICLES

Abstract

In order to study the importance of surface phonons on the electron-phonon relaxation in plasmonic nanoparticles, the effect of size, shape and materials have recently been studied. Gold and silver nanoparticles have shown no dependence on size and shape while copper nanoparticles have shown some size dependence. This suggests that the bulk phonons, which are sensitive to the bulk phase structure, are solely responsible for the relaxation of the hot electron in gold and silver plasmonic nanoparticles. In the present study, we performed time-resolved transient absorption experiments with different laser pump powers on gold nanoparticles of nearly single crystalline and polycrystalline internal structures. A simple thermal annealing is used to transform the as-deposited polycrystalline prismatic nanoparticles into nearly single crystalline spherical nanoparticles. We observed a large difference in the electron-phonon relaxation times for the polycrystalline prismatic and nearly single crystalline spherical nanoparticle pumped at the same laser pulse energy. The different e-ph relaxation dynamics in these two kinds of nanoparticles are attributed to the effect of the internal crystalline structure on the bulk phonon structure. Since polycrystalline prismatic gold nanoparticles has a high density of grain boundaries, which are efficient in inelastic electron scattering, this results in a shorter electron-phonon relaxation time. Another way

of saying this is that amorphous or polycrystalline solids have a high density of short wavelength or high frequency phonons (or even localized molecular type vibrations), which are more efficient in removing high electronic energy resulting in faster electron-phonon relaxation processes. This work has been accepted for publishing in *J. Phys. Chem. C*, 2007.

3.1 Introduction

Electron-phonon interaction is the most important energy relaxation processes in materials and determines many important properties, such as thermal conductivity, electrical conductivity, and the nature of superconductivity [1]. Therefore, the electronic energy relaxation processes of laser excited plasmonic nanoparticles have received extensive research efforts [2-6]. A general energy relaxation process of a plasmonic nanoparticle excited with an ultrafast laser pulse is summarized as the following. The ultrafast laser excited coherent electrons rapidly lose their phases via electron-electron interaction on a time scale of tens of femtoseconds [7]. After the pure electron dephasing processes, an electron lattice equilibrium state is established by transferring the electronic energy to the lattice through electron-phonon interaction on a sub-picosecond to several picosecond time scale [8]. The energy is finally transferred to the medium by phonon-phonon interaction, which is dependent on the thermal conductivity and heat capacity of the medium and the coupling between the nanoparticle and the surrounding medium.

With the advancement of ultrafast laser spectroscopic techniques, the effects of the size, shape, and material of plasmonic nanoparticles on their electron-phonon

relaxation dynamics have been studied extensively [9-17]. One interesting question raised by quantum-kinetic calculations was that the electron-phonon relaxation rate should increase if the nanoparticle's diameter was decreased below than the mean free path of the conductive electrons in the material (40-50 nm in gold) due to the interaction between the electrons and the surface phonons. However, many experiments performed by our group and Hartland's group didn't observe such a trend. Within our group, El-Sayed and co-workers [10-12] found that electron-phonon relaxation times are very close for gold spherical nanoparticles whose sizes were varied from 9 nm to 48 nm. The same behavior was also observed for gold cylindrical nanoparticles (aspect ratio of 3.8) probed at both their longitudinal (750 nm) and transverse (520 nm) plasmon band [12]. Experiments performed by Hartland's group [9, 13, 18] also found that the electron-phonon coupling constants are very close to each other for gold and silver nanoparticles of different sizes in aqueous solutions. They also found the coupling constants are similar to the corresponding bulk values [13, 19]. The above observations indicate that the changes in the gold nanoparticle's shape, size, and the mode of surface plasmon oscillation do not affect their electronic energy relaxation dynamics.

However, for sub-10 nm silver nanoparticles imbedded in a glass matrix, Del Fatti et al. [14] and Halte et al. [20] found that the rate of electron-phonon relaxation increases with a decrease in the diameter of the nanoparticle. These results were explained by the enhanced interaction between electrons and surface phonons, while the effect of heat transfer to the matrix environment could also play a large role, especially for small nanoparticles that have high surface to volume ratio [20]. The size dependent electron-phonon relaxation dynamics in copper nanoparticles (larger than 10 nm) was also

observed. Darugar et al. [21] found the electronic energy relaxation in spherical copper nanoparticles of 12 nm is faster than that in 30 nm nanoparticles. This means that the size dependent electron-phonon relaxation dynamics resulting from the participation of surface phonons in copper nanoparticles is detected more readily than in gold or silver nanoparticles. This is because the contribution of surface phonon modes to the total e-ph coupling is given by the ratio of the valence of the metal to its atomic mass (n/m) [19, 22]. This ratio for copper is twice as large as that for silver and three times as large as that for gold.

From the above, it is clear that most of the electron-phonon relaxation involves bulk phonons. These phonons, however, should be sensitive to the degree of crystallinity of the nanoparticle, i.e., whether it is in a single crystalline, polycrystalline, or amorphous state. Most of the lithographically made nanostructures have polycrystalline or amorphous structures due to the nature of the fast rate of atomic deposition. However, upon thermal treatment of these nanoparticles, they can be annealed to form a crystalline nanoparticle. In the present study, we have found that the electron-phonon relaxation rate decreases greatly when polycrystalline prismatic gold nanoparticles are annealed and transformed into nearly single crystalline nanospheres. The results are explained by the presence of high-density grain boundaries, at which dense, high-frequency vibrations are effective in removing the energy of excited electrons, in the polycrystalline prismatic nanoparticles.

3.2 Experimental Section

The nanoparticle was fabricated on a quartz substrate using the third version NSL (air-water interface self-assembly). The experimental details are introduced in Chapter 2 (Section 2.1.3). The diameter of the PS spheres used in our experiments was 0.45 μm. The mask was then mounted in a thermal evaporator (PVD75 Filament Evaporator, Kurt J. Lesker Company), where a 34 nm of gold (99.99%) is deposited onto the PS sphere mask and into the voids between the spheres measured by a quartz crystal thickness monitor. The prepared prismatic nanoparticle has a bisector of 100 nm.

Thermal annealing is performed at 1000 ^{o}C for 90 sec in an N_2 atmosphere to transform as-deposited polycrystalline nanoprisms into single or nearly single crystalline nanospheres on a quartz substrate. The gold prismatic or spherical nanoparticle monolayer arrays on quartz substrates are analyzed using scanning electron microscopy (LEO 1530 Thermally-Assisted Field Emission SEM, Zeiss/LEO). For the transmission electron microscopy (JEOL 4000EX High Resolution TEM, JEOL Ltd.) measurement, a TEM grid is used to pick up the closely packed polystyrene sphere monolayer from the water surface. The deposition and lift-off processes are kept the same as those performed on a quartz substrate. To protect the carbon film on the TEM grid, the annealing is performed at 771 ^{o}C for 15 min in a high vacuum TEM chamber.

The absorption spectra of the prismatic and spherical nanoparticle arrays are recorded with a Beckman DU-650 spectrophotometer. The incident light is perpendicular to the array substrate. The transmitted light through the sample has a cross section of several square millimeters. The femtosecond laser pump-probe setup [23] is described in Chapter 2 (Section 2.6).

3.3 Results and Discussion

3.3.1 Sample Characterization:

Figure 3-1a is an SEM image of the as-deposited prismatic nanoparticle array on a quartz substrate fabricated with the NSL technique. Since the spherical shape is the most thermodynamically stable, the spherical nanoparticle array on a quartz substrate shown in **Figure 3-1b** is prepared by thermal annealing (at 1000 ^{o}C for 1.5 minutes) of the prismatic nanoparticle array shown in **Figure 3-1a**. After thermal annealing, the gold nanospheres remain in the same periodic hexagonal arrangement as that of the original prismatic nanoparticles.

To examine the internal crystal structure of the prismatic and spherical nanoparticles with High-Resolution Transmission Electron Microscopy (HRTEM), we fabricated the same sample on TEM grids. **Figure 3-2a** is a bright-field TEM image of the as-deposited prismatic nanoparticle array. Even though the thermal annealing temperature of nanoprisms on the TEM grids (771 ^{o}C) is lower than that on the quartz substrate (1000 ^{o}C), the gold nanoprisms are also transformed to spherical or nearly spherical nanoparticles (**Figure 3-2b**). The nanoprism can be annealed to a spherical shape at a temperature that is much lower than the bulk melting temperature. This is due to the relatively lower melting temperature of the nanoscale material than that of its bulk, which has been observed in non-spherical platinum [24] and silver [25] nanoparticles. Furthermore, the sharp apexes of silver prismatic nanoparticles can transfer to rounded shape even at room temperature [25].

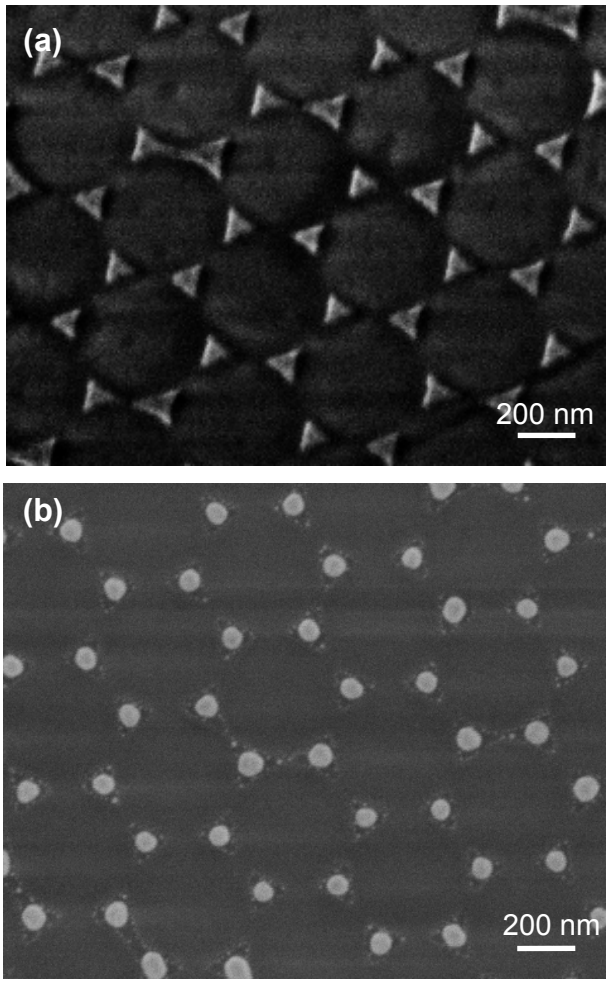

Figure 3-1: (a) and (b) are SEM images of the gold nanoprism and nanosphere arrays, respectively. The periodic arrays of spherical gold nanoparticles are formed by thermal annealing the original prismatic gold nanoparticle arrays sample in an oven at 1000 ^{o}C for 90 seconds.

Figure 3-2c is a dark-field TEM image of the as-deposited gold nanoprism, which shows different grain sizes and domains in each nanoprism as indicated by contrast variation. After thermal annealing, the grain size becomes much larger in the spherical nanoparticles as shown in **Figure 3-2d**. Due to the different lattice orientations of nanospheres relative to the incident electron beam, some of the spheres can diffract more electrons and thus are shown as brighter spots. Some of the spheres are still not single

crystalline as indicated by the sharp contrast in the dark-field images (marked by red arrows), still, the grain size in those nanospheres is much larger than that in the nanoprisms. Higher annealing temperatures or longer annealing time is needed for these polycrystalline nanospheres to fully transfer to signal crystals. In the following discussion, we consider all of the nanospheres as nearly single crystal nanoparticles.

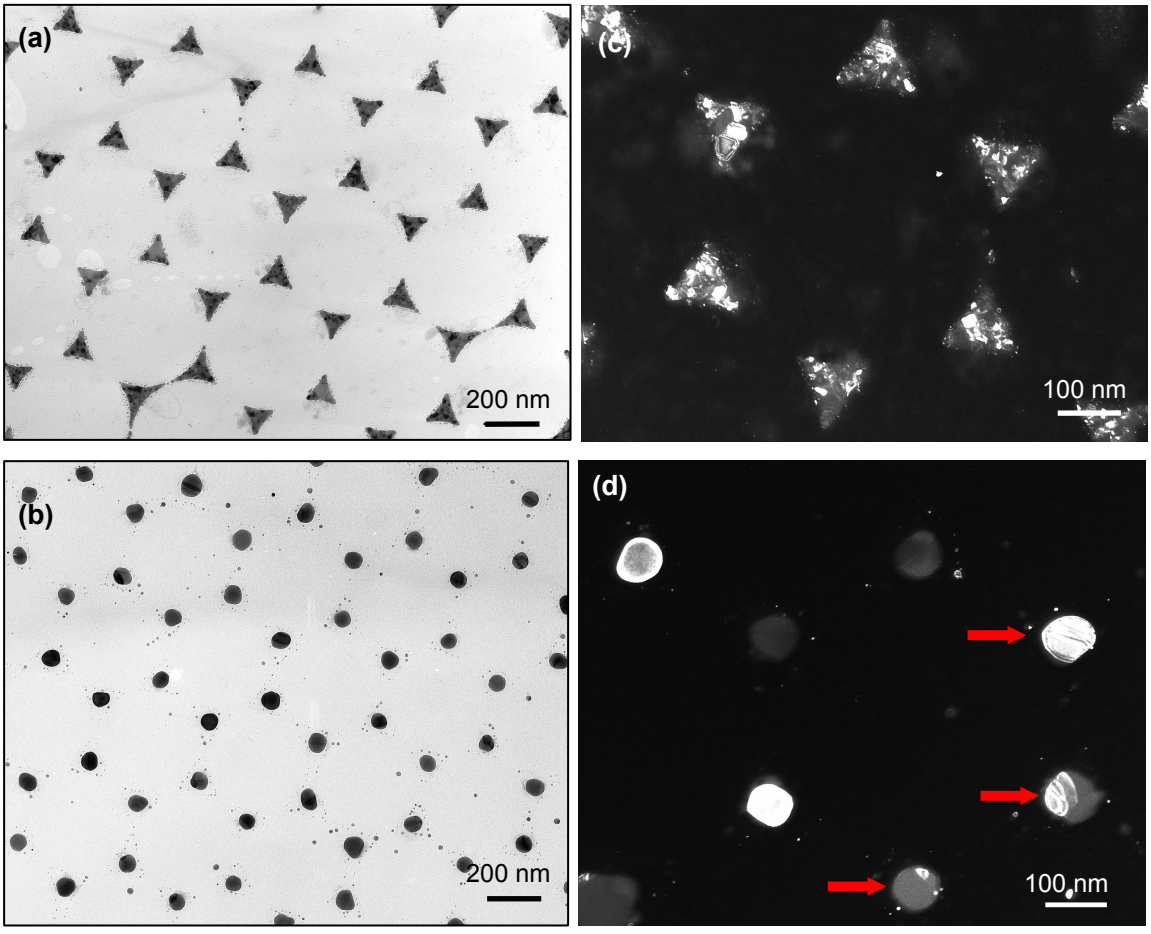

Figure 3-2: (a) is a TEM image of the gold nanoprism array. After *in situ* heading the sample to 771 ^{o}C in the TEM chamber, the morphology of gold particles is more like spherical array, which is displayed in (b). The different grain size of gold particles in nanoprism and nanosphere arrays can be identified in their dark-field TEM images, which are displayed in (c) and (d), respectively.

Figure 3-3a is a dark-field TEM image of a single nanoprism in high magnification where the polycrystalline structure of the nanoparticle is very clear. In **Figure 3-3b**, the well-observed thickness fringes indicate that the thermally annealed nanoparticle is a single grain. The polycrystalline structure of the nanoprism is further confirmed by the ring structure in the selected-area electron diffraction (SAED) pattern as shown in **Figure 3-3c**. The bright spots in the SAED pattern indicate there are some larger crystal grains within the nanoprism. The SAED pattern of a thermally annealed nanosphere is shown in **Figure 3-3d**, the corresponding SAED pattern reveals that most of the defect structures present in the prismatic nanoparticles have been eliminated and the nanosphere has a single crystalline structure. **Figure 3-4** is a high resolution TEM image of the tip of one nanoprism before annealing, which clearly shows all kinds of defects present among different grains of the nanoparticle, such as twin boundaries and stacking faults. Due to the great difference in crystal structure between the as-deposited prismatic and the thermally annealed spherical nanoparticles, they are ideal systems to study the effect of crystallinity on electron-phonon relaxation dynamics in gold nanoparticles.

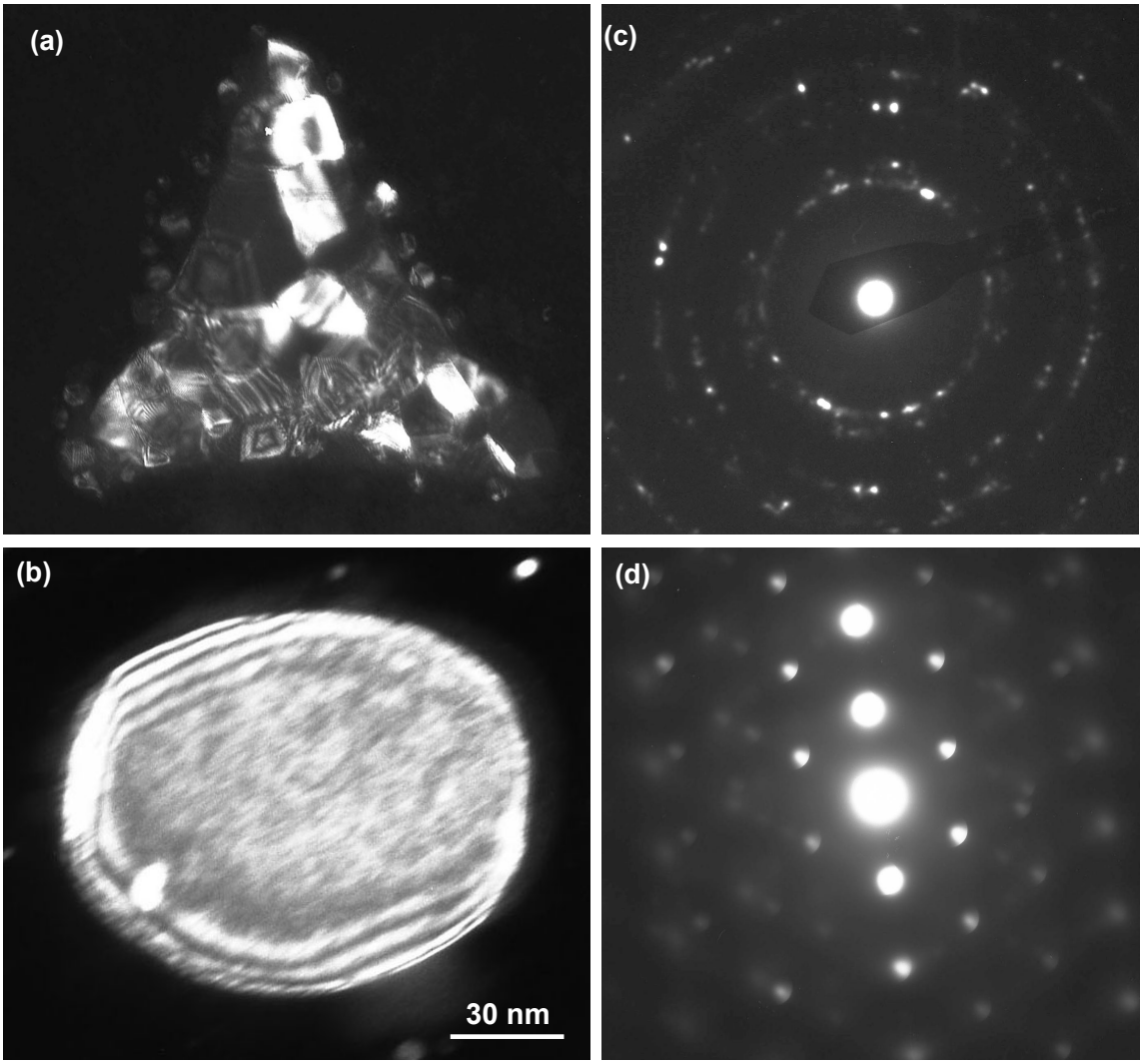

Figure 3-3: (a) and (b) are dark-field TEM images of a gold nanoprism and a nanosphere respectively. The different contrast in the dark-field image (a) indicates that the as-deposited gold nanoparticle is polycrystalline. The well-observed thickness fringes in the dark-field image of the nanosphere indicate that the thermal annealed particle is a single grain. The polycrystalline and single crystalline structures of nanoprism and nanosphere can be further confirmed by their selected-area electron diffraction patterns, which are displayed in (c) and (d), respectively.

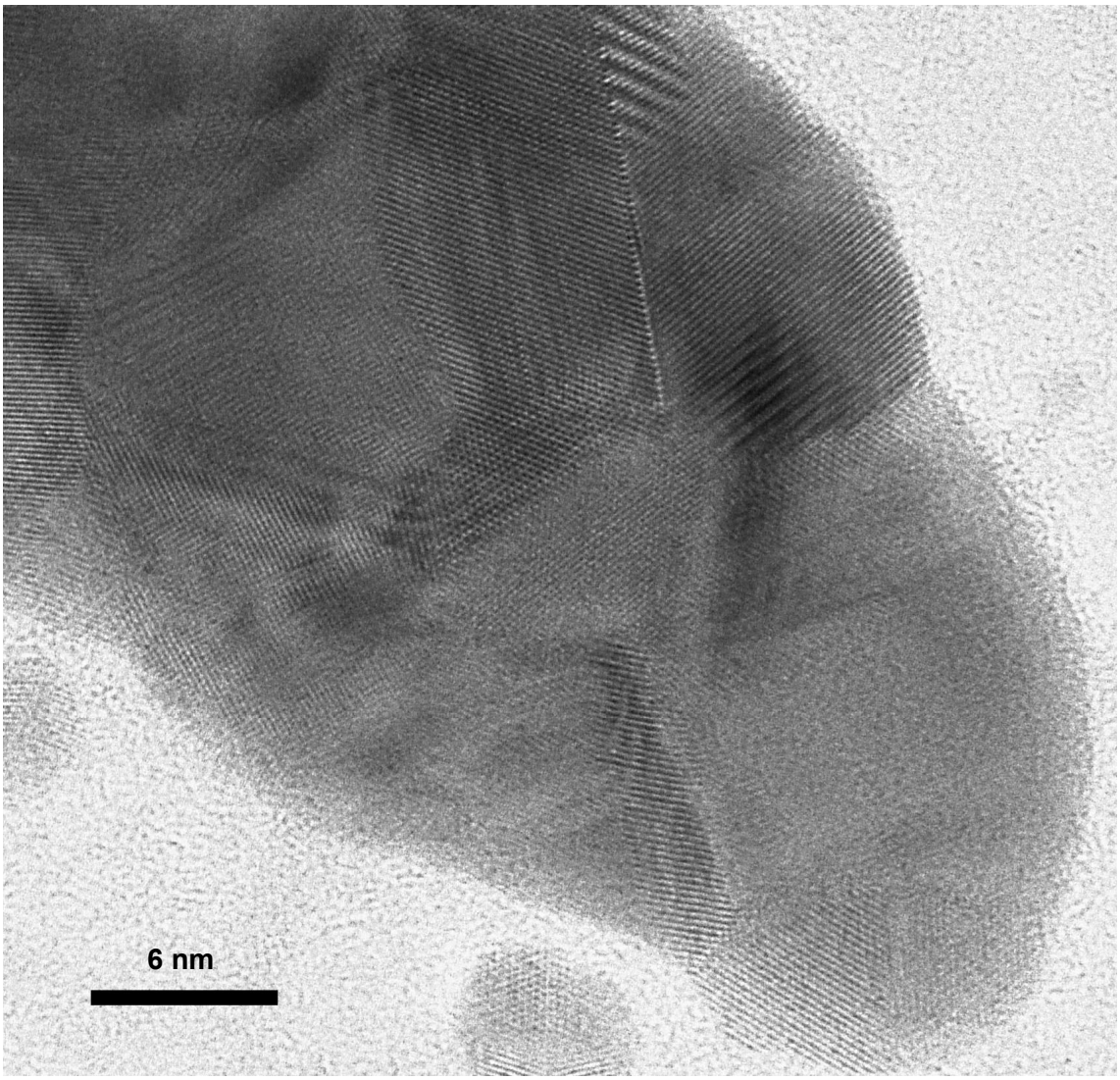

Figure 3-4: A high resolution TEM image of one tip of a nanoprism, which clearly shows that the prismatic gold nanoparticles are polycrystalline nanoparticles with a lot of lattice defects structures like twin boundaries and stacking faults.

3.3.2 Optical Transient Spectroscopy and Electron Phonon Dynamics:

Before we carried out the femtosecond pump-probe experiment, we checked the extinction spectra of the nanoprism and nanosphere arrays to find the difference in their pump efficiency at 400 nm. The extinction spectra of the gold nanoprism and nanosphere arrays are shown in **Figure 3-5**, which indicate that the extinction intensity of the

nanoprism array at 400 nm is ~ 10 % higher than that of the nanosphere array. The extinction of gold nanoparticles at 400 nm corresponds to the absorption of the electron interband transition. With the same femtosecond pump-pulse power, the energy deposited to the electrons of the two kinds of nanoparticles is within 10 %. This absorption difference at 400 nm is most likely due to the difference in the cross-section of prismatic and spherical nanoparticles of the same amount of atoms. The bisector of the prismatic nanoparticle is around 100 nm and the radius of the corresponding spherical nanoparticle is around 40 nm. The cross-section of prismatic nanoparticles is 15 % larger than that of spherical nanoparticles. The absorption intensity is particularly important for comparing the electron-phonon relaxation dynamics since more energy absorbed by electrons results in a longer electron-phonon relaxation time. The surface plasmon resonance maxima of the nanoprism and nanosphere arrays are located at 860 nm and 560 nm as shown in **Figure 3-5**, respectively. The surface plasmon resonance extinction intensity of the nanoprism array is three times stronger than that of the nanosphere array, even though both arrays have the same amount of gold atoms. The stronger surface plasmon absorption of nanoprisms than nanospheres indicates that the prismatic nanoparticle has a higher extinction efficiency than the spherical nanoparticle [26, 27]. The probe wavelength is kept near the extinction peak (850 nm for the nanoprism array and 560 nm for the nanosphere array) to maximize the intensity of the femtosecond transient bleach signal.

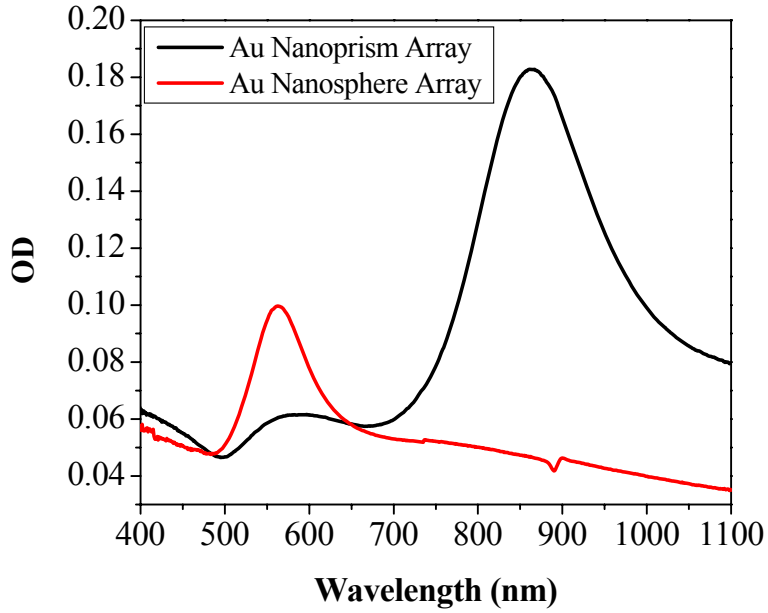

Figure 3-5: The absorption spectra of gold nanoprism and nanosphere arrays. The absorption at the femtosecond pump pulse wavelength (400 nm) is very close for both samples. This guarantees the same pump efficiency under the same pump power of femtosecond pulse.

Figure 3-6a and **b** are femtosecond transient bleach signals of the nanoprism and nanosphere arrays under different pump power, respectively. The pump power dependent femtosecond transient bleach technique is a powerful method to measure the electron-phonon coupling constant, *g*. The coupling constant is calculated by fitting the power dependent electron-phonon relaxation time with a linear equation. The intercept of the linear equation corresponding to $\gamma T_0 / g$ [9, 18], where T_0 is the ambient temperature and $\gamma = \pi^2 k_B^2 g(\varepsilon_F)/3$ (k_B is Boltzmann's constant, $g(\varepsilon_F)$ is the electron density of states at the Fermi level) is $66 Jm^{-3}K^{-2}$ for gold [28]. The inserts in Fig 4a and b are linear fits of

the power dependent electron-phonon relaxation times of the nanoprism and nanosphere arrays, respectively. From the intercepts of the linear equation, the electron-phonon coupling constant *g* for the nanoprism and nanosphere are calculated to be $(2.2 \pm 0.3) \times 10^{16} Wm^{-3} K^{-1}$ and $(2.6 \pm 0.5) \times 10^{16} Wm^{-3} K^{-1}$, respectively. The two electron-phonon coupling constants are very close to the value observed for bulk gold [7, 29], $(3.0 \pm 0.5) \times 10^{16} Wm^{-3} K^{-1}$. This is due to the fact that the matrix elements involve one center term on the gold atoms.

Our experimental results show that the effect of crystalline structure (polycrystalline or nearly single crystalline) does not affect the electron-phonon coupling constant of the gold nanoparticles, but we do observe that there is a large difference in the relaxation dynamics of transient bleach signals between the nanosphere and nanoprism arrays under the same laser pump pulse energy. With 75 nJ/pulse pump power, the electron-phonon relaxation time is 1.2 ± 0.2 ps for the gold nanoprism and 2.1 ± 0.3 ps for the gold nanosphere. With 150 nJ/pulse pump power, the electron-phonon relaxation time is 1.6 ± 0.3 ps for the gold nanoprism and 3.1 ± 0.4 ps for the gold nanosphere. The relaxation time of the gold spherical nanoparticles is nearly twice as large as that of prismatic nanoparticles under the same pump power. The difference in the electron-phonon relaxation time in the nearly single crystalline and polycrystalline gold nanoparticles can be predicted by the inserts of **Figure 3-6**, the electron-phonon relaxation time vs. the pump power. Since the linear fits of the two series experimental data give the same intercept but different slopes (0.015 for the nearly single crystalline nanosphere, 0.003 for the polycrystalline nanoprism), we can predict that as the pump

pulse energy increases, the difference in the electron-phonon relaxation time between the nanosphere and nanoprism arrays will also increase.

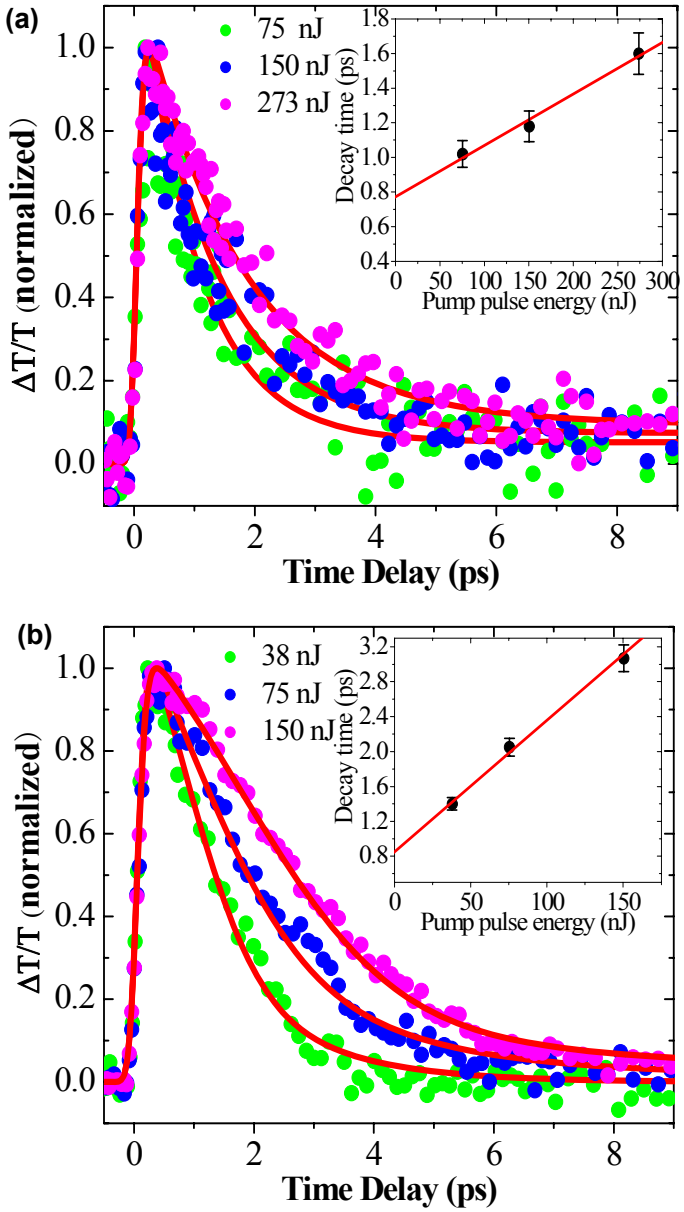

Figure 3-6: The normalized traces of the pump power dependent transient bleach signals with pump at 400 nm of (a) prismatic gold nanoparticle array probe at 850 nm and (b) spherical gold nanoparticle arrays probe at 560 nm. The inserts are linear fits of relaxation time versus the pump pulse energy.

The observed difference in the electron-phonon relaxation dynamics between spherical and prismatic nanoparticles can be explained as more energy being deposited into conduction electrons in spherical gold nanoparticles. The electron temperature in spherical gold nanoparticles is thus higher than that in prismatic gold nanoparticles, and the electronic energy relaxation time of the spherical gold nanoparticles is longer than that of the prismatic gold nanoparticles. However, this argument is not true in our case, where the energy deposited in the nanosphere array is 10 % less than that in the nanoprism array. If the nanosphere array absorbs 10 % more energy, their electron-phonon relaxation time will be even longer and can be calculated as the following. Since electrons in the nanosphere absorb 10 % less energy, the final electron temperature of the nanosphere is also ~ 10 % lower than that of the nanoprism in the low pump power region. For low pump laser power, the electron-phonon relaxation time τ_{e-ph} is given by [9, 18]

$$\tau_{e-ph} = \gamma\left(T_0 + \Delta T\right)/ g\,, \tag{3-1}$$

where γ equal 66 J m^{-3} K^{-2}, T_0 is the ambient temperature, ΔT is the increase of the electronic temperature induced by the energy deposited by the laser pulse, and g is the electron-phonon coupling constant. Since $\gamma T_0 / g$ is given by the intercept of the linear fit of the power dependent electron-phonon coupling time ($\gamma T_0 / g \approx$ 0.8 ps from inserts of **Figure 3-6**), Eq. (3-1) can be reformatted as

$$\tau_{e-ph} = \gamma\Delta T / g + 0.8\,. \tag{3-2}$$

From Eq. (3-2), we can get the e-ph relaxation time for gold nanospheres when the energy delivered to them by the pump laser pulse is the same as that given to the nanoprisms. If gold nanospheres absorb 10 % more energy, ΔT would be 10 % larger and ($\tau_{e-ph} - 0.8$) would also increase 10 %. The electron-phonon relaxation time of the nanosphere array would be 2.2 ± 0.3 and 3.3 ± 0.4 ps for pump powers of 82.5 and 165 nJ/pulse, respectively. Now we can compare the electron-phonon relaxation time of the nanosphere array and the nanoprism array under the same energy deposition. The electron-phonon relaxation times of the nanoprism array are 1.2 ± 0.2 and 1.6 ± 0.3 ps for the pump power of 75 and 150 nJ, respectively. The difference of the electron-phonon relaxation time between the nanosphere and the nanoprism is even larger for the same energy deposition by the pump laser pulse.

3.3.3 Grain Boundary Mechanism:

The shorter relaxation time for prismatic gold nanoparticles compared to that for the spherical nanoparticles is a consequence of the difference in the internal crystalline structures. The prismatic gold nanoparticles are polycrystalline nanoparticles with many defects like grain boundaries as shown in the high resolution TEM image (**Figure 3-4**). The spherical gold nanoparticles have much fewer defects after the high temperature annealing as shown in **Figure 3-3b** and **d**. The shorter relaxation time for prismatic gold nanoparticles than that for spherical nanoparticles could be due to the more effective inelastic scattering of electrons by these defects (the collisions of electrons with lattice imperfections). In single crystal metal, the conductive electron collides with a phonon within the mean free path of the electron (40-50 nm). From the high resolution TEM

image of polycrystalline gold nanoprisms, the averaged grain size is $\sim 13.3 \pm 3.1$ nm, which is much smaller than the mean free path of electrons in gold. In the nearly single crystalline gold nanosphere, the grain size is very close to the size of the nanosphere (~ 80 nm). Therefore, the collision of electrons with grain boundaries happens more frequently than the electron-phonon collisions in the polycrystalline gold nanoprism [30, 31]. Among all kinds of crystal defects (e.g. dislocation, stacking fault, and grain boundary), grain boundaries are one of the most efficient structures for electron scattering. Reiss et al. [32] theoretically calculated the transmission probability of an electron through a single grain boundary in a polycrystalline metal film. They found the probability is close to 0.7 ± 0.1. This probability means that ~ 30 % of the electrons will be scattered (elastically or inelastically) when they try to pass through a grain boundary. Another way to interpret this probability is that each electron will be scattered once on average if it pass three grain boundaries. In the polycrystalline gold nanoprism, the hot electron collides with grain boundaries several times before it transfers the energy to the lattice through electron-phonon interaction. Part of these electron grain boundary collisions would be inelastic and the electronic energy could be transferred to the defect sites. Therefore, the electron-grain boundary interaction could account for the observed shorter electron-phonon relaxation time of gold nanoprisms than gold nanospheres under the same energy deposition of the pump laser pulse.

The extra electron-grain boundary collisions in polycrystalline nanoprisms provide additional channels for the relaxation of hot electronic energy, which do not exist in single crystalline nanospheres. Thus, the electronic energy relaxation in nanoprisms is faster than that in nanospheres. Furthermore, the extrapolations of liner fits to zero pump

pulse energy shown in the inserts of **Figure 3-6** are close to 0.8 ps. This indicates that at lower pump pulse energy, the effect of the electron-grain boundary interaction to the electronic energy relaxation in polycrystalline gold nanoprisms is very small, which leads to the similar electronic energy relaxation time in both of the polycrystalline and the single crystalline gold nanoparticles. As the energy of the laser pump pulse increases, the hot electrons are pumped to higher temperatures and the contribution from inelastic scattering with the grain boundaries to the electronic energy relaxation increases.

An alternative explanation of the difference in the rate of electron-phonon relaxation is the difference in the phonon density and phonon frequencies in the two lattices. We have previously measured that the symmetric coherent phonon vibration period in the prismatic nanoparticle was 74 ps while it is 27 ps in the spherical nanoparticle [33]. This means that the phonon frequency in the spherical nanoparticle is almost three times larger than that in the prism. The exact density of the phonon states for different frequencies that can couple with the electrons will determine the relaxation rates. Since the frequencies of the phonon are different in the two lattices, the density of states and thus the rates of the energy transfer will undoubtedly be different. For real amorphous solids, there are no phonons, but rather highly localized, high density, and high frequency (molecular type) vibrations. The selection rules governing the transfer of momentum or energy from the electron to these vibrations are not as restrictive as the transfer to the phonons. As a result, the electron-lattice relaxation in the disordered prism is expected to be faster than that in the more crystalline lattice.

3.4 Conclusion

We studied the electron phonon relaxation processes in periodic monolayer arrays of polycrystalline prismatic and nearly single crystalline spherical gold nanoparticles. In these two systems, we found the electron-phonon coupling constants are the same within experimental errors and very close to the value of bulk gold. This is because the size of nanoparticles studied here is much larger than the mean free path of conductive electrons in gold, so the surface contribution to the electronic energy relaxation is negligible. We also found that with higher pump laser pulse energy, the electron-phonon relaxation of polycrystalline structured prismatic nanoparticles is faster than that of nearly single crystalline spherical nanoparticles. The difference in electron-phonon relaxation time increases as the energy of the pump laser pulse increases. This means that collisions of electrons with lattice imperfections (grain boundaries) in prismatic gold nanoparticles accelerate the relaxation of the absorbed electronic energy under high pump pulse energy, while the relaxation of electronic energy is dominated by electron-phonon interaction and the lattice imperfections have small contribution to the electronic energy relaxation under lower pump pulse energy. In the present study, we have found that electron-phonon relaxation rate decreases greatly when polycrystalline prismatic gold nanoparticles are annealed and transformed into nearly single crystalline nanospheres. The results are discussed by the presence of high density grain boundaries as the presence of dense high frequency phonons in amorphous prismatic nanoparticles.

3.5 References

[1] Lee, P. A.; Ramakrishnan, T. V., *Rev. Mod. Phys.* **1985,** 57, (2), 287-337.

[2] Zhang, J. Z., *Acc. Chem. Res.* **1997,** 30, (10), 423-429.

[3] Link, S.; El-Sayed, M. A., *J. Phys. Chem. B* **1999,** 103, (40), 8410-8426.

[4] Link, S.; El-Sayed, M. A., *Int. Rev. Phys. Chem.* **2000,** 19, (3), 409-453.

[5] Voisin, C.; Del Fatti, N.; Christofilos, D.; Vallee, F., *J. Phys. Chem. B* **2001,** 105, (12), 2264-2280.

[6] Link, S.; Ei-Sayed, M. A., *Annu. Rev. Phys. Chem.* **2003,** 54, 331-366.

[7] Groeneveld, R. H. M.; Sprik, R.; Lagendijk, A., *Phys. Rev. B* **1995,** 51, (17), 11433-11445.

[8] Link, S.; Burda, C.; Wang, Z. L.; El-Sayed, M. A., *J. Chem. Phys.* **1999,** 111, (3), 1255-1264.

[9] Hodak, J.; Martini, I.; Hartland, G. V., *Chem. Phys. Lett.* **1998,** 284, (1-2), 135-141.

[10] Ahmadi, T. S.; Logunov, S. L.; ElSayed, M. A., *J. Phys. Chem.* **1996,** 100, (20), 8053-8056.

[11] Logunov, S. L.; Ahmadi, T. S.; ElSayed, M. A.; Khoury, J. T.; Whetten, R. L., *J. Phys. Chem. B* **1997,** 101, (19), 3713-3719.

[12] Link, S.; Burda, C.; Mohamed, M. B.; Nikoobakht, B.; El-Sayed, M. A., *Phys. Rev. B* **2000,** 61, (9), 6086-6090.

[13] Hodak, J. H.; Henglein, A.; Hartland, G. V., *J. Chem. Phys.* **1999,** 111, (18), 8613-8621.

[14] Del Fatti, N.; Flytzanis, C.; Vallee, F., *Appl. Phys. B: Lasers Opt.* **1999,** 68, (3), 433-437.

[15] Arbouet, A.; Voisin, C.; Christofilos, D.; Langot, P.; Del Fatti, N.; Vallee, F.; Lerme, J.; Celep, G.; Cottancin, E.; Gaudry, M.; Pellarin, M.; Broyer, M.; Maillard, M.; Pileni, M. P.; Treguer, M., *Phys. Rev. Lett.* **2003,** 90, (17), 177401.

[16] Sun, C. K.; Vallee, F.; Acioli, L. H.; Ippen, E. P.; Fujimoto, J. G., *Phys. Rev. B* **1994,** 50, (20), 15337-15348.

[17] Roberti, T. W.; Smith, B. A.; Zhang, J. Z., *J. Chem. Phys.* **1995,** 102, (9), 3860-3866.

[18] Hodak, J. H.; Martini, I.; Hartland, G. V., *J. Phys. Chem. B* **1998,** 102, (36), 6958-6967.

[19] Hodak, J. H.; Henglein, A.; Hartland, G. V., *J. Chem. Phys.* **2000,** 112, (13), 5942-5947.

[20] Halte, V.; Bigot, J. Y.; Palpant, B.; Broyer, M.; Prevel, B.; Perez, A., *Appl. Phys. Lett.* **1999,** 75, (24), 3799-3801.

[21] Darugar, Q.; Qian, W.; El-Sayed, M. A.; Pileni, M. P., *J. Phys. Chem. B* **2006,** 110, (1), 143-149.

[22] Nisoli, M.; Stagira, S.; DeSilvestri, S.; Stella, A.; Tognini, P.; Cheyssac, P.; Kofman, R., *Phys. Rev. Lett.* **1997,** 78, (18), 3575-3578.

[23] Logunov, S. L.; Volkov, V. V.; Braun, M.; El-Sayed, M. A., *Proc. Natl. Acad. Sci. U. S. A.* **2001,** 98, (15), 8475-8479.

[24] Wang, Z. L.; Petroski, J. M.; Green, T. C.; El-Sayed, M. A., *J. Phys. Chem. B* **1998,** 102, (32), 6145-6151.

[25] Huang, W. Y.; Qian, W.; El-Sayed, M. A., *J. Phys. Chem. B* **2005,** 109, (40), 18881-18888.

[26] Jensen, T. R.; Schatz, G. C.; Van Duyne, R. P., *J. Phys. Chem. B* **1999,** 103, (13), 2394-2401.

[27] Jain, P. K.; Lee, K. S.; El-Sayed, I. H.; El-Sayed, M. A., *J. Phys. Chem. B* **2006,** 110, (14), 7238-7248.

[28] Ashcroft, N. W.; Mermin, N. D., *Solid State Physics*. Holt, Rinehart & Winston: New York, 1976.

[29] Groeneveld, R. H. M.; Sprik, R.; Lagendijk, A., *Phys. Rev. Lett.* **1990,** 64, (7), 784-787.

[30] Elsayedali, H. E.; Juhasz, T., *Phys. Rev. B* **1993,** 47, (20), 13599-13610.

[31] Elsayedali, H. E.; Juhasz, T.; Smith, G. O.; Bron, W. E., *Phys. Rev. B* **1991,** 43, (5), 4488-4491.

[32] Reiss, G.; Vancea, J.; Hoffmann, H., *Phys. Rev. Lett.* **1986,** 56, (19), 2100-2103.

[33] Huang, W.; Qian, W.; El-Sayed, M. A., *Proc. SPIE-Int. Soc. Opt. Eng.* **2005,** 5927, (Plasmonics: Metallic Nanostructures and Their Optical Properties III), 592701.

CHAPTER 4

COHERENT PHONON OSCILLATIONS IN GOLD PRISMATIC MONOLAYER PERIODIC NANOPARTICLE ARRAYS

Abstract

We studied the ultrafast laser-induced coherent oscillation resulting from the symmetric lattice vibrations in monolayer periodic arrays of gold prismatic nanoparticles produced by the NSL technique. We observed strong coherent oscillation signals in a single monolayer structure due to the large sensitivity of their absorption spectra to size and the very narrow size distribution of the nanoparticles in the arrays. We found the period of the coherent phonon oscillation to be proportional to the bisector of nanoparticles, while the thickness of nanoparticles has no effect on the oscillation period. When we transform a nanoprism array into a nanosphere array, the period of the coherent phonon oscillation decreases three times. We also performed wavelength dependent coherent phonon oscillation measurements, from which we proposed a simple phenomenological model to estimate the percentage change in the nanoparticle size during the vibration from the dependence of the amplitude and phase of the oscillation on the monitoring wavelength. The observed large change in the size of the prismatic nanoparticle compared to the small change reported previously for nanosphere oscillations is discussed. This work has been published in *Nano Letters*, 2004, 4(9),1741; *J. Phys. Chem. B*, 2005, 109(40), 18881; and *Proc. SPIE-Int. Soc. Opt. Eng.* **2005,** 5927, (Plasmonics: Metallic Nanostructures and Their Optical Properties III), 592701.

4.1 Introduction

Coherent phonon oscillations in noble metals [1-9] and semiconductors [10-14] can be induced with ultrafast laser excitation. These coherent phonon oscillations can be detected by pump-probe techniques using ultrafast optical [1-12], X-ray [13,14], or electron probe pulses [15-17]. For X-ray and electron probe pulses, the diffraction patterns of metals or semiconductors are recorded, which modulate due to the lattice vibration. For optical probe pulses, the transmission, reflection, or absorption intensities of metals and semiconductors modulate due to the lattice vibration. In noble metal nanoparticles, the lattice vibration causes a periodic change in the size of the metal nanoparticles, which changes the free electron density in the particle, and thus a periodic shift of the plasmon absorption band is expected. If we monitor the change in the transient absorption intensity at a particular wavelength, an oscillation of the optical signal is observed whose period equals the coherent lattice oscillation period of the metal nanoparticles. The detection of the coherent lattice oscillation of metallic nanoparticles provides a powerful tool to characterize the mechanical and structural properties of nanostructures, which are difficult to detect with traditional macroscopic techniques.

The period of this oscillation is found to be proportional to the dimension of the nanoparticles [4,18,19]. Ultrafast laser-induced coherent lattice oscillations also depend on the shapes of the metal nanoparticles. This is because particles of different shapes have different vibrational modes. Coherent lattice oscillation experiments have been carried out on noble metal nanoparticles of different shapes, such as spherical silver nanoparticles [2], spherical gold nanoparticles [1,7,20], ellipsoidal silver nanoparticles

[21], cylindrical gold nanoparticles [6,22], and aggregated gold particles [23]. Phonon oscillations have also been seen in different environments, mainly in glass matrices [2,21] and in colloidal solutions [1,6,7,20,22,23]. These coherent oscillations have been attributed to the symmetric acoustic lattice vibration (periodic size change) of the metal nanoparticles caused by ultrafast laser-induced impulsive heating. The lattice vibration of the metal nanoparticles induces a periodic shift of the plasmon absorption band, which causes a corresponding oscillation in the transient absorption intensity if it is monitored at a fixed wavelength. The frequency of this oscillation is found to be inversely proportional to the dimension of the nanoparticles, which can be predicted accurately by classical mechanics calculations [4].

Here, we report on the first study of ultrafast laser-induced coherent oscillations in a periodic monolayer array of prismatic gold nanoparticles prepared by the NSL technique. We studied the effects of the nanoprisms' bisector, thickness, and shape on their coherent phonon oscillations. Due to the strong absorption of the dipolar surface plasmon oscillation and the sensitivity of the oscillation frequency to the size of the truncated tetrahedral nanoparticles with sharp tips, it was possible to obtain excellent oscillation amplitudes from a monolayer array of these nanoparticles with good signal to noise ratio. In addition, due to the sharp tips of the prismatic nanoparticles, large changes in the size are observed during the coherent lattice oscillations.

4.2 Experimental Section

The nanoparticle was fabricated on a quartz substrate using the second version NSL (Concentration Optimized Self-assembly). The experimental details are introduced

in Chapter 2 (Section 2.1.2). The diameter of the PS spheres used in our experiments was 0.36, 0.45, 0.60 and 0.74 μm. The mask was mounted in a thermal evaporator (Denton DV-502A) to deposit 30 or 50 nm thick silver or gold (99.999 %, Alfa Aesar) into the voids between the spheres. The thickness of the deposited metal was monitored by a quartz crystal thickness monitor (Inficon). After deposition, the PS spheres were removed by sonication in absolute ethanol. The formed silver and gold prismatic monolayer nanoparticle arrays were checked by using scanning electron microscopy (SEM).

Shimadzu UV-3101-PC and Beckman DU-650 spectrophotometers were used to record the absorption spectra of the arrays. The examined area of the nanoparticle array samples was several square millimeters, which allowed us to check the absorbance of the nanoparticle arrays on a large scale. The overall sample quality can be evaluated in this way because the intensity of the surface plasmon resonance absorption peak reflects the number of nanoparticles in the sampled area of the array. The micro-absorption spectrum was taken by a SEE 1100 Micro-spectrometer in transmission mode and the examined area was $3.75 \times 3.75\ \mu m^2$. With the micro-spectrometer, the sample area could be viewed directly, which allowed us to record the absorption of the array of nanoparticles and avoided most of the large defects.

The details of the femtosecond laser pump-probe experiment are described in Chapter 2 (Section 2.6).

4.3 Results and Discussion

4.3.1 SEM Images and Absorption Spectra of the Nanoparticle Arrays:

Figure 4-1a is a typical SEM image of the closely packed polystyrene spheres on the quartz substrate. The diameter of the polystyrene spheres is $0.60\,\mu m$. **Figures 4.1b-d** are SEM images of the hexagonal patterned gold array particles (shown in golden color) that are produced with different size PS spheres. The black spheres in **Figure 4-1b-d** represent the positions of the etched PS sphere masks that are used during the Au deposition. The size of the particles is represented by the bisector, *a*, of the triangle. The bisectors of the particles are 104, 138 and 166 nm for the samples made with 0.45, 0.60 and 0.74 μm PS spheres, respectively. The size distribution of the particles is very narrow with a standard deviation between 5-8 % (excluding the large defects when the long axis is larger than 2*a*). Although there are some defects on the sample caused by misalignment of the PS spheres, which produce stacking defects in the mask, the size of the defects is much larger than the average size of the array particles examined. Jensen et al. [49] have shown that those defects on the array have negligible effect on the plasmon absorption band by comparing the micro- and macro-absorption spectra of their silver array samples.

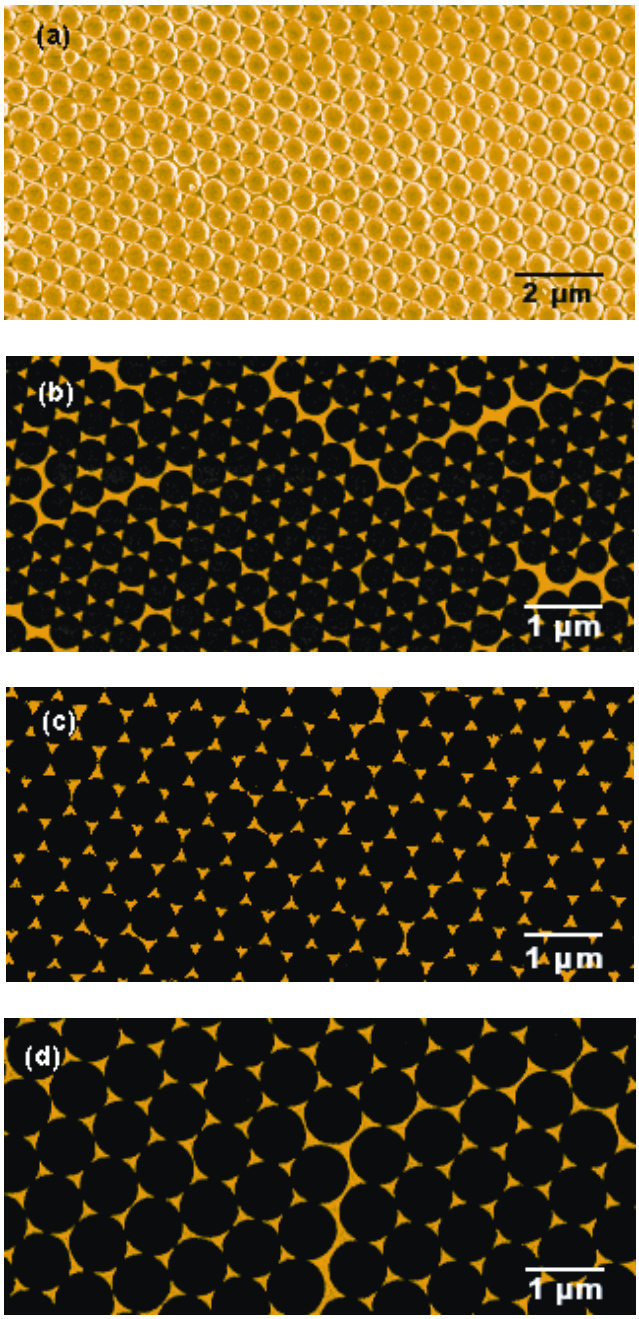

Figure 4-1: SEM image of (a) a highly ordered self-assembled monolayer of PS spheres on a quartz substrate (The spheres have a diameter of 0.60 µm). (b-d) show the periodic gold particle monolayer arrays (shown in gold color) produced with 0.45, 0.60 and 0.74 µm PS spheres, respectively (Black spheres represent the positions of the PS sphere mask used during the Au deposition).

The black spectra in **Figure 4-2a-c** show the LSPR extinction spectra of different sized gold nanoparticles correspondingly shown in **Figure 4-1b-d**. The red and black spectra in **Figure 4-2a** are the micro- and macro-absorption spectra of array nanoparticles with a particle size *a* equal to 104 nm, respectively. For this array, the LSPR maxima of the two spectra in **Figure 4-2a** are around 742 nm. In the macro-absorption spectra, there is a dip around 500 nm which results from the gold film [50] or large defects formed during the sample preparation. This dip is not observed in the micro-absorption spectrum since a spot that is free of defects has been selected for the absorption measurement.

As show in **Figure 4-2a-c**, the LSPR extinction band red shifts as the size of the particle increases. This type of dependence was used by Jensen and co-workers [43] to make silver arrays with tunable LSPR bands. The macro-absorption spectra also show a weak band around 550-600 nm on the blue side of the main plasmon resonance band, which is clearly observed in the micro-absorption spectra (red spectrum in **Figure 4-2a**). Compared to the macro-absorption spectrum (in which the area examined was larger than several square millimeters), the micro-absorption spectrum is much sharper and seems to eliminate most of the inhomogeneous broadening due to defects in the nanoparticle array. This is supported by the better fit of the micro-absorption spectrum to the Lorentzian line shape (blue dotted spectrum in **Figure 4-2a**) than the macro-spectrum. Since the micro-spectrometer is capable of recording only the sample absorbance between 400 and 850 nm, we could not get the full absorption spectrum for the large array samples (134 and 166 nm). These macro-spectra are broader than the corresponding Lorentzian fits (blue dotted spectra in **Figure 4-2a-c**), indicating the presence of inhomogeneous broadening. The absorption spectrum increased below 500 nm, which was due to the absorption of the

electron interband transition from the Au 5*d* band to empty 6*sp* bands above the Fermi level [72].

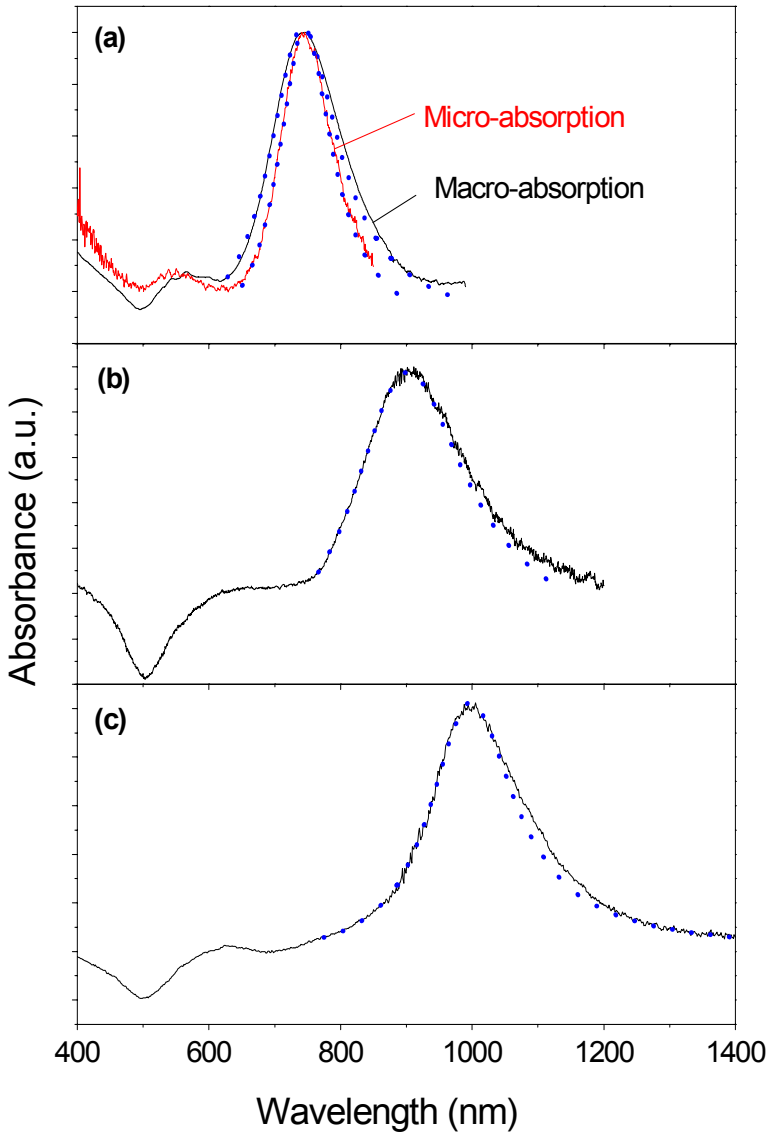

Figure 4-2: (a-c) Absorption spectra of the periodic array samples made with 0.45, 0.60, and 0.74 μm PS spheres, respectively. Red line in (a) is micro-absorption spectra of a 3.75×3.75 μm^2 area on the array sample made with 0.45 μm PS spheres. The difference between the red and black spectra in (a) is a result of a small amount of broadening in the macro-absorption spectrum due to inhomogeneity. The spectra shown in blue dots in (a-c) are fits of the original absorption spectra to Lorentzian shapes.

The weak surface plasmon band at 550 nm observed in the micro-absorption spectrum was also observed by Mohamed [51] from triangular gold nanoplatelets. From the absorption spectrum and discrete dipole calculations, Jin et al. [52] found that the plasmon resonance of silver prism nanoparticles, having an edge length of 150 ± 16 nm, had three absorption bands located at 340 nm (assigned to out-of-plan quadrupole resonance), 600 nm (assigned to in-plane quadrupole resonance), and the strong band at 1065 nm (assigned to in-plane dipole resonance). Due to the similarity of the particle shape in our case, it is likely that the weak 550 nm plasmon resonance band in our gold array sample (104 nm particles) results from the in-plane quadrupole resonance transition and the strong absorption bands shown in **Figure 4-2a-c** are the in-plane dipolar transitions.

Figure 4-3 shows the dependence of the plasmon absorption maximum λ_{max} on the size of gold spherical nanoparticles [1,27] and prismatic array nanoparticles. This illustrates a much more pronounced sensitivity of the plasmon absorption maximum on the size of prismatic nanoparticles compared to that of spherical nanoparticles. For gold spherical nanoparticles, the plasmon absorption maximum increases by 0.64 nm for every 1 nm increase in the diameter of nanospheres. For gold prismatic array nanoparticles, the plasmon absorption maximum increases by 4.4 nm for every 1 nm increase in the bisector of the nanoprism.

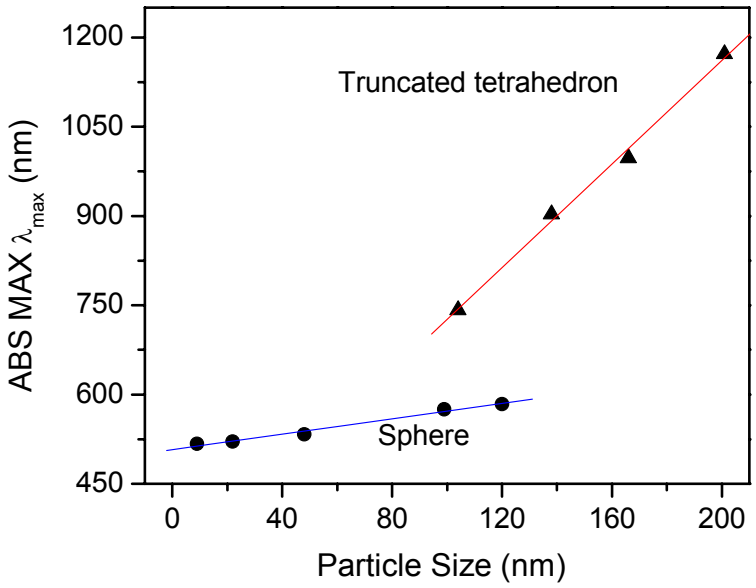

Figure 4-3: The dependence of the wavelength maxima (λ_{max}) of the surface plasmon absorption spectra on the size of gold spherical nanoparticles [1,27] (●) and prismatic array nanoparticles (▲). This illustrates the much more pronounced sensitivity of λ_{max} on the size of prismatic nanoparticles compared to spherical nanoparticles. For gold spherical nanoparticles, the plasmon absorption maximum increases by 0.64 nm for every 1 nm increase in the diameter of nanospheres. For gold prismatic array nanoparticles, the plasmon absorption maximum increases by 4.4 nm for every 1 nm increase in the bisector, *a*, of the nanoprism.

4.3.2 Size Dependence of the Phonon Oscillation Period:

Figure 4-4 shows the laser-induced phonon oscillations for different size gold nanoparticle arrays. According to this simple monolayer packing geometry (P_{6mm}) and the laser focus point area (4.91×10^{-4} cm^2 for a 250 μm diameter focus spot), we can calculate the number of nanoparticles that are excited by the pump laser pulse. About 2.1×10^{5} gold array nanoparticles are irradiated by the pump laser in the 166 nm bisector

nanoparticle array. Even for the smallest nanoparticle array sample (a = 104 nm), only 5.7×10^5 particles are irradiated. The concentrations of the nanoparticle arrays are several orders of magnitude lower than that in common experiments carried out using colloidal nanoparticle solutions. Nevertheless, there are two reasons why we can observe these strong coherent oscillation signals. The first is the strong absorption coefficient of the prisms and the large sensitivity of the absorption spectrum to the size of the nanoprisms (**Figure 4-3**). The second is the very narrow size distribution of NSL prepared array nanoparticles.

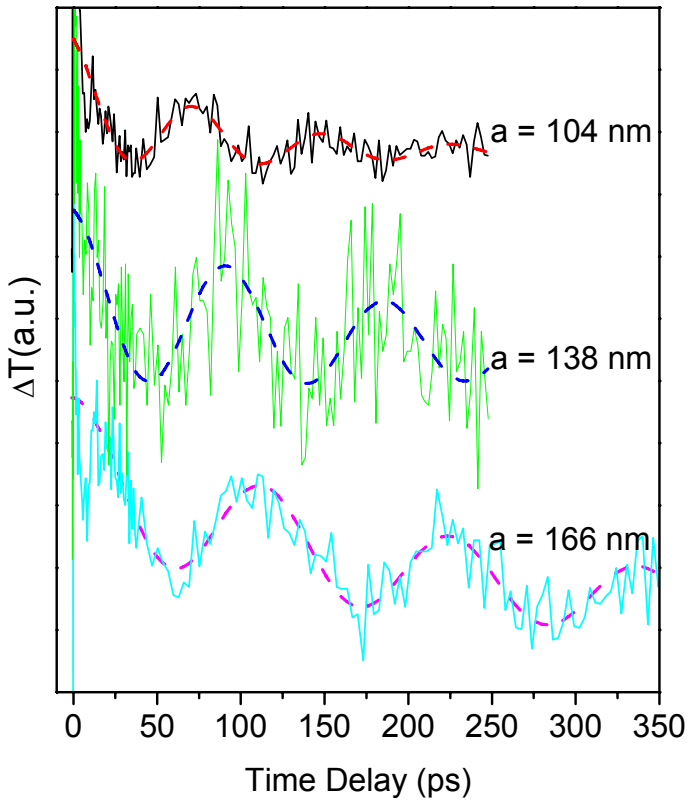

Figure 4-4: Lattice phonon oscillations induced in the prismatic gold nanoparticle monolayer arrays with a 100 fs laser pulse of 250 nJ at 400 nm and monitored close to the absorption maximum of each nanoparticle (solid line). The oscillation was fitted with a damped cosine function (dash line), from which the oscillation period is calculated.

The experimental oscillation signals in **Figure 4-4** are fitted to a damped cosine function (dash line) in order to obtain the frequency and the phase of modulations. The damped cosine function used has the form

$$S(t) = A_0 \exp(-t/\tau_d)\cos(2\pi t/T + \varphi), \tag{4-1}$$

where A_0 is the initial amplitude, τ_d is the damping time, T is the period of the oscillation and φ is the initial phase of the oscillation signal. In addition, a one

component exponential decay is used to fit the slowly varying background in the decay trace, which is due to the phonon-phonon relaxation. For the traces in **Figure 4-4**, the initial oscillation amplitudes, A_0, are 0.090, 0.135, and 0.104 for nanoprisms of a respective size of 104, 138, and 166 nm nanoparticles. The damping times τ_d are 102, 258 and 419 ps for the three different sized nanoparticles, respectively. The initial phases φ of the three oscillation traces are 7.7°, 8.7° and -8.3° for the three different size nanoparticles, respectively. The plot of the oscillation period T vs. the nanoparticle size a is shown in **Figure 4-5**. The period of the oscillation increases almost linearly with the size of the array particles.

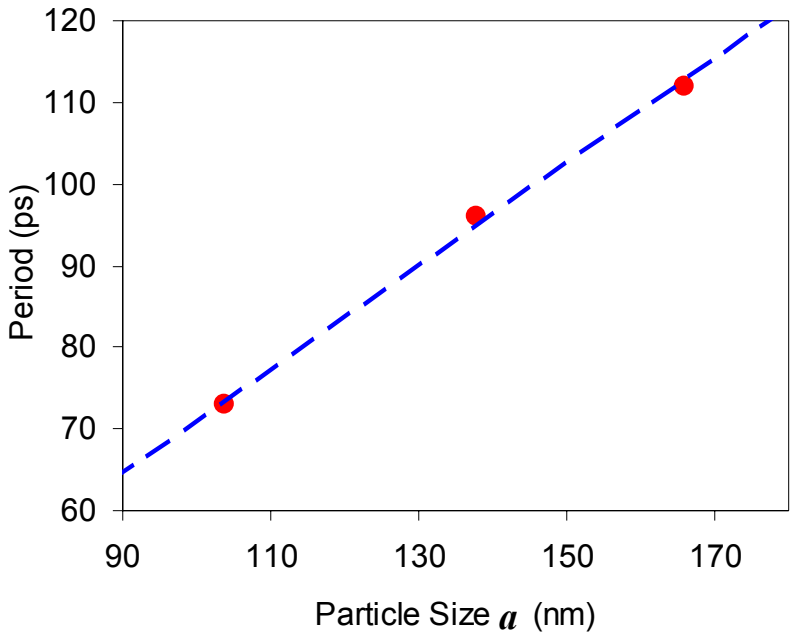

Figure 4-5: The linear dependence of the oscillation period verses the particle size. The solid line is a linear fit of the experimental data.

4.3.3 Shape Dependence of the Coherent Phonon Oscillation Period:

In Chapter 1 (Section 1.4), the oscillation periods of nanospheres, nanorods, and nanoshells were discussed. The periods of coherent phonon oscillations varied for nanoparticles of different shapes. However, the periods of nanoparticles of different shapes were mostly detected from nanoparticles in different condition (i.e. concentration and capping material). To eliminate the effect of variation in the condition parameters on the coherent phonon oscillations, a straightforward comparison was performed by transforming prismatic nanoparticles to spherical nanoparticles and measuring their coherent phonon oscillation period before and after the shape change. Two samples in nearly the same conditions were used in this experiment [56]. One was a monolayer of prismatic gold nanoparticles with a 104 nm bisector and 50 nm thickness assembled into periodic hexagonal arrays on a quartz substrate (insert in **Figure 4-6a**). In order to observe shape effects on the coherent acoustic phonon oscillation, the other sample was prepared by transforming prismatic gold nanoparticles into spherical nanoparticles using thermal annealing. The thermal annealing was carried out by heating the original prismatic gold nanoparticle array sample in an oven at 1000 ^{o}C for 1.5 minutes. The SEM image of the thermally annealed sample (insert in **Figure 4-6b**) shows that the spherical gold nanoparticles have a diameter of 84 nm and retain the same periodic hexagonal arrangement following the annealing step. Since the annealing temperature was much lower than the boiling temperature of gold (2856 ^{o}C), there was no atomic loss during the annealing process and the amount of gold atoms in the two arrays was nearly the same.

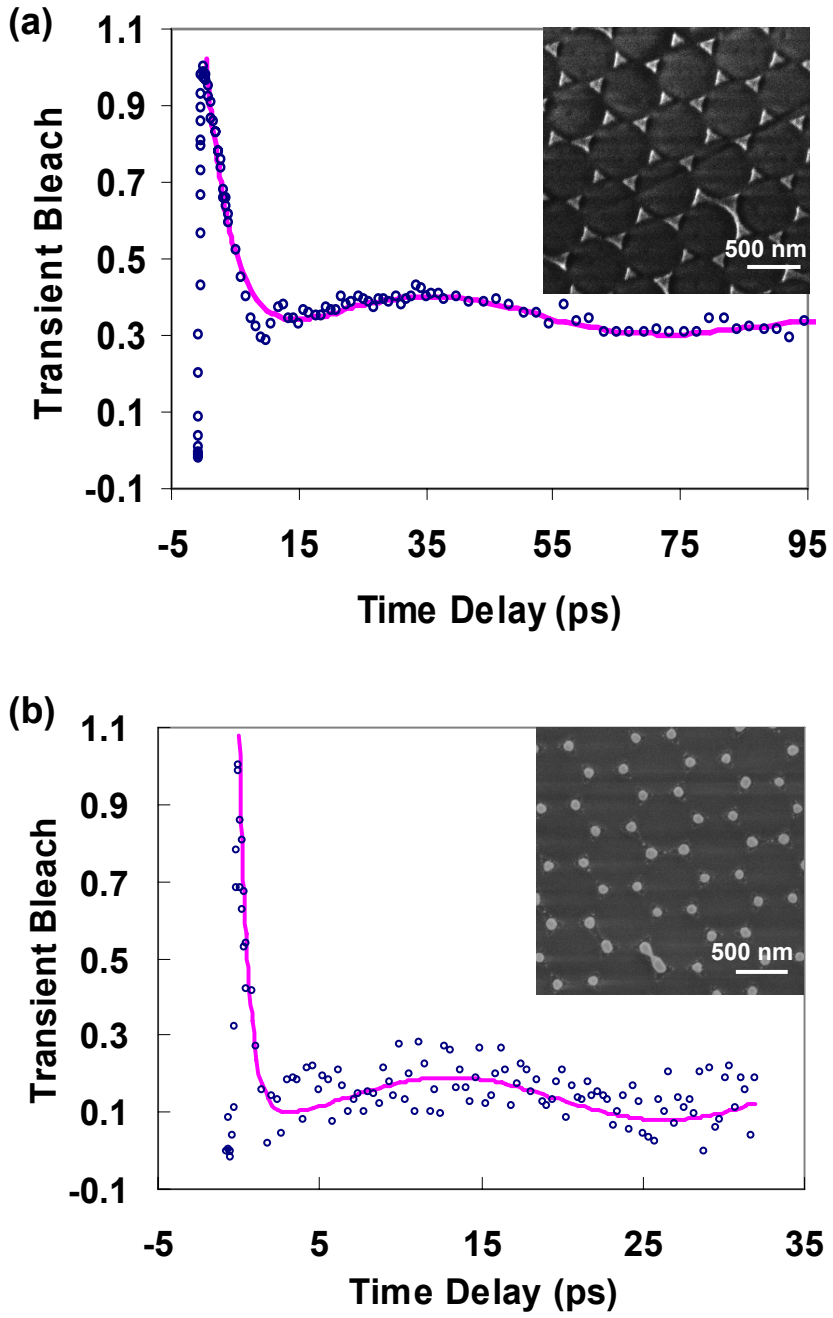

Figure 4-6: (a) Optically detected coherent phonon oscillations for prismatic nanoparticle arrays. The insert in (a) is a SEM image of the prismatic nanoparticle array prepared with NSL. (b) Optically detected coherent phonon oscillations for spherical nanoparticle arrays. The insert in (b) is a SEM image of the nanoparticle array after thermal annealing at 1000 ^{o}C for 1.5 min. The scale bars in the SEM images represent 500 nm [56].

Femtosecond pump-probe measurements have been performed on both samples with a pump wavelength of 400 nm and a probe wavelength located within each plasmon absorption band. Oscillating transient bleach signals were observed for both samples due to the generation of coherent acoustic phonons (**Figure 4-6**). The periods of coherent acoustic phonon oscillations were obtained by fitting transient oscillation signals to damped cosine functions. The oscillation periods were found to be 74 ps and 27 ps for prismatic gold nanoparticles (104 nm bisector) and spherical gold nanoparticles (84 nm diameter), respectively [56]. It is interesting to see how dramatic the change in the coherent acoustic phonon oscillation periods is in metallic nanoparticles as their shape is transformed from prismatic to spherical. These experimental results reveal that large tuning of the coherent acoustic phonon properties of metallic nanoparticles could be better achieved by changing their shape rather than changing their size. Because the coherent acoustic phonon oscillation period is linearly dependent on size, if we want to decrease (increase) the coherent acoustic phonon oscillation period by 3 times, we need to decrease (increase) the size of the nanoparticles by 3 times. However, the same change in the period can be achieved by simply changing the shape of the nanoparticle from prismatic to spherical, while keeping the number of gold atoms the same.

4.3.4 Thickness Independence of Coherent Phonon Oscillations of Prismatic Nanoparticles:

For prismatic nanoparticles, one interesting question was if their thickness had any effect on the optically detected coherent phonon oscillation period? We examined the

effect of a thickness change on the period of the prismatic array nanoparticles by using two prismatic array nanoparticles of the same bisector but different thickness. **Figure 4-7** is the differential transmission signals from the Au prismatic monolayer nanoparticle arrays produced with $0.36\,\mu m$ polystyrene sphere mask. The deposition thickness of the Au is changed from 50 nm (**Figure 4-7a**) to 30 nm (**Figure 4-7b**) as measured with the quartz crystal thickness monitor in the thermal evaporator. From the SEM images of the two nanoparticle array samples, the bisector of the Au prismatic nanoparticles is measured to be 85.7 nm for the 30 nm thick particles and 86.8 nm for the 50 nm thick particles. The slight increase of the in-plane size with the increase of the deposition time is quite reasonable due to the scattering of the Au atoms away from the direct path perpendicular to the substrate plane. Otherwise, we would obtain perfect prismatic particles instead of the truncated tetrahedral array nanoparticles. The oscillation periods are $61.6 \pm 2\,ps$ and $60.8 \pm 2\,ps$ for the 30 nm and 50 nm nanoparticle thickness (d), respectively, and are equivalent within experimental error.

In order to optically observe the lattice oscillation, the oscillation must induce changes in the electron density, which changes the dipolar surface plasmon absorption band whose frequency at the absorption maxima $\nu_{sp}^{\max}$ is related to the electron density by Eq. (1-1) in Chapter 1 (Section 1.1). From Eq. (1-1), it is clear that a volume change of a nanoparticle should lead to a change in the surface plasmon absorption maximum. It is also clear that the symmetric breathing oscillation induces the largest change in volume and thus the electron density. The strong surface plasmon absorption results from the coherent in-plane electronic oscillation. This induces in-plane polarization of the ionic lattice, due to electron-phonon coupling, which causes the in-plane lattice oscillation. We

thus assign the lattice oscillation observed optically to be due to the symmetric in-plane breathing lattice oscillation. In fact we like to generalize this to all the optically detected lattice oscillation of the plasmonic particles. This assignment is supported by the observation of the oscillation period not being sensitive to the thickness of the nanoprisms.

The ultra-weak dependence of the observed coherent phonon oscillation period on thickness is also observed for the gold array sample produced with a 0.45 μm polystyrene sphere mask (a period of 75 ps for a particle thickness of 50 nm and 73 ps for a particle thickness of 30 nm).

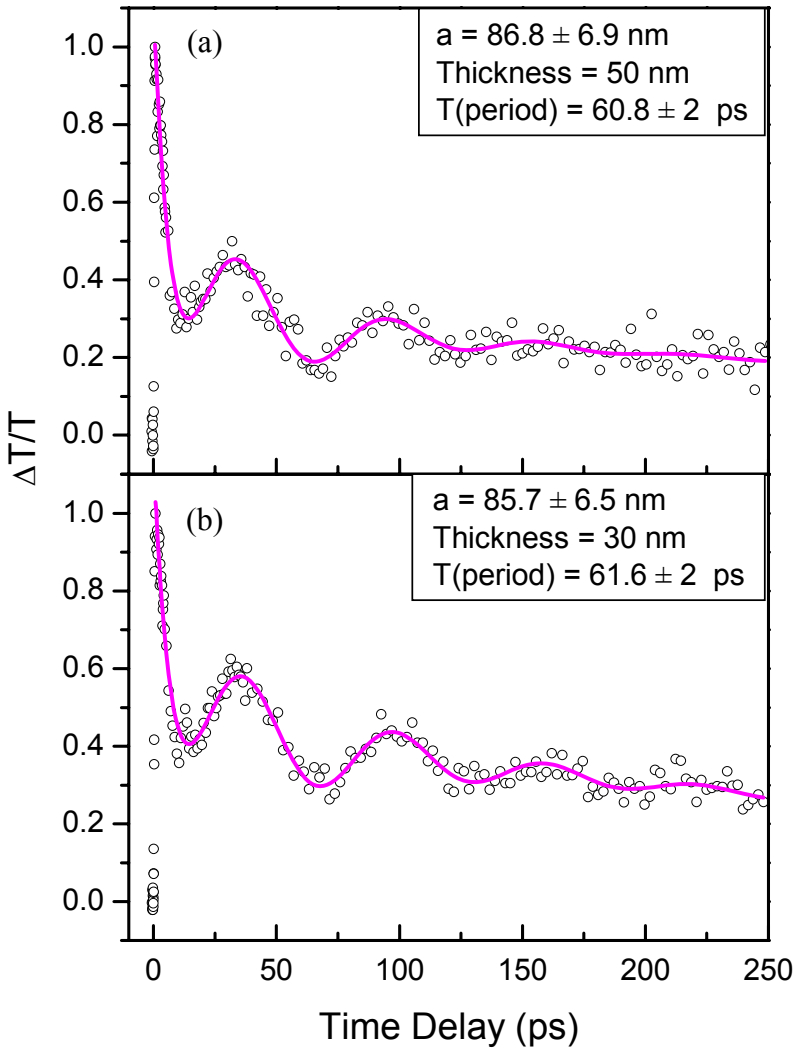

Figure 4-7: The thickness independence of the coherent phonon oscillation on (a) a 50 nm and (b) a 30 nm prismatic Au nanoparticle array (solid dots). The oscillation period was calculated by fitting the experimental data with a damped cosine function (solid line) plus two exponential decays to account for electron-phonon and phonon-phonon relaxation processes [57].

4.3.5 Monitoring Wavelength Dependence of the Observed Amplitude and Phase of the Coherent Phonon Oscillation:

Figure 4-8 shows the dependence of the observed oscillation amplitude and phase of the monitoring wavelength on the blue side of their surface plasmon absorption spectra for both the 104 and 166 nm nanoparticles. As the wavelength decreases below the maximum, the amplitude of the oscillation decreases, reaches zero then slowly increases again but with opposite phase. In order to understand this behavior and make use of it, we need to examine what determines the observed bleach intensity, $\Delta I_{\lambda,t}$.

In **Figure 4-8**, the percentage change in the transmission, $\Delta T/T$, is given by Eq. 2-1 in Chapter 2 (Section 2.6). The pump laser excites the surface plasmon electrons, creating an optical hole in its homogeneously broadened absorption, which increases the transmission intensity of the monitoring light with a profile that mimics the surface plasmon absorption spectrum. This phenomenon is due to a hole that is created by reducing the full absorption profile as the absorption is homogeneously broadened [27]. Very rapidly (in ~ 1 ps), electron phonon relaxation occurs [27], which heats up the lattice instantly. The transmission is reduced to the value observed at the beginning of the oscillation. The pulsed excitation of the lattice leaves it either in the extreme contracted or extreme expanded configuration of its phonon breathing mode (in addition to many other modes).

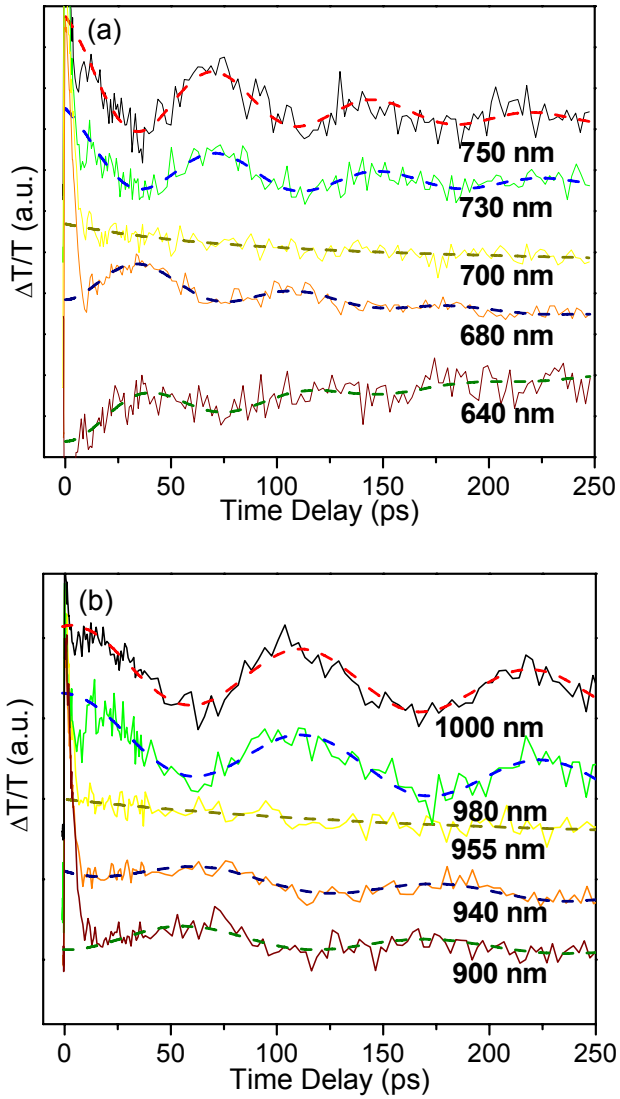

Figure 4-8: The wavelength dependence of the amplitude (the percentage transmission change of the monitoring light as a result of laser pump) and phase (the sign of the change) resulting from the coherent lattice phonon oscillation in a = 104 nm (a) and a = 166 nm (b) gold particle arrays. The observed oscillation is fitted to a damped cosine function (dash line). It is interesting to observe that as we decrease the monitoring wavelength of the bleach created by the 400 nm pump laser, the amplitude decreases, reaches zero value (i.e. the oscillation disappears), and then reappears with opposite sign (phase). From the wavelength at which the oscillation disappears, the absorption maximum, and its dependence on size, the change in the nanoparticle size during the oscillation is estimated.

As the electron phonon coupling creates an hot coherently vibration in the lattice, it oscillates between two configurations, the contracted and expanded forms, with the frequency of the symmetric breathing vibration mode. Thus at any time (t), the wavefunction of the system can be written as a linear combination of the two forms

$$\Psi_t = a_{con}(t)\psi_{con} + (1 - a_{con}^2)^{1/2}\psi_{exp} . \quad (4\text{-}2)$$

This wavefunction suggests that the absorption spectrum is oscillating between the absorption spectrum of the contracted configuration (*con*) and that of the expanded (stretched) configuration (*exp*), moving through the equilibrium configuration. This leads to changes in surface plasmon absorption spectra with the maxima at shorter wavelength for the contracted lattice and at longer wavelength for the expanded lattice, as compared to that of the equilibrium configuration of the nanoparticles.

Under our experimental conditions, the observed light intensity change in transmission (recorded in the femtosecond bleach experiment) is less than 1 %. It is equal to the change of the sample absorption upon laser excitation. The observed signal at a certain wavelength as a function of time thus results from the net absorption changes at this wavelength between a bleached equilibrium spectrum (induced by the pump laser) and the new oscillating absorption spectra of the two configurations. Thus the observed signal A, at a certain wavelength λ at time t is given by

$$A_{\lambda,t} = A_{\lambda,0} \exp(-t/\tau_d)\cos\omega t , \quad (4\text{-}3)$$

where

$$A_{\lambda,0} = (A_{\lambda,0,con} + A_{\lambda,0,exp})^{absorption} - A_{\lambda,0,eq}^{bleach} , \quad (4\text{-}4)$$

and $A_{\lambda,0}$ is the observed initial oscillation amplitude, *eq* represents the equilibrium ground state configuration. At the wavelength where the oscillation is not observed by the transient spectroscopic technique:

$$(A_{\lambda,0,con} + A_{\lambda,0,exp})^{absorption} - A_{\lambda,0,eq}^{bleach} = 0 . \quad (4\text{-}5)$$

To simulate the observed oscillation by monitoring light intensity changes, we draw the normalized Lorentzian type spectra for nanoparticles in the ground state (the Lorentzian fitted absorption spectrum) and that for the contracted and expanded form, each drawn with half the integrated intensity of the ground state configuration (**Figure 4-9**). The contracted and expanded spectra are placed relative to the ground state spectrum so that Eq. (4-5) is satisfied at the wavelength for which the observed intensity vanishes as shown in **Figure 4-8** (i.e. at λ = 700 nm and 955 nm for the 104 and 166 nm particles, respectively). Once we draw the three spectra relative to one another in this manner, we use Eq. (4-4) to calculate the non-vanishing intensities of the signal at $t = 0$ ($A_{\lambda,0}^{Cal}$) for other wavelengths and compare them with the observed ones ($A_{\lambda,0}^{Obs}$) (The observed initial intensities of the oscillations are determined by fitting the experimental oscillation traces in **Figure 4-8**). This is given in **Table 4.1**. **Table 4.1** shows a better fit for the 166 nm array nanoparticles than for the small 104 nm ones. This might be explained by the fact that the array of the largest particle has a narrow spectrum that could be fit very well to a Lorentzian line shape, including its "tail". The Lorentzian fitting could not be carried out at the spectrum tails of the two smallest array particles due to overlapping bands.

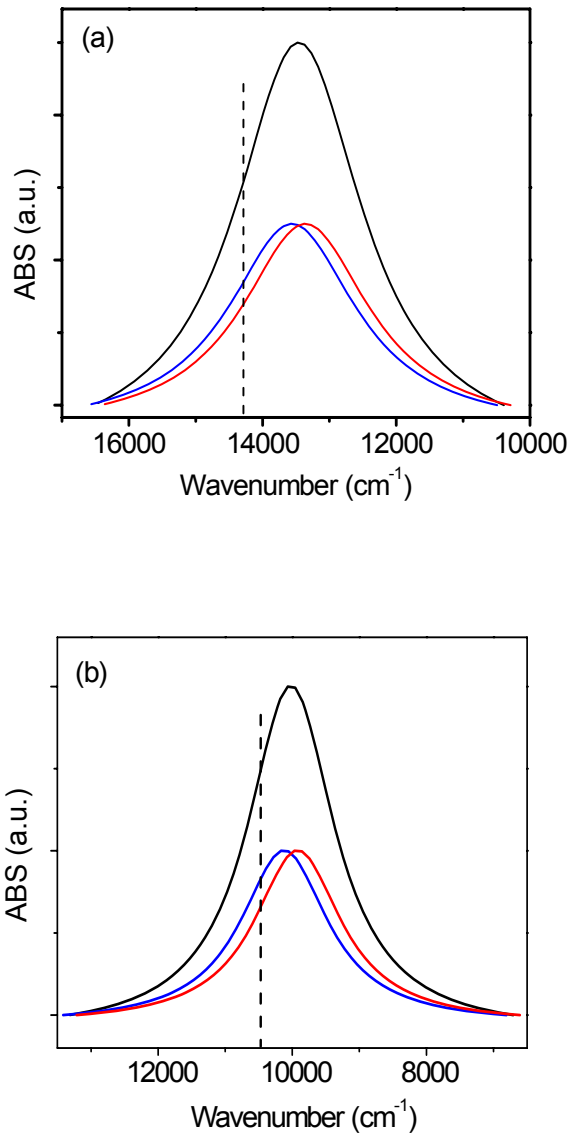

Figure 4-9: Estimation of the size change during lattice symmetric vibration. The black spectrum is the Lorentzian fit of the experimental absorption spectrum of the gold array sample of nanoparticle of size a = 104 (a) and 166 nm (b). The blue and the red spectra correspond to the assumed absorption spectra of the vibrating nanoparticle at its extreme contracting (blue) and its extreme expanding configuration (red), respectively (see text). Each of the colored spectra are drawn with the same band width but at half the integrated intensity of that of the observed non-vibrating nanoparticles (black spectrum). The energies of the maxima of the colored spectra are adjusted so that the difference between the sum of their intensity and that of the black spectra disappear at the observed wavelength (indicated by the dashed vertical lines) where the oscillation amplitude disappears.

In order to determine the percentage change in size due to the oscillation, we should apply this model to the array of the 166 nm particles for which the agreement with experiment is the best (**Table 4-1**). From **Figure 4-9b**, the surface plasmon absorption maximum of the contracted 166 nm nanoparticle is found to be 988 nm. From the dependence of the wavelength maximum on size (**Figure 4-3**), this corresponds to a size of 163.7 nm. From the size of the non-vibrating nanoparticles (166 nm), these correspond to a change of 2.3 nm. Then the change in size due to contraction from the vibration is 1.4 %.

Table 4-1: Comparison of the observed and calculated oscillation amplitude for the 104 and 166 nm array particles at different probe wavelengths.

	a = 104 nm			a = 166 nm	
λ (nm)	$A_{\lambda,0}^{Obs}$	$A_{\lambda,0}^{Cal}$	λ (nm)	$A_{\lambda,0}^{Obs}$	$A_{\lambda,0}^{Cal}$
750	-1	-1	1000	-1	-1
730	-0.65	-0.83	980	-0.85	-0.72
700	0	0	955	0	0
680	0.5	0.27	940	0.29	0.20
640	0.48	0.11	900	0.36	0.20

For spheres having a diameter of 24.2 nm, the change in size during the oscillation is found [7] to be ~ 0.4 %. This is one third of that observed for the prismatic nanoparticles. The tip of the prismatic shape is shown to give these particles large radiative probability, which induces a larger electronic oscillation and thus a larger transition dipole moment [58]. We thus believe that because of the tip, the bisector in a prismatic nanoparticle undergoes a larger percentage change in dimension during the

symmetric vibration than the diameter of a comparable sphere. This is also reflected in the observed larger dependence of the surface plasmon oscillation frequency on the size of prismatic nanoparticles compared to that of the spherical ones (see **Figure 4-3**).

4.4 Conclusion

We studied the ultrafast laser-induced coherent phonon oscillation in prismatic gold nanoparticles assembled in monolayer periodic arrays by using the nanosphere lithographic technique. We studied the effect of size, shape, and thickness of the prismatic array nanoparticles on the period of their coherent phonon oscillations. The amplitude and phase of the oscillation was also studied as we decreased the monitoring wavelength. At a certain wavelength, the oscillation could not be observed. As the monitoring wavelength decreases further, the sign of the amplitude changes. From the wavelength at which the oscillation is not detected, the dependence of the absorption maxima on the size of the nanoparticles, the changes in the nanoparticle size are estimated during its oscillation. This large change in the size of prismatic nanoparticles compared to the small change reported previously for nanosphere oscillations is discussed.

4.5 References

[1] Hodak, J. H.; Henglein, A.; Hartland, G. V., *J. Chem. Phys.* **1999,** 111, (18), 8613-8621.

[2] Del Fatti, N.; Voisin, C.; Chevy, F.; Vallee, F.; Flytzanis, C., *J. Chem. Phys.* **1999,** 110, (23), 11484-11487.

[3] Hodak, J. H.; Henglein, A.; Hartland, G. V., *J. Phys. Chem. B* **2000,** 104, (21), 5053-5055.

[4] Hodak, J. H.; Henglein, A.; Hartland, G. V., *J. Phys. Chem. B* **2000,** 104, (43), 9954-9965.

[5] Qian, W.; Lin, L.; Deng, Y. J.; Xia, Z. J.; Zou, Y. H.; Wong, G. K. L., *J. Appl. Phys.* **2000,** 87, (1), 612-614.

[6] Hartland, G. V.; Hu, M.; Wilson, O.; Mulvaney, P.; Sader, J. E., *J. Phys. Chem. B* **2002,** 106, (4), 743-747.

[7] Hartland, G. V., *J. Chem. Phys.* **2002,** 116, (18), 8048-8055.

[8] Hartland, G. V.; Hu, M.; Sader, J. E., *J. Phys. Chem. B* **2003,** 107, (30), 7472-7478.

[9] Huang, W. Y.; Qian, W.; El-Sayed, M. A., *Nano Lett.* **2004,** 4, (9), 1741-1747.

[10] Thomsen, C.; Strait, J.; Vardeny, Z.; Maris, H. J.; Tauc, J.; Hauser, J. J., *Phys. Rev. Lett.* **1984,** 53, (10), 989-992.

[11] Thoen, E. R.; Steinmeyer, G.; Langlois, P.; Ippen, E. P.; Tudury, G. E.; Cruz, C. H. B.; Barbosa, L. C.; Cesar, C. L., *Appl. Phys. Lett.* **1998,** 73, (15), 2149-2151.

[12] Krauss, T. D.; Wise, F. W., *Phys. Rev. Lett.* **1997,** 79, (25), 5102-5105.

[13] Cavalleri, A.; Siders, C. W.; Brown, F. L. H.; Leitner, D. M.; Toth, C.; Squier, J. A.; Barty, C. P. J.; Wilson, K. R.; Sokolowski-Tinten, K.; von Hoegen, M. H.; von der Linde, D.; Kammler, M., *Phys. Rev. Lett.* **2000,** 85, (3), 586-589.

[14] Lindenberg, A. M.; Kang, I.; Johnson, S. L.; Missalla, T.; Heimann, P. A.; Chang, Z.; Larsson, J.; Bucksbaum, P. H.; Kapteyn, H. C.; Padmore, H. A.; Lee, R. W.; Wark, J. S.; Falcone, R. W., *Phys. Rev. Lett.* **2000,** 84, (1), 111-114.

[15] Cao, J.; Hao, Z.; Park, H.; Tao, C.; Kau, D.; Blaszczyk, L., *Appl. Phys. Lett.* **2003,** 83, (5), 1044-1046.

[16] Park, H.; Wang, X.; Nie, S.; Clinite, R.; Cao, J., *Phys. Rev. B* **2005,** 72, (10).

[17] Park, H.; Wang, X.; Nie, S.; Clinite, R.; Cao, J., *Solid State Commun.* **2005,** 136, (9-10), 559-563.

[18] Lamb, H., *Proc. London Math. Soc.* **1882,** 13, 189.

[19] Bullen, K. E.; Bolt, B. A., *An introduction to the theory of seismology*. Cambridge: New York, **1985**.

[20] Hodak, J. H.; Martini, I.; Hartland, G. V., *J. Chem. Phys.* **1998,** 108, (22), 9210-9213.

[21] Perner, M.; Gresillon, S.; Marz, J.; von Plessen, G.; Feldmann, J.; Porstendorfer, J.; Berg, K. J.; Berg, G., *Phys. Rev. Lett.* **2000,** 85, (4), 792-795.

[22] Hu, M.; Wang, X.; Hartland, G. V.; Mulvaney, P.; Juste, J. P.; Sader, J. E., *J. Am. Chem. Soc.* **2003,** 125, (48), 14925-14933.

[23] Grant, C. D.; Schwartzberg, A. M.; Norman, T. J.; Zhang, J. Z., *J. Am. Chem. Soc.* **2003,** 125, (2), 549-553.

[24] Del Fatti, N.; Voisin, C.; Christofilos, D.; Vallee, F.; Flytzanis, C., *J. Phys. Chem. A* **2000,** 104, (18), 4321-4326.

[25] Sun, C. K.; Vallee, F.; Acioli, L. H.; Ippen, E. P.; Fujimoto, J. G., *Phys. Rev. B* **1994,** 50, (20), 15337-15348.

[26] Perner, M.; Bost, P.; Lemmer, U.; vonPlessen, G.; Feldmann, J.; Becker, U.; Mennig, M.; Schmitt, M.; Schmidt, H., *Phys. Rev. Lett.* **1997,** 78, (11), 2192-2195.

[27] Link, S.; El-Sayed, M. A., *J. Phys. Chem. B* **1999,** 103, (40), 8410-8426.

[28] Mohamed, M. B.; Ahmadi, T. S.; Link, S.; Braun, M.; El-Sayed, M. A., *Chem. Phys. Lett.* **2001,** 343, (1-2), 55-63.

[29] Link, S.; Hathcock, D. J.; Nikoobakht, B.; El-Sayed, M. A., *Adv. Mater.* **2003,** 15, (5), 393-396.

[30] Link, S.; Furube, A.; Mohamed, M. B.; Asahi, T.; Masuhara, H.; El-Sayed, M. A., *J. Phys. Chem. B* **2002,** 106, (5), 945-955.

[31] Link, S.; El-Sayed, M. A., *J. Chem. Phys.* **2001,** 114, (5), 2362-2368.

[32] Stepanov, A. L.; Hole, D. E.; Bukharaev, A. A.; Townsend, P. D.; Nurgazizov, N. I., *Appl. Surf. Sci.* **1998,** 136, (4), 298-305.

[33] Kaempfe, M.; Rainer, T.; Berg, K. J.; Seifert, G.; Graener, H., *Appl. Phys. Lett.* **1999,** 74, (9), 1200-1202.

[34] Bargheer, M.; Zhavoronkov, N.; Gritsai, Y.; Woo, J. C.; Kim, D. S.; Woerner, M.; Elsaesser, T., *Science* **2004,** 306, (5702), 1771-1773.

[35] Plech, A.; Kotaidis, V.; Gresillon, S.; Dahmen, C.; von Plessen, G., *Phys. Rev. B* **2004,** 70, (19), 195423.

[36] Henglein, A.; Meisel, D., *Langmuir* **1998,** 14, (26), 7392-7396.

[37] Henglein, A., *Langmuir* **1999,** 15, (20), 6738-6744.

[38] Borek, R.; Berg, K. J.; Berg, G., *Glass Sci. Technol.* **1998,** 71, (12), 352-359.

[39] Haynes, C. L.; Van Duyne, R. P., *J. Phys. Chem. B* **2001,** 105, (24), 5599-5611.

[40] Fischer, U. C.; Zingsheim, H. P., *J. Vac. Sci. Technol.* **1981,** 19, (4), 881-885.

[41] Deckman, H. W.; Dunsmuir, J. H., *J. Vac. Sci. Technol. B* **1983,** 1, (4), 1109-1112.

[42] Hulteen, J. C.; Van Duyne, R. P., *J. Vac. Sci. Technol. A* **1995,** 13, (3, Pt. 2), 1553-8.

[43] Jensen, T. R.; Malinsky, M. D.; Haynes, C. L.; Van Duyne, R. P., *J. Phys. Chem. B* **2000,** 104, (45), 10549-10556.

[44] Haynes, C. L.; McFarland, A. D.; Smith, M. T.; Hulteen, J. C.; Van Duyne, R. P., *J. Phys. Chem. B* **2002,** 106, (8), 1898-1902.

[45] Huang, Z. P.; Carnahan, D. L.; Rybczynski, J.; Giersig, M.; Sennett, M.; Wang, D. Z.; Wen, J. G.; Kempa, K.; Ren, Z. F., *Appl. Phys. Lett.* **2003,** 82, (3), 460-462.

[46] Kempa, K.; Kimball, B.; Rybczynski, J.; Huang, Z. P.; Wu, P. F.; Steeves, D.; Sennett, M.; Giersig, M.; Rao, D.; Carnahan, D. L.; Wang, D. Z.; Lao, J. Y.; Li, W. Z.; Ren, Z. F., *Nano Lett.* **2003,** 3, (1), 13-18.

[47] Wang, X.; Summers, C. J.; Wang, Z. L., *Nano Letters* **2004,** 4, (3), 423-426.

[48] Logunov, S. L.; Volkov, V. V.; Braun, M.; El-Sayed, M. A., *Proc. Natl. Acad. Sci. U. S. A.* **2001,** 98, (15), 8475-8479.

[49] Jensen, T. R.; Schatz, G. C.; Van Duyne, R. P., *Journal of Physical Chemistry B* **1999,** 103, (13), 2394-2401.

[50] Norrman, S.; Andersson, T.; Granqvist, C. G.; Hunderi, O., *Phys. Rev. B* **1978,** 18, (2), 674-695.

[51] Mohamed, M. B. Metallic and semiconductor nanoparticles : synthesis, characterization and femtosecond laser spectroscopic studies. Ph. D. Thesis, Georgia Institute of Technology, Atlanta, GA, **2002**.

[52] Jin, R. C.; Cao, Y. C.; Hao, E. C.; Metraux, G. S.; Schatz, G. C.; Mirkin, C. A., *Nature* **2003,** 425, (6957), 487-490.

[53] Sader, J. E.; Hartland, G. V.; Mulvaney, P., *J. Phys. Chem. B* **2002,** 106, (6), 1399-1402.

[54] *CRC Handbook of Chemistry and Physics, 80th ed.* Lide, David R., Ed.; CRC Press: Boca Raton, FL, **1999**.

[55] Jin, R. C.; Cao, Y. W.; Mirkin, C. A.; Kelly, K. L.; Schatz, G. C.; Zheng, J. G., *Science* **2001,** 294, (5548), 1901-1903.

[56] Huang, W.; Qian, W.; El-Sayed, M. A., *Proc. SPIE-Int. Soc. Opt. Eng.* **2005,** 5927, (Plasmonics: Metallic Nanostructures and Their Optical Properties III), 592701.

[57] Huang, W. Y.; Qian, W.; El-Sayed, M. A., *J. Phys. Chem. B* **2005,** 109, (40), 18881-18888.

[58] Kelly, K. L.; Coronado, E.; Zhao, L. L.; Schatz, G. C., *J. Phys. Chem. B* **2003,** 107, (3), 668-677.

CHAPTER 5

COHERENT PHONON OSCILLATIONS IN SILVER AND GOLD MONOLAYER PERIODIC NANOPRISM ARRAYS: THE EFFECT OF INTERPARTICLE INTERACTION

Abstract

We report on optically detected coherent lattice oscillations induced by femtosecond laser pulses in periodic monolayers of prismatic silver and gold nanoparticle arrays prepared by NSL. We find that while the oscillation periods in the Ag nanoprisms of different size agree with those calculated, the Au nanoprisms do not. Furthermore, for particles of comparable size, gold nanoparticles are found to have much longer oscillation periods. The SEM images of the two types of arrays have been determined and showed clearly that the sharp tips observed for the Au nanoprisms are rounded for the Ag nanoprisms. The different properties of the two types of nanoparticles are blamed fully or partially on the difference in the dipolar interparticle coupling present in the two types of particles. The difference in the sharpness of the tip could give rise to large difference in the electrostatic coupling between the particles. The effect of the partial surface oxidation of the Ag nanoparticles and the difference in the substrate-nanoparticle interaction could also contribute to the observed difference in the observed lattice oscillation characteristics. This work has been published in *J. Phys. Chem. B*, 2005, 109(40), 18881.

5.1 Introduction

The ultrafast laser-induced coherent lattice oscillations have been observed for noble metal nanoparticles of different shapes and also in different environments, such as spherical nanoparticles (silver nanoparticles in glass matrix [1] and gold nanoparticles in colloidal solution [2-4]), ellipsoidal silver nanoparticles in glass matrix [5], and cylindrical gold nanoparticles in colloidal solution [6,7]. However, the nanoparticles in all of these systems are randomly distributed in solution or in a matrix, in which interparticle interactions during the coherent phonon oscillations of nanoparticles are negligible. In order to study the coupling among nanoparticles, a system with well defined particle size, shape and interparticle seperation is required, which can be synthesized with lithographic technique such as NSL [8]. Lithographically synthesized 2D periodic nanostructures have been used for fundamental researches [9-15] on the coupling between the individual nanostructures. With the nanosphere lithography (NSL) technique [16], 2D nanoparticle arrays can be prepared in well defined size, shape and interparticle seperation. The sample prepared with NSL technique also has very narrow size distribution, which is a necessary condition to optically resolve the coherent lattice oscillations with large amplitudes.

In the present study, we found the measured period of the gold prismatic array nanoparticle is longer than the calculated one, while there is perfect match for silver nanoparticle. This period deviation for gold array nanoparticles can be explained by a considering interparticle coupling. A simple interparticle lattice oscillating dipolar coupling model of the dimer was proposed to qualitatively account for both the sign and

the dependence of the deviation on size. The absence of this deviation in the silver nanoparticle arrays was also discussed.

5.2 Experimental Section

The nanoparticle was fabricated on a quartz substrate using the second version NSL (Concentration Optimized Self-assembly). The experimental details are introduced in Chapter 2 (Section 2.1.2). The diameter of the polystyrene (PS) spheres used in our experiments was 0.26, 0.36, and 0.45 μm . The mask was then mounted in a thermal evaporator (Denton DV-502A) to deposit 30 nm thick silver or gold (99.999%, Alfa Aesar) in the voids between the spheres. The thickness of the deposited metal was monitored by a quartz crystal thickness monitor (Inficon). After deposition, the PS spheres were removed by sonication in absolute ethanol. The formed silver and gold prismatic monolayer nanoparticle arrays were checked by using Scanning electron microscopy (SEM).

A Beckman DU-650 spectrophotometer is used to record the absorption spectra of the arrays. The incident light is perpendicular to the array substrate. The transmitted light through the sample has a cross section of several square millimeters.

The detail of the femtosecond laser pump-probe experiment is described in Chapter 2 (Section 2.6).

5.3 Results and Discussion

5.3.1 SEM Images and Absorption Spectra of the Nanoparticle Arrays:

The SEM images in **Figure 5-1a-c** are the hexagonal patterned Ag prismatic periodic monolayer nanoparticle arrays that are produced with PS sphere masks. The same series of polystyrene sphere masks are also used to make Au prismatic nanoparticle arrays as shown in **Figure 5-1d-f**. The black spheres in **Figure 5-1** represent the positions of the etched PS spheres masks that are used during the metal deposition and are removed with sonication in ethanol after deposition. The size of the particle is represented by the bisector, ***a***, of the triangle. Based on more than 400 nanoparticles, the bisector of particles are measured to be 52.4 ± 4.2, 79.6 ± 6.4, and 99.3 ± 8.0 nm for the Ag array samples shown in **Figure 5-1a-c**, respectively. For Au array nanoparticles shown in **Figure 5-1d-f**, the bisector of the particles are 60.5 ± 5.7, 85.7 ± 6.5, and 103.7 ± 6.8 nm, respectively. In spite of the fact that the same three sizes of PS spheres are used (0.26, 0.36 and 0.45 μm spheres), the Ag array nanoparticles formed are smaller than the corresponding Au array nanoparticles. This is due to the more rounded tips of Ag array nanoparticles than those of Au array nanoparticles and will be discussed in the next Section). **Figure 5-1g** is a low magnification SEM image of the silver array sample made with 0.26 μm PS sphere mask, which shows a large area and thus can illustrate the very homogeneous nanoparticles that can be prepared by the NSL technique.

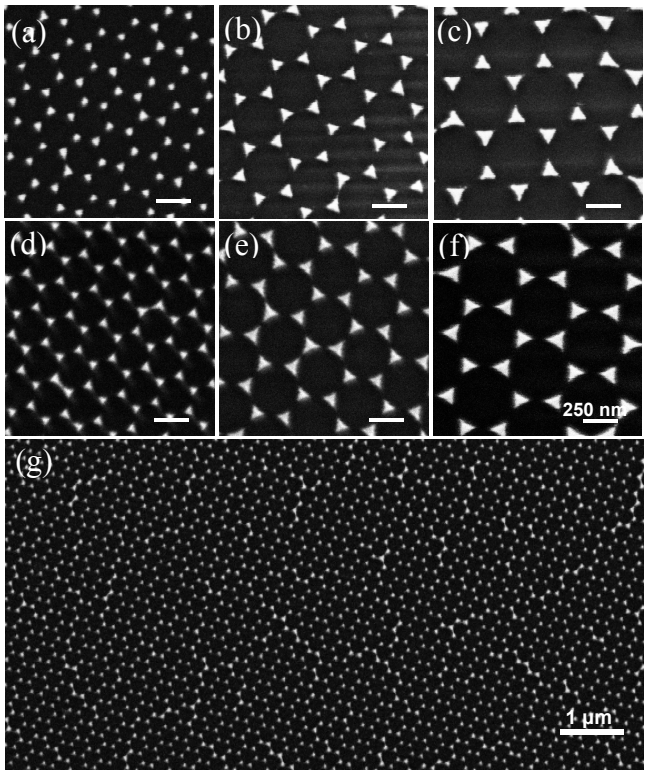

Figure 5-1: SEM images of the prismatic silver (a-c) and gold (d-f) nanoparticles monolayer arrays (in white color) made with nanosphere lithograph technique. The black spheres represent the positions of the PS spheres mask that is used during the Au deposition. The diameters of the PS spheres are 0.26 (a, d), 0.36 (b, e) and 0.45 μm (c, f), respectively. The deposition thickness is 30 nm. (g) Low magnification SEM image of a silver nanoparticles monolayer arrays made with 0.26 μm PS spheres mask. The scale bars in (a-f) represent 250 nm.

5.3.2 Silver Prisms Have More Rounded Tips:

Figure 5-2a-f show the large magnification of the SEM images of the silver (a, c and e) and gold (b, d, and f) nanoparticle arrays made from 0.45, 0.36 and 0.26 μm PS spheres as masks, respectively. The SEM images clearly show that the silver array nanoparticles have more rounded tips than gold nanoparticles and it is more obvious for smaller particles than larger ones.

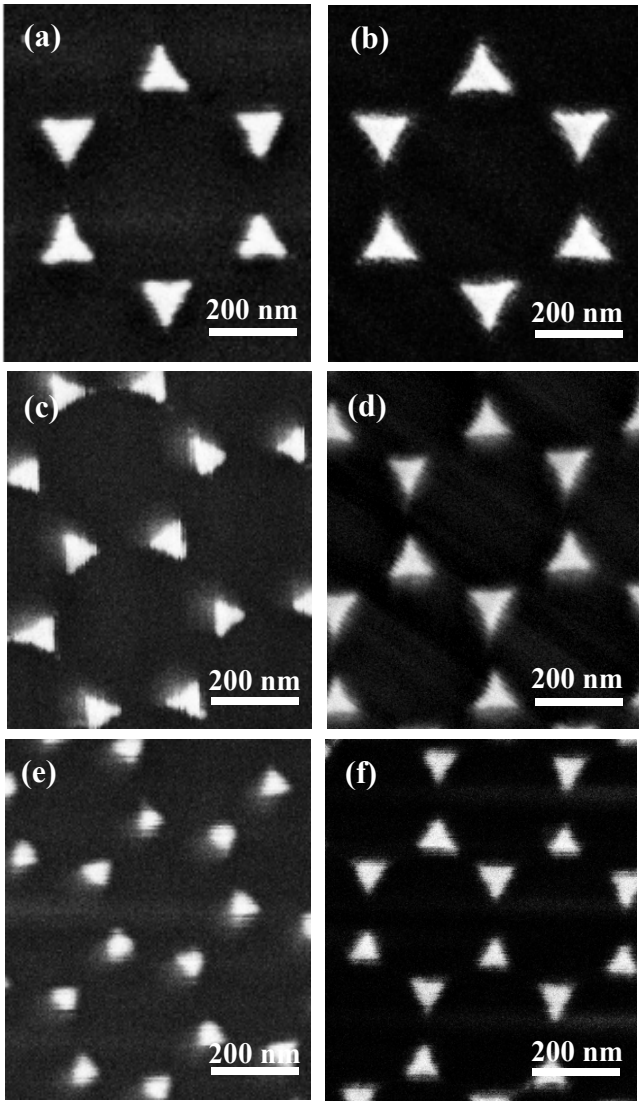

Figure 5-2: The high magnification SEM images of the prismatic silver (a,c,e) and gold(b,d,f) nanoparticles monolayer arrays made from 0.45 (a,b), 0.36 (c,d) and 0.26 (e,f) μm PS spheres masks. The tips of the prismatic silver nanoparticles are not as sharp as the gold nanoparticles.

The reason for the observed more rounded tips for the Ag prisms is its dewetting properties on quartz substrate and lower size-dependent surface melting temperature [17]. For a spherical nanoparticle with radius r, the size-dependent surface melting temperature T has the following relationship [18,19]:

$$\frac{T}{T_0} = 1 - \frac{2}{\rho_s L}\left[\frac{\gamma_{sl}}{r-\delta} + \frac{\gamma_l}{r}\left(1 - \frac{\rho_s}{\rho_l}\right)\right] \tag{5-1}$$

where T_0 is the bulk melting temperature, ρ_s (or ρ_l) is the solid (or liquid) density, L is the heat of fusion, γ_{sl} (or γ_l) is the surface tension of the solid-liquid interface (or liquid), and δ is the melting layer thickness. For Au and Ag, ρ_s is approximately equal to ρ_l, so Eq. (5-1) can be simplified to

$$\frac{T}{T_0} = 1 - \frac{2\gamma_{sl}}{\rho_s L(r-\delta)} \tag{5-2}$$

The tip of the prismatic array nanoparticles can be approximated as a hemisphere, so a sharp tip has a radius. **Figure 5-3** shows the dependence of the melting temperature on the radius of spherical nanoparticles for assumed solid-liquid interfacial tension γ_{sl} of 2 N m^{-1}. For silver and gold, L = 105 and 62.7 kJ kg^{-1}, respectively [17,19]. The bulk melting temperature (T_0) for silver and gold is 1235 K and 1338 K, respectively. δ is supposed to be 0.25r [17,20]. **Figure 5-3** clearly shows that the melting temperature is about 100 K lower for silver than gold spherical nanoparticles of the same radius. Since the melted tips of Ag array nanoparticles will retract due to its surface tension and dewetting properties on quartz substrate, the tips will be more rounded (forming hemispheres of larger radius r) for silver prismatic array nanoparticles than gold at the same temperature. The E-field enhancement (local charge density) is higher at the sharper tips due to the lightning-rod effect [21], which also suggests that gold prismatic array nanoparticles with sharper tips may have stronger surface enhancement than silver array nanoparticles and thus more attractive for applications in surface enhanced spectroscopy and environmental sensing.

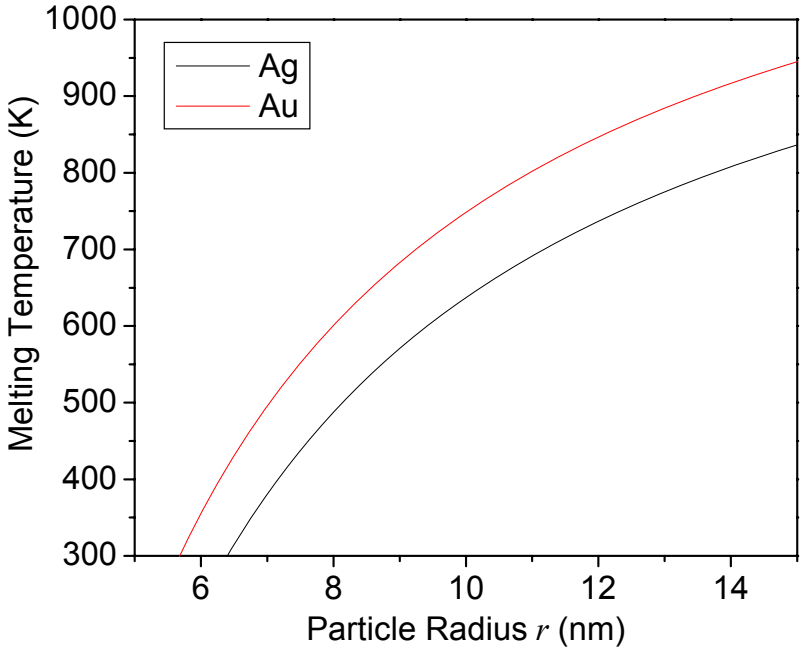

Figure 5-3: The dependence of the melting temperature on the radius of spherical gold and silver nanoparticles. The calculation is based on the solid-liquid interfacial tension $\gamma_{sl} = 2\ \mathrm{N\ m^{-1}}$ and the melting layer thickness $\delta = 0.25r$.

5.3.3 Absorption Spectra of the Nanoparticle Arrays:

Figure 5-4a shows the absorption spectra of the Ag periodic nanoparticle arrays made with the 0.26 (blue), 0.36 (green) and 0.45 μm (red) PS spheres shown in **Figure 5-1a-c**. As the size of the particle increases, the surface plasmon resonance absorption shifts to the lower energy side of the spectrum (red shift). The inset of **Figure 5-4a** shows the linear dependence of the plasmon absorption maximum on the size of the array nanoparticles. For silver prismatic array nanoparticles, the plasmon absorption maximum increases by 4.1 nm for every 1 nm increase in the bisector of the nanoparticles, i.e.

$\Delta\lambda_{max}/\Delta a = 4.1$. This number agrees very well with the study on silver array nanoparticles [22]. For Au nanoparticle arrays, the surface plasmon resonance absorption band is more red-shifted than the Ag array made with the same PS sphere masks (**Figure 5-4b**). The plasmon absorption maximum still has a linear dependence on the size of the Au array nanoparticles with $\Delta\lambda_{max}/\Delta a = 4.4$, which is larger than that for Ag array.

There are also weak absorption bands ranging from 390 to 420 nm for Ag arrays as the size of the nanoparticle increases. These weak absorption bands are also observed in Au prismatic array nanoparticles, while the weak absorption bands for Ag nanoparticles are higher in energy than for Au nanoparticles with absorption maxima located in the 530 – 600 nm region (**Figure 5-4b**). The weak absorption bands are assigned to the in-plane quadrupole resonance absorption from both experimental [23] and the discrete dipole approximation calculation [24] on silver prismatic nanoparticles. The strong absorption band results from the in-plane dipolar electronic surface plasmon transitions in the nanoparticles [23,24].

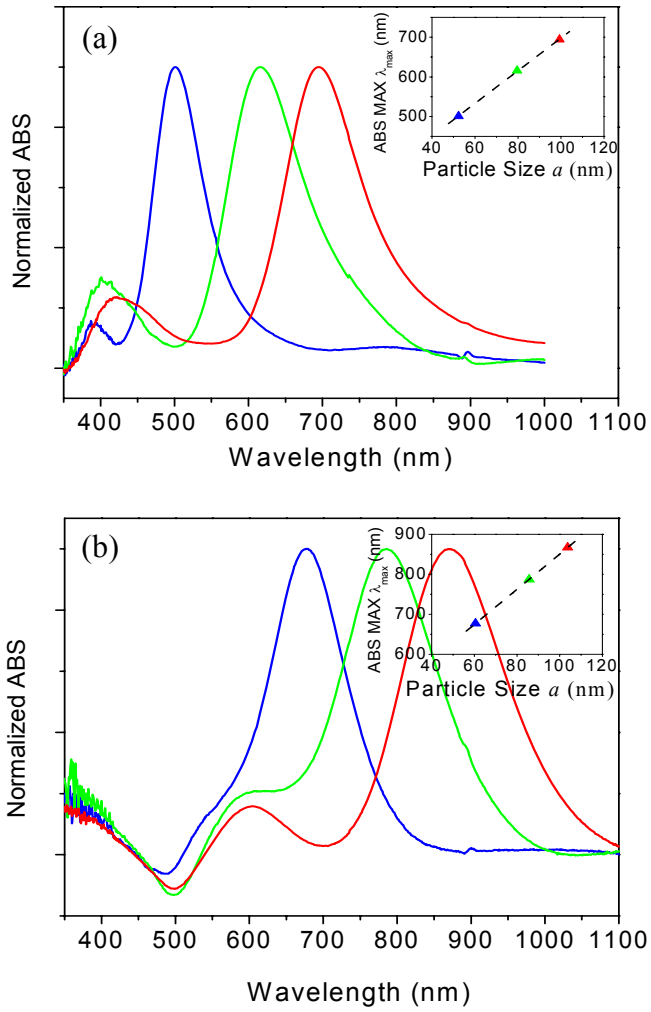

Figure 5-4: The absorption spectra of the silver (a) and gold (b) periodic array samples made with the 0.26 (blue spectrum), 0.36 (green spectrum) and 0.45 μm (red spectrum) PS spheres, respectively. The insets show the dependence of the wavelength maxima (λ_{max}) of the surface plasmon absorption spectra on the size of the silver or gold truncated tetrahedron (prismatic) array nanoparticles. The dash line is a linear fit of the values of the band wavelength maxima and the bisector values of the nanoparticles.

For the absorption spectrum of the silver array sample made with 0.26 μm PS spheres (blue spectrum in **Figure 5-4a**), there is also an ultra-weak absorption band around 790 nm, which could be due to some defects within the examined area (such as

two or more particles connected to each other). We have to point out that the defects on the array samples are unavoidable because of the size distribution of the PS spheres and stacking defects of the mask caused by misalignment of the PS spheres. However, those defects do not affect the coherent phonon oscillation results because of two facts. First, we observe the coherent phonon oscillation of the nanoparticle array by optically monitoring the periodic shift of the plasmon absorption of nanoparticles at a certain wavelength. The plasmon absorption of those defects is far away from our monitoring wavelength. Second, the surface plasmon absorption of the defects is ultra-weak compare to the major surface plasmon absorption band, which is unlikely to affect intensity changes at the monitoring wavelength due to the periodic shift of the major plasmon absorption of array nanoparticles.

5.3.4 Optically Detected Phonon Oscillations on Ag and Au Periodic Nanoparticle Arrays:

Figure 5-5a-c show the differential transmission $\Delta T/T$ of the monitoring laser at a wavelength near the strong surface plasmon absorption maxima of the different Ag nanoparticle arrays studied and shown in **Figure 5-1a-c** when excited with 400 nm femtosecond laser. All of the three signals show a fast increase due to the bleach of the electronic surface plasmon absorption upon femtosecond laser excitation. The decay of the signal fits two exponential decays with decay times of several picoseconds and several hundred picoseconds, respectively. In colloidal gold nanospheres and rods, the corresponding decays were attributed [25] to electron-phonon and phonon-phonon relaxation processes, respectively. A relatively strong modulation of the optical signal is

clearly observed during the second decay (the phonon-phonon relaxation process). We are able to detect these oscillations using a small number of the irradiated array nanoparticles (~10^5 particles within the laser focus point). This is due to three facts: (1) the strong absorption coefficient of the triangular nanoparticles [26], (2) the large sensitivity of the absorption spectrum to size ($\Delta\lambda_{max}/\Delta a = 4.4$) compared to spherical nanoparticles [27] ($\Delta\lambda_{max}/\Delta a = 0.64$), and (3) the very narrow size distribution of the nanoparticles in the arrays made with the NSL technique. The observed periods of coherent phonon oscillations for a nanoparticle array are almost independent of the monitored wavelength, which is undoubtedly due to the fact that the absorption spectra are homogeneously broadened (because of the narrow size distribution of the nanoparticles in the array samples).

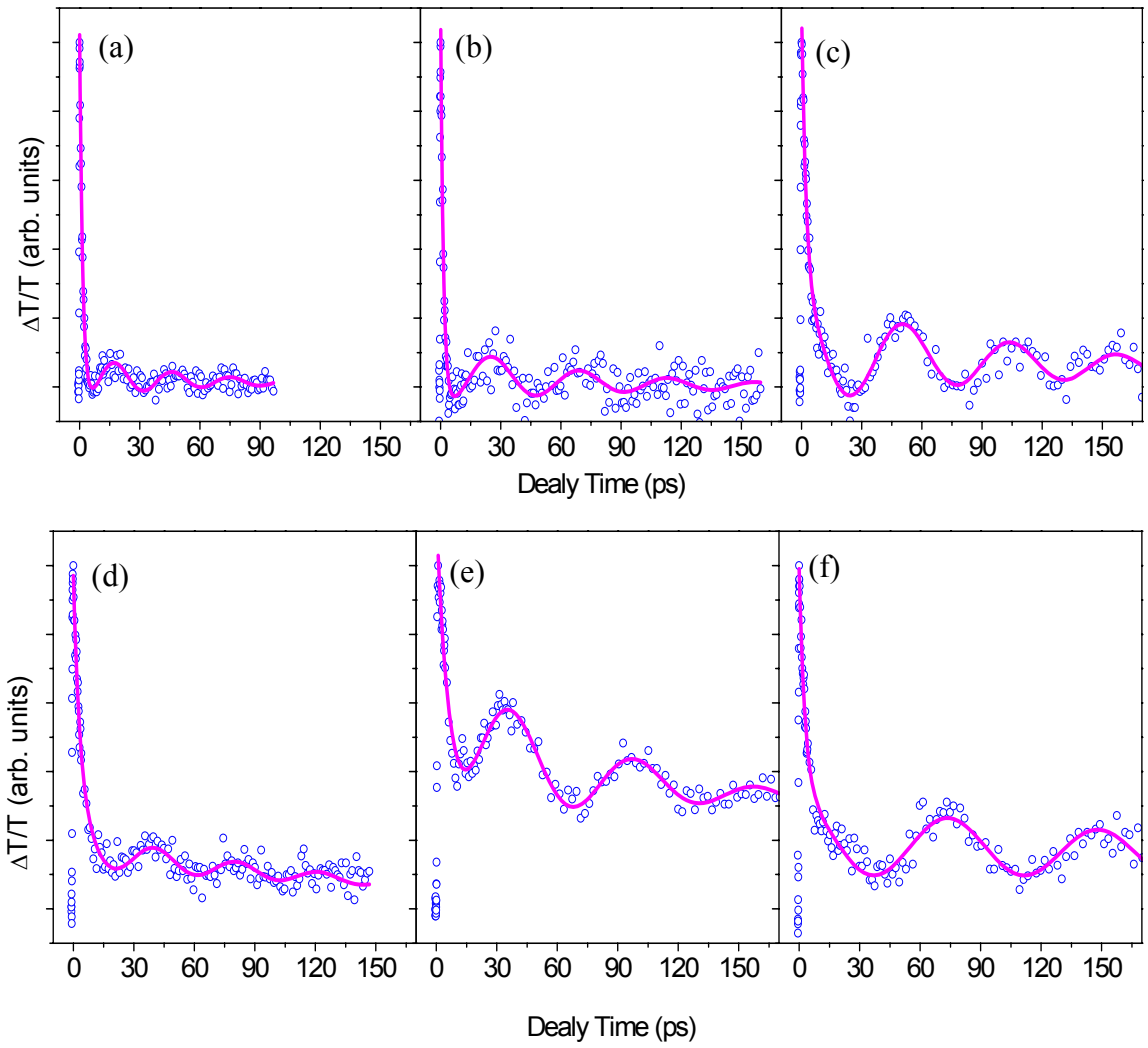

Figure 5-5: Optically detected lattice phonon oscillations induced in the prismatic Ag (a,b,c) and Au (d,e,f) nanoparticles monolayer arrays with a 100 fs laser pulse at 400 nm and monitored near the absorption maximum of each nanoparticle (solid dots). The size (bisector) of the silver nanoparticles is around (a) 52.4, (b) 79.6 and (c) 99.3 nm. The size of the Au nanoparticles is around (d) 60.5, (e) 85.7 and (f) 103.7 nm. The oscillation is fitted with a damped cosine function (solid line) plus two exponential decays (to account for the electron-phonon and phonon-phonon relaxation processes), from which the oscillation period is calculated. For easy comparison of the coherent phonon oscillation period, the delay time scale (x axis) is kept the same for all of the transient transmission traces.

The differential transmission ΔT/T signals of Au nanoparticle arrays show the same feature as Ag arrays but with longer coherent phonon oscillation periods as shown in **Figure 5-5d-f** compared with the corresponding Ag arrays made with same PS sphere masks in **Figure 5-5a-c**, respectively. Two reasons could account for the observed longer period in Au arrays than Ag arrays. One is that the Au array nanoparticles have relative larger size than Ag nanoparticles made with the same PS sphere masks (because the tips of the silver array nanoparticles are more rounded than gold nanoparticles, which will be discussed later). The other reason is that the longitude speed of sound in Au is lower than that in silver, which means the lattice vibration in Au is slower than that in Ag and thus a longer period of the coherent phonon oscillation is observed for Au nanoparticle arrays.

5.3.5 Linear Dependence of Coherent Phonon Oscillation Periods on Nanoparticle Sizes:

The experimental decays of the signals in **Figure 5-5** are fitted to two exponential decays plus a damped cosine modulation (solid line) in order to obtain the period of the coherent phonon oscillation. The period of the coherent phonon oscillation increases with the size of the arrays nanoparticles. **Figure 5-6a** and **b** are plots of the oscillation period vs. the nanoparticle size for Ag and Au nanoparticle arrays, respectively. For the period of Au array nanoparticles in **Figure 5-6b**, the first to the third points are from array nanoparticles of 30 nm thickness and the last two points are from the array nanoparticles of 50 nm thickness [27] (because thickness has minor effect on the coherent lattice oscillation period).

The period of the oscillation increases almost linearly with the size of the array particles. The vibration periods of single particle can be calculated accurately from the continuum elastic theory for both homogeneous [28,29] and core-shell spherical nanoparticles [30], while there is no such available model that can be used to describe the vibration mode of the prismatic nanoparticles studied here. Perner et al.[5] probed the aligned silver ellipsoid nanoparticles along the short (40 nm) and the long (100nm) axes and found the period to be 22 ps for the short axis and 52 ps for the long axis. This is very close to the calculated values of 23 ps and 56 ps for the short and long axes respectively, which is obtained by using the approximation that the vibration mode of the silver ellipsoids is a one-dimensional standing acoustic wave with free boundary conditions (with period $\tau = 2a/v_{l,}$ where a is the width or length of the silver ellipsoids and v_l is the longitude sound velocity in bulk silver). Using the same approximation, we calculate the periods for our array particles. For Ag nanoparticle arrays, the calculated linear dependence of oscillation period on size is shown by the dash line in **Figure 5-6a** ($\tau = 2a/v_{l,}$ where a is the bisector of the silver prismatic nanoparticles and v_l is the longitude sound velocity in bulk silver [31], $v_l = 3650$ m/s). For gold, the calculated size dependence is shown by the dashed line in **Figure 5-6b**, using the value of $v_l = 3240$ m/s [31] for gold.

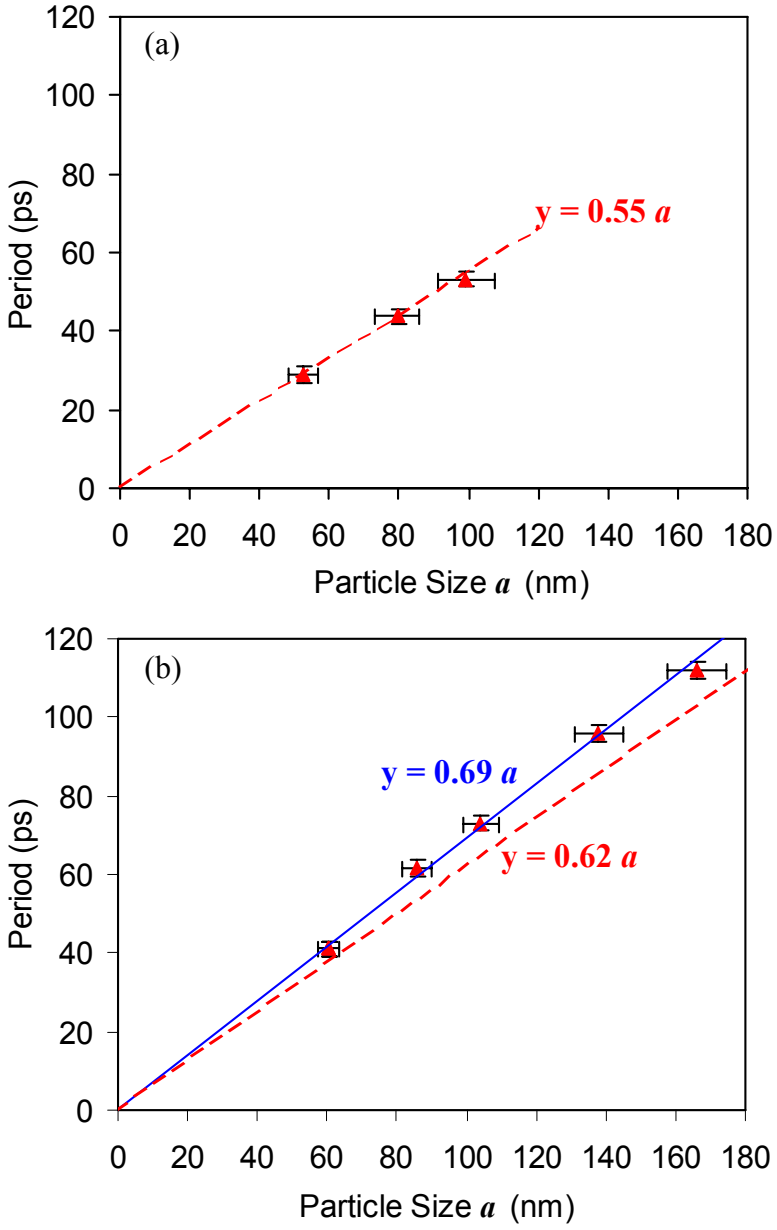

Figure 5-6: The coherent phonon oscillation period verses particle size for the prismatic silver (a) and gold (b) monolayer nanoparticle arrays. The dash line in (a) and (b) is the calculated linear relation between the period and the particle size (calculated from $\tau = 2a/v_l$, where v_l is the longitude sound velocity in bulk silver (or gold) and a is the particle bisector). The solid line in (b) is a linear fit of the experimental data. While the Ag results fit the calculated ones of the single nanoparticle dependence of the period on size, the gold results deviate and the deviation increase as the size of the particle becomes larger and larger. These observations can be explained by the simple dipole exciton model of coupling between the sharper prismatic gold nanoparticles in the array.

For Ag arrays, the observed agreement with the calculation means that the bisector of the sliver prismatic nanoparticles can be used as the characteristic parameter for the period of the observed coherent phonon oscillation in the Ag array nanoparticles. However, the observation is different for gold array nanoparticles produced with the same PS sphere masks, which shows that while the linear dependence still holds, the actual values are larger than those calculated. Furthermore, the deviation from the calculated value increases as the size of the gold nanoparticle increases. Below, we examine the inter-particle coupling between the array nanoparticles, in order to examine if it is a viable mechanism to explain this observed difference for gold and silver array nanoparticles.

5.3.6 A Simple Exciton Model:

The interaction between oscillating dipoles resulting from the oscillating lattice within the array is simplified to interaction between a pair of prismatic (triangular) nanoparticles with their vertices facing one another. This dimer structure is used previously as the unit cell by Van Duyne et al. [8] for the crystal structure of the monolayer assembly as shown in **Figure 5-7a**.

Assuming that the excited vibration state of the lattice in a monomer on the substrate has an energy E_m^* (the two monomers in a dimer are at infinite separation of one another), and wavefunction ψ_m^*. As the prisms approach one another, the two resulting exciton state wavefunctions are

$$\Psi^{\pm} = \frac{1}{\sqrt{2}}(\psi_{m1}^0 \psi_{m2}^* \pm \psi_{m1}^* \psi_{m2}^0), \tag{5-3}$$

and the resulting energies are

$$E^{\pm} = \left\langle \Psi^{\pm} \middle| H \middle| \Psi^{\pm} \right\rangle = \left\langle \Psi^{\pm} \middle| H_1^0 + H_2^0 + H_{12} \middle| \Psi^{\pm} \right\rangle = E_m^0 + E_m^* + D \pm I \,, \qquad (5\text{-}4)$$

where $D = \left\langle \psi_{m1}^* \psi_{m2}^0 \middle| H_{12} \middle| \psi_{m1}^* \psi_{m2}^0 \right\rangle$, is the interaction between an excited particle with its unexcited partner, and $I = \left\langle \psi_{m1}^* \psi_{m2}^0 \middle| H_{12} \middle| \psi_{m1}^0 \psi_{m2}^* \right\rangle$ is the energy exchange interaction term. The ground state wavefunction $\psi^0 = \psi_{m1}^0 \psi_{m2}^0$ and its energy $E^0 = E_{m1}^0 + E_{m2}^0 = 2E_m^0$.

The absorption of the dimer occurs at energy

$$\Delta E^{\pm} = E^{\pm} - E^0 = E_m^* - E_m^0 + D \pm I = \Delta E_m + D \pm I \,, \qquad (5\text{-}5)$$

The energy level scheme is given in **Figure 5-7b**. It is expected that as the size of the particle increases, the dipole of the excited monomer increases as well as the polarizability of the unexcited monomer. This suggests that the sign of *D* is negative (stabilization energy) and the absolute value of *D* increases as the size of the nanoparticles increases.

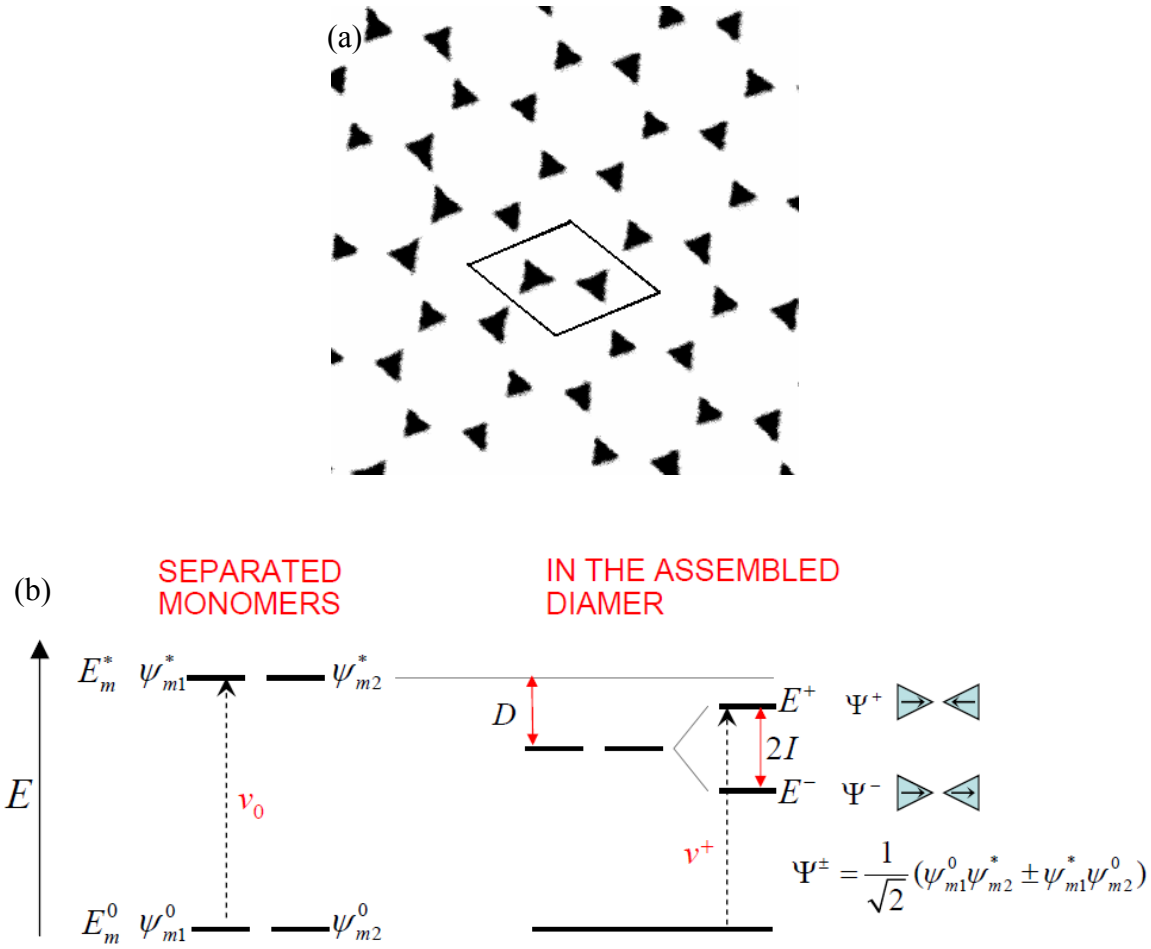

Figure 5-7: (a) The unit cell (in solid line) of the monolayer periodic nanoparticle arrays, which have two particles per unit cell. (b) The proposed coupling model for the nanoparticles of the array samples. The energy of the system will decrease first by *D* due to the interaction between an excited particle with its unexcited partner and split by 2*I* due to energy exchange term according to the exciton dipolar coupling model. This model is found to explain the deviation of the experimental lattice vibration period from theoretical calculation based on single particle.

The exchange energy term

$$\Delta E_{exch.} = E^+ - E^- = 2I = 2\left\langle \psi_{m1}^* \psi_{m2} \middle| H_{12} \middle| \psi_{m1} \psi_{m2}^* \right\rangle . \tag{5-6}$$

The value of this integral can be calculated in principle if a number of approximations are made. H_{12} is usually the repulsion between the electrons in the two prisms during the

oscillation. This can be expressed in a multipole expansion form. The dipole-dipole interaction term is usually assumed to be the dominant term. The question one can raise is whether or not a dipole moment will be induced by the symmetric lattice oscillation. A change in polarizability is expected during the symmetric lattice vibration of an *isolated* monomer, but not a dipole moment since this is a conductor. However, in a strongly coupled dimer, the tip of one monomer can induce a dipole moment in the other monomer which could be changed as the polarizability changes during the lattice oscillation. How small or how large is the induced dipole moment remains to be seen after a good calculation is made. Here we will assume that it is nonzero and see if this simple model can account qualitatively for the observed trends.

The exchange interaction energy is thus assumed to result from the interaction between the lattice oscillating induced dipoles, μ, placed along the center axis connecting their two bisectors. The split exciton levels would correspond to levels with energies corresponding to head to head (⊳⊲) and head to tail (⊳⊲) dipoles along the center axis connecting them. The latter is the most stable level and thus has the lowest energy (see **Figure 5-7b**). This oscillation will not produce a net change in the dimer volume, thus it will not be optically detected. However, this oscillation could be observed in microwave region since it has a nonvanishing dipole. Since the out-of-phase (head to head) oscillation (E^+) gives rise to a change in the dimer volume, it will cause a change in the surface plasmon spectrum, and thus will be optically detected in our experiment. Therefore,

$$2I = 2\frac{\mu^2}{\varepsilon R_{12}^3}, \qquad (5\text{-}7)$$

where R is the inter-nuclear distance, and μ is the lattice oscillation induced dipole. It is clear that as the particle size increases, μ increases and to a less extent R increases.

In this model, the deviation of the oscillation energy from that of the single particle oscillation equals to $D+I$. We experimental observe that the frequencies of the coherent phonon oscillation of gold array nanoparticles are lower than those calculated values, which means $D+I$ is a negative value ($D<0$ and $|D|>|I|$). We believe that $|D|$ is larger than $|I|$ for two reasons. First, $|I|$ depends on the dipole moment which is induced from the change in the polarizability during the lattice oscillation. $|D|$ results from an interaction that depends on the polarizability of the monomer. Secondly, $|I|$ depends not only on the dipole moment but is inversely proportional to the cube of the dimer separation. As the size of the prismatic particles increases, while μ increases, its separation also increases, and thus the effect of size changes on $|I|$ might not be as large as that on $|D|$. Thus, as the size increases, the polarizability increases and the Ψ^+ level is expected to decrease in energy since ($D + I$) is negative.

Assuming that the monomer oscillation frequency is given by $\nu_0 = \upsilon_l / 2a$, then the corrected frequency due to the above dimer type interparticle coupling become

$$\nu = \frac{\upsilon_l}{2a} + \frac{D+I}{h} \approx \frac{\upsilon_l}{2a} - \frac{|D|}{h} \tag{5-8}$$

Experimentally, ν is observed to depend linearly on $1/a$. Thus the term $(D+I)/h \approx D/h$ should depend on $1/a$. Since we can not calculate $|D|$, the above model only explains the fact that the deviation from the calculated single particle frequency has the correct sign, i.e. the observed frequency is smaller than the value calculated from single particle.

Furthermore, the deviation should increases as the size of the nanoparticle increase since the value of *D* increases with the size of the nanoparticle. The fact that no such deviation is observed for the Ag nanoparticle oscillation might support the proposal that the interparticle coupling between their oscillating lattices is not large. This could be due to more rounded tips as we discussed in Section 5.3.2. This might suggests that it is the electric field due to the sharp tips of prismatic array nanoparticles that induces the coupling between the dimer pair. Additional reason might be the partial oxidation of silver surface [32,33], which acts as a screen that can weaken the interaction between the silver array nanoparticles.

5.4 Conclusion

Using femtosecond transient spectroscopy, we studied the optically detected laser-induced coherent phonon oscillations of monolayers periodic arrays of prismatic shaped silver and gold nanoparticles assembled by using the technique of nanosphere lithography. In this method, the same size of polystyrene sphere and the same vacuum conditions were used. Under these circumstances, the gold nanoprisms formed were found to have sharper tips than the corresponding silver nanoprisms. For both gold and silver nanoparticles, the coherent lattice oscillation periods were found to linearly depend on the size of nanoparticles. However, while the observed dependence for silver nanoparticle was found to follow the calculated dependence of single particle on size (based on a one-dimensional standing wave model), gold nanoparticle deviated and the deviation was found to increase with the size of nanoparticles. This deviation can be explained by considering interparticle coupling. A simple interparticle lattice oscillating dipolar

coupling model of the dimer was proposed to qualitatively account for both the sign and the dependence of the deviation on size. The absence of this deviation in the silver nanoparticle arrays was blamed on the weak interparticle coupling due to their rounded tips and the possibility of the oxidation of their surfaces.

5.5 References

[1] Del Fatti, N.; Voisin, C.; Chevy, F.; Vallee, F.; Flytzanis, C., *J. Chem. Phys.* **1999,** 110, (23), 11484-11487.

[2] Hodak, J. H.; Martini, I.; Hartland, G. V., *J. Chem. Phys.* **1998,** 108, (22), 9210-9213.

[3] Hodak, J. H.; Henglein, A.; Hartland, G. V., *J. Chem. Phys.* **1999,** 111, (18), 8613-8621.

[4] Hartland, G. V., *J. Chem. Phys.* **2002,** 116, (18), 8048-8055.

[5] Perner, M.; Gresillon, S.; Marz, J.; von Plessen, G.; Feldmann, J.; Porstendorfer, J.; Berg, K. J.; Berg, G., *Phys. Rev. Lett.* **2000,** 85, (4), 792-795.

[6] Hartland, G. V.; Hu, M.; Wilson, O.; Mulvaney, P.; Sader, J. E., *J. Phys. Chem. B* **2002,** 106, (4), 743-747.

[7] Hu, M.; Wang, X.; Hartland, G. V.; Mulvaney, P.; Juste, J. P.; Sader, J. E., *J. Am. Chem. Soc.* **2003,** 125, (48), 14925-14933.

[8] Hulteen, J. C.; Van Duyne, R. P., *J. Vac. Sci. Technol. A* **1995,** 13, (3, Pt. 2), 1553-8.

[9] Heitmann, D.; Kotthaus, J. P., *Physics Today* **1993,** 46, (6), 56-63.

[10] Haynes, C. L.; McFarland, A. D.; Zhao, L. L.; Van Duyne, R. P.; Schatz, G. C.; Gunnarsson, L.; Prikulis, J.; Kasemo, B.; Kall, M., *J. Phys. Chem. B* **2003,** 107, (30), 7337-7342.

[11] Marlo, M.; Harju, A.; Nieminen, R. M., *Phys. Rev. Lett.* **2003,** 91, (18), 187401.

[12] Zou, S.; Janel, N.; Schatz, G. C., *J. Chem. Phys.* **2004,** 120, (23), 10871-10875.

[13] Krenn, J. R.; Dereux, A.; Weeber, J. C.; Bourillot, E.; Lacroute, Y.; Goudonnet, J. P.; Schider, G.; Gotschy, W.; Leitner, A.; Aussenegg, F. R.; Girard, C., *Phys. Rev. Lett.* **1999,** 82, (12), 2590-2593.

[14] Rechberger, W.; Hohenau, A.; Leitner, A.; Krenn, J. R.; Lamprecht, B.; Aussenegg, F. R., *Opt. Commun.* **2003,** 220, (1-3), 137-141.

[15] Zhao, L.; Kelly, K. L.; Schatz, G. C., *J. Phys. Chem. B* **2003,** 107, (30), 7343-7350.

[16] Haynes, C. L.; Van Duyne, R. P., *J. Phys. Chem. B* **2001,** 105, (24), 5599-5611.

[17] Hulteen, J. C.; Treichel, D. A.; Smith, M. T.; Duval, M. L.; Jensen, T. R.; Van Duyne, R. P., *J. Phys. Chem. B* **1999,** 103, (19), 3854-3863.

[18] Coombes, C. J., *J Phys. F: Met. Phys.* **1972,** 2, (3), 441-449.

[19] Buffat, P.; Borel, J. P., *Phys. Rev. A* **1976,** 13, (6), 2287-2298.

[20] Wang, Z. L.; Petroski, J. M.; Green, T. C.; El-Sayed, M. A., *J. Phys. Chem. B* **1998,** 102, (32), 6145-6151.

[21] Novotny, L.; Bian, R. X.; Xie, X. S., *Phys. Rev. Lett.* **1997,** 79, (4), 645-648.

[22] Jensen, T. R.; Malinsky, M. D.; Haynes, C. L.; Van Duyne, R. P., *J. Phys. Chem. B* **2000,** 104, (45), 10549-10556.

[23] Jin, R. C.; Cao, Y. C.; Hao, E. C.; Metraux, G. S.; Schatz, G. C.; Mirkin, C. A., *Nature* **2003,** 425, (6957), 487-490.

[24] Kelly, K. L.; Coronado, E.; Zhao, L. L.; Schatz, G. C., *J. Phys. Chem. B* **2003,** 107, (3), 668-677.

[25] Link, S.; El-Sayed, M. A., *J. Phys. Chem. B* **1999,** 103, (40), 8410-8426.

[26] Jensen, T. R.; Schatz, G. C.; Van Duyne, R. P., *J. Phys. Chem. B* **1999,** 103, (13), 2394-2401.

[27] Huang, W. Y.; Qian, W.; El-Sayed, M. A., *Nano Lett.* **2004,** 4, (9), 1741-1747.

[28] Lamb, H., *Proc. London Math. Soc.* **1882,** 13, 189.

[29] Bullen, K. E.; Bolt, B. A., *An introduction to the theory of seismology*. Cambridge: New York, 1985.

[30] Sader, J. E.; Hartland, G. V.; Mulvaney, P., *J. Phys. Chem. B* **2002,** 106, (6), 1399-1402.

[31] *CRC Handbook of Chemistry and Physics, 80th ed.* Lide, David R., Ed.; CRC Press: Boca Raton, FL, 1999.

[32] Cai, W. P.; Zhong, H. C.; Zhang, L. D., *J. Appl. Phys.* **1998,** 83, (3), 1705-1710.

[33] *Smithells Metals Reference Book, 6th ed.* Brandes, E. A., Ed.; London ; Boston : Butterworths, 1983.

[34] Hao, E.; Schatz, G. C., *J. Chem. Phys.* **2004,** 120, (1), 357-366.

[35] Jin, R. C.; Cao, Y. W.; Mirkin, C. A.; Kelly, K. L.; Schatz, G. C.; Zheng, J. G., *Science* **2001,** 294, (5548), 1901-1903.

CHAPTER 6

THE DISTANCE DEPENDENCE OF THE EFFECT OF SURFACE PLASMON FIELD ON THE COHERENT LATTICE PHONON OSCILLATION IN ELECTRON BEAM NANOFABRICATED GOLD PARTICLE PAIRS

Abstract

We measured the changes in the coherent phonon vibration frequency of gold nanodisk pairs as their inter-particle separation changes. Electron beam lithography was used to make nanoparticles having diameter of 88 nm each and separation that varies between 7 and 212 nm. Double beam femtosecond transient transmission spectroscopy was used to determine the coherent lattice phonon frequency (in the presence of the monitoring exciting plasmon field) as a function of the interparticle separation. It is found that the fractional change in the vibration frequency decreases exponentially with increasing the ratio of the interparticle separation to the particle diameter. We found that for the same set of nanoparticle pairs, the observed scaling exponential law governing the change in the coherent phonon frequency with distance is the same as that observed for the change in the surface plasmon electronic frequency with distance. They both have an exponential behavior with the same decay constant. This strongly suggests that it is the plasmonic field that changes both the electronic plasmon frequency as well as the coherent phonon frequency.

6.1 Introduction

In recent years, great interest has been directed to the effect of interparticle interaction on SPR band in self-assembled two dimensional superlattice [1,2], in electron beam lithographic (EBL) made nanodisk or prism [3-9], and by theoretical modeling [10-14]. The observed band shift of the surface plasmon resonance (SPR) upon changing the interparticle distance had been used as plasmonic biosensor [15] and dynamic molecular ruler [16-18]. One of the most attractive aspects of interacting noble metal nanoparticles is the ability that they can transfer light (SPR) below the diffraction limit of light [19]. The ability of electromagnetic wave transfer in the nanoparticles is due to the near-field coupling of SPR modes of neighboring nanoparticles. With collective excitation of a chain of Au nanoparticles, it was found that the plasmon coupling of particles can squeeze the optical near-field zone between the neighboring nanoparticles [3]. With localized excitation source and detector, the direct observation of the plasmon transfer is realized over 500 nm in closely spaced silver rods [20]. The plasmon waveguide is predicted to have low radiative loss during the energy transmission due to the near-field coupling mechanism [21,22]. The confinement of the squeezed optical near-field zone between the neighboring nanoparticles enhances the local electromagnetic field within the gap of nanoparticles, which lead to other attractive applications in many fields, such as single molecule traps [23], single molecular surface-enhanced Raman scattering (SERS) [24,25], and second-harmonic generation [26].

Due to the above superior merits of SPR coupling, extensive studies have been performed on the near-field SPR coupling between closely placed plasmonic nanoparticles to understand their interaction properties. The near-field interaction

between sphere-, disk-, and prism-shaped particle pair has been examined by several groups [5-8,17,27]. It is found that the shift of surface plasmon band decrease exponentially for nanosphere and nanodisk pairs as the gap between two pair nanoparticles increases [5,8,17]. If the relative shifts of surface plasmon band is plotted against the gap in unit of the particle diameter, an exponential decay curves is observed for nanoparticles of different sizes [5,8]. This scaling law is recently found to be valid for nanoparticle pairs of different size, shape, materials (gold and silver), and in different media [18]. To the best of our knowledge, all of these studies are focused on coherent electron property changes upon interparticle interaction and studied by using steady state spectroscopy. Here, we study the effect of coupling on the coherent phonon vibration in presence of plasmonic field of nanodisk pairs prepared with EBL and studied by ultrafast transient absorption spectroscopy.

The ultrafast laser-induced coherent phonon vibrations of noble metal nanoparticles have been optically detected in noble metal nanoparticles of different shapes and also in different environments [28-33]. However, the nanoparticles in all of these systems are randomly distributed in solution or in a matrix, in which the interparticle interactions during the coherent phonon vibrations are negligible. We first studied the coherent phonon vibrations in a two dimension periodic array prepared with nanosphere lithography [34]. Recently, the coupling effect on the coherent phonon vibration was discovered by our group in monolayer periodic gold nanoparticle arrays [35]. Pileni's group also studied the effect of coupling in self-assembled periodic f.c.c. arrangements of silver nanocrystals coated with dodecanethiol chains [36,37]. However, the effect of the interparticle separation between the coupled nanoparticles on the lattice

vibration has not been studied because the interparticle distance can not be changed systematically due to the limitation of the sample preparation method used. In the current report, we examine the effect of interparticle separation on the coherent phonon vibration coupling properties of pair nanoparticles in the presence of plasmonic field. The coherent lattice oscillation fractional frequency shift is found to decay with the separation scaled by the nanoparticle size with the same decay constant as that found previously for the surface plasmon oscillation. This strongly suggest that the observed frequency shift of the coherent lattice oscillation is due to the near-field interparticle coupling resulting from the surface plasmon fields induced by the monitoring light.

6.2 Experimental Section

The gold nanoparticle pairs are prepared on quartz slides by electron-beam lithography (EBL) using a JEOL JBX-9300FS 100kV EBL system in the Microelectronics Research Center (MiRC) at Georgia Institute of Technology. Quartz slides (Technical Glass Products, Inc.) are cleaned in piranha solution (3:1 H_2SO_4:30% H_2O_2) at 80 ^oC for 1.5 h and dried in air. The cleaned quartz slide is spin coated with 65 nm PMMA 950k electron-sensitive resist and cured at 180 ^oC for 3 minutes. The slide is mounted in a thermal evaporator and coated with 10 nm gold, making the substrate conductive. After pattern writing, the gold film is etched in gold etchant GE-8148 (an aqueous solution of KI and I_2). The pattern is developed in 1:3 MIBK:IPA (Methyl Isobutyl Ketone:Isopropyl Alcohol) solvent for 180 s, followed by washing in IPA for 30 seconds and drying in pure N_2. The substrate was mounted in an electron beam evaporator to deposit a thin Cr layer (~ 0.4 nm), which increases the Au nanoparticle

adhesion to the quartz substrate, followed by a deposition of 25 nm Au with a deposition rate of 0.5 $\mathring{A}$/s . We perform the lift-off step in hot acetone (~ 63 ^{o}C) to remove the resist and the metal film on top of it.

The polarized micro-absorption spectrum was taken by a SEE 1100 Micro-spectrometer in the transmission mode and the examined area was 8×8 μm^2 with a $20\times$ objective lens.

The coherent lattice oscillation period was determined OPTICALLY. A frequency-doubled Nd:Vanadate laser (Coherent Verdi) is used as the pump for the Ti:Sapphire laser system (Clark MXR CPA 1000). This generates laser pulses of 100 fs duration (fwhm) with energy of 1 mJ at 800 nm at a repetition rate of 1 kHz. The second harmonic of the 800 nm fundamental at 400 nm is used as the excitation (pump) source. The pump beam is mechanically chopped with a light beam chopper (HMS 221) at 500 Hz. The diameter of the laser focus spot on the sample is 250 μm. The laser pump pulse energy used in our experiment is reduced to less than 200 nJ with neutral density filters. A white-light continuum probe is generated by focusing a small portion (4%) of the 800 nm fundamental beam of the Ti:Sapphire laser onto a 1 mm sapphire plate. The differential transmission signal $S(t)$ is recorded with a pair of silicon photodiodes (Thorlab) and a lock-in amplifier (Stanford Research Systems). The recorded signal $S(t)$ can be expressed as

$$S(\lambda,t)=\frac{\Delta T}{T}=\frac{I_{\lambda,t}-I_{\lambda,0}}{I_{\lambda,0}},$$

where $\Delta T/T$ is the % change in the transmission of the probe (monitoring) light, $I_{\lambda,t}$ is the intensity of the probe light at wavelength λ after a delay time t from the pump laser

pulse, and $I_{\lambda,0}$ is the intensity of the probe light at λ without the pump. λ is selected to be within the surface plasmon absorption band. As a result, the recorded signal represents a transient bleach when $S(\lambda,t)$ is larger than zero. It should be mentioned that the measurement of the coherent lattice vibration is carried out when the disks are exposed to the monitoring white light, which is capable of exciting their surface plasmon resonance. Phenomenologically, the experiment can be visualized as initiating the coherent lattice oscillation with the pump beam in presence of a continuous monitoring light at λ within the surface plasmon absorption and measuring $S(\lambda,t)$ at different time after the pump pulse excitation.

6.3 Results and Discussion

6.3.1 SEM Images and Absorption Spectra of the Nanodisk pair Arrays:

A set of gold nanoparticle pairs with 88 nm diameter disks and several different interparticle distances are fabricated for the experiment. The size and the shape are almost the same for all nanodisks; thus, their effects can be excluded from both the absorption and the coherent phonon vibration measurements. Extensive care is brought to the preparation of sub 10 nm separation of nanodisks within each pair. We try to get a gap as small as 2 nm. However, as shown in **Figure 6-1a**, it is very difficult to control such a small gap and two nanodisks in some pairs are connected (indicated by red arrows in **Figure 6-1a**). The smallest gap of the nanodisk pair array without touching is around 7 nm as shown in **Figure 6-1b**. **Figure 6-1c-f** show the representative SEM images of the samples used in the experiments with diameter of 88 nm and the gaps are 12 nm, 17 nm,

27 nm, and 212 nm, respectively. The inserts in **Figure 6-1a-e** are the magnified nanodisk pair to clearly show the increase in the gap between the two nanodisks in the dimer pairs and in **Figure 6-1a** it also shows that at 2 nm gap some of the two nanodisks interconnect.

Polarized micro-absorption spectroscopy is used to characterize optical properties of the nanodisk pairs for demonstrating the effect of near-field coupling on the width and frequency of SPR. The experiments have been done with two configurations, in which the polarization of the incident light is parallel or perpendicular to the axis connecting the centers of the two nanodisks in a pair (also called long axis of the nanodisk pair). For the two configurations of the incident light polarization, we observed different behavior with changing the gap between the two nanodisks. The parallel and perpendicular polarized micro-absorption spectra are shown in **Figure 6-2a** and **b**, respectively. With the incident light parallel to the long axis of the nanodisk pair, the plasmon band blue shift from 608 to 571 nm as the gap increasing from 7 nm to 27 nm (shown in **Figure 6-2a**). We also notice that the plasmon band shift 32 nm as the gap increasing from 7 to 17 nm, while it only shift 4 nm as the gap increasing from 17 to 27 nm. The absolute shift of the plasmon band decrease dramatically as the gap increase linearly, which indicate the interaction strength between the nanodisk pair will decrease exponentially with increase of the gap [8].

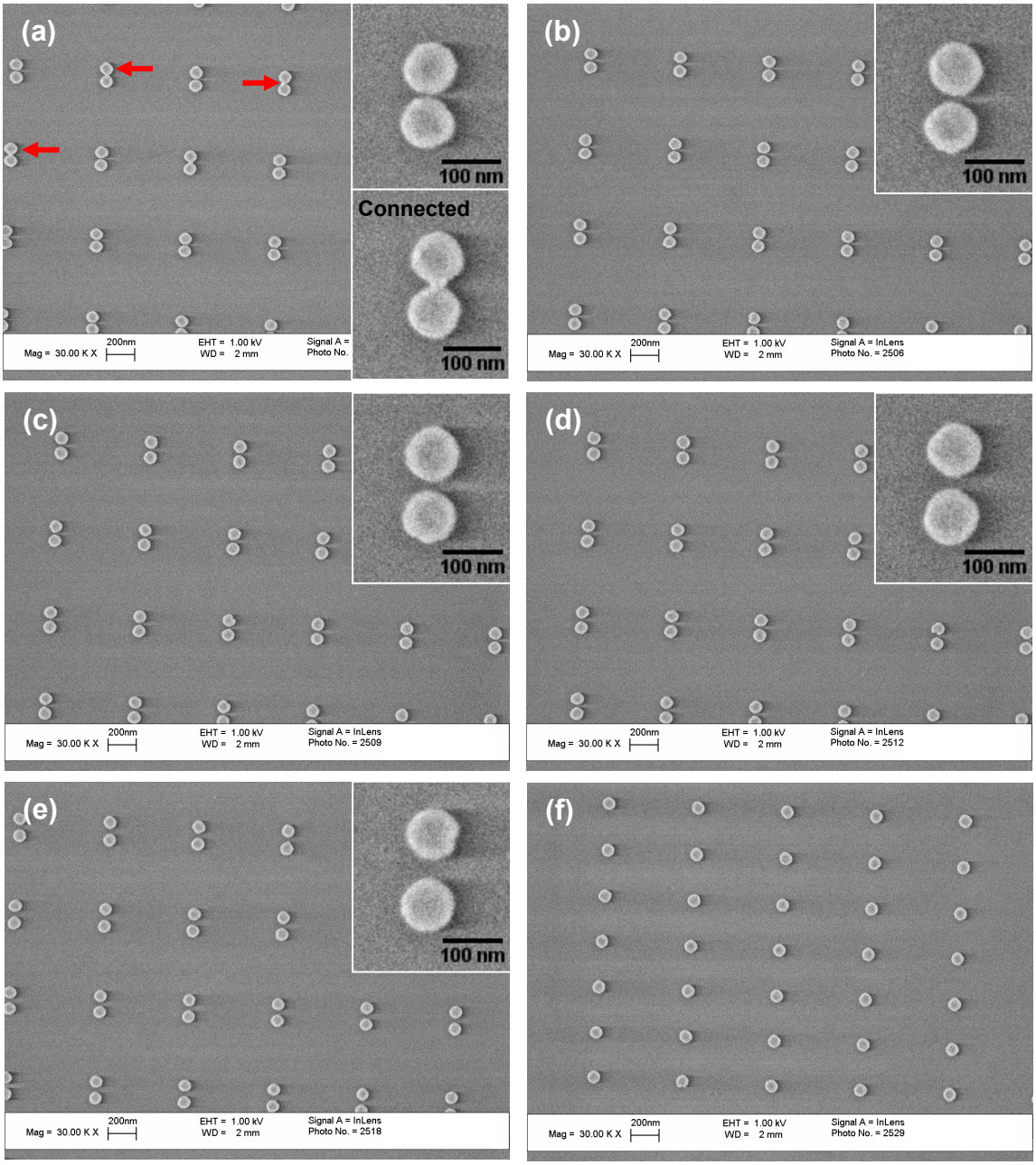

Figure 6-1: SEM images of the different nanodisk pairs used in the present study, having gaps of (a) 2 nm (b) 7 nm, (c) 12 nm, (d) 17 nm, (e) 27, and (f) 212 nm. The inserts in (a-e) are the magnified nanodisk pair to clearly show the increase in the gap between the two nanodisks in the dimer pairs and in (a) it also shows that at 2 nm gap some of the two nanodisks interconnect. The diameter of each nanodisk is 88 nm and the thickness of each nanodisk is 25 nm.

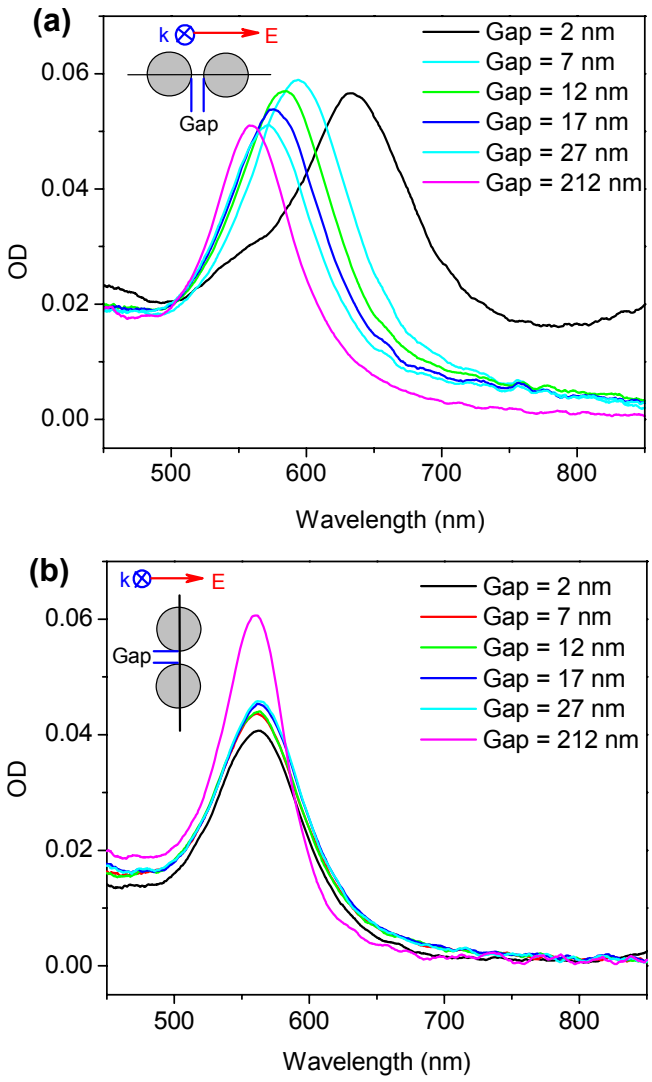

Figure 6-2: The absorption spectra of the nanodisk pairs as a function of decreasing the interparticle separation with the incident light polarized (a) parallel and (b) perpendicular to the axis connecting the centers of two nanodisks in a pair. Red shifts are observed with decreasing interparticle distance for the light polarized parallel to the connecting axis but a slight blue shift is observed when the polarization of the light is perpendicular to the connecting axis. This difference was recently explained by simple dipole or exciton picture [38].

We observe a totally different behavior when the incident light is perpendicular to the long axis of the nanodisk pair. When the gap is small (from 7 nm to 27 nm), the maximum of the plasmon absorption red shift from 561 to 563 nm as the gap increase from 7 nm to 27 nm, which is exactly reverse the blue shift trend of parallel geometry [4]. This small red shift suggests that very weak dipole coupling exists when the excited electronic dipole are in shoulder to shoulder configuration. We also observe a slightly increase in the intensity of the plasmon band. The intensity of the plasmon absorption band increase dramatically as the gap increase to 212 nm. The maximum of the band located at 560 nm, which slightly blue shift (~ 1 nm) than the nanodisk pair with small gap. The band also becomes sharper. The width at half maximum of the plasmon band decrease from 2005 cm^{-1} to 1715 cm^{-1}. The decrease in the band width of the surface plasmon absorption can be attributed to the diffractively coupling in one or two dimensional array of cylindrical nanoparticles predict and observed by Schatz and Van Duyne's group [11,12].

6.3.2 Observation of Coherent Phonon Coupling:

For the coherent phonon vibration experiment, we did not use the nanodisk pair with 2 nm gap because the connected nanodisk pair will change the surface plasmon absorption dramatically. As shown in Figure2a, the absorption spectrum of 2 nm gap show three bands, a weak shoulder peak around 550 nm, a strong peak around 635 nm, and a peak beyond 850 nm. The 635 nm peak represents the nanodisk pair of 2 nm gap. The 550 and the beyond 850 nm peaks are the quadrupole and the dipole absorption of connected nanodisks [8]. For the 2 nm gap nanodisk pairs, the effect of inter-particle

coupling on the coherent phonon vibration can not be investigate clearly because we do not know if the observed difference in vibration period is come from coupled nanodisk pairs or from connected nanodisk pairs. Therefore, we do the coherent phonon vibration study from the gap of 7 nm and above to get a clear picture of the effect of coupling on the properties of coherent phonon vibration of the gold nanodisk pair.

Coherent phonon vibrations have been excited and detected in all the nanodisk pair samples of different gaps with the polarization of the laser light parallel to the long axis of the nanodisk pair (**Figure 6-3**). We find in **Figure 6-3** that when the dimmer structures are formed, the vibration periods highly depend on the gap sizes of nanodisk pairs. With gap distances of 7 nm, 12 nm, 17 nm, 27 nm, and 212 nm, the corresponding vibration periods obtained from transient absorption experiments are 78.1 ps, 68.3 ps, 63.4 ps, 57.6 ps and 52.8 ps, respectively. As increasing the gap distance, there is an exponential decrease in the vibration period, which demonstrates the near-field nature of the coherent phonon coupling. For 212 nm gap, it is reasonable to think that there is no coupling effect and the vibration period (52.8 ps) is come from a single nanodisk.

The one-dimensional acoustic wave model [31] has been extensively used to precisely calculate the vibration period of isolated nonspherical metal nanoparticles, such as nanoprism on the surface of quartz substrates [35] or in colloidal solution [39], and ellipsoid-shaped nanoparticle embedded in glass matrix [31]. Unlike the coherent electronic vibration (the SPR) that is sensitive to the embedded environment, the period (or frequency) of the coherent phonon vibration is independent of the dielectric constant of media. The insensitivity of the phonon vibration period is quite reasonable since the period is decided by the internal lattice interaction of the nanoparticle based on the elastic

continuum model [31,40-42]. For Au nanodisks with 88 nm diameter, the model gives a period of 53.7 ps ($T = 2d/v_l$, v_l = 3240 m/s for bulk gold). The measured vibration period of 52.8 ps is very close to the theoretical calculated period for isolate nanodisk and confirms again the general validity of the one-dimensional acoustic wave model [31].

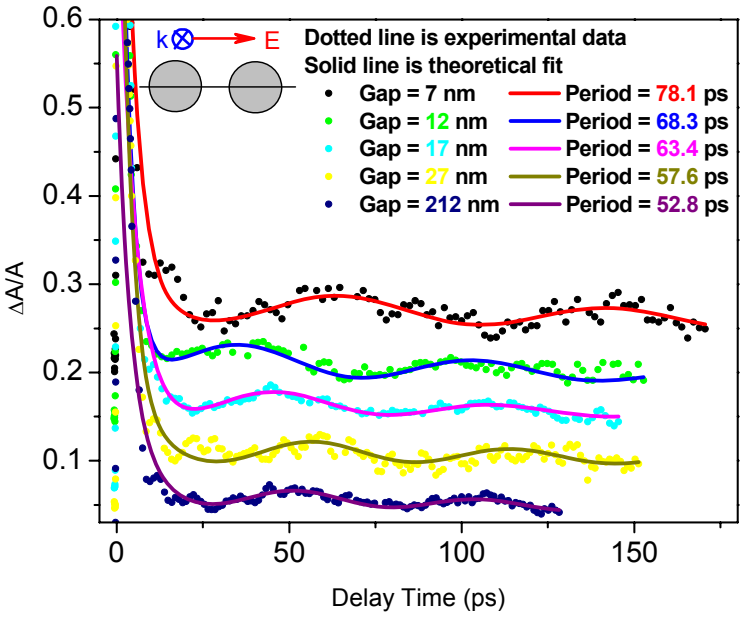

Figure 6-3: The optically detected coherent phonon vibration signal for gold nanodisk pairs of different interparticle separations (gaps) when the exciting and monitoring lights are parallel to the axis connecting the centers of two nanodisks in a pair. For the smallest gap (7 nm), the vibration period is 78.1 ps. As we increase the gap between the two nanodisks within the pairs, we observe that the vibration period decreases. For the pairs with an interparticle separation of 212 nm, we observe a vibration period of 52.8 ps, which is very close to the theoretically calculated period ($2d/v_l$ = 53.7 ps) for a single nanoparticle without coupling to its neighbors.

6.3.3 Coupling Mechanisms:

The increase in the coherence could be attributed to one of the following two reasons. One is the coupling of their motion through the medium. Since the nanoparticles are deposited on the surface of a quartz substrate, the quartz substrate can transfer the acoustic vibration between the two close placed pair nanodisks. This causes the vibration of each nanodisk to be correlated with the vibration of its pair partner. However, this is unlikely in the present nanodisk pair system. We studied a similar system [35] which have hexagonal patterned arrays of gold or silver nanoprisms formed on quartz substrates. We found the measured vibration period in gold nanoprism arrays is longer than the theoretically calculated period from the uncoupled gold nanoprism, while the measured period in silver nanoparticle arrays is the same as the theoretical calculated period from uncoupled silver nanoprism. If the increase in the vibration period is build up through the substrate, we should observe the increase of periods in both gold and silver nanoparticle arrays (assuming the similar nanoparticle substrate interaction). We did not observe the same effect in the gold and silver nanoprism arrays which indicate the interaction through the substrate is not sufficient to increase the vibration period of the array nanoparticle. In a Raman experiment on f.c.c. supracrystals of silver nanocrystals [36], Pileni and co-workers also found that the coupling of silver nanocrystals through the van der Waals force of the dodecanethiol chains to its surrounding silver nanocrystals is not sufficient to change the vibration frequency of the silver nanocrystals.

Another possible explanation of the increase in the coherent lattice vibration period in the nanodisk pair could be attributed to the electric field induced in each nanodisk by the excited strong surface plasmon dipole of its pair partner. It is known

from many experimental [3-9] and theoretical [10-14] studies that the electronic excitation of metal nanoparticles with large polarizability induces an enhanced electrical field extending up to several tens nanometers away from the nanoparticle surface. This surface enhanced electrical field will affect the lattice vibration in the nearby metal nanoparticle. This effect is similar to the electronic softening of the crystal lattice, which has been found in semiconductor crystals and is used to explain the decrease in the coherent phonon vibration frequency with increasing the photoexcited carrier density [43]. This induced electric field was also used by Pileni and co-workers to explain the Raman peak shift of self-organized silver nanocrystals in f.c.c. supra-crystals [36]. In the Raman experiment, the induced electric field in the nanocrystal by the excited strong surface plasmon dipole of its neighbors is always presented during its vibration. In our experiment, the lattice vibration is observed optically by use of another pulse in resonance with the surface plasmon absorption. Thus the observed vibration is determined in the plasmon fields induced by the monitoring laser pulse.

Analogues to the electromagnetic interaction between coherent electronic vibrations [4], the increase in the period of coherent phonon oscillation for the two closely placed nanodisks via monitoring light induced surface plasmon field is shown in **Figure 6-4**. When two nanodisks are placed very close to each other, the presence of the monitoring light induced surface plasmon field splits the phonon vibration energy of the nanoparticle pair into two levels, corresponding to the energy of the in-phase and the out-of-phase vibrations. The in-phase vibration induces large change in volume of the pair, which causes a change in oscillation frequency of the surface plasmon band and thus gives an observed optical signal. The coherent phonon vibration corresponding to the out-

of-phase coupling is not observed. In the experiment, we can only detect vibration mode of in-phase coupling with lower energy, since the volume of the nanoparticle pair increases and decreases during the oscillation giving rise to large surface plasmon signal to be observed with the monitoring light and a decrease in the oscillation frequency due to the interparticle coupling.

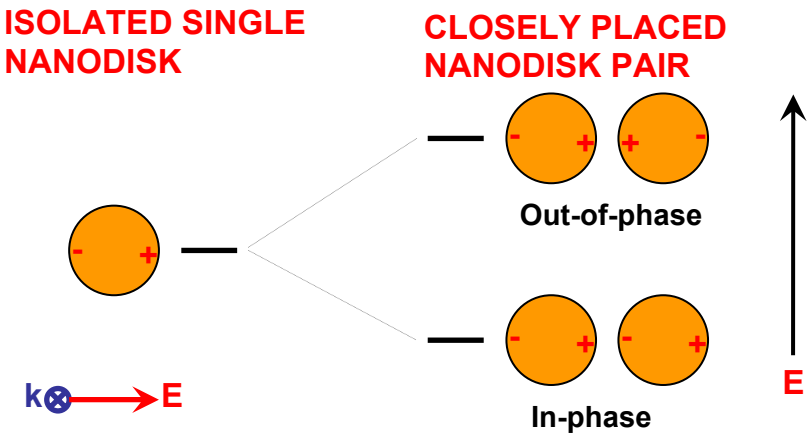

Figure 6-4: Effect of coupling of the coherent lattice mode on their energies.

6.3.4 The Use of the Universal Scaling Law [18]:

Recently, a universal scaling law for coupled pairs of plasmonic nanoparticles was published that showed the dependence of the fractional SPR shift on the interparticle distance scaled by the particle size is near exponential with an exponent that is independent of the size, shape, materials, dielectric constant of the medium, and that of the metal used [18].

Figure 6-5 gives a comparison of the effect of changing the scaled interparticle separation on the fractional shift of the coherent phonon vibration frequency (**Figure 6-5a**) and that of the SPR frequency (**Figure 6-5b**) for the same set of the gold nanodisks examined. It is interesting to observe that both properties give an exponential dependence. It is even more interesting that the decay constant (k) for both exponential dependences are very close to one another (k = 5.8 for the exponential decay of CPV frequency, and k = 5.5 for that of SPR frequency).

From the result of **Figure 6-5**, it is obvious that the coupling affecting the phonon vibration frequency has the same distance dependence as that affecting the electronic surface plasmon vibration frequency. The same scaling law suggests similar dipole-dipole interaction of the coupled coherent electron and phonon oscillations. This can be explained by the effect of the field produced by excitation of the surface plasmon oscillation on the lattice vibration frequency. The excitation of surface plasmon results from the monitoring light. The amplitude (a constant) in front of the exponential part is almost five times larger for the lattice vibration dependence. This suggests that the maximum $\Delta f / f$ is five times larger for the observed effect on phonons. A calculation for the two particles with 7 nm seperation gives a ratio of $\Delta f / f$ for the observed effect on phonon to electronic plasmon a value of ~ 5. This is a result of the fact that while the shift in frequency is very small for the phonon vibration compared to that for the electronic oscillation, the value of the frequency of the phonon vibration is so much smaller than that of the electronic oscillation frequency [44].

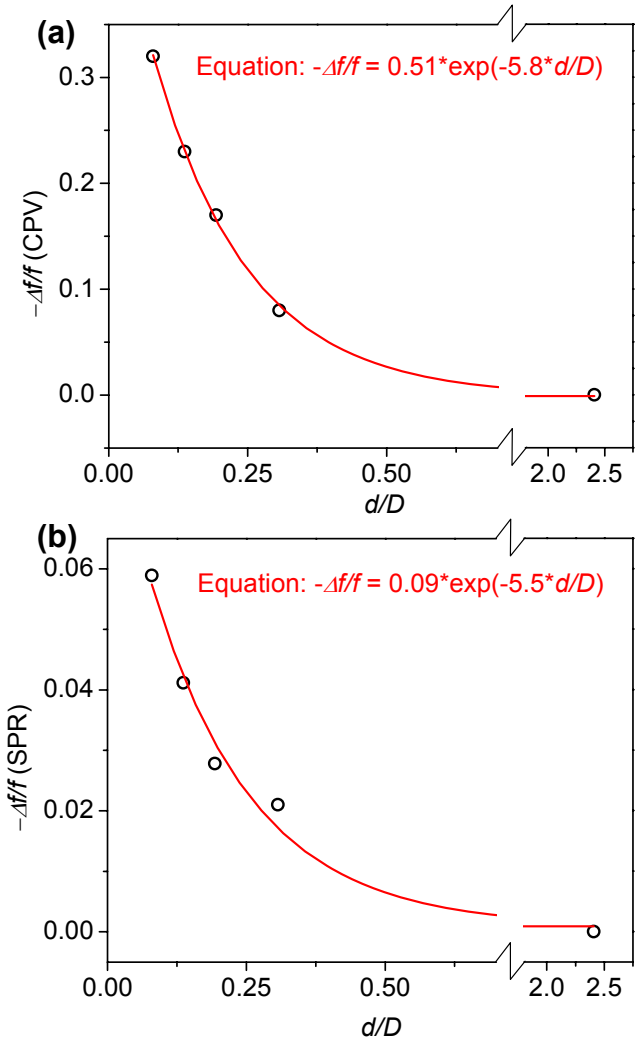

Figure 6-5: The exponential fits of the relative changes of the frequency of (a) the coherent phonon vibration (CPV) and (b) the surface plasmon resonance (SPR) with increasing of the interparticle separation *d* divided by the particle diameter *D*. Both of the relative change of the CPV and SPR frequencies decreases when *d/D* increases.

While the experimental result supports a dipolar coupling mechanism, it does not suggest on how this mechanism decrease the phonon frequency. One could suggest that the plasmon fields on each nanodisk are to polarize its electrons and increase the electronic volume. This could then lead to a decrease in the effective electron density in each nanodisk and as a result a decrease in its phonon oscillation frequency.

6.4 Conclusion

We used electron beam lithography to fabricate nanodisks having diameter of 88 nm each and separation that varies between 7 and 212 nm. We used femtosecond transient transmission spectroscopy to optically determine the phonon vibration frequency as a function of the interparticle separation. It is found that the fractional change in the vibration frequency increases exponentially with decreasing the ratio of the interparticle separation to the particle diameter. The increase in the vibration period of the coherent phonon when two nanodisks are closely placed is due to the coupling of lattice oscillation dipoles. For the same set of nanoparticle pairs, we found that the observed scaling exponential law governing the coherent phonon vibration frequency with distance is the same as that observed for the change in the surface plasmon electronic resonance frequency with distance. This was theoretically shown to result from the dipolar coupling induced by the plasmonic field. They both have an exponential behavior with the same decay constant, which suggest the same dipole-dipole interaction nature of the coupled coherent electron and lattice oscillation in the close-placed pair nanodisks.

6.5 References

[1] Pinna, N.; Maillard, M.; Courty, A.; Russier, V.; Pileni, M. P., *Phys. Rev. B* **2002,** 66, (4).

[2] Wormeester, H.; Henry, A. I.; Kooij, E. S.; Poelsema, B.; Pileni, M. P., *J. Chem. Phys.* **2006,** 124, (20), 204713.

[3] Krenn, J. R.; Dereux, A.; Weeber, J. C.; Bourillot, E.; Lacroute, Y.; Goudonnet, J. P.; Schider, G.; Gotschy, W.; Leitner, A.; Aussenegg, F. R.; Girard, C., *Phys. Rev. Lett.* **1999,** 82, (12), 2590-2593.

[4] Rechberger, W.; Hohenau, A.; Leitner, A.; Krenn, J. R.; Lamprecht, B.; Aussenegg, F. R., *Opt. Commun.* **2003,** 220, (1-3), 137-141.

[5] Su, K. H.; Wei, Q. H.; Zhang, X.; Mock, J. J.; Smith, D. R.; Schultz, S., *Nano Lett.* **2003,** 3, (8), 1087-1090.

[6] Fromm, D. P.; Sundaramurthy, A.; Schuck, P. J.; Kino, G.; Moerner, W. E., *Nano Lett.* **2004,** 4, (5), 957-961.

[7] Schuck, P. J.; Fromm, D. P.; Sundaramurthy, A.; Kino, G. S.; Moerner, W. E., *Phys. Rev. Lett.* **2005,** 94, (1), 017402.

[8] Gunnarsson, L.; Rindzevicius, T.; Prikulis, J.; Kasemo, B.; Kall, M.; Zou, S. L.; Schatz, G. C., *J. Phys. Chem. B* **2005,** 109, (3), 1079-1087.

[9] Atay, T.; Song, J. H.; Nurmikko, A. V., *Nano Lett.* **2004,** 4, (9), 1627-1631.

[10] Zhao, L. L.; Kelly, K. L.; Schatz, G. C., *J. Phys. Chem. B* **2003,** 107, (30), 7343-7350.

[11] Zou, S.; Janel, N.; Schatz, G. C., *J. Chem. Phys.* **2004,** 120, (23), 10871-10875.

[12] Hicks, E. M.; Zou, S. L.; Schatz, G. C.; Spears, K. G.; Van Duyne, R. P.; Gunnarsson, L.; Rindzevicius, T.; Kasemo, B.; Kall, M., *Nano Lett.* **2005,** 5, (6), 1065-1070.

[13] Sundaramurthy, A.; Crozier, K. B.; Kino, G. S.; Fromm, D. P.; Schuck, P. J.; Moerner, W. E., *Phys. Rev. B* **2005,** 72, (16), 165409.

[14] Nordlander, P.; Oubre, C.; Prodan, E.; Li, K.; Stockman, M. I., *Nano Lett.* **2004,** 4, (5), 899-903.

[15] Elghanian, R.; Storhoff, J. J.; Mucic, R. C.; Letsinger, R. L.; Mirkin, C. A., *Science* **1997,** 277, (5329), 1078-1081.

[16] Sonnichsen, C.; Reinhard, B. M.; Liphardt, J.; Alivisatos, A. P., *Nat. Biotechnol.* **2005,** 23, (6), 741-745.

[17] Reinhard, B. M.; Siu, M.; Agarwal, H.; Alivisatos, A. P.; Liphardt, J., *Nano Lett.* **2005,** 5, (11), 2246-2252.

[18] Jain, P. K.; Huang, W. Y.; El-Sayed, M. A., *Nano Lett.* **2007**, In Press.

[19] Barnes, W. L.; Dereux, A.; Ebbesen, T. W., *Nature* **2003,** 424, (6950), 824-830.

[20] Maier, S. A.; Kik, P. G.; Atwater, H. A.; Meltzer, S.; Harel, E.; Koel, B. E.; Requicha, A. A. G., *Nat. Mater.* **2003**, 229-232.

[21] Maier, S. A.; Brongersma, M. L.; Kik, P. G.; Meltzer, S.; Requicha, A. A. G.; Atwater, H. A., *Adv. Mater.* **2001,** 13, (19), 1501-+.

[22] Maier, S. A.; Kik, P. G.; Atwater, H. A., *Appl. Phys. Lett.* **2002,** 81, (9), 1714-1716.

[23] Xu, H. X.; Kall, M., *Phys. Rev. Lett.* **2002,** 89, (24).

[24] Xu, H. X.; Aizpurua, J.; Kall, M.; Apell, P., *Phys. Rev. E* **2000,** 62, (3), 4318-4324.

[25] Hao, E.; Schatz, G. C., *J. Chem. Phys.* **2004,** 120, (1), 357-366.

[26] Bozhevolnyi, S. I.; Beermann, J.; Coello, V., *Phys. Rev. Lett.* **2003,** 90, (19).

[27] Klar, T.; Perner, M.; Grosse, S.; von Plessen, G.; Spirkl, W.; Feldmann, J., *Phys. Rev. Lett.* **1998,** 80, (19), 4249-4252.

[28] Hodak, J. H.; Martini, I.; Hartland, G. V., *J. Chem. Phys.* **1998,** 108, (22), 9210-9213.

[29] Hodak, J. H.; Henglein, A.; Hartland, G. V., *J. Chem. Phys.* **1999,** 111, (18), 8613-8621.

[30] Hartland, G. V., *J. Chem. Phys.* **2002,** 116, (18), 8048-8055.

[31] Perner, M.; Gresillon, S.; Marz, J.; von Plessen, G.; Feldmann, J.; Porstendorfer, J.; Berg, K. J.; Berg, G., *Phys. Rev. Lett.* **2000,** 85, (4), 792-795.

[32] Hartland, G. V.; Hu, M.; Wilson, O.; Mulvaney, P.; Sader, J. E., *J. Phys. Chem. B* **2002,** 106, (4), 743-747.

[33] Hu, M.; Wang, X.; Hartland, G. V.; Mulvaney, P.; Juste, J. P.; Sader, J. E., *J. Am. Chem. Soc.* **2003,** 125, (48), 14925-14933.

[34] Huang, W. Y.; Qian, W.; El-Sayed, M. A., *Nano Lett.* **2004,** 4, (9), 1741-1747.

[35] Huang, W. Y.; Qian, W.; El-Sayed, M. A., *J. Phys. Chem. B* **2005,** 109, (40), 18881-18888.

[36] Courty, A.; Mermet, A.; Albouy, P. A.; Duval, E.; Pileni, M. P., *Nat. Mater.* **2005,** 4, (5), 395-398.

[37] Duval, E.; Mermet, A.; Courty, A.; Albouy, P. A.; Pileni, M. P., *Phys. Rev. B* **2005,** 72, (8), 085439.

[38] Jain, P. K.; Eustis, S.; El-Sayed, M. A., *J. Phys. Chem. B* **2006,** 110, (37), 18243-18253.

[39] Hu, M.; Petrova, H.; Wang, X.; Hartland, G. V., *J. Phys. Chem. B* **2005,** 109, (30), 14426-14432.

[40] Lamb, H., *Proc. London Math. Soc.* **1882,** 13, 189.

[41] Bullen, K. E.; Bolt, B. A., *An introduction to the theory of seismology*. Cambridge: New York, 1985.

[42] Hodak, J. H.; Henglein, A.; Hartland, G. V., *J. Phys. Chem. B* **2000,** 104, (43), 9954-9965.

[43] Hunsche, S.; Wienecke, K.; Dekorsy, T.; Kurz, H., *Phys. Rev. Lett.* **1995,** 75, (9), 1815-1818.

[44] For the nanodisk pair of 7 nm gap (the strongest coupling situation), the absolute frequency change in the coherent phonon vibration from the uncoupled situation (212 nm gap) is 6.14×10^{9} Hz, which corresponds to an energy change of 2.54×10^{-5} eV. For the same nanodisk pair, the frequency change in the SPR(coherent electron oscillation) from the uncoupled situation is 3.16×10^{13} Hz, which corresponds to an energy change of 1.31×10^{-1} eV. Therefore, the energy required to change the coherent vibration frequency of the phonon is four orders of magnitude smaller than that of SPR.

CHAPTER 7

GIGAHERTZ OPTICAL MODULATION RESULTING FROM COHERENT LATTICE OSCILLATIONS INDUCED BY FEMTOSECOND LASER PUMPING OF 2D PHOTONIC CRYSTALS OF GOLD CAPPED POLYSTYRENE MICRO-SPHERES

Abstract

We report on an all-optical gigahertz modulation mechanism in an opto-mechanical nano-system (OMNS), in which the modulated transmission light is induced by the coherent oscillations of the phonon modes of gold caps on periodic polystyrene (PS) sphere monolayer arrays. The gigahertz phonon oscillation modes in this two dimensional photonic crystal system are generated by excitation with a low repetition rate femtosecond pulsed laser. The coherent phonon oscillation in this system has long dephasing time (more modulation periods) due to the slow phonon-phonon relaxation. The optical modulation amplitude is 2 to 3 orders higher than a plan metal film or metal nanoparticles due to the sharp transmission dip formed by the periodically arrayed PS sphere monolayer. We demonstrated that the phonon oscillation of the OMNS can modulate the transmitted light in the gigahertz bandwidth, which is tunable by changing the diameter of PS spheres.

7.1 Introduction

The ultrafast modulation of light in a compact system is an active area of research in many fields [1-3], such as optical communications, inter-electronic chip optical connections, and photonic circuits. The importance of the optical modulation has driven extensive efforts [4-15] in the discovery of new techniques and the optimization of existing techniques of light modulation.

Several techniques have been used to modulate light in optical modulators. One of them uses the quantum-confined stark effect [4,5], which is induced by applying electric fields perpendicular to quantum well layers. The applied electric field separates the electrons and holes within the quantum well layers. The separation of the electrons and holes reduces the excitation energy of electron-hole pairs, thus causing a red shift in the spectrum. By applying periodic electric fields, the light passing through the quantum well layers is modulated accordingly. Due to the ultrafast response time (subpicosecond), it is expected that quantum wells can modulate light at a terahertz bandwidth [6,7]. Experimentally, Lewen et al. [8] have fabricated a device that can modulate light at a frequency greater than 50 GHz. However, the quantum wells with strong quantum-confined stark effect are usually made from III-V semiconductors such as InP, GaAs, and their alloys, which are hard to be integrated with current silicon devices. Recently, a breakthrough is demonstrated in a silicon-based germanium quantum-well structure, which has strong quantum-confined stark effect comparable to the III-V semiconductor structures [5].

Another widely used technique to modulate light is based on a Mach-Zehnder interferometer [9-12], where the source waveguide is split into two arms, the gate arm

and the reference arm. The optical source signal in the gate arm is phase shifted by an electrically produced perturbation in critical carrier concentration. The optical source signal in the reference arm remains unaltered. When the gate and reference arms are recombined, the phase shifted optical signal from the gate arm interferes with the original optical signal in the reference arm. An intensity modulation of the optical source signal is then generated. Based on Mach-Zehnder geometry, Lee and co-workers [10] fabricated a polymeric electro-optical modulator that modulates light at 200 GHz. Shi et al. [9] demonstrated that by using a certain chromophore, a polymeric electro-optic modulator could operate at a voltage as low as 0.8 V. Compared to the typical operating voltage of polymeric and lithium niobate modulators (~ 5 V), the tremendous decrease in the attenuation voltage was attributed to the strong electrostatic interactions between molecules [9].

Other light modulating techniques have also been reported. Solgaard et al. [13] fabricated an attenuated total internal reflection modulator driven by photon-surface plasmon coupling. Jones et al. [14] reported an optical modulation in a silicon waveguide based on stimulated Raman scattering with bandwidth of 80 MHz. de Lima et al. [15] demonstrated a compact optical waveguide modulator driven by surface acoustic waves, which induce changes in the refractive index based on an elasto-optical effect.

Recently, all-optical modulation [16-19] has received substantial attention due to its potential to realize terahertz optical modulation, optical system miniaturization, and all-optical computation. Almeida et al. [16] fabricated a silicon planar ring resonator that functions as an all-optical gate with a picosecond laser excitation. The enhanced transmission response from a small refractive index variation in silicon is based on a

highly confined resonant structure. Marki et al. [18] used a planar photonic crystal silicon waveguide to modulate the in-plane transmission by an optical pump induced microcavity change. Hochberg and Baehr-Jones et al. [19] fabricated an optically controlled modulator in a silicon-polymer hybrid system based on the Mach-Zehnder interferometer. The phase shift of the optical source signal in the gate arm of the interferometer is optically induced by the nonlinear Kerr effect. Ebbesen et al. [20] used the surface plasmon related transmission change from a subwavelength hole array to modulate light. The transmission change is caused by the refractive index change that is induced by the excitation of chromophore molecules.

In the above modulation techniques, the mechanisms of optical modulations at high frequencies involve electrical, acoustic, or optical gating signals modulated at the same frequency. In the current report, we describe a new technique, in which gigahertz optical modulations are induced by low repetition femtosecond laser pulses, which excite the coherent lattice phonon motion of gold capped polystyrene spheres. The periodic change in the radius of the gold cap during the lattice oscillation induces a corresponding periodic change in the transmission spectra of the gold capped PS sphere 2D array, which modulates the intensity of the monitoring light.

7.2 Experimental Section

The nanoparticle was fabricated on a quartz substrate using the third version NSL (Air-Water Interface Self-assembly). The experimental details are introduced in Chapter 2 (Section 2.1.3). The diameter of the polystyrene (PS) spheres used in our experiments

was 0.45, 0.60, and 0.74 μm . The mask was then mounted in a thermal evaporator (Denton DV-502A) to deposit 50 nm thick gold (99.999%, Alfa Aesar). The thickness of the deposited metal was monitored by a quartz crystal thickness monitor (Inficon). The formed gold capped PS sphere monolayer arrays were examined using scanning electron microscopy (SEM).

A Shimadzu UV-3101-PC spectrophotometer is used to record the transmission spectra of the arrays. The incident light is perpendicular to the array substrate. The transmitted light through the sample has a cross section of several square millimeters.

The detail of the femtosecond laser pump-probe experiment is described in Chapter 2 (Section 2.6).

7.3 Results and Discussion

7.3.1 SEM Image of Gold Capped Close Packed PS Sphere Monolayer:

Three PS sphere suspensions of different sphere diameters are used to form monolayers on the surface of quartz substrates by the modified NSL technique [21-23]. This NSL technique allows the PS spheres to form a monolayer crystal and cover several square millimeters to a square centimeter area on the substrate. **Figure 7-1a** is a typical SEM image taken at normal incidence of a 740 nm diameter polystyrene sphere monolayer array capped with 50 nm of gold. The PS spheres form a closely packed triangular lattice. **Figure 7-1b** and **c** are SEM images of the gold capped 740 nm PS sphere monolayer array taken at 30^o and 0^o incidence on cleavage sites, respectively. The deposited gold forms a cap on the top of each PS sphere. The gold cap on each PS sphere is connected with its six neighbors. **Figure 7-1b** and **c** also show that a lot of isolated small gold islands (clusters) are formed on the edge of the gold cap. The deposited gold forms clusters initially and coalesce into a film as the deposition continuing (thickness increase) [24]. If the homogeneous deposited gold atoms do not migrate on the surface of the substrate, the thickness of the gold deposition on a curved surface (d) depends on the angle (θ) between the gold atom propagation direction and the surface normal ($d = d_0 \cos\theta$, where d_0 is the deposition thickness when $\theta = 0$). On the edge of the gold cap, the angle θ is close to 90^o and only a very thin layer of gold can be formed there, so the ultra-thin gold stays in cluster format, a stage before coalescence.

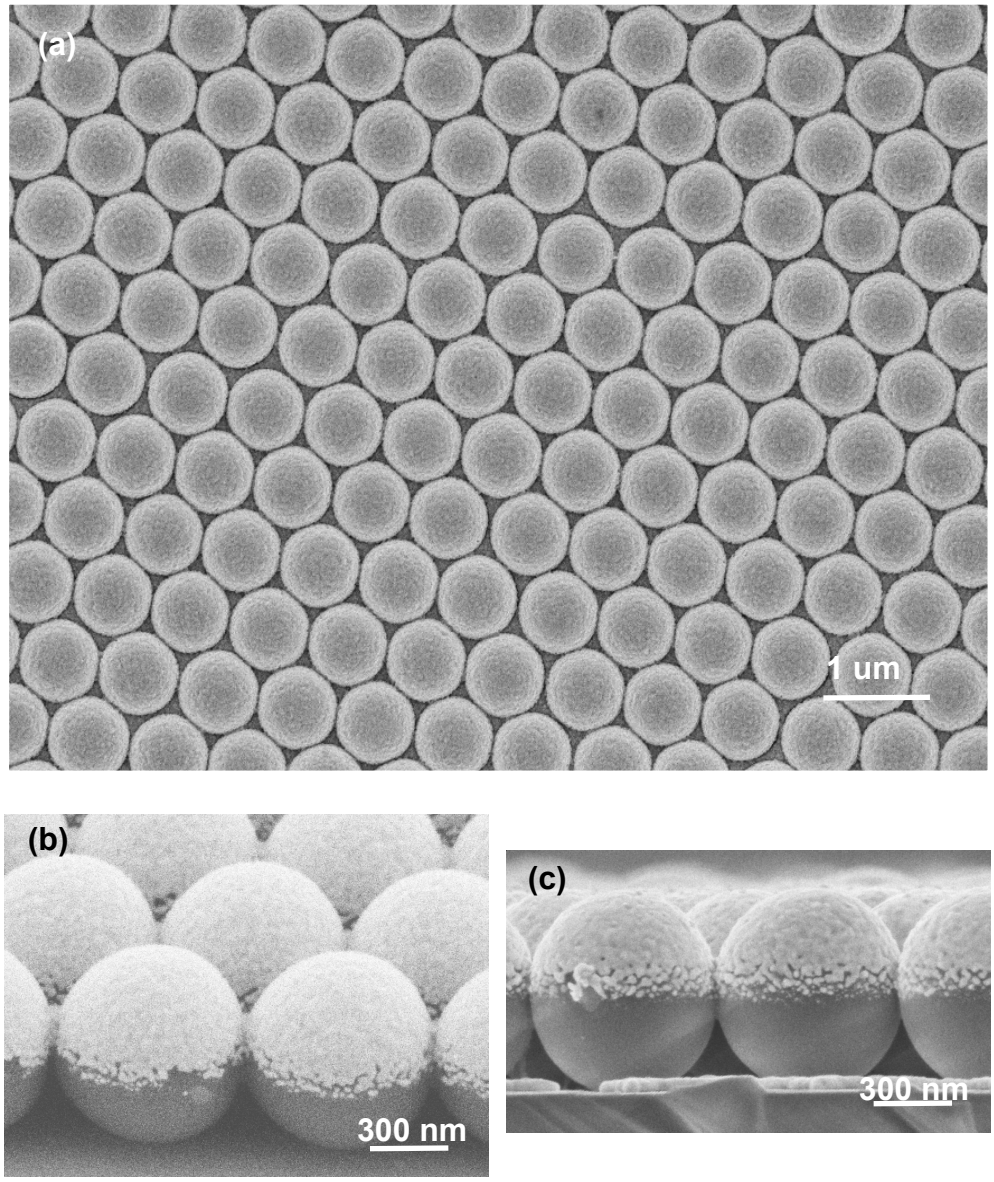

Figure 7-1: (a) SEM image of a 50 nm gold capped PS sphere on quartz substrate. The PS spheres form a close-packed triangular monolayer lattice. (b) The 60^{o} view of the gold capped PS sphere monolayer array from a cleavage site. (c) The 90^{o} view (side view) of the gold capped PS sphere monolayer array from a cleavage site.

7.3.2 Transmission Spectra of Gold Capped Close Packed PS Sphere Monolayers:

The transmission spectra of the PS sphere was taken at perpendicular incidence. The transmission spectra of the monolayer of close-packed dielectric spheres on a dielectric substrate have be reported experimentally and predicted theoretically by Miyazaki and co-workers [25-27]. Several factors affect the intensity of the transmission spectrum as shown by the black lines in **Figure 7-2**. These are the incident electromagnetic waves, the scattered electromagnetic waves by the PS spheres, the multiple intrasphere and intersphere scattering within the closely packed sphere monolayer, and the extra energy dissipation channel provided by the substrate. Dips in the transmission spectrum correspond to the excitation of the system's eigenstates. After excitation, the energy is dissipated out of the system, which determines the lifetime of the excited eigenstates and thus the width of the dips of transmission spectrum. The calculation for a monolayer of closely packed PS spheres shows very sharp dips in transmission spectrum without a substrate. When the monolayer of PS spheres is placed on a semi-infinite substrate, the dips are shifted slightly due to the change of the media dielectric constant induced by the substrate. The largest change is the broadening of the dips, which is due to the extra energy dissipation channel provided by the substrate [26]. The extra energy dissipation channel shortens the lifetime of the excited eigenstates of the system resulting in the broadening of the dips in the transmission spectra.

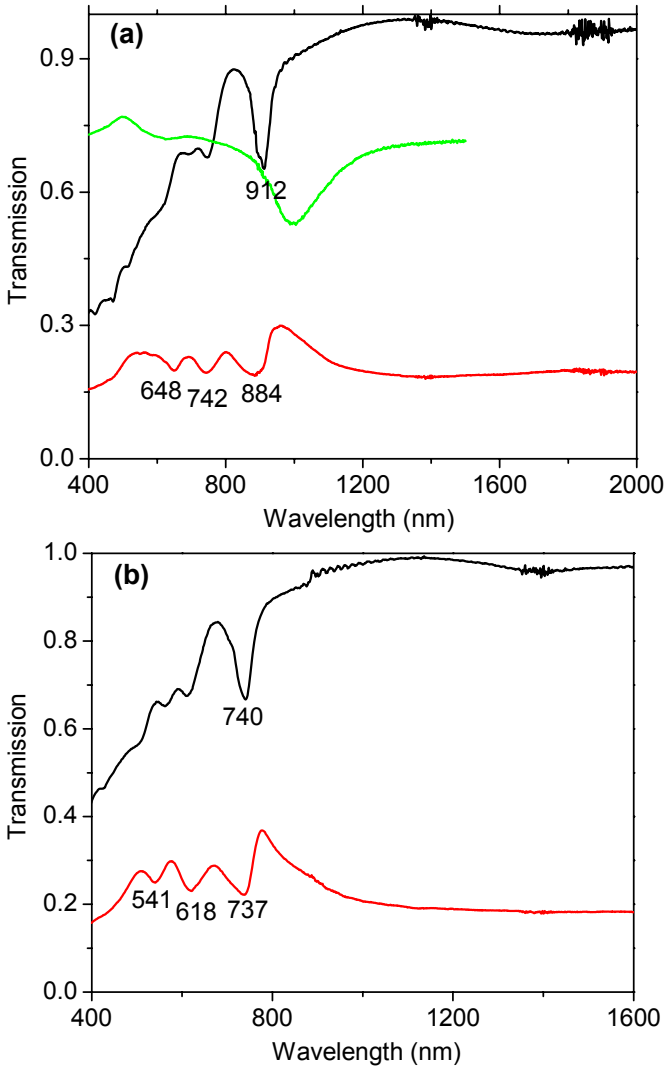

Figure 7-2: (a) The black spectrum is recorded on a close packed 740 nm PS sphere monolayer. After deposition of 50 nm Gold, the spectrum is shown by the red line. After lift-off of the PS sphere, the formed gold prismatic nanoparticle array shows a spectrum as the green line. The surface plasmon resonance band of the gold nanoparticle array is located at 997 nm. (b) The black spectrum is recorded on a close packed 600 nm PS sphere monolayer. After deposition of 50 nm Gold, the spectrum is shown by the red line.

After gold deposition, the transmission spectra is shown in red color in **Figure 7-2a** and **b** for 740 and 600 nm diameter PS sphere arrays, respectively. The transmission of the system decreases dramatically, which is due to the enhanced absorption and

scattering induced by the plasmon fields of the gold layer. The transmission spectra show three major dips. The transmission dips shift to lower wavelength and broaden compare to the closely packed PS sphere monolayer without the gold coating (black lines in **Figure 7-2**). The shift of the transmission dips is due to the change in the dielectric constant of the media after gold coating. The broadening of the transmission dips is caused by the extra energy dissipation channel introduced by the deposited gold layer, which have the same effect as the substrate in shorting the lifetime of the excited eigenstates of the system. The dip of the green line in **Figure 7-2a** is due to the absorption and scattering of the gold prismatic nanoparticles after removing the PS spheres. The gold nanoparticles are formed in the void of the closely packed PS sphere monolayer on the quartz substrate.

If the transmission spectra are due to the scattering of light by the PS sphere system, the spectra should only depend on the size of the PS sphere as predicted by the scaling rule of photonic crystal [28]. To prove that the scaling rule is valid for the current system, we plot the transmission spectra recorded on 740 and 600 nm vs. the dimensionless parameter λ/D, where λ is the transmission wavelength and D is the diameter of the PS sphere. This is confirmed by the black and green lines in **Figure 7-3**, where the transmission spectra for the 740 and 600 nm PS sphere monolayer are almost overlap with one another. The overlap of the transmission spectra from different sized PS sphere monolayer after using the dimensionless parameter proves the scattering nature of recorded transmission spectra. After gold deposition, the transmission spectra are slightly shifted from each other, which could be due to the absorption and scattering of the gold layer, which is not linearly dependent on the size of the PS sphere.

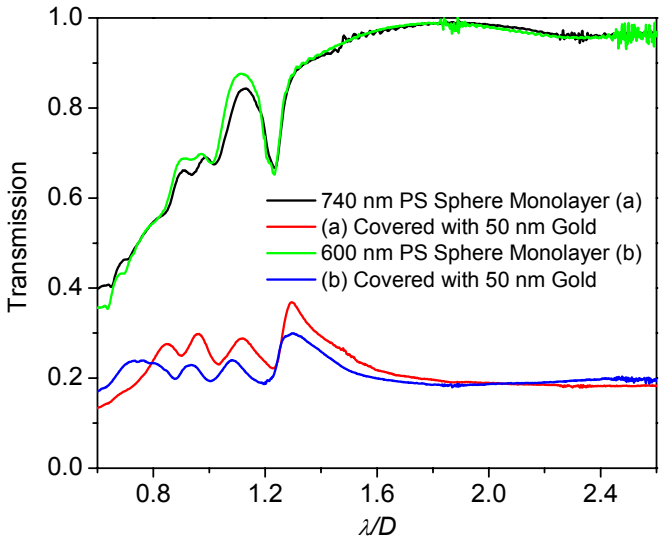

Figure 7-3: The scaled (λ/D, D is the diameter of the PS sphere) transmission spectra of the PS sphere monolayer and the 50 nm gold capped PS monolayer. The spectra from the PS sphere monolayer of two different sizes are overlap with each other, which means the bands are come from the size dependent scattering. After gold coating, the dips of the transmission spectra of the two different sized PS sphere monolayer do not overlap with each other (slight shift), which could be due to the gold induced refractive index change and the surface plasmon absorption of gold (highly dependent on the dimension of the gold).

7.3.3 Optical Modulation Generated by Femtosecond Pumping of Gold Capped PS Sphere Monolayer:

Figure 7-4 shows the transient transmission spectra of the gold capped 740 nm PS sphere system recorded by femtosecond pump-probe technique. The wavelength of the probe light is tuned around the strongest dip (minimum ~ 884 nm) in the transmission spectrum. The modulation of the probe laser light is clearly indicated by the intensity change in the transmitted probe light as we increase the delay time between pump and probe pulse. The modulated signal is fitted with a damped cosine function, from which the period of the modulation is ~ 422 ps. Most of the previously reported modulation of

light in high frequency is induced by electrical, acoustic, or optical gate signals that modulate in the same frequency. In many cases, the generation of a high frequency gate signal is difficult. In our experiment, the gigahertz optical modulation is truly "generated" by a low repetition rate pulsed laser, which is due to the extremely slow phonon-phonon relaxation that can reserve the phonon energy within the system. Another reason is the long dephasing time of the coherent phonon oscillation of the gold capped PS sphere monolayer system, which maintains the phase of oscillated phonons. The dephasing time represents the number of modulation periods can be generated with one pump pulse. The dephasing time (τ) of the optical modulation is four times of the period of the modulation ($\tau = 4\ T$) in the current system, which is much longer than the core-shell nanoparticle with an enclosed shell ($\tau = 1.6\ T$) [29]. This superior property could be employed in an optical multiplier or encoder in optical communication [30].

The transient transmission spectrum of the 740 nm PS sphere system monitored at 910 nm is shown by black dots in **Figure 7-4**, where the amplitude of the modulation is more than 1% of the total transmission. The modulation amplitude is 2 to 3 orders stronger than the modulation generated from a nanoparticle or a planer metal film [31] due to the sharp transmission dip formed by the periodically arrayed PS sphere monolayer. This modulation amplitude is comparable to that generated in semiconductor multiple quantum well with a strain induced piezoelectric field [32]. The modulation amplitude can be further enhance by using an ultrathin (hundreds of nanometer) substrate for the PS sphere monolayer. The PS sphere monolayer on a thin substrate gives sharp dips in the transmission spectrum [26,27], where a slight position change of dips can cause a big intensity change in the transmitted light [17]. The ultrafast rise (turn on) time

is another superior property of the all-optically controlled system [33]. In our system, the rise (turn on) time for the optical modulation is less than 10 ps after the femtosecond pump pulse.

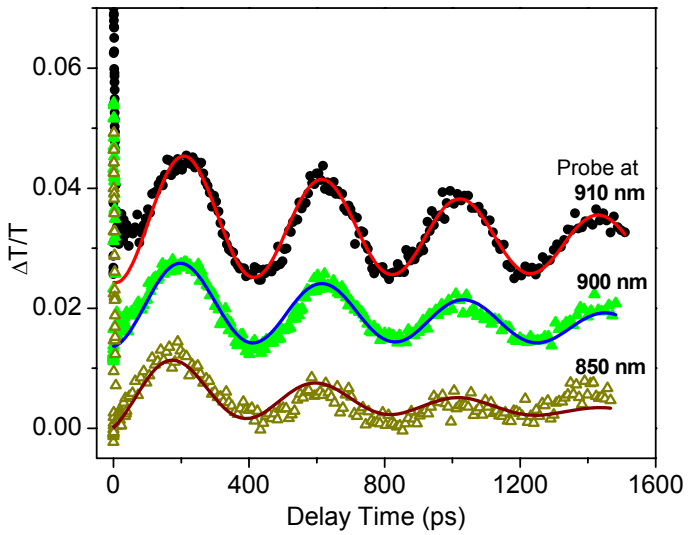

Figure 7-4: The optical modulation generated with the 400 nm femtosecond laser pump of the 50 nm gold capped periodically arrayed monolayer PS spheres of 740 nm diameter. The dotted lines are experimental data, and the solid lines are theoretical fits. The spectra are vertically shifted for clear view. The optical modulation period is 422 ± 12 ps. The modulation at 910 nm has an amplitude larger than 1 %. The dephasing time (τ) is four times of the period of the modulation ($\tau = 4\ T$), which is much longer than the core-shell nanoparticle with enclosed shell ($\tau = 1.6\ T$) [29].

7.3.4 The Generation Mechanism of the Optical Modulation:

Despite the above mentioned superior properties of this optical modulation system, to fully characterize the system, we need to understand the origin of the observed modulation and how to control the modulation frequency. To understand the mechanism behind the femtosecond laser induced optical modulation, we need start from the femtosecond pump process in metal. Right after femtosecond pump of the gold coated PS

sphere monolayer array at 400 nm, a rapid increase (tens of femtosecond) and then decrease (several picosecond) in the transient transmission spectrum of the monitoring light represent the excitation of electron and the electron-phonon relaxation in gold film, respectively. During the electron-phonon relaxation, the electronic energy is rapidly dissipated into lattice. Since the electron-phonon relaxation time is very short (~ 1 ps) [34], the gold lattice is heated up instantly. The instant heating of the gold expands its lattice coherently. The lattice gold ions are moved away from the ground state equilibrium position. Due to the inertia, the gold ions vibrate around their equilibrium positions coherently. This coherent vibration of gold lattice has been indirectly observed in previous studies on gold and silver plasmonic nanoparticles by monitoring the shift of their surface plasmon resonance absorption [35-38].

The coherent vibration of the gold lattice induces two changes in the gold capped PS sphere monolayer system. First, the coherent vibration of the gold lattice at specific frequency changes the volume of the gold hemispherical shell (cap). The volume expansion of the gold shell separates the gold shell from the PS sphere surface due to the smaller or absence expansion of the dielectric PS sphere compared to the metal shell [29]. The disengagement of the gold shell from the PS sphere changes the surrounding environment of PS spheres. The surrounding medium dielectric constant of the PS spheres is thus changed. Second, the density of the conductive electrons is modulated due to the volume change of the gold lattice during the coherent vibration, which changes the dielectric constant of gold. The periodic change of the dielectric constant induced by the above two reasons causes the vibration of dips in the transmission spectrum with the same frequency. The transmitted light at particular wavelength within dips is also

modulated at the same frequency. Therefore, the optical modulation is generated by the transmission property change induced by the coherent phonon oscillation of gold shell on PS spheres.

The weak gold-polystyrene coupling and the disengagement of the gold shell from the PS sphere could explain the decrease of the rate of phonon energy dissipation from the gold shell to the PS sphere. Thus, the lifetime of the coherent phonons of the gold shell (~ 3 ns) is much longer than that of gold prismatic nanoparticles deposited on quartz substrates by NSL (< 1 ns) [36].

7.3.5 Optical Modulation Period:

To predict the modulation period of gold capped PS sphere monolayer array, we first check to see if the experimental values agree with the calculated values from a solid spherical particle. For a spherical particle, ultrafast laser heating induces a breathing mode vibration. The period of the breathing mode vibration (T_{br}) can be calculated by equation (1-9) [39,40]. The values of η are calculated to be 2.94 and 2.75 for gold and polystyrene, respectively. The periods of the breathing mode vibration are calculated by equation (1-9) to be 244 and 261 ps for solid gold and polystyrene spheres, respectively. There are differences between these values and the experimental value (~ 422 ps), so equation (1-9) can not be used to calculate the period of the coherent phonon vibration in the current system, which is because the shape of the gold coating is a thin hemispherical shell and the equation is for solid spherical particles.

Another model system that is close to our gold capped PS sphere monolayer array is a full metal shell enclosed dielectric core system. Guillon et al. [29] performed both

experimental and theoretical studies on Au_2S/Au core/shell (dielectric core/metal shell) particles. From their theoretical calculation, the vibration mode of the metal shell dielectric core system is found to be a fundamental breathing mode [29]. Several parameters affect the calculation of the coherent phonon oscillation period, such as the relative thickness of the shell to the over-all size, the density of the shell, and the sound velocity in the shell material. In the current system, the gold coating is 50 nm. The ratio of core radius to overall radius is close to 0.9 for the 740 nm PS sphere and the density of the shell is much higher than that of the surrounding medium (air). For this thin heavy shell, the coherent phonon oscillation period is given by equation (1-14) [29]. For a PS sphere enclosed with 50 nm thick gold shell, the oscillation period calculated by equation (1-14) is 112 ps, which is almost four times smaller than the experimentally measured period from the PS sphere monolayer capped by gold hemispherical shell (~ 422 ps).

Guillon et al. [29] also observed that the calculated vibration period from their core-shell particle was two times smaller than the period measured from their experiment. The deviation is attributed to the inhomogeneous metal shell structure, which is not smooth and has interstices. The vibrational modes of the shell are more likely to move to the effectively thinner part (because of the increased surface to volume ratio), which has longer vibration period. In our system, the gold cap does not have an ideal hemispherical shape because the thickness of gold layer is not uniform across the hemisphere. Only the thickness at the top of the PS sphere is 50 nm. On the edge of the gold cap, only a very thin layer of gold can be formed because the angle, θ, between the incident beam of gold atoms and the surface normal of PS sphere is close to 90^o. The thickness of gold is consistently decreasing from the top to the edge of the cap on each PS sphere. The

thickness decrease of the gold layer could elongate the coherent phonon oscillation period if the vibration mode moves to the thinner shell [29]. The physical connection of each gold cap with its six neighbors introduces coupling within the system, which could elongate the coherent phonon oscillation further [37]. Therefore, both equation (1-9) and (1-14) can not be used to calculate the acoustic vibration period of the gold hemispherical shell capped PS sphere.

Since there is no available equation or model to be used to predict the optical modulation (acoustic vibration) period of this unique system, we can obtain an empirical equation by fitting the experimental data from the monolayer of 50 nm thick gold capped PS sphere of different diameters. We measured the oscillation period from two additional gold capped PS sphere monolayer systems made with 600 and 450 nm PS spheres, in which the optical modulation periods (frequencies) are monitored around the strongest dip in their transmission spectrum. These periods are found to be 348 and 259 ps (2.87 and 3.86 GHz), respectively. The periods (T) from the three systems fit a linear equation, $T = 0.56\ D$ with an R-squared value of 0.9989 as shown in **Figure 7-5**. This equation suggests that the modulation period is linearly proportional to the PS sphere diameter in this sphere size range. By using PS spheres of diameters less than 450 nm, optical modulation frequencies higher than 3.86 GHz can be achieved by this simple technique. In contrast, the traditional way to generate a gigahertz acoustic wave (as the gate for the optical modulation system) is difficult with the inverse piezoelectric effect of interdigital transducers (IDT) in GaAs bases structures [41].

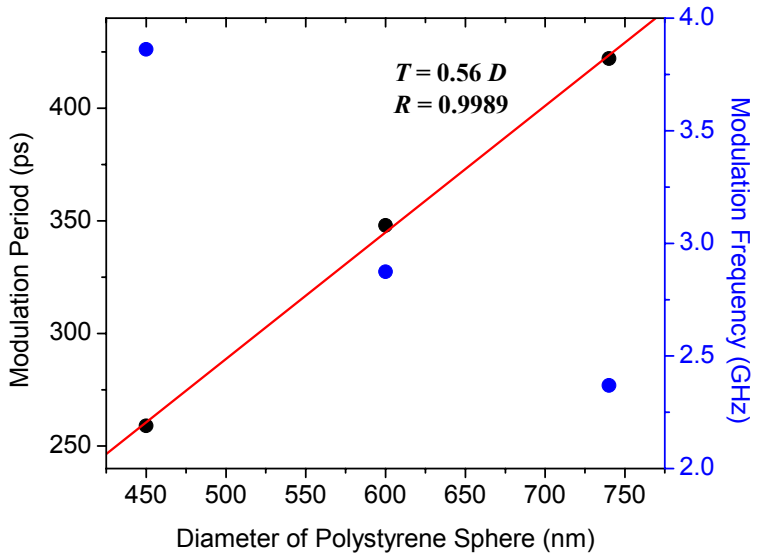

Figure 7-5: The experimental optical modulation periods (black dots) are linear dependent on diameters of the PS spheres. Red line is a linear fit of the experimental modulation periods. The blue dots are the optical modulation frequencies (the reciprocal of periods).

7.4 Conclusion

We describe a new all-optical modulation mechanism induced by an opto-mechanical Nano- system (OMNS), where the transmitted light is modulated by the coherent oscillation of the phonon modes of gold capped periodic polystyrene (PS) monolayer arrays. The modulation is caused by the phonon oscillations in this two dimensional photonic crystal system, which are induced by excitation with a low energy femtosecond pulsed laser. Most of the previously reported modulation of light in high frequency is induced by electrical, acoustic, or optical gate signals that are modulated at the same frequency. In many cases, the generation of a high frequency gate signal is

difficult. In our experiment, the gigahertz optical modulation is "generated" by a low repetition rate femtosecond laser. In order to observe these oscillations, the excitation time (the laser pulse width) has to be shorter than the period of the coherent oscillations. The optical modulation amplitude is two to three orders of magnitude higher in the gold capped PS system than that of a metal thin film or metal nanoparticles on quartz substrate. The dephasing time of the oscillation in the gold capped PS sphere monolayer is two to three times longer than that in prismatic array nanoparticles on quartz substrate. The nanometer thin gold layer is essential in our system because the observed coherent phonon oscillation modes in our system are those of the gold nanoshell generated by its strong absorption and ultrafast photothermal processes. We demonstrated that the phonon oscillation of the OMNS can modulate the transmitted light in gigahertz bandwidth, which is tunable by changing the diameter of the PS spheres.

7.5 References

[1] Miller, D. A. B., *Proceedings of the Ieee* **2000,** 88, (6), 728-749.

[2] Eldada, L., *Rev. Sci. Instrum.* **2004,** 75, (3), 575-593.

[3] Winzer, P. J.; Essiambre, R. J., *Proceedings of the Ieee* **2006,** 94, (5), 952-985.

[4] Miller, D. A. B.; Chemla, D. S.; Damen, T. C.; Gossard, A. C.; Wiegmann, W.; Wood, T. H.; Burrus, C. A., *Phys. Rev. Lett.* **1984,** 53, (22), 2173-2176.

[5] Kuo, Y. H.; Lee, Y. K.; Ge, Y. S.; Ren, S.; Roth, J. E.; Kamins, T. I.; Miller, D. A. B.; Harris, J. S., *Nature* **2005,** 437, (7063), 1334-1336.

[6] Schmittrink, S.; Chemla, D. S.; Knox, W. H.; Miller, D. A. B., *Opt. Lett.* **1990,** 15, (1), 60-62.

[7] Maslov, A. V.; Citrin, D. S., *J. Appl. Phys.* **2003,** 93, (12), 10131-10133.

[8] Lewen, R.; Irmscher, S.; Westergren, U.; Thylen, L.; Eriksson, U., *J. Lightwave Technol.* **2004,** 22, (1), 172-179.

[9] Shi, Y. Q.; Zhang, C.; Zhang, H.; Bechtel, J. H.; Dalton, L. R.; Robinson, B. H.; Steier, W. H., *Science* **2000,** 288, (5463), 119-122.

[10] Lee, M.; Katz, H. E.; Erben, C.; Gill, D. M.; Gopalan, P.; Heber, J. D.; McGee, D. J., *Science* **2002,** 298, (5597), 1401-1403.

[11] Gu, L. L.; Jiang, W.; Chen, X. N.; Wang, L.; Chen, R. T., *Appl. Phys. Lett.* **2007,** 90, (7).

[12] Jacobsen, R. S.; Andersen, K. N.; Borel, P. I.; Fage-Pedersen, J.; Frandsen, L. H.; Hansen, O.; Kristensen, M.; Lavrinenko, A. V.; Moulin, G.; Ou, H.; Peucheret, C.; Zsigri, B.; Bjarklev, A., *Nature* **2006,** 441, (7090), 199-202.

[13] Solgaard, O.; Ho, F.; Thackara, J. I.; Bloom, D. M., *Appl. Phys. Lett.* **1992,** 61, (21), 2500-2502.

[14] Jones, R.; Liu, A. S.; Rong, H. S.; Paniccia, M.; Cohen, O.; Hak, D., *Optics Express* **2005,** 13, (5), 1716-1723.

[15] de Lima, M. M.; Beck, M.; Hey, R.; Santos, P. V., *Appl. Phys. Lett.* **2006,** 89, (12).

[16] Almeida, V. R.; Barrios, C. A.; Panepucci, R. R.; Lipson, M., *Nature* **2004,** 431, (7012), 1081-1084.

[17] Xu, Q. F.; Schmidt, B.; Pradhan, S.; Lipson, M., *Nature* **2005,** 435, (7040), 325-327.

[18] Marki, I.; Salt, M.; Herzig, H. P.; Stanley, R.; El Melhaoui, L.; Lyan, P.; Fedeli, J. M., *Opt. Lett.* **2006,** 31, (4), 513-515.

[19] Hochberg, M.; Baehr-Jones, T.; Wang, G. X.; Shearn, M.; Harvard, K.; Luo, J. D.; Chen, B. Q.; Shi, Z. W.; Lawson, R.; Sullivan, P.; Jen, A. K. Y.; Dalton, L.; Scherer, A., *Nat. Mater.* **2006,** 5, (9), 703-709.

[20] Dintinger, J.; Robel, I.; Kamat, P. V.; Genet, C.; Ebbesen, T. W., *Adv. Mater.* **2006,** 18, (13), 1645-+.

[21] Wang, X. D.; Summers, C. J.; Wang, Z. L., *Nano Lett.* **2004,** 4, (3), 423-426.

[22] Kosiorek, A.; Kandulski, W.; Chudzinski, P.; Kempa, K.; Giersig, M., *Nano Lett.* **2004,** 4, (7), 1359-1363.

[23] Huang, W.; Qian, W.; El-Sayed, M. A., *J. Am. Chem. Soc.* **2006,** 128, (41), 13330-13331.

[24] Ievlev, V. M.; Shvedov, E. V., *Physics of the Solid State* **2006,** 48, (1), 144-149.

[25] Miyazaki, H. T.; Miyazaki, H.; Ohtaka, K.; Sato, T., *J. Appl. Phys.* **2000,** 87, (10), 7152-7158.

[26] Kurokawa, Y.; Miyazaki, H.; Jimba, Y., *Phys. Rev. B* **2002,** 65, (20), 201102.

[27] Kurokawa, Y.; Miyazaki, H.; Jimba, Y., *Phys. Rev. B* **2004,** 69, (15), 155117.

[28] Joannopoulos, J. D.; Meade, R. D.; Winn, J. N., *Photonic crystals : molding the flow of light*. Princeton University Press: Princeton, N.J., 1995.

[29] Guillon, C.; Langot, P.; DelFatti, N.; Vallee, F.; Kirakosyan, A. S.; Shahbazyan, T. V.; Cardinal, T.; Treguer, M., *Nano Lett.* **2007,** 7, (1), 138-142.

[30] Pudo, D.; Chen, L. R., *J. Lightwave Technol.* **2005,** 23, (4), 1729-1733.

[31] Del Fatti, N.; Voisin, C.; Christofilos, D.; Vallee, F.; Flytzanis, C., *J. Phys. Chem. A* **2000,** 104, (18), 4321-4326.

[32] Sun, C. K.; Liang, J. C.; Yu, X. Y., *Phys. Rev. Lett.* **2000,** 84, (1), 179-182.

[33] Bristow, A. D.; Wells, J. P. R.; Fan, W. H.; Fox, A. M.; Skolnick, M. S.; Whittaker, D. M.; Tahraoui, A.; Krauss, T. F.; Roberts, J. S., *Appl. Phys. Lett.* **2003,** 83, (5), 851-853.

[34] Link, S.; El-Sayed, M. A., *Int. Rev. Phys. Chem.* **2000,** 19, (3), 409-453.

[35] Del Fatti, N.; Voisin, C.; Chevy, F.; Vallee, F.; Flytzanis, C., *J. Chem. Phys.* **1999,** 110, (23), 11484-11487.

[36] Huang, W. Y.; Qian, W.; El-Sayed, M. A., *Nano Lett.* **2004,** 4, (9), 1741-1747.

[37] Huang, W. Y.; Qian, W.; El-Sayed, M. A., *J. Phys. Chem. B* **2005,** 109, (40), 18881-18888.

[38] Hartland, G. V., *Annu. Rev. Phys. Chem.* **2006,** 57, 403-430.

[39] Lamb, H., *Proc. London Math. Soc.* **1882,** 13, 189.

[40] Bullen, K. E.; Bolt, B. A., *An introduction to the theory of seismology*. Cambridge: New York, 1985.

[41] de Lima, M. M.; Santos, P. V., *Reports on Progress in Physics* **2005,** 68, (7), 1639-1701.

CHAPTER 8

PHOTOTHERMAL RESHAPING OF PRISMATIC GOLD NANOPARTICLES IN PERIODIC MONOLAYER ARRAYS BY FEMTOSECOND LASER PULSES

Abstract

The prismatic gold nanoparticles in the periodic monolayer arrays prepared with the nanosphere lithography (NSL) technique can be reshaped with femtosecond laser pulses at different powers and wavelengths. At 400 nm, changes in the original prismatic particles into tip-rounded, tripodal, and spherical shapes are observed as the laser power density increases. The formation of tip-rounded nanoprisms is attributed to the dewetting properties of gold on quartz surface, a decreased melting temperature at the prism tips, and the intense electromagnetic energy at the tips. Formation of tripodal nanoparticles is attributed to the inhomogeneous heating and lattice rearrangement of the as-deposited nanoparticles to a metastable state, which is more stable than the prismatic shape but less stable than the spherical shape. With 800 nm femtosecond laser irradiation, only tip-rounded nanoprisms are observed. This is attributed to the fact that as the prismatic shape is deformed, the plasmon absorption band blue shifts, which reduce the absorption coefficient at 800 nm, thus reducing the photothermal heating of the particle. No spherical nanoparticle are formed with 800 nm laser irradiation at the laser powers used because the transformed tripodal particles will not absorb the required energy to overcome the thermodynamic barrier in order to form the spherical shape due to this blue

shift of the absorption band. With 700 nm femtosecond laser irradiation, the tip-rounded and tripod nanoparticles are also formed with only a few spherical particles at the higher laser power densities. From the results of this work, it is shown that by changing the wavelength and power of the femtosecond laser, one can control the shape of the particles formed from the original prismatic nanoparticles. This work has been published in *J. Appl. Phys.* **2005,** 98, (11), 114301.

8.1 Introduction

Great interest has been directed lately to the interaction between plasmonic metal nanoparticles and pulsed lasers [1-14]. Unlike traditional thermal processing techniques, the ultrafast pulsed laser processing of metal nanoparticles has two distinct merits. Firstly, the irradiation of metallic nanoparticles with pulsed lasers results in an ultrafast temperature rise in the nanoparticle lattice (within a few picoseconds when using femtosecond laser pulses), while the temperature of the environment remains constant initially. Since the phonon-phonon relaxation times are usually on the order of several hundreds of picoseconds [5,7], pulsed laser irradiation can lead to size and shape changes of the nanoparticles before the deposited laser energy is given to the surrounding medium. Secondly, ultrafast laser pulses have extremely high peak intensities at substantially reduced total laser energy, which makes the processing of materials with ultrafast laser pulses inherently different from traditional thermal processing techniques. For example, the ablation and ionization of nanomaterials can be easily induced with ultrafast laser irradiation. This special property leads to the important chemical and physical

applications of short-pulsed lasers for preparation and modification of nanoparticles. Metallic nanoparticles have been synthesized with pulsed laser ablation of metallic bulk material in solution [15-23] and pulsed laser deposition on substrate [24-27]. It is also found that the pulsed laser is a convenient tool to control the size and shape distribution of an inhomogeneous nanoparticle sample in colloidal solutions [28-30], on substrates [27,31,32], and in glass matrices [12,13].

In the majority of pulsed laser photothermal studies, nanoparticles were randomly distributed in media. The total energy of the laser pulse was used as the control parameter and the final irradiated products were measured, which normalized the positional variation in the pulse energy associated with the Gaussian distribution of the beam. We report here on a more detailed study of a femtosecond laser induced photothermal reshaping of a monolayer two-dimensional array of highly monodisperse periodic gold prismatic nanoparticles. Assuming the laser pulses have a Gaussian distribution, different laser irradiation intensities induced shape and optical property changes can be determined accurately with SEM and micro-absorption measurements.

8.2 Experimental Section

The nanoparticle was fabricated on a quartz substrate using the second version NSL technique (Concentration Optimized Self-assembly). The experimental details are expounded on in Chapter 2 (Section 2.1.2). The diameter of the polystyrene (PS) spheres used in our experiments was $0.45\,\mu m$. The mask was mounted in a thermal evaporator (Denton DV-502A) to deposit 30 nm thick gold (99.999%, Alfa Aesar) into the voids between spheres. The thickness of the deposited metal was monitored by a quartz crystal

thickness monitor (Inficon). After deposition, the PS spheres were removed by sonication in absolute ethanol. The formed silver and gold prismatic monolayer nanoparticle arrays were checked using a scanning electron microscope (SEM).

The details of the femtosecond laser pump-probe experiment are described in Chapter 2 (Section 2.6). The 400 nm laser pulse was generated by the second harmonic of the 800 nm fundamental. The 700 nm laser was produced with optical parametric oscillators (TOPAS [Traveling-wave Optical Parametric Amplifier of Superfluorescence] generator from Light Conversion, Vilnius, Lithuania). The sample was irradiated with femtosecond laser pulses for 3 min. The size of the laser spot used (150–250 μm in diameter) was larger than the resolution of the micro-absorption experiments ($3.75 \times 3.75\ \mu m^2$) and the SEM images recorded ($1.50 \times 1.50\ \mu m^2$). It was possible to observe the changes of the absorption spectra and the SEM images as a function of distance from the center of the laser pulse. Thus, for any laser power, the laser intensity decreases as a function of distance from the spot of the maximum intensity. For any specific total pulse energy (which can be altered by adding neutral density filters), a study of the effect of energy on the nanoparticle shape can be examined.

We assumed the energy of the laser pulse had a Gaussian distribution. The transverse profile of the optical intensity of a Gaussian laser beam [33] is

$$I(r,z) = \frac{2P}{\pi w(z)^2} \exp\left(-2\frac{r^2}{w(z)^2}\right) \tag{8-1}$$

where P is the total power in the beam and $w(z)$ is the beam radius. The smallest beam radius w_0 occurs at $z = 0$, where the Gaussian beam has a flat phase profile.

The radius and power distribution of the laser pulse were determined from the SEM measurement of the laser irradiation spot. In Eq. (8-1), $w(z)$ is the only unknown and can be calculated by assuming the sample is placed at $z = 0$. The radius of the irradiation spot on the sample then changes with the power of the laser beam. Under two different total powers, P_1 and P_2, the laser power intensity $I(r_1)$ at the edge of the laser irradiation spot 1 is equal to intensity $I(r_2)$ at the edge of the laser irradiation spot 2, so we have

$$\frac{2P_1}{\pi w_0^{\,2}} \exp\left(-2\frac{r_1^2}{w_0^{\,2}}\right) = \frac{2P_2}{\pi w_0^{\,2}} \exp\left(-2\frac{r_2^{\,2}}{w_0^{\,2}}\right) \tag{8-2}$$

thus,

$$w_0^{\,2} = -2(r_1^2 - r_2^{\,2})\left(\ln\frac{P_2}{P_1}\right)^{-1} \tag{8-3}$$

and r_1 and r_2 can be measured from the SEM image of the two laser irradiation spots where the array nanoparticles have the same changes. Then the power intensity at any radius r is given by

$$I(r) = \frac{2P}{\pi w_0^{\,2}} \exp\left(-2\frac{r^2}{w_0^{\,2}}\right) \tag{8-4}$$

The micro-absorption spectrum is recorded on a SEE 1100 Micro-spectrometer in transmission mode and the examined area is $3.75 \times 3.75\ \mu m^2$ ($50\times$ objective lens). With the micro-spectrometer, the laser irradiation spot can be optically viewed directly, which allows us to record the absorption spectra of the laser irradiated spot with a spatial resolution of the examined area. A series of absorption spectra and SEM images are taken

from different areas of the laser irradiation spot with various distances *r* from the center, which correspond to different laser power intensities $I(r)$ calculated by Eq. (8-4).

8.3 Results and Discussion

8.3.1 Photothermal Reshaping of Prismatic Au Nanoparticles with 400 nm Femtosecond Laser:

A series of irradiation experiments using 400 nm femtosecond laser pulses were performed on a sample made with 0.45 μm polystyrene spheres by the NSL technique [34-36]. The size of the as-deposited nanoparticle was 103.7 ± 6.8 nm in bisector based on a measurement of over 500 particles from SEM measurements. The thickness of the nanoparticles was 30 nm monitored by quartz crystal thickness monitor. In **Figure 8-1**, the spectrum represented by filled black squares (■) indicates that the prismatic nanoparticle array had a strong absorption band with a maximum at 850 nm prior to laser irradiation. The SEM image in **Figure 8-2a** shows the nanoparticle array before laser irradiation. The micro-absorption spectra also show a weak band around 570 nm, on the blue side of the main plasmon resonance band. This weak surface plasmon band was also observed by Mohamed [37] from triangular gold nanoplatelets. The higher energy weak plasmon resonance bands in the gold array samples were due to in-plane quadrupole resonance transitions and the strong absorption bands shown in **Figure 8-1** were due to in-plane dipolar transitions [38].

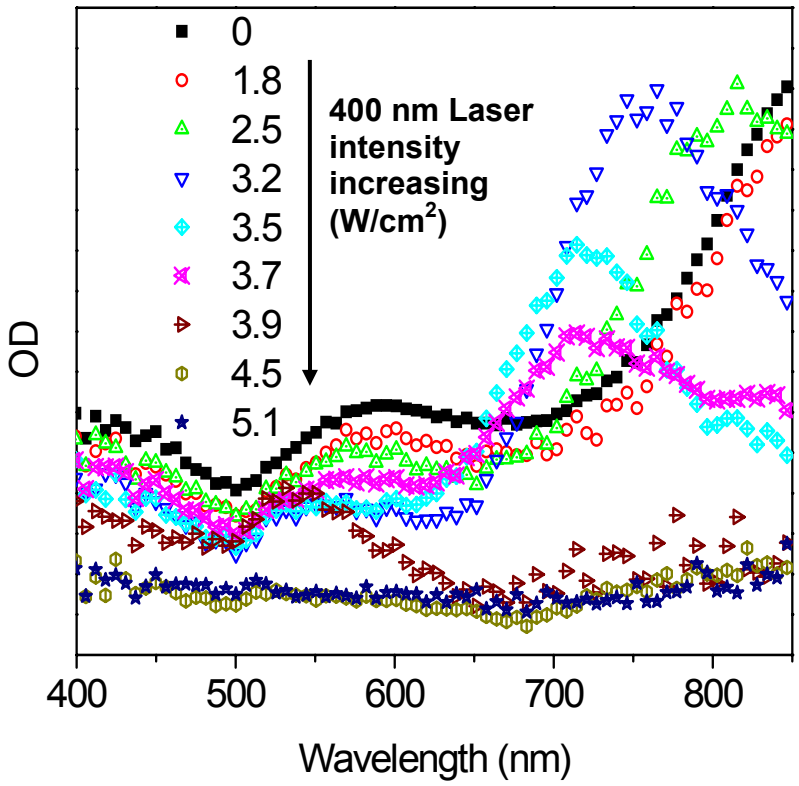

Figure 8-1: Micro-absorption spectra of a periodic monolayer array of prismatic gold nanoparticles after irradiation with 400 nm femtosecond laser pulses at different intensities. The numbers in the plot correspond to different power densities (W/cm^2) of the examined region on the substrate within the laser profile calculated by assuming the energy in the laser pulse has a Gaussian distribution. The arrow shows the energy density goes from low to high as one moves from the edge to the center of the laser irradiation profile on the array. The diameter of the laser spot on the array was 250 μm.

There is also a dip around 500 nm which result from the gold film [39] or large defects formed during the sample preparation. The absorption spectrum increases below 500 nm due to electron transitions from the Au 5*d* band to empty 6*sp* bands above the

Fermi level (interband transitions) [40]. With 400 nm laser light, both of the free electrons and the 5*d* electrons can be excited.

As shown in **Figure 8-1**, the in-plane dipolar transition band blue shifts as the power density of the laser irradiation increases from 0 to 3.2 W/cm^2, which could be due to the photothermal annealing of the prismatic nanoparticle arrays. Similar phenomena have been observed for thermal annealing [41] and solvent treatment [42] of Ag prismatic nanoparticle arrays. In the thermal annealing experiment, Van Duyne and co-workers [41] found that silver nanoparticles change from a triangular to an elliptical shape after annealing at 300 °C for one hour. This shape change results in a blue shift of the surface plasmon absorption maximum by more than 200 nm. In the solvent treatment experiment [42], a 100 nm blue shift of the absorption peak was observed after exposure to two solvent cycles of water and methanol. AFM measurement of the sample before and after the solvent exposure reveals that the height of the particle increases 4 nm and the tips of the nanoparticles become round. Both of these changes induce a blue shift of the surface plasmon absorption maximum [41]. **Figure 8-2b** is an SEM image of the sample after irradiation by 400 nm femtosecond laser at 3.1 W/cm^2, which clearly shows the rounding of the apexes of prismatic nanoparticles. This is due to the dewetting properties of gold on a quartz surface and a lower melting temperature at the apex due to the size-dependent surface melting temperature [43-45]. Thus, the tips of the prismatic nanoparticles are initially melted and retract to form rounded tips.

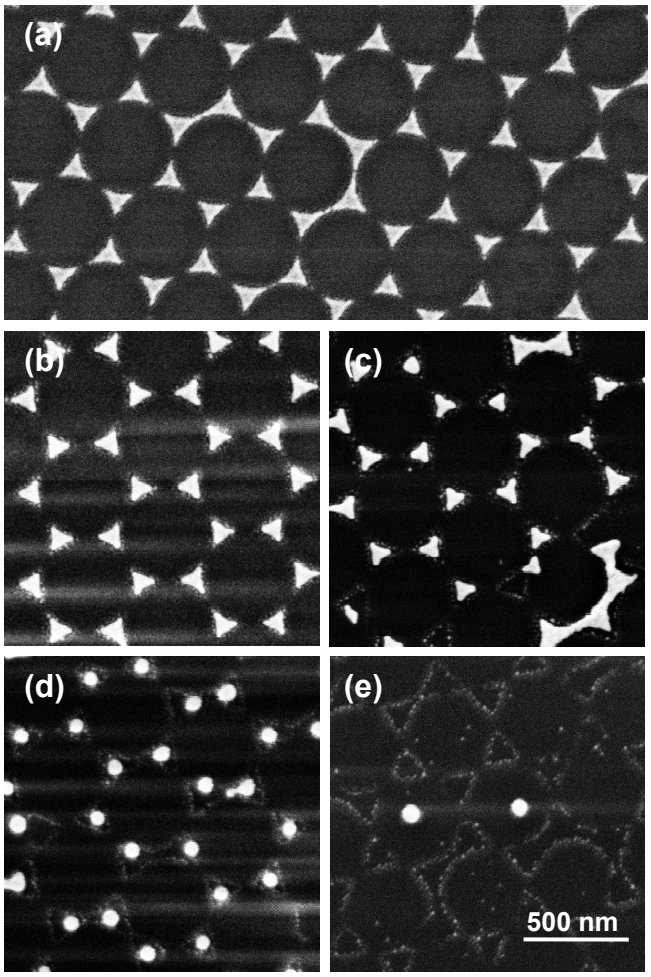

Figure 8-2: The SEM images of periodic monolayer prismatic gold nanoparticle arrays at exposed regions within the laser pulse profile (i.e. at different laser power densities) (a) before and (b-e) after irradiation with 400 nm femtosecond laser. From the Gaussian laser energy distribution profile, the calculated laser energy densities are: (b) 3.1 (c) 3.5, (d) 3.9, and (e) 5.1 W/cm^2.

As the power density increases above 3.5 W/cm^2, the intensity of the absorption bands decreases because the cross-section of the particle becomes smaller (**Figure 8-1**). The spectra also show a tail at the red side of the dipolar plasmon absorption maximum, which may be due to the large defects on the sample that are hard to change under these laser power densitites. Quite interestingly, we found tripod-shaped particles when we

measure the SEM image in the same region as shown in **Figure 8-2c**. Since the spherical shape is the most thermodynamically favored particle shape with a lower surface energy than any other shapes, the gold tripodal nanoparticles are quite unusual. Apparently, the gold nanoparticle is not totally melted, else it would make the shape transformation from prismatic directly to spherical (**Figure 8-2d**). It is obvious that the tripodal shape has a lower surface energy than that of the prismatic shape.

A possible explanation of the formation of tripod-shaped nanoparticles by femtosecond laser irradiation is the lattice rearrangement [46] of as-deposited gold prismatic array nanoparticles to form a metastable tripodal shape. This is supported by the successful synthesis of gold tripodal nanocrystals in solution. Schatz, Hupp and co-workers [47] showed that the gold tripod can be formed within a mixture solution of sodium citrate and 30 % H_2O_2. The citrate method is one of the most well known methods for the synthesis of spherical gold nanoparticles [48]. In this method, citrate acts not only as a reducing agent to reduce $HAuCl_4$, but also as the capping material to stabilize the synthesized gold nanoparticles. With the assistance of the H_2O_2 at room temperature, the gold tripod can be formed with 40-50 % yield [47]. With the same citrate capping agent, both the gold spherical and tripodal nanoparticles can be synthesized, indicating that the tripodal shape is a metastable shape that can coexist with the spherical shape. This supports our conclusion that the tripodal shape is a metastable state of gold nanoparticles on their way to the most stable spherical shape as shown in **Figure 8-3**. With an appropriate laser irradiation energy density (~ 3.5 W/cm^2 in this case), the supported prismatic nanoparticles can be transformed to the tripodal shape, while the energy is not sufficient to change the particle further to the spherical shape.

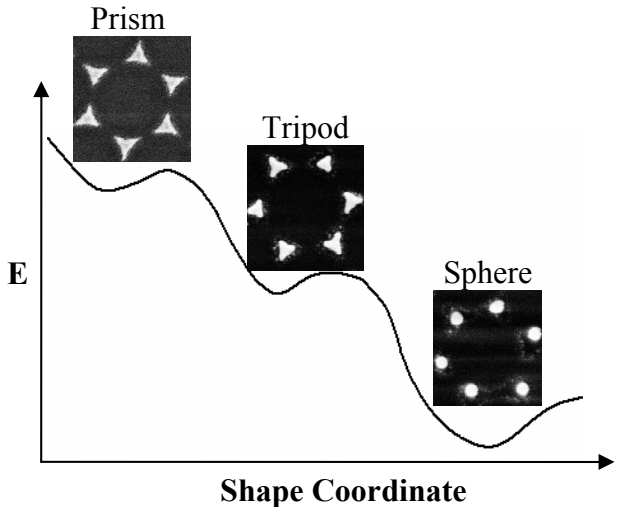

Figure 8-3: A proposed energy potential curve of nanoparticle arrays of different shapes. The surface potential decreases as the original prismatic nanoparticle changes to a tripodal shape and finally to a spherical shape as the laser energy input increases. The tripodal shape is believed to be a metastable configuration during the transformation (the gold tripod nanoparticles have also been synthesized in solution) [47,49].

As the power density of the laser irradiation reaches 3.9 W/cm^2, we find that the dipolar absorption band at 850 nm completely disappears, while an absorption band at 540 nm appears (**Figure 8-1**). The SEM image taken in the same region (**Figure 8-2d**) shows that a spherical gold nanoparticle array is formed with the diameter of the particles around 70 nm. The formation of the spherical shape suggests that the absorbed irradiation energy is sufficient to melt the entire particle to form the most thermodynamically stable shape. In aqueous solution, a 70 nm gold nanosphere will give surface plasmon absorption at 553 nm [7,14]. The small difference between the surface plasmon absorption maxima is a result of the difference in the dielectric constants of the surrounding medium [42].

The absorption band around 540 nm disappears when the power density of the laser irradiation is increased above 4.5 W/cm^2 (**Figure 8-1**). The SEM image acquired in this area indicates that most of the nanoparticles have disappeared, likely due to ablation of the gold nanoparticles array (**Figure 8-2e**).

8.3.2 Photothermal Reshaping of Prismatic Au Nanoparticles with 800 nm Femtosecond Laser:

Using 400 nm laser pulses at appropriate power densities, we can reshape prismatic gold nanoparticles into tripodal and spherical shaped particles. Upon using an 850 nm laser as the irradiation source to excite the dipolar surface plasmon, Schatz's calculation showed that the tips absorb more of the incident laser light [50] than the sides of the prismatic array nanoparticles. This induces a higher temperature at the tips than at the sides. As a result, the tips of the nanoparticles become rounded.

Figure 8-4 shows a change in the absorption spectra due to irradiation of the gold prismatic nanoparticles with 800 nm femtosecond laser pulses. As the power density increases, the dipolar resonance absorption band initially broadens (3.3 W/cm^2) and then forms two populations (3.6 W/cm^2), one with a peak at 750 nm and the other at 850 nm with an absorption dip at 800 nm. This split absorption spectrum results from the dual absorption of reshaped particles and unchanged particles. As the power density increases to 4.5 W/cm^2, the absorption band at 850 nm decreases while the band at 750 nm increases in intensity. This intensity shift indicates that the prismatic nanoparticles with an absorption at 850 nm photothermally change to particles with a shorter absorption maximum at 750 nm. The SEM images taken in the same area further support this

explanation. **Figure 8-5a** is recorded within the area that has a power density of 2.1 W/cm^2. No obvious shape change is observed and the absorption spectrum only blue shifts slightly, as shown in **Figure 8-4**. **Figure 8-5b** is from the area that has a laser energy density of 3.0 W/cm^2. The corresponding image shows that the tips of the smaller particles are rounded, which causes the broadening of the absorption spectrum. As the power density increases to 4.5 W/cm^2, the tips of most of the particles become rounded, thus the absorption at 750 nm increases (**Figure 8-4**).

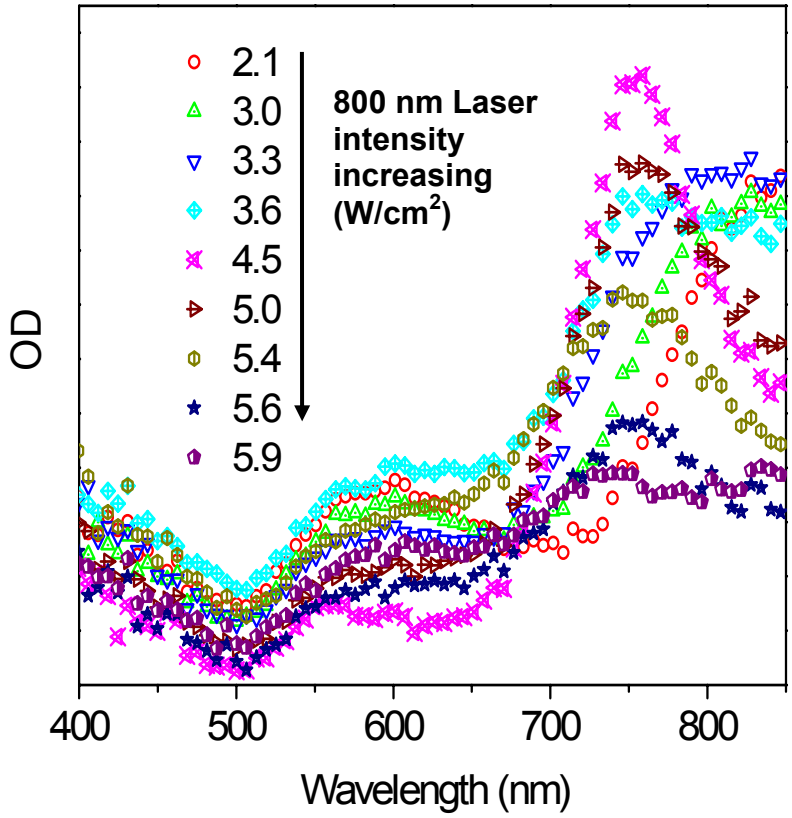

Figure 8-4: Micro-absorption spectra of a periodic monolayer array of prismatic gold nanoparticles after 800 nm femtosecond laser irradiation at various intensities. The numbers in the plot correspond to different power densities (W/cm^2) of the examined region on the substrate within the laser profile, calculated by assuming the energy in the laser pulse has a Gaussian distribution. The arrow indicates that the energy density moves from low to high as the selected area shifts from the edge to the center of the laser irradiation profile on the array. The diameter of the laser spot on the array is 250 μm.

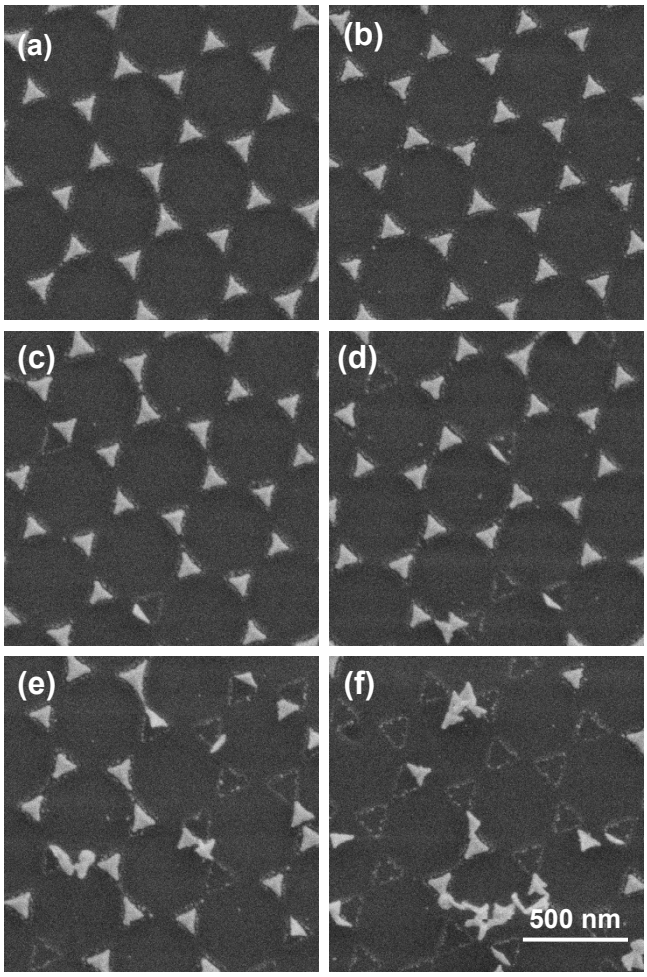

Figure 8-5: SEM images of the periodic monolayer prismatic gold nanoparticle array at various exposed regions within the laser pulse profile (i.e. at different laser power densities) after irradiation with 800 nm femtosecond laser. From the Gaussian laser energy distribution profile, the calculated laser energy densities are (a) 2.1, (b) 3.0, (c) 4.5, (d) 5.0, (e) 5.6, and (f) 5.9 W/cm^2.

As the power density further increases to 5.0–5.6 W/cm^2, the plasmon absorption bands at 750 nm drop in intensity dramatically, while their maxima don't change. This suggests that the shape of the nanoparticles doesn't change but rather the particle density decreases (the particles that have an absorption band at 750 nm). From the SEM images of the area (**Figure 8-5d** and **e**), we can see that some of the particles are removed from

their original location and begin to contact each other, which will shift the plasmon absorption band substantially because of the increase in the size of the joined nanoparticles, which would lead to a decrease in the absorption at 750 nm, as observed. We also observe that some of the particles are turned on their sides. The calculation on silver prismatic nanoparticles by Schatz and co-workers [50] shows that only the weaker out-of-plane plasmon resonance absorption will be excited when the polarization of the incident light is along the z-axis of the particle (perpendicular to the prism surface). Both of these effects cause a decrease in the dipole resonance absorption of the array nanoparticles at 750 nm.

When the power density of the laser irradiation increases to 5.9 W/cm^2, most of the array nanoparticles leave their original positions and form large aggregates. This phenomenon further decreases the absorption at 750 nm and increases the absorption at the red side of the plasmon band (> 820 nm).

From the SEM measurement (**Figure 8-5**), we don't observe spherical nanoparticles in the array even when the power density is increased to 5.9 W/cm^2. This is most likely due to the fact that rounding the tips leads to shifting of the surface plasmon band to ~750 nm. Thus, particle absorption at 800 nm becomes weak. This decreases the probability of heating the nanoparticles as a result of exposure to the 800 nm laser pulses. The observation that most of the particles are removed from their original positions suggests that the absorbed energy is sufficient to break the nanoparticle-substrate "bonds" but not sufficient to overcome the barrier to form the spherical shape.

8.3.3 Photothermal Reshaping of Prismatic Au Nanoparticles with 700 nm Femtosecond Laser:

Since the nanoparticle weakly absorbs the 800 nm laser after its tips are rounded, we used a 700 nm laser as the irradiation source to ensure that the tip-rounded nanoparticle could further absorb energy in order to further alter the shape. **Figure 8-6** shows the changes in the absorption spectra with increasing power density of the femtosecond laser pulses. The plasmon band blue shifts to 750 nm by increasing the laser power density from 1.8 to 2.8 W/cm^2. As the power density increases to 3.0 W/cm^2, another band at 660 nm appears. The band intensity at 660 nm continuously increases when the laser power density approaches 3.1 W/cm^2. At the same time, the band intensity at 750 nm decreases. There is also a dip located at 700 nm between the two bands. This is similar to the observations made when the 800 nm laser is used as the excitation source, where two populations result from the absorption of the reshaped particles and the unchanged particles.

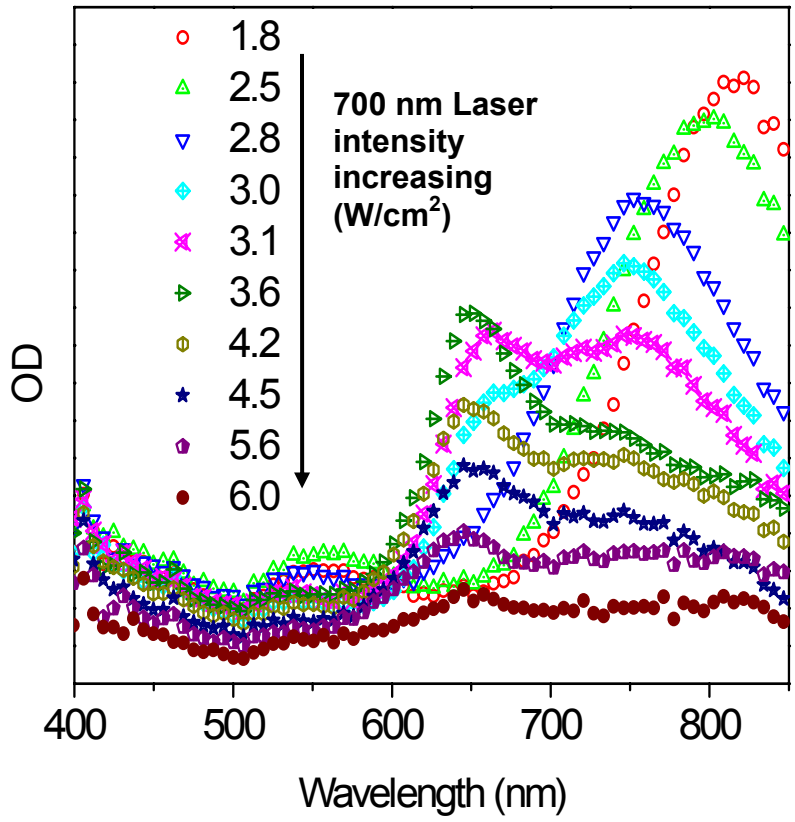

Figure 8-6: Micro-absorption spectra of a periodic monolayer array of prismatic gold nanoparticles after irradiation with 700 nm femtosecond laser pulses at different intensities. The numbers in the plot correspond to various power densities (W/cm^2) of the examined region on the substrate within the laser profile calculated by assuming the energy in the laser pulse has a Gaussian distribution. The arrow shows the energy density increasing from low to high as the selected area moves from the edge to the center of the laser irradiation profile on the array. The diameter of the laser spot on the array is 250 μm .

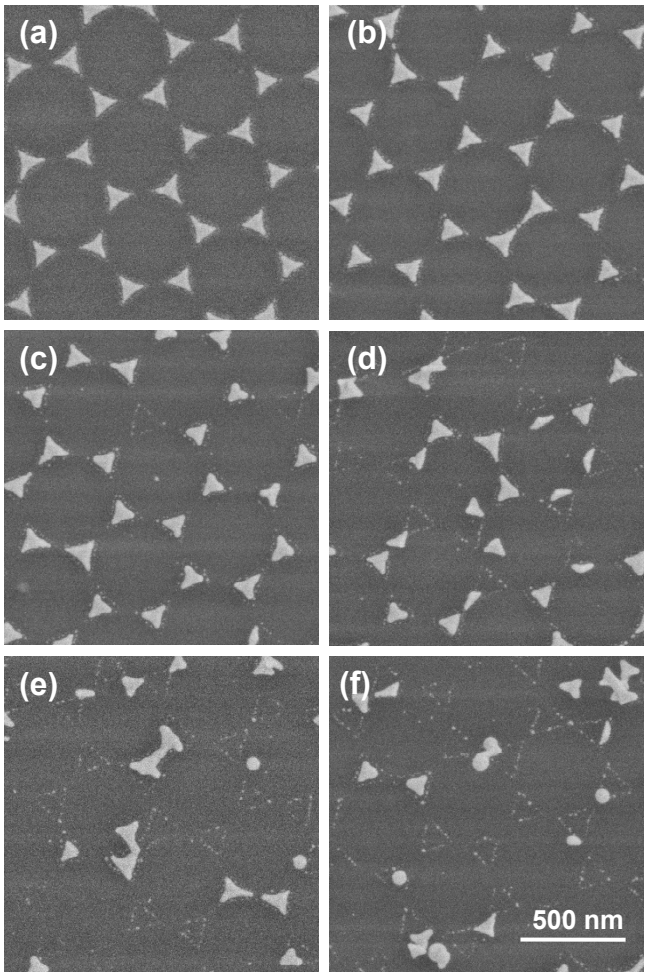

Figure 8-7: SEM images of the periodic monolayer prismatic gold nanoparticle arrays at exposed regions within the laser pulse profile (i.e. at different laser power densities) after irradiation with 700 nm femtosecond laser pulses. From the Gaussian laser energy distribution profile, the calculated laser densities are (a) 1.8, (b) 2.8, (c) 3.1, (d) 4.5, (e) 5.6, and (f) 6.0 W/cm^2.

The band at 660 nm continuously decreases as the power density increases from 3.6 to 6.0 W/cm^2, which is also observed when we excite the array nanoparticles with the 800 nm laser. Again, the reason that the shift in the plasmon bands does not occur past 660 nm is that the particles' absorption crosssections at 700 nm decrease greatly as the particles' shape changes. The intensity of the absorption at 660 nm decreases because

some of the particles are oriented on their sides with the incident light parallel to the particle surface or the particles are removed from their original position and form aggregates (**Figure 8-7d-f**). Both of these changes decreas the number of particles that absorb at 660 nm. The band at 750nm not only decreases in intensity but also shifts to longer wavelength as a result of forming larger aggregates. From **Figure 8-7e-f**, we can see some nanospheres that formed. This is most likely due to two photon absorption. The nanoparticles absorb enough energy from one laser pulse to alter the entire nanoparticle shape, resulting in aspherical nanoparticle.

We also see tripod-shaped gold nanoparticles formed at 3.1 W/cm^2 (**Figure 8-7c**), even though it is not as obvious as the tripod formed when we use 400 nm laser pulses. The formation of the metastable tripodal shape can also be explained by the laser induced lattice rearrangement [46] of as-deposited gold prismatic nanoparticles. Our results suggest that the energy barrier of transformation of gold nanoparticles from prismatic to tripodal shapes is smaller than that from prismatic shape to the spherical shape. Thus it is kinetics rather than thermodynamics that determines the nanoparticle shape transformation, similar to synthetic methods in solution [51].

8.4 Conclusion

The monolayer periodic gold prismatic nanoparticles can be reshaped using femtosecond laser pulses from the prismatic shape to a tip rounded triangular shape, to a tripodal shape, and finally to a spherical shape by increasing the power density of laser pulses at 400 nm. The tip rounded nanoprisms formed because of the dewetting properties of gold on quartz and the low melting temperature at the tips. The formation of

the tripodal nanoparticles is attributed to their increased stability compared to the prismatic shape. With the 800 nm femtosecond laser irradiation, only tip rounded nanoprisms are observed. With 700 nm femtosecond laser irradiation, the tip rounded and tripodal nanoparticles and very few spheres (at high power densities) are formed. Both 800 nm and 700 nm laser irradiation show a two population absorption spectra (separated band) under appropriate power densities, which indicate that the prismatic nanoparticles with an strong absorption at 850 nm photothermally change to a particle with a shorter absorption maximum.

8.5 References

[1] Del Fatti, N.; Voisin, C.; Christofilos, D.; Vallee, F.; Flytzanis, C., *J. Phys. Chem. A* **2000,** 104, (18), 4321-4326.

[2] Del Fatti, N.; Voisin, C.; Chevy, F.; Vallee, F.; Flytzanis, C., *J. Chem. Phys.* **1999,** 110, (23), 11484-11487.

[3] Hodak, J. H.; Henglein, A.; Hartland, G. V., *J. Phys. Chem. B* **2000,** 104, (21), 5053-5055.

[4] Hodak, J. H.; Henglein, A.; Hartland, G. V., *J. Phys. Chem. B* **2000,** 104, (43), 9954-9965.

[5] Perner, M.; Bost, P.; Lemmer, U.; vonPlessen, G.; Feldmann, J.; Becker, U.; Mennig, M.; Schmitt, M.; Schmidt, H., *Phys. Rev. Lett.* **1997,** 78, (11), 2192-2195.

[6] Perner, M.; Gresillon, S.; Marz, J.; von Plessen, G.; Feldmann, J.; Porstendorfer, J.; Berg, K. J.; Berg, G., *Phys. Rev. Lett.* **2000,** 85, (4), 792-795.

[7] Link, S.; El-Sayed, M. A., *J. Phys. Chem. B* **1999,** 103, (40), 8410-8426.

[8] Mohamed, M. B.; Ahmadi, T. S.; Link, S.; Braun, M.; El-Sayed, M. A., *Chem. Phys. Lett.* **2001,** 343, (1-2), 55-63.

[9] Link, S.; Hathcock, D. J.; Nikoobakht, B.; El-Sayed, M. A., *Adv. Mater.* **2003,** 15, (5), 393-396.

[10] Link, S.; Furube, A.; Mohamed, M. B.; Asahi, T.; Masuhara, H.; El-Sayed, M. A., *J. Phys. Chem. B* **2002,** 106, (5), 945-955.

[11] Link, S.; El-Sayed, M. A., *J. Chem. Phys.* **2001,** 114, (5), 2362-2368.

[12] Stepanov, A. L.; Hole, D. E.; Bukharaev, A. A.; Townsend, P. D.; Nurgazizov, N. I., *Appl. Surf. Sci.* **1998,** 136, (4), 298-305.

[13] Kaempfe, M.; Rainer, T.; Berg, K. J.; Seifert, G.; Graener, H., *Appl. Phys. Lett.* **1999,** 74, (9), 1200-1202.

[14] Huang, W. Y.; Qian, W.; El-Sayed, M. A., *Nano Lett.* **2004,** 4, (9), 1741-1747.

[15] Mafune, F.; Kohno, J.; Takeda, Y.; Kondow, T.; Sawabe, H., *J. Phys. Chem. B* **2000,** 104, (39), 9111-9117.

[16] Mafune, F.; Kohno, J.; Takeda, Y.; Kondow, T.; Sawabe, H., *J. Phys. Chem. B* **2001,** 105, (22), 5114-5120.

[17] Kabashin, A. V.; Meunier, M., *J. Appl. Phys.* **2003,** 94, (12), 7941-7943.

[18] Sylvestre, J. P.; Kabashin, A. V.; Sacher, E.; Meunier, M.; Luong, J. H. T., *J. Am. Chem. Soc.* **2004,** 126, (23), 7176-7177.

[19] Tsuji, T.; Iryo, K.; Watanabe, N.; Tsuji, M., *Appl. Surf. Sci.* **2002,** 202, (1-2), 80-85.

[20] Compagnini, G.; Scalisi, A. A.; Puglisi, O., *J. Appl. Phys.* **2003,** 94, (12), 7874-7877.

[21] Tsuji, T.; Kakita, T.; Tsuji, M., *Appl. Surf. Sci.* **2003,** 206, (1-4), 314-320.

[22] Chen, Y. H.; Yeh, C. S., *Colloids Surf. A-Physicochem. Eng. Asp.* **2002,** 197, (1-3), 133-139.

[23] Dolgaev, S. I.; Simakin, A. V.; Voronov, V. V.; Shafeev, G. A.; Bozon-Verduraz, F., *Appl. Surf. Sci.* **2002,** 186, (1-4), 546-551.

[24] Ausanio, G.; Barone, A. C.; Iannotti, V.; Lanotte, L.; Amoruso, S.; Bruzzese, R.; Vitiello, M., *Appl. Phys. Lett.* **2004,** 85, (18), 4103-4105.

[25] Gonzalo, J.; Babonneau, D.; Afonso, C. N.; Barnes, J. P., *J. Appl. Phys.* **2004,** 96, (9), 5163-5168.

[26] Pham, M. T. N.; Boukamp, B. A.; Rijnders, G.; Bouwmeester, H. J. M.; Blank, D. H. A., *Appl. Phys. A: Mater. Sci. Process.* **2004,** 79, (4-6), 907-910.

[27] Chen, X. Y.; Lu, Y. F.; Wu, Y. H.; Cho, B. J.; Yang, B. J.; Liew, T. Y. F., *J. Vac. Sci. Technol. B* **2004,** 22, (4), 1731-1737.

[28] Link, S.; Burda, C.; Nikoobakht, B.; El-Sayed, M. A., *J. Phys. Chem. B* **2000,** 104, (26), 6152-6163.

[29] Mafune, F.; Kohno, J.; Takeda, Y.; Kondow, T., *J. Phys. Chem. B* **2003,** 107, (46), 12589-12596.

[30] Miranda, M. H. G.; Falcao, E. L.; Rodrigues, J. J.; de Araujo, C. B.; Acioli, L. H., *Phys. Rev. B* **2004,** 70, (16), 161401.

[31] Wenzel, T.; Bosbach, J.; Goldmann, A.; Stietz, F.; Trager, F., *Appl. Phys. B: Lasers Opt.* **1999,** 69, (5-6), 513-517.

[32] Bosbach, J.; Martin, D.; Stietz, F.; Wenzel, T.; Trager, F., *Appl. Phys. Lett.* **1999,** 74, (18), 2605-2607.

[33] Skinner, D. R.; Whitcher, R. E., *J. Phys. E: Sci. Instrum.* **1972,** 5, (3), 237-238.

[34] Hulteen, J. C.; Van Duyne, R. P., *J. Vac. Sci. Technol. A* **1995,** 13, (3, Pt. 2), 1553-8.

[35] Wang, X. D.; Summers, C. J.; Wang, Z. L., *Nano Lett.* **2004,** 4, (3), 423-426.

[36] Kosiorek, A.; Kandulski, W.; Chudzinski, P.; Kempa, K.; Giersig, M., *Nano Lett.* **2004,** 4, (7), 1359-1363.

[37] Mohamed, M. B. Metallic and semiconductor nanoparticles : synthesis, characterization and femtosecond laser spectroscopic studies. Ph. D. Thesis, Georgia Institute of Technology, Atlanta, GA, 2002.

[38] Jin, R. C.; Cao, Y. C.; Hao, E. C.; Metraux, G. S.; Schatz, G. C.; Mirkin, C. A., *Nature* **2003,** 425, (6957), 487-490.

[39] Norrman, S.; Andersson, T.; Granqvist, C. G.; Hunderi, O., *Phys. Rev. B* **1978,** 18, (2), 674-695.

[40] Hodak, J. H.; Henglein, A.; Hartland, G. V., *J. Chem. Phys.* **1999,** 111, (18), 8613-8621.

[41] Jensen, T. R.; Malinsky, M. D.; Haynes, C. L.; Van Duyne, R. P., *J. Phys. Chem. B* **2000,** 104, (45), 10549-10556.

[42] Malinsky, M. D.; Kelly, K. L.; Schatz, G. C.; Van Duyne, R. P., *J. Am. Chem. Soc.* **2001,** 123, (7), 1471-1482.

[43] Hulteen, J. C.; Treichel, D. A.; Smith, M. T.; Duval, M. L.; Jensen, T. R.; Van Duyne, R. P., *J. Phys. Chem. B* **1999,** 103, (19), 3854-3863.

[44] Ercolessi, F.; Andreoni, W.; Tosatti, E., *Phys. Rev. Lett.* **1991,** 66, (7), 911-914.

[45] Lewis, L. J.; Jensen, P.; Barrat, J. L., *Phys. Rev. B* **1997,** 56, (4), 2248-2257.

[46] Wang, Z. L.; Gao, R. P.; Nikoobakht, B.; El-Sayed, M. A., *Journal of Physical Chemistry B* **2000,** 104, (23), 5417-5420.

[47] Hao, E.; Bailey, R. C.; Schatz, G. C.; Hupp, J. T.; Li, S., *Nano Letters* **2004,** 4, (2), 327-330.

[48] Turkevich, J.; Stevenson, P. C.; Hillier, J., *Discuss. Faraday Soc.* **1951,** 11, 55-75.

[49] Chen, S. H.; Wang, Z. L.; Ballato, J.; Foulger, S. H.; Carroll, D. L., *Journal of the American Chemical Society* **2003,** 125, (52), 16186-16187.

[50] Kelly, K. L.; Coronado, E.; Zhao, L. L.; Schatz, G. C., *J. Phys. Chem. B* **2003,** 107, (3), 668-677.

[51] Petroski, J. M.; Wang, Z. L.; Green, T. C.; El-Sayed, M. A., *J. Phys. Chem. B* **1998,** 102, (18), 3316-3320.

CHAPTER 9

GOLD NANOPARTICLE PROPULSION FUELED BY ABSORPTION OF FEMTOSECOND LASER PULSE AT THEIR SURFACE PLASMON RESONANCE

Abstract

Femtosecond laser irradiation of assembled nanoprisms on a quartz substrate at their strong absorbing surface plasmon resonance frequency caused their propulsion from the substrate. This phenomenon was attributed to a pressure generated beneath the particle by ablated gold atoms, calculated to be twenty-five thousand atmospheres. The rapid build up of this pressure under the particle is proposed to create an impulse that propels the nanoparticle away from the substrate within time of 40 ps. From the kinetic energy associated with the flying nanoparticle, an initial velocity of 164 m/s (367 miles/hour) is calculated. These mechanical properties are much more powerful than those recently determined in a Science paper for the same types of nanoparticles when nanosecond pulses are used [1]. In that report, a change in surface energy and in the particle's center of mass is proposed to be the mechanism by which propels the nanoparticle away from the substrate with a velocity of 20 m/s. We also studied the effect of substrate roughness on the propulsion of nanoparticles. This work has been published in *J. Am. Chem. Soc.* **2006**, *128*, 13330-13331.

9.1 Introduction

Many biological functions involve motions on the nanometer length scale, which are fueled by biochemical enzymatic catalysis, electrical energy derived from charge gradients, or optical (solar) energy. In the field of nanotechnology and in the interest of making nano-motors, clever demonstrations of motion fueled by chemical catalysis and electrical energy have recently been demonstrated. Whitesides and co-workers [2] used gases produced in a chemical reaction to fuel autonomous motion. Mallouk and co-workers [3] used a gold-platinum rod that moves in H_2O_2 solution. The platinum catalyzed production of O_2 breaks the hydrogen bonding network in H_2O, creating a gradient in the liquid surface tension, which then induced motion. Zettl and co-workers [4] reported a nanorotor based on converting electrical energy into the rotational motion of a metal plate attached to a multi-walled carbon nanotube. Chien and co-workers [5] described a controllable high-speed rotation of nanowires when they were suspended in water between four microelectrodes with applied ac voltages, each out of phase by ninety degrees.

So far in the published works, only chemical and electrical energy have been used to fuel the motion of nanoparticles. In the present report, photon energy is used to fuel the propulsion of gold nanoprisms. Gold nanoparticles have unique photothermal properties resulting from their characteristic electronic surface plasmon resonance (SPR) [6] and possess extremely large absorption cross-sections. The absorbed energy is rapidly converted into thermal energy on a picosecond time scale [7-10].

It has previously been shown that laser pulses of nanosecond [1] and femtosecond [11] duration at a specific energy melt assembled nanoprisms on a quartz substrate into

spheres. In a recent Science paper [1], Habenicht et al. showed that the melting of nanoprisms on a quartz substrate can lead to lifting of the sphere from the substrate with a velocity of 20 m/s. The energetic gain from the shift in surface energy and the change in the center of mass during the melting process fueled the nanoparticle's lift off.

In the present report, we show that when femtosecond pulses are used and the rate of absorption and heating is increased, a higher energy channel involving atomic ablation takes over, which fuels the prism's dissociation from the substrate. The velocity of the propelled nanoparticle is eight times higher than that produced when the nanoparticle is irradiated with a nanosecond laser pulse, which has a slower heating rate; this increase in the propulsion capabilities is due to a different mechanism being responsible for the particle's motion, namely the rapid build-up of an ultrahigh gold atomic pressure between the prism and the substrate.

9.2 Experimental Section

The nanoparticles were fabricated on a quartz substrate using the third version NSL (Air-Water Interface Self-assembly). The experimental details are introduced in Chapter 2 (Section 2.1.3). The diameter of the polystyrene (PS) spheres used in our experiments was $0.45\,\mu m$. The mask was mounted in a thermal evaporator (Denton DV-502A) to deposit ~ 30 nm of silver or gold (99.999%, Alfa Aesar) into the voids between the spheres. The thickness of the deposited metal was monitored by a quartz crystal thickness monitor (Inficon). After deposition, the PS spheres were removed by sonication in absolute ethanol.

The prepared prismatic nanoparticles have a bisector of 100 nm, a thickness of 34 nm, and a weight of 4 femtograms each. Unlike the vertical sample geometry commonly used in pump-probe experiments, we place our sample substrate horizontally with the nanoparticles on the top surface of the substrate. The laser pulse is directed to irradiate the sample from the top (nanoparticle side).

A Beckman DU-650 spectrophotometer is used to record the absorption spectra of the arrays. The incident light is perpendicular to the array substrate. The transmitted light through the sample has a cross section of several square millimeters.

9.3 Results and Discussion

9.3.1 Propulsion of Gold Prismatic Nanoparticles from Substrate:

Figure 9-1a is an SEM image taken in the region irradiated with a laser pulse energy density of 4.1 mJ/cm^2 at 800 nm. Under this laser irradiation intensity, the absorbed energy is not sufficient to fully dissociate the particle from the substrate. The SEM image clearly shows that these particles had sufficient energy to loose from the substrate but not enough for them to fly. They "stand up" on their bases. Particles 1 and 2 have enough energy to "stand up" perpendicular to the substrate plane, while particle 3 is tilted. These particles receive enough energy to release them from the substrate (i.e., to overcome the adhesion energy); however, the energy is not sufficient to allow them to lift off completely from the substrate. The particles standing on their bases also suggest that the force responsible for the detachment process is anisotropic.

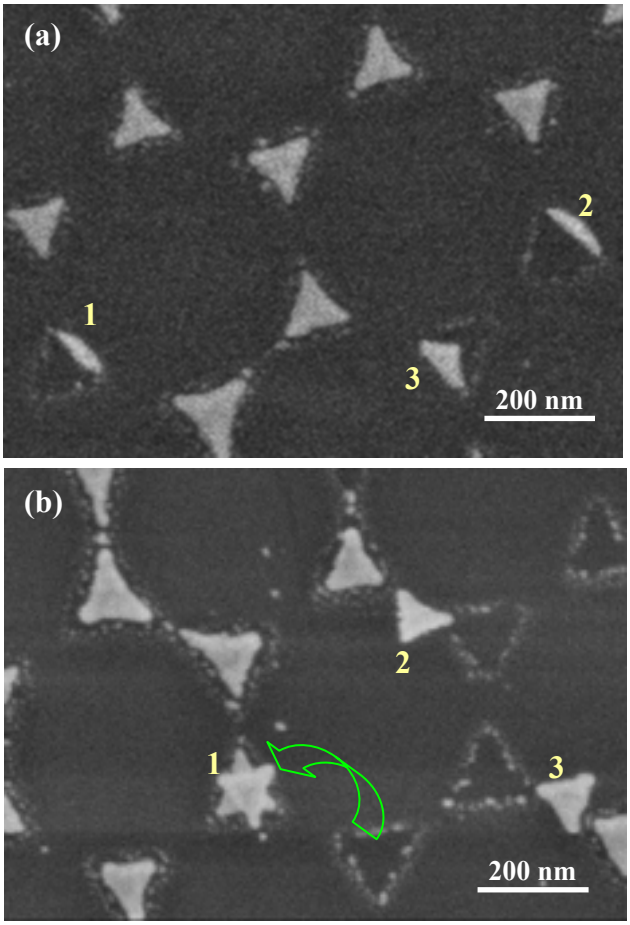

Figure 9-1: (a) An SEM image taken at the femtosecond laser irradiation area with a laser pulse energy density of 4.1 mJ/cm^2. It is clear that particles 1 and 2 stand up vertically, while particle 3 stands at a tilt. (b) Flying prismatic gold nanoprisms: The SEM image of assembled gold nanoprisms in a monolayer array after exposure to femtosecond laser pulses with an energy density of 5.1 mJ/cm^2. It is clear that particle 1 jumped from its original position, flew away, and then landed on top of another particle (green arrow). While maintaining its prismatic shape, it is reduced in size due to atomic ablation. Particles 2 and 3, which absorbed less energy, seem to be "stuck" at one corner but flipped over. The difference in the behavior depends on the intensity of the laser at each prism, the absorption profile of the individual nanoprism, and the anisotropy of the interaction at the substrate-nanoparticle interfaces.

Under a femtosecond laser irradiation intensity of 5.1 mJ/cm^2 at 800 nm, we observe that particle 1 in **Figure 9-1b** lifts up from its original position, flies a certain distance, and lands on top of a second nanoparticle (indicated by the green arrow in

Figure 9-1b). The original position of particle 1 is shown by the dark image decorated by bright small gold clusters. (The clusters are formed during the gold deposition step of the NSL technique by scattered gold atoms). It is clear that the prism that lifted away from its position is smaller in size than both its initial empty location and the nanoprisms that did not dissociate. This observation suggests that atomic ablation has taken place on the flying nanoprisms due to its high energy absorption rate.

The standing configuration of particles 1 and 2 in **Figure 9-1a** is further confirmed by AFM measurement, as shown in **Figure 9-2a**. The particle indicated by the red cursors has a height of 108.6 nm, which is near the bisector length of the original prismatic nanoparticles. We also find that some particles have a height of ~ 70 nm, which is consistent with a particle that is tilted by an angle of 42 degree from the substrate surface, like particle 3 shown in **Figure 9-1a**.

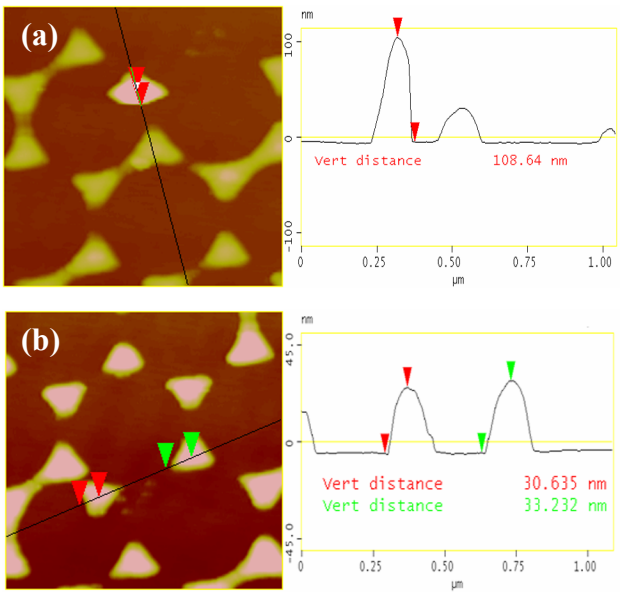

Figure 9-2: (a) An AFM image of a standing nanoparticle. The height of the standing particle is found to be very near the value of its bisector. This observation indicates that the particle is standing on its base. (b) The displaced prisms are thinner. An AFM image of a displaced nanoparticle. Its thickness (indicated by the red cursor) is thinner than the undisplaced one (indicated by the green cursor).

9.3.2 Femtosecond Laser Excitation Induced Nanoparticle Propulsion:

Unlike the shape transformation induced jumping of nanoparticles observed with nanosecond laser irradiation [1], the nanoparticles in the present experiment maintain their prismatic shape. A different mechanism must then account for the propulsion of the nanoprisms with femtosecond laser irradiation.

There are a number of non-radiative relaxation processes that can take place following the surface plasmon excitation of nanoparticles. Following electron-electron relaxation processes on the femtosecond time scale, electron-phonon processes occur on the one picosecond range in gold nanoparticles [6]. If the rate of energy deposition is faster than this, electron ionization occurs, with no size, shape, or lattice temperature

changes in the nanoparticle. If the energy deposition rate allows for electron-phonon relaxation to take place, the lattice heats up. There are a number of channels responsible for cooling the lattice phonons, depending on the energy deposited. At energys that are not high enough to displace the atoms from their equilibrium position, phonon energy of the lattice is transferred to the environment by phonon-phonon processes without a change in shape or size. This usually occurs on the hundreds of picosecond scale [12]. As the energy deposition rate increases and the particle temperature is allowed to reach the melting temperature of the lattice, the nanoparticle changes shape. With sufficient energy and time, the nanoprism is transformed into the thermodynamically most stable shape, which is a sphere. The final temperature depends on the rate of energy deposition compared to the rate of cooling.

The most distinct difference between nanosecond and femtosecond laser irradiation experiments is the rate of energy deposition to the nanoprisms. With nanosecond laser irradiation, the optical excitation rate allows sufficient time for the lattice to melt. With more rapid femtosecond laser excitation, the melting channel is bypassed and the higher energy ablation channel takes over, causing a loss of atoms from the nanoprism surface. This ablation causes the nanoprisms to decrease in size yet retain its original shape. It is well known [13] that atoms can be ejected from a gold surface by high intensity laser irradiation. We believe that the ablation of surface atoms from the nanoprism is due to rapid photothermal heating of the nanoparticles under irradiation at their SPR band by femtosecond laser pulses of an appropriate fluence. The rapid build up of pressure underneath the nanoparticle gives it a sudden impulse that is sufficient for it to dissociate from the substrate and fly.

If the above mechanism is correct, we should observe a change in the nanoparticle thickness as most of the ablated atoms will be from the top and bottom surfaces of the nanoprisms. The resulting pressure at the particle-substrate interface would result from gold atoms ablated from the bottom surface of the particle. We measured the thickness of the displaced nanoparticles with atomic force microscopy (AFM). **Figure 9-2b** clearly shows that the displaced nanoparticle is thinner than the undisplaced nanoparticle. AFM measurements of the non-irradiated nanoparticles indicates an average thickness of 34.1 ± 1.1 nm, while the average thickness of the displaced nanoparticles is 30.8 ± 0.6 nm. If soft melting rather than ablation is responsible for the observed decrease in thickness, an increase in the nanoparticle in-plane dimension should be observed. We observe that the in-plane dimension of the prism decreases as well, again suggesting that ablation, not soft melting, must be responsible for the energy relaxation process.

9.3.3 Calculation of the Ablation Thickness of Flied Nanoprisms:

In order to further examine this mechanism, we calculate the decrease in the nanoprism thickness by ablation. If the ablation of surface atoms is the only mechanism by which the nanoparticle releases the absorbed laser energy, a simple model is proposed, in which all of the absorbed energy from a single pulse is used to vaporize gold atoms from the surface of the nanoparticle. We observed that at the threshold energy, the pulse rate did not change the damage pattern of the nanoprisms on the substrate. This observation suggests that it is the energy spatial distribution of the first laser pulse that governs the damage pattern on the substrate. From the absorption spectrum and the spatial energy density distribution of the laser pulse calculated with Eq. (8-4), we

calculate that one nanoparticle can absorb 7.37×10^{-13} J of energy from one femtosecond laser pulse. The number of ablated gold atom n can be calculated with

$$E = nc_p^s(T_m - T_{r.t.}) + n\Delta H_{fus} + nc_p^l(T_b - T_m) + n\Delta H_{vap}, \quad (9\text{-}1)$$

where c_p^s, c_p^l are the specific heat capacities of solid (25.4 J mol^{-1} K^{-1})and liquid (29.3 J mol^{-1} K^{-1}) gold, respectively; $\Delta H_{fus}, \Delta H_{vap}$ are the enthalpies of fusion (12.55 kJ/mol) and vaporization (324.4 kJ/mol), respectively; T_m, T_b are the melting (1337.73 K) and boiling points (3080 K) of gold, respectively [14]. The number of ablated gold atoms is calculated to be 1.8×10^{-18} mol, which corresponds to a thickness loss of 2.9 nm.

9.3.4 Calculation of the Initial Speed of Flied Nanoparticles:

It is also possible to quantitatively calculate the initial speed of the nanoprism. We assume that the difference between the absorbed energy of the standing nanoparticle (that does not fly) shown as particle 1 and 2 in **Figure 9-1a** and the particle that is able to fly (particle 1 in **Figure 9-1b**) is the kinetic energy given to the flying nanoparticle. We measured the distance from the center of the irradiation point for the standing (r_S) and flying (r_f) nanoparticle under different irradiation intensities. From Eq. (8-4), the intensity difference is given by

$$\Delta I(r_f, r_S) = \frac{2P}{\pi {w_0}^2}\left\{\exp\left(-2\frac{{r_f}^2}{{w_0}^2}\right) - \exp\left(-2\frac{{r_S}^2}{{w_0}^2}\right)\right\}. \quad (9\text{-}2)$$

The measured optical density of the nanoparticle array at 800 nm is 0.1, which consists of absorption and scattering. We assume that the absorption corresponds to 50% of the measured optical density. The particle density is 7.11×10^{8}/cm^2, so the energy

absorbed per particle can be calculated for different irradiation intensities. Based on seven measurements, the difference of absorbed energy between the standing and the flying nanoparticles, $\Delta E(r_f, r_s)$, is calculated to be 51 ± 15 fJ/particle. The initial flying speed at threshold condition can then be calculated to be 164 ± 26 m/s (~367 ± 58 miles/hour) by

$$v = \sqrt{\frac{2\Delta E(r_f, r_s)}{m}}, \tag{9-3}$$

where m is the weight of the nanoprism (3.71 ± 10^{-18} kg). This calculation can then be compared to the reported jumping speed of a nanoprism irradiated by nanosecond laser irradiation (20 m/s) [1].

9.3.5 Calculation of the Lift-off Time of Propelled Nanoparticles:

From the initial speed, we can calculate the take off time of the nanoprism if we assume the pressure generated underneath the nanoprism is constant during the take off step. Since we use femtosecond laser as the ablation source, atomic ablation is very fast. We can assume that the ablated gold atoms have the density of solid gold. Thus, the pressure generated by the ablated gold atoms, P, can be calculated with the ideal gas equation

$$P = \frac{\rho RT}{M}, \tag{9-4}$$

where ρ is the density of solid gold (19.3 g/cm^3), M is the molar mass of gold (196.97 g/mol), and T is the boiling point of gold. P is calculated to be 2.5×10^9 Pa. The force (F) generated by this pressure is 1.6×10^{-5} N ($F = PS$, where S is the base area of the nanoprism, $S = 6.24 \times 10^{-15}$ m^2) if the pressure is assumed to be uniformly applied to the

base of the nanoprism. If we assume the pressure does not change during the full take off step, Newton's second law (the impulse generated by a force is equal to the momentum change of the object) can be used to calculate the take off time Δt from the impulse of the atomic gold pressure.

$$F\Delta t = m\Delta v\,, \tag{9-5}$$

Here, Δv is the initial speed of flying nanoprism after the take off step (164 ± 26 m/s). The take off time is calculated to be 39 ± 6 ps.

9.3.6 The Effect of Substrate Roughness on the Propulsion of Nanoparticles:

The trajectory of the flying nanoprisms must depend on the anisotropy of the pressure build up underneath the nanoparticle. This depends on the interfacial structure between the gold nanoprism and the substrate. We are currently carrying out a study to understand the details of this anisotropy in hopes of being able to control the trajectory of the motion.

To exam the effects of substrate surface roughness on the jumping of gold nanoprisms, we prepared gold nanoprisms on SiO_2 single crystalline surfaces. The surface plasmon bands of these samples are close to 800 nm. We compared the effect of using a rough quartz surface and an ultra smooth SiO_2 single crystal surface on the jumping of the gold nanoprism. Initially, we only compared the standing threshold, which were equal within experimental error. Later we carefully compared the SEM images of various areas of the nanoparticle array around the region that nanoparticle jumping occurs. We find the irradiation patterns on the quartz surface (**Figure 9-3**) have obvious differences compared to those on SiO_2 single crystal surface (**Figure 9-4**) under

equivalent laser irradiation intensity. The nanoparticles on quartz are more disturbed than those on SiO_2. In **Figure 9-3**, aggregates of jumped nanoparticles can be found. Especially In **Figure 9-3a**, the aggregates do not come from nearby nanoparticles because most of the particles still remain at their original locations. The aggregates must jump from higher power irradiation regions, which suggest long distance jumping occurs. However, no aggregates are found on the irradiation pattern of array nanoparticles on SiO_2 single crystal substrate (**Figure 9-4**), which means the nanoparticles do not jump long distance on SiO_2 single crystal substrate.

We statistically compared jumping distances in addition to the jumping thresholds. We counted ~100 jumped particles on each substrate. Particles which appeared to jump more than 450 nm were not include in the statistic measurement since the distance is greater than one period of the array, making it very difficult to accurately find its original position. There were only a few particular situations in which we could measure the jumping distance where the original position was easy to determine.

The histogram of the jumping nanoparticle displacement is shown in **Figure 9-5**, from which it is apparent that the nanoparticle displacement on quartz is greater than that on SiO_2. The same experiment was repeated again to see the reproducibility of the result. The data from two separate days is in good agreement. The distribution of displaced nanoparticles in the histogram resembles a Gaussian distribution. From **Figure 9-5**, we can see that the mean jumping distance on Quartz is around 225 nm, while the mean jumping distance on SiO_2 is between 150 and 175 nm.

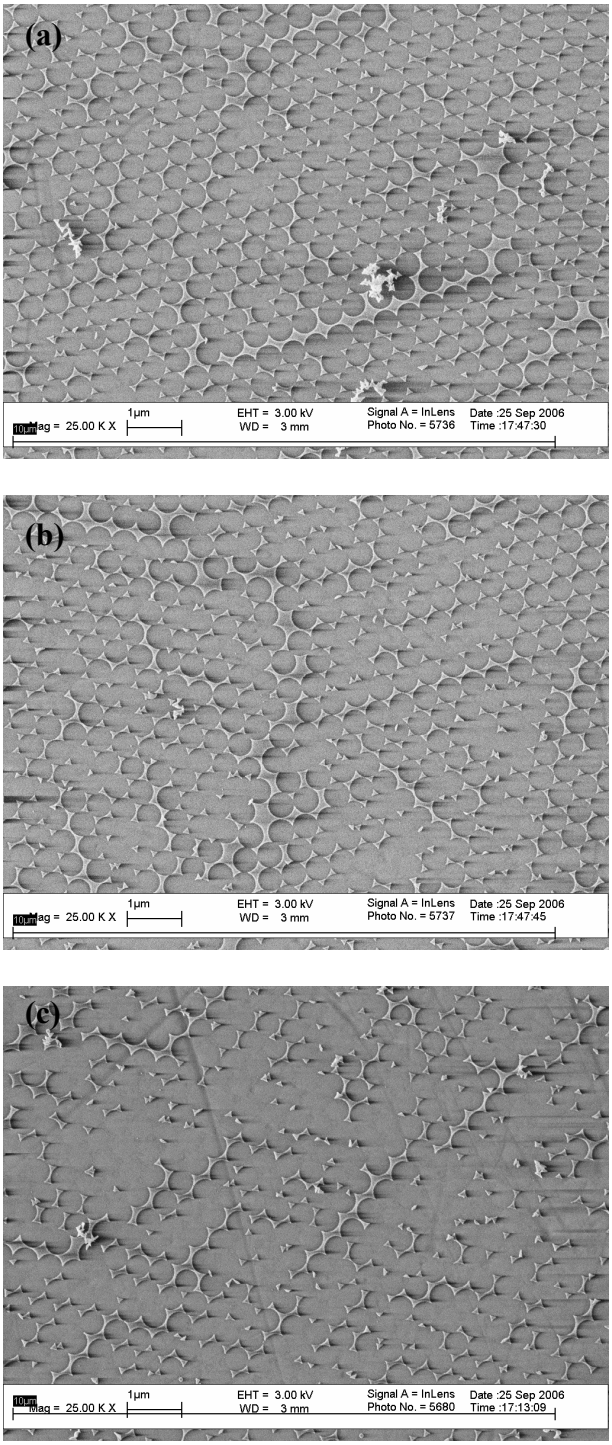

Figure 9-3: SEM images of Au array nanoparticles on the surface of a quartz substrate irradiated near the jumping threshold. From (a) to (c), the irradiation power increases.

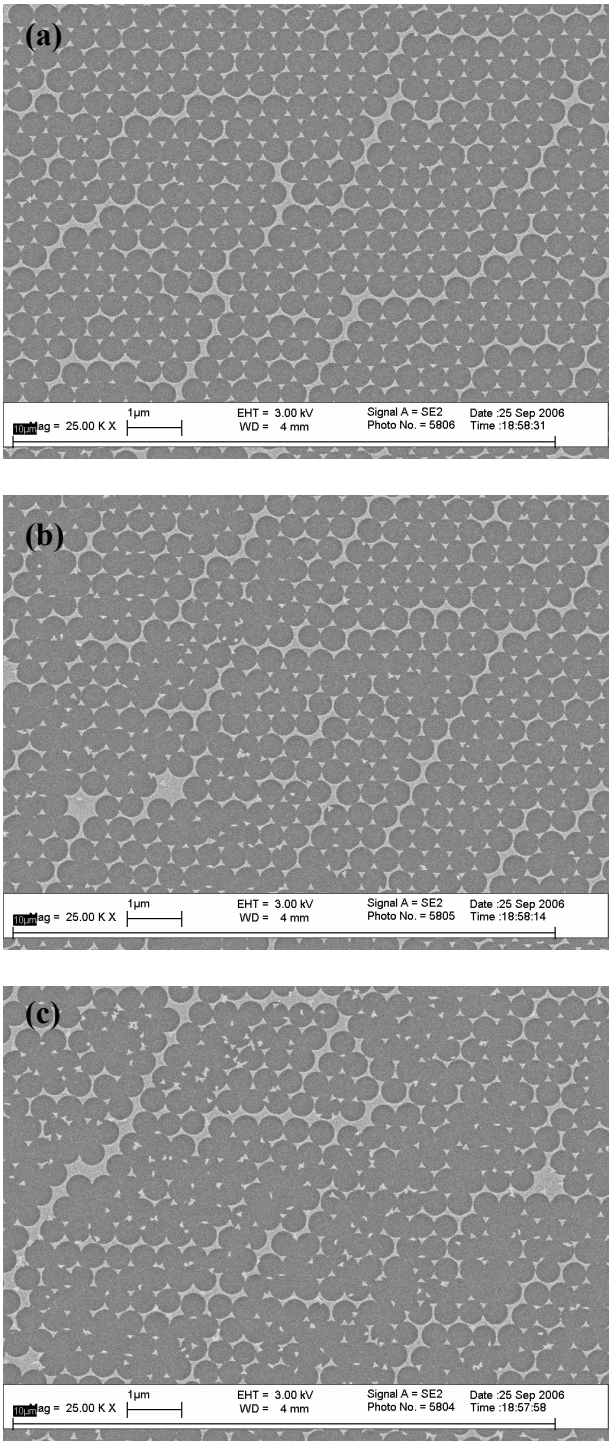

Figure 9-4: SEM images of Au nanoparticles in an array on the surface of a SiO_2 single crystal irradiated near the jumping threshold. From (a) to (c), the irradiation power increases.

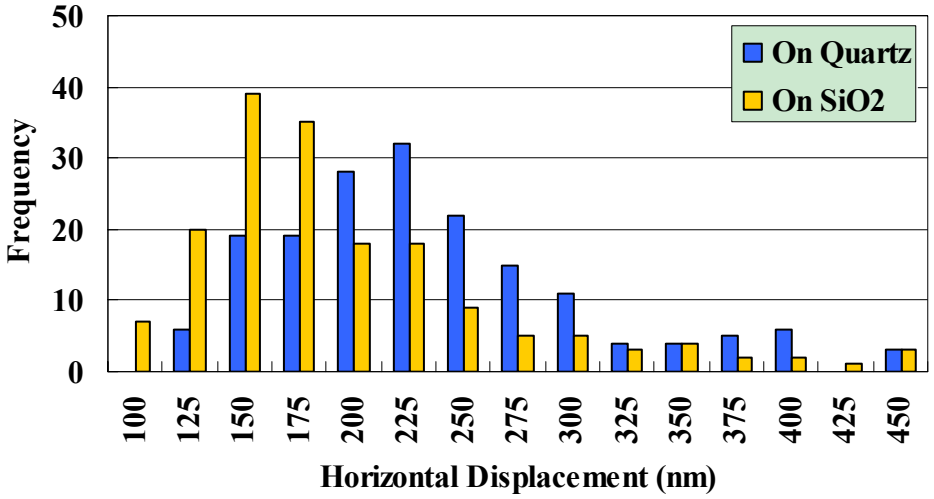

Figure 9-5: The horizontal displacement of jumping nanoparticles on rough quartz and smooth SiO_2 substrate.

Since it is impossible to include long jumping distances (> 450nm), this data should be interpreted as the minimum jumping distances. The actual jumping displacements may differ from the result suggested herein. Comparing the SEM figures, we can qualitatively see that more particles jumped out of the irradiation area on a quartz substrate (**Figure 9-3a**) than on a SiO_2 substrate (**Figure 9-4a**), which suggests that particles on a quartz substrate jump longer distance than those on SiO_2. Therefore, we can draw the conclusion that the horizontal displacement of the jumping gold nanoparticle is larger on the more anisotropic rough quartz surface than that on the isotropic single crystal SiO_2 surface.

In ideal conditions, the gold nanoparticle on a SiO_2 substrate shouldn't have any horizontal displacement if the gold-SiO_2 interface is homogeneous. However, the as-deposited gold nanoparticle itself is not uniform, which consists of many grain

boundaries and cavities. Therefore, the interface of the gold nanoparticle and SiO_2 substrate is not uniform, which is probably the reason that we still observe horizontal displacement for the gold nanoparticle on an isotropic single crystal SiO_2 surface.

9.4 Conclusion

In summary, we observed that the femtosecond laser irradiation of the nanoprisms at the surface plasmon resonance absorption maximum can cause a nanoparticle of 4 femtograms to detach from the substrate and "fly away" at an average threshold energy of 740 fJ/particle. We believe that the forces involved in the motion of the nanoprisms are different from those proposed in the nanosecond laser pulse irradiation [1], in which melting of the nanoparticle necessarily occurs prior to nanoparticle ejection. AFM measurements revealed that the displaced nanoparticles are thinner and smaller than the undisplaced ones, which supports an atomic ablation mechanism. A mechanical mechanism is proposed, in which at threshold or higher fluence rapid atomic ablation rapidly builds up pressure underneath the nanoparticle, which transfers a strong impulse to the nanoparticle. Depending on the laser fluence, this impulse can flip the nanoparticle over or, at higher fluences, can cause the nanoparticle to fly away. The initial speed of the femtosecond laser irradiated nanoparticle is calculated to be eight times faster than that of the nanosecond laser irradiated nanoparticle, which is attributed to the difference in the involved mechanism. The trajectory of the flying nanoprisms must depend on the anisotropy of the pressure build up underneath the nanoparticle. This depends on the interfacial structure between the gold nanoprism and the substrate.

9.5 References

[1] Habenicht, A.; Olapinski, M.; Burmeister, F.; Leiderer, P.; Boneberg, J., *Science* **2005,** 309, (5743), 2043-2045.

[2] Ismagilov, R. F.; Schwartz, A.; Bowden, N.; Whitesides, G. M., *Angew. Chem., Int. Ed.* **2002,** 41, (4), 652-4.

[3] Paxton, W. F.; Kistler, K. C.; Olmeda, C. C.; Sen, A.; St Angelo, S. K.; Cao, Y. Y.; Mallouk, T. E.; Lammert, P. E.; Crespi, V. H., *J. Am. Chem. Soc.* **2004,** 126, (41), 13424-13431.

[4] Fennimore, A. M.; Yuzvinsky, T. D.; Han, W. Q.; Fuhrer, M. S.; Cumings, J.; Zettl, A., *Nature* **2003,** 424, (6947), 408-410.

[5] Fan, D. L.; Zhu, F. Q.; Cammarata, R. C.; Chien, C. L., *Phys. Rev. Lett.* **2005,** 94, (24), 247208.

[6] Link, S.; Ei-Sayed, M. A., *Annu. Rev. Phys. Chem.* **2003,** 54, 331-366.

[7] Link, S.; El-Sayed, M. A., *J. Phys. Chem. B* **1999,** 103, (40), 8410-8426.

[8] Hodak, J. H.; Henglein, A.; Hartland, G. V., *J. Phys. Chem. B* **2000,** 104, (43), 9954-9965.

[9] Zhang, J. Z., *Acc. Chem. Res.* **1997,** 30, (10), 423-429.

[10] Voisin, C.; Del Fatti, N.; Christofilos, D.; Vallee, F., *J. Phys. Chem. B* **2001,** 105, (12), 2264-2280.

[11] Huang, W. Y.; Qian, W.; El-Sayed, M. A., *J. Appl. Phys.* **2005,** 98, (11), 114301.

[12] Link, S.; Hathcock, D. J.; Nikoobakht, B.; El-Sayed, M. A., *Adv. Mater.* **2003,** 15, (5), 393-396.

[13] Gamaly, E. G.; Rode, A. V.; Luther-Davies, B.; Tikhonchuk, V. T., *Phys. Plasmas* **2002,** 9, (3), 949-957.

[14] *CRC Handbook of Chemistry and Physics, 80th ed.* Lide, David R., Ed.; CRC Press: Boca Raton, FL, 1999.

[15] Skinner, D. R.; Whitcher, R. E., *J. Phys. E: Sci. Instrum.* **1972,** 5, (3), 237-238.

APPENDIX: LIST OF PUBLICATIONS

Huang, W. Y.; Qian, W.; El-Sayed, M.A. "The Distance Dependence of the Effect of Surface Plasmon Field on the Coherent Lattice Phonon Oscillation in Electron Beam Nanofabricated Gold Particle Pairs", In Preparation.

Huang, W. Y.; Qian, W.; El-Sayed, M.A. "Gigahertz Optical Modulation Resulting from Coherent Lattice Oscillations Induced by Femtosecond Laser Pumping of 2D Photonic Crystals of Gold Capped Polystyrene Micro-spheres" ***Adv. Mater.***, Submitted.

Huang, W. Y.; Qian, W.; El-Sayed, M.A. "The Optically Detected Coherent Lattice Oscillations in Silver and Gold Monolayer Periodic Nanoprism Arrays: The Effect of Interparticle Coupling," ***J. Phys. Chem. C*****, 2007**, In Press.

Jain, P. K.; Huang, W. Y.; El-Sayed, M. A. "On the Universal Scaling Behavior of the Distance Decay of Plasmon Coupling in Metal Nanoparticle Pairs: A Plasmon Ruler Equation" ***Nano Lett.***, **2007**, ASAP.

Huang, W. Y.; Qian, W.; El-Sayed, M.A. "Gold Nanoparticles Propulsion from Surface Fueled by Absorption of Femtosecond Laser Pulse at Their Surface Plasmon Resonance" ***J. Am. Chem. Soc.*:*Communication***, **2006**, 128 (41), 13330-13331.

Qian, W.; Huang, W. Y.; Darugar, Q.; El-Sayed, M. A. "Ultrafast Electronic and Lattice Process of Plasmonic Nanoparticles of Different Shape," ***Femtochemistry VII: Fundamental Ultrafast Processes in Chemistry, Physics, and Biology*****,** eds. A. W. Castleman, Jr. and Michele Kimble, Amsterdam: Elsevier, **2006**, 260-273.

Huang, W. Y.; Qian, W.; El-Sayed, M.A. "The Optically Detected Coherent Lattice Oscillations in Silver and Gold Monolayer Periodic Nanoprism Arrays: The Effect of Interparticle Coupling," ***J. Phys. Chem. B*****, 2005**, *109*, 18881-18888.

Huang, W. Y.; Qian, W.; El-Sayed, M.A. "Photothermal Reshaping of Prismatic Au Nanoparticles in Periodic Monolayer Arrays by Femtosecond Laser Pulses," ***J. App. Phys.***, **2005**, *98*, 114301.

Huang, W. Y.; Qian, W.; El-Sayed, M.A. "Optically Detected Coherent Picosecond Lattice Sscillations in Two Dimensional Arrays of Gold Nanocrystals of Different Sizes and Shapes Induced by Femtosecond Laser Pulses," ***Proc. SPIE Int. Soc. Opt. Eng.*** **2005**, 5927, 592701.

Huang, W. Y.; Qian, W.; El-Sayed, M.A. "Coherent Vibrational Oscillation in Gold Prismatic Monolayer Periodic Nanoparticle Arrays," ***Nano Lett.*** **2004**, *4*, 1741-1747.

Eustis, S.; Krylova, G.; Smirnova, N.; Eremenko, A.; Tabor, C.; Huang, W. Y.; El-Sayed, M. A. "Using silica films and powders modified with benzophenone to photoreduce silver nanoparticles," ***J. Photochem. Photobiol. A*** **2006,** 181, (2-3), 385-393.

Gnatyuk, Yu.; Manuilov, E.; Smirnova, N.; Huang, W.Y.; Eremenko, A. "Sol-gel produced mesoporous TiO_2/Ag coatings effective in Rhodamine B photooxidation," ***NATO Science series "Funtional properties of nanostructured materials"*** edited by R. Kassing, P.Petkov, W.Kulish and C.Popov, II. Mathematics, Physics and Chemistry **2006**, 223, 485-490

Vityuk, N.; Busko, T.; Eremenko, A.; Smirnova, N.; Kulish, M.; Dmitrenko, O.; Stashuk, V.; Huang, W. Y. "Spectral, electronic and photocatalytic properties of sol-gel derived ternary $TiO_2/ZrO_2/SiO_2$ films and powders modified with noble metal particles" ***Proceedings of X Ukrainian-Polish symposium*** **2006**, 206-208.